GEM TN-93-408

GEM Central Tracker

Progress Report

May 15, 1993

TN-93-408

GEM CENTRAL TRACKER

PROGRESS REPORT

MAY 15, 1993

The Central Tracking Group

Academia Sinica, Taiwan, R.O.C.
A. Antos, Y.C. Chen, T.L. Chu, M. Huang, S.C. Lee, A. Sumarokov, P.K. Teng, M.J. Wang, P. Yeh

Brookhaven
P. O'Connor, V. Radeka, G. Smith, B. Yu

Indiana University
C. Bender, C. Bower, M. Gebhard, R. Heinz, S. Mufson, J. Musser, J. Pitts

Los Alamos
R. Barber, J.G. Boissevain, M. Brooks, D. Brown, M. Cafferty, B. Cooke, K. Fuller,, S.F. Hahn, J. Hanlow, C. Johnson, J. Kapustinsky, W.W. Kinnison, D.M. Lee, R. Martin, G.B. Mills, R. Prael, G.H. Sanders, W.E. Sondheim, T. Thompson, J. VanAnne, L. Waters, B. Weinstein,

Moscow State University
G. Bashindzhagyan, Y. Fisyak, D. Karmanov, E. Kuznetsov, A. Larichev, M. Merkin, A. Savin, A. Voronin, V. Zhukov

Nanjing University
E. Chen, D. Gao, M. Qi, D.X. Xie, N.G. Yao, Z.W. Zhang

Oak Ridge National Laboratory
C. Britton, K. Read

Rutgers University
P. Jacques, M. Kalelkar, R.J. Plano, P. Stamer, G.B. Word

SSCL
S. Blumberg, H. Fenker, K. Morgan, I. Sheer, J. Thomas

University of Albany
M.S. Alam, I.J. Kim, B. Neman, J. O'Neill, H. Severini, C.R. Sun, L. Zhichao

University of Michigan
D Kouba, D. Levin, J. Mann, S. McKee, G. Tarle

University of Oregon
A. Arodzero, J. Brau, R. Frey, K. Furuno, R.T. Kollipara, D. Strom

Yale University
C. Baltay, M.B. Barakat, R. Ben-David, W. Emmet, S. Manly, D. Pilon, S. Sen, J. Sinnott, J. Turk, E. Wolin

Central Tracker Steering Committee
C. Baltay (Chairman), J. Brau, D. Lee, S.C. Lee, K. Morgan, J. Musser, T. Thompson

Contents

1. Introduction **1**
1.1. Physics Goals of the Central Tracker 1
1.2. Design Considerations 2
1.3. Detector Configuration 5
1.4. Rationale for Choice of Detector Configuration 6
1.5. Performance Parameters 10

2. Detector Simulation and Performance **16**
2.1. Tracker Parameters 16
2.1.1. Position Resolutions 16
2.2 Tracker Intrinsic Performance 18
2.2.1. Detector Resolutions 18
2.2.2. Pattern Recognition 21
2.2.3. Multitrack Resolution 23
2.2.4. Vertex Z Resolution 27
2.3. Physics Performance 28
2.3.1. Vertex Z Resolution and γ Direction Measurements 28
2.3.2. Electron/Gamma ID 29
2.3.3. Electron/Hadron Separation 31
2.3.4. Muon Identification and Measurement 32
2.3.5. Charge Sign Determination for Electrons 35
2.3.6. Help with Isolation Cuts 37
2.3.7. Tau Identification 38
2.3.8. Secondary Vertex (b-tagging) 39
2.4. Alignment and Calibration 40
2.5 References 41

3. The Silicon Detector **42**
3.1. Design Considerations 42
3.1.1. Design Parameters 42
3.1.2. Choice of Silicon Microstrip for Inner Tracker 42
3.1.3. Microstrip response 43
3.1.4. Strip Length Considerations 45

3.2. Silicon Tracking System Mechanical Design 47
3.2.1. Material Considerations 51
3.2.2. Gas Enclosures 54
3.2.3. Space Frame 58
3.2.4. Central Region 67
3.2.5. Forward Region 71
3.2.6. Cooling System 74
3.2.7. Silicon Alignment and Detector Monitoring Systems 84
3.2.8. Silicon Ladder 87
3.2.9 Central Tracker Stability 97
3.3 The Silicon Tracker Electronics 102
3.3.1 Introduction 102
3.3.2 Electronics Design 107

4. The IPC Detector 121
4.1 The Interpolating Pad Chamber Outer Tracker 121
4.1.1. Interpolating Pad Chambers 121
4.1.2. Geometrical Charge Division 122
4.1.3. Design Parameters 123
4.1.4. Chamber Geometry 123
4.1.5. Occupancy 123
4.1.6. Position Resolution 125
4.1.7. Position Resolution Degradation Due to Non-Normal Incidence 127
4.1.8. Rate Effects 132
4.2 IPC Tracker Mechanical Design 133
4.2.1 Introduction 133
4.2.2 IPC Barrel Superlayer Module Design 135
4.2.3 IPC Endcap Superlayer Module Design 148
4.2.4 IPC Endcap Support Structure 148
4.2.5. OuterSupport Structure 150
4.2.6. IPC Detector Gas System 156
4.2.7 IPC Detector Electronics Cooling System 163
4.3 IPC Front End Electronics 174

5. Integration into GEM **191**
5.1. Installation and Alignment 191
5.2. Services and Connections 192
5.3. Access 193
5.4. Surface Facilities 193
5.5. Safety and Environmental Impact 194

6. Radiation Environment **195**
6.1. Radiation Dose Due to Charged Particles 195
6.2. Neutral Particle Backgrounds 197
6.2.1. Neutral Particle Fluences and Dose Rates 197
6.2.2 Backgrounds from Neutral Particles 198
6.2.3 Activation of Central Tracker Components 198
6.3. Lifetime Expectancy of the Central Tracker 199

7. R & D Program **200**
7.1 Silicon R&D 200
7.1.1 Microstrip Detector R&D 200
7.2 IPC R&D Program 207
7.2.1. Chamber Development 207
7.2.2 Generic IPC Chamber R&D 207
7.2.3. IPC Mechanical R&D 216
7.2.4. The Full Scale IPC Prototype Project 216
7.2.5. Interpolating Pad Chamber Electronics R&D 219
7.3. Test Beam Plans 220
7.3.1. Silicon Detectors 220

8. Organization & Management **225**
8.1. The Central Tracker Group 225
8.2. Personal and Institutional Responsibilities 227

9. Schedules **229**

1. INTRODUCTION

1.1. Physics Goals of the Central Tracker

The physics goals for the central tracking in GEM can be divided into two categories. The first are those features that are required to support the primary objectives of GEM, namely the detection of gammas, electrons and muons at high p_t. Some examples of these are:

- Identify the primary vertex of an event of interest, so that it can be separated from other pileup events in the memory time of the detector.
- Separate electrons and gammas using the presence or absence of a charged track pointing to an electromagnetic shower in the calorimeter.
- Help with electron-hadron separation by providing a momentum measurement that can be compared with the energy deposition in the calorimeter.
- Help with rejection of fake muon backgrounds by matching the muon momentum measured in the central tracker with the momentum measured in the muon chambers.
- Determine the electron sign up to ~600 GeV/c.
- Provide track information for e, μ or γ isolation cuts, and to help with rejection of conversions and Dalitz pairs.
- Separation of close together multi-charged particle tracks from single charged particle tracks which will be useful in tagging tau decays and γ conversions.

The tracker should be able to fulfull these goals well at the design luminosity of $10^{33}\text{cm}^{-2}\text{s}^{-1}$. These capabilities should also survive to luminosities up to $10^{34}\text{cm}^{-2}\text{s}^{-1}$. These minumum goals do not require full pattern recognition, but can be met by looking for hits in the tracker in a specific road extrapolated from the calorimeter or the muon system.

The second category of physics goals are more ambitious:

- Full reconstruction of the charged tracks in the event.
- Secondary vertex finding.
- Tracking at low momenta with good resolution.

These features would enhance GEM's ability to address issues such as b and top physics. They are more demanding in that they require pattern recognition capabilities and very good vertex resolution. It is expected that these more ambitious goals can be met at luminosities up to $10^{33}cm^{-2}s^{-1}$, but probably not much higher. This, however, seems satisfactory since the physics topics requiring these more ambitious features have relatively large crossections and can thus be studied at luminosities of $10^{33}cm^{-2}s^{-1}$ or below.

1.2. Design Considerations

The Central Tracker of the GEM detector is designed to operate in the 0.8 Tesla magnetic field of the large GEM superconducting solenoid. The tracker is compact, with a 90 cm outer radius and a total length of 350 cm. It covers a pseudorapidity range of ± 2.5units. The present baseline design consists of a Silicon Microstrip (SM) inner tracker and an Interpolating Pad Chamber (IPC) outer tracker. The geometry of the Central Tracker in this design is shown in Figures 1-1 and 1-2.

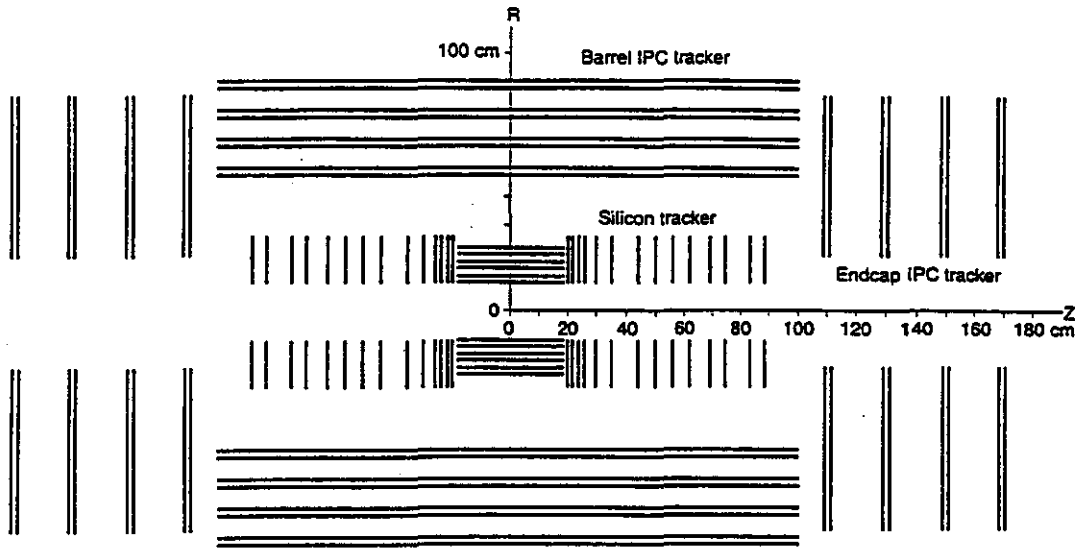

Figure 1-1(a)

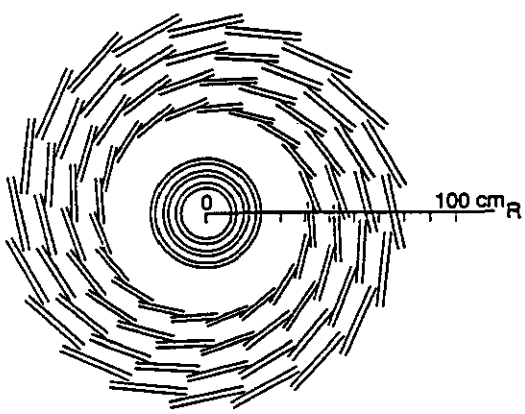

Section at 90°

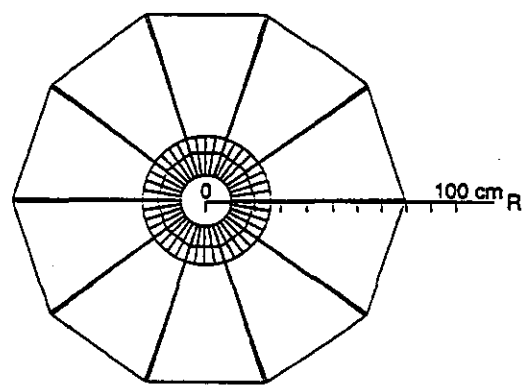

View in Z direction

Figure 1-1(b)

Figure 1-1(c)

Figure 1-1 Schematic layout of the detector elements in the GEM Central Tracker, (a) Plan view. b) Section through the barrel at 90^0 c) End view of the forward detectors

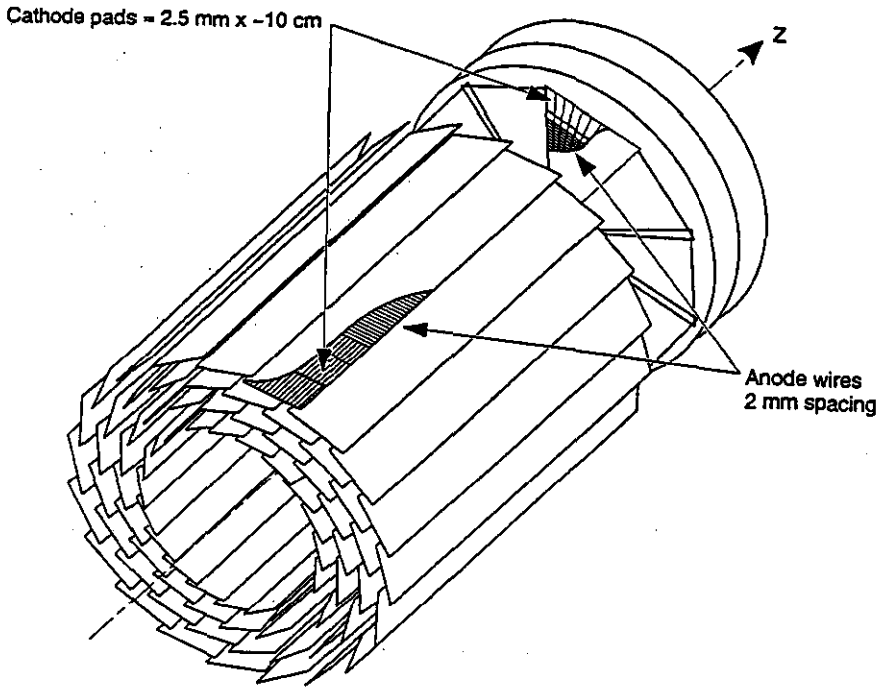

Figure 1-2 Schematic layout of the detector elements in the GEM Central Tracker

Since the submission of the GEM Expression of Interest, a variety of technologies were pixels and long drift length silicon detectors were discussed. Silicon pixel and long drift silicon detectors were considered to be too immature, with large uncertainties of performance, radiation resistance, and costs, to be a sensible choice at this time. Silicon microstrip detectors were chosen as the baseline design for the following reason:

1. The very fine segmentation possible combined with proven high radiation resistance make this detector ideal as the element closest (~ 10 cm) to the interaction point.

2. Very high spatial resolution allows very precise vertex position and track impact parameter measurement.

3. It is a mature technology, which is presently in use in a number of fixed target and collider experiments with relatively well understood performance, radiation resistance and cost properties.

Silicon detectors were considered to be too expensive for the outer tracker. Technnologies under serious discussion for outer tracker were Straw Tubes, Scintillating Fibers and Interpolating Cathode Pad Chambers. The Interpolating Pad Chambers were chosen for the baseline design for the following reasons:

4. Pad sizes of the order of a few cm^2 in area are quite natural. This allows for a low occupancy even at a luminosity of $10^{34} cm^{-2} sec^{-1}$. Thus, this technology is suitable even at the highest luminosities of the SSC. The other technologies would result in considerably higher occupancies.

5. The pads, in some approximation, approach 3 dimensional points, which is quite important for good tracking in the high rate and multiplicity environment of the SSC. The two other technologies produce stereo images i.e. all tracks projected onto a plane, which make pattern recognition more difficult in this environment.

6. Interpolating Pad Chambers are not a new technology; they have been demonstrated to have the resolution needed with chamber sizes similar to those required for the GEM tracker design.

1.3. Detector Configuration

The Silicon Microstrip inner tracker consists of six layers of silicon strip detectors. Each layer is composed of two back-to-back single sided silicon sensors with a ± 5 mrad stereo angle between the two sensors. Each sensor is 300 μm thick with a strip pitch of 50 μm. Each pair of sensors provides a space point with a resolution of 15 μm in the r-ϕ plane and 3 mm in the r-z projection. The six layers of ladders are organized into three superlayers, each of which provides a track stub to a track finding algorithm. In the forward region, the silicon sensors are mounted into disks with the strips projecting radially inward toward the beam axis. The Silicon Tracker is ~200 cm long and extends in a radius from 10 to 35 cm. The total area of silicon ladders in the detector is about 7 m^2 with about 3.5×10^6 strips to be read out. The read-out will be highly multiplexed, with 1028 strips to one fiber optic readout channel, for a total readout channel count of 3500.

The outer tracker consists of 8 layers of pad chambers, both in the barrel region at radii between 35 and 80 cm, and in the forward region which extends from 110 to 170 cm from the interaction point. The 8 layers are arranged in 4 superlayers with 2 layers each. Each barrel layer will consist of 20 chambers, each covering 18° in azimuth, with the largest chamber being 30 cm wide × 200 cm long. The forward layers will be disks divided into ten trapezoidal chambers about 60 cm × 60 cm each.

The pad sizes vary around an average of $\Delta\eta \times \Delta\phi = 0.0007$ which insures a low occupancy even at luminosities of 10^{34} / cm^2 / sec, with a total of just under 400,000 pads for the entire device. The pads are 2.5 mm wide (in the "ϕ direction") and a few centimeters long (in the z direction, which is the direction along the beams). With an analog readout we expect to interpolate to obtain a precision in the "ϕ direction" of ~ 50 μm. To obtain better precision than the pad length in the z direction, the pads will be tilted by ±50 mrad in the two layers of each superlayer, respectively. This stereo angle will provide a z resolution of ~ 700 μm, which is good enough to provide a vertex z resolution of ≤ 2 mm from the IPC's alone, so that this vertex z resolution will be available at the highest luminosities at the SSC.

The wires will not be read out in the IPC's since all of the information comes from the pads. The readout electronics for each pad include a fast front end amplifier and shaper feeding an analog pipeline which is multiplexed at the output by a factor of 128, giving a total of 3200 channels.

1.4. Rationale for Choice of Detector Configuration

The brief summary for the choice of the various parameters that define the configuration of the Central Tracker are as follows.

a) Inner radius of silicon detector. The impact parameter resolution improves as the inner radius of the Silicon Detector is decreased. However, the radiation dose of the innermost silicon layer increases as $1/R^2$. The resolution and the radiation dose are shown as a function of R_{min}, the inside radius of the Silicon detector, in Figure 1-3. A safe lifetime dose that silicon detectors can tolerate is around 5 Mrads. This sets the safe lower limit on the inner radius to around 10 cm.

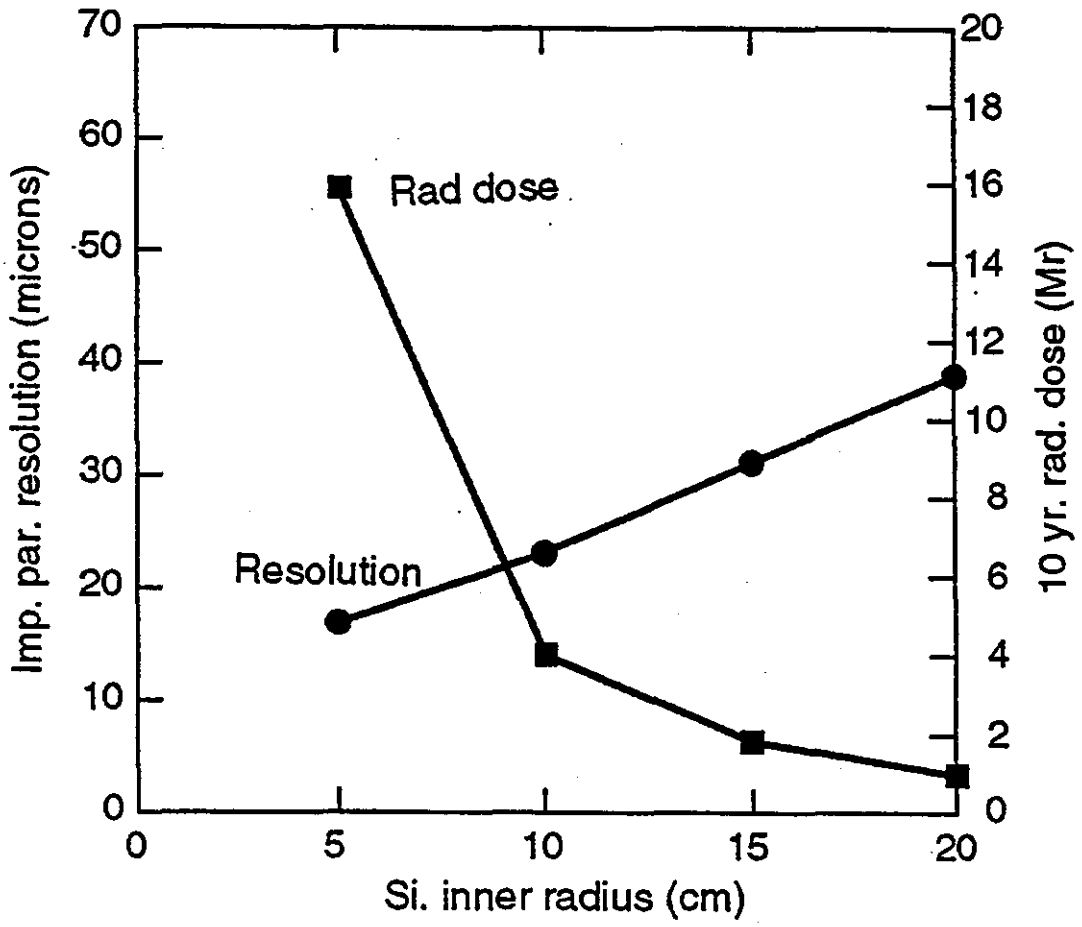

Figure 1-3 Impact parameter resolution and 10-year radiation dose as a function of the inner radius of the silicon detector.

b) Outside radius of the Silicon Detector. Increasing R_{max}, the outer radius of the silicon detector, improves the impact parameter determination. However, the area of silicon required and therefore the cost (~2M$ per square meter, including electronics) goes up like R^2_{max} (keeping the same y coverage). These quantities are show as a function of R_{max} in Figure 1-4. R_{max} was chosen to be 22 cm in the present design. R_{max} smaller than this is not practical mechanically. Increasing R_{max} beyond this value does not improve the impact parameter resolution very rapidly, but would drive up the cost of the silicon system considerably (see Figure 1-4).

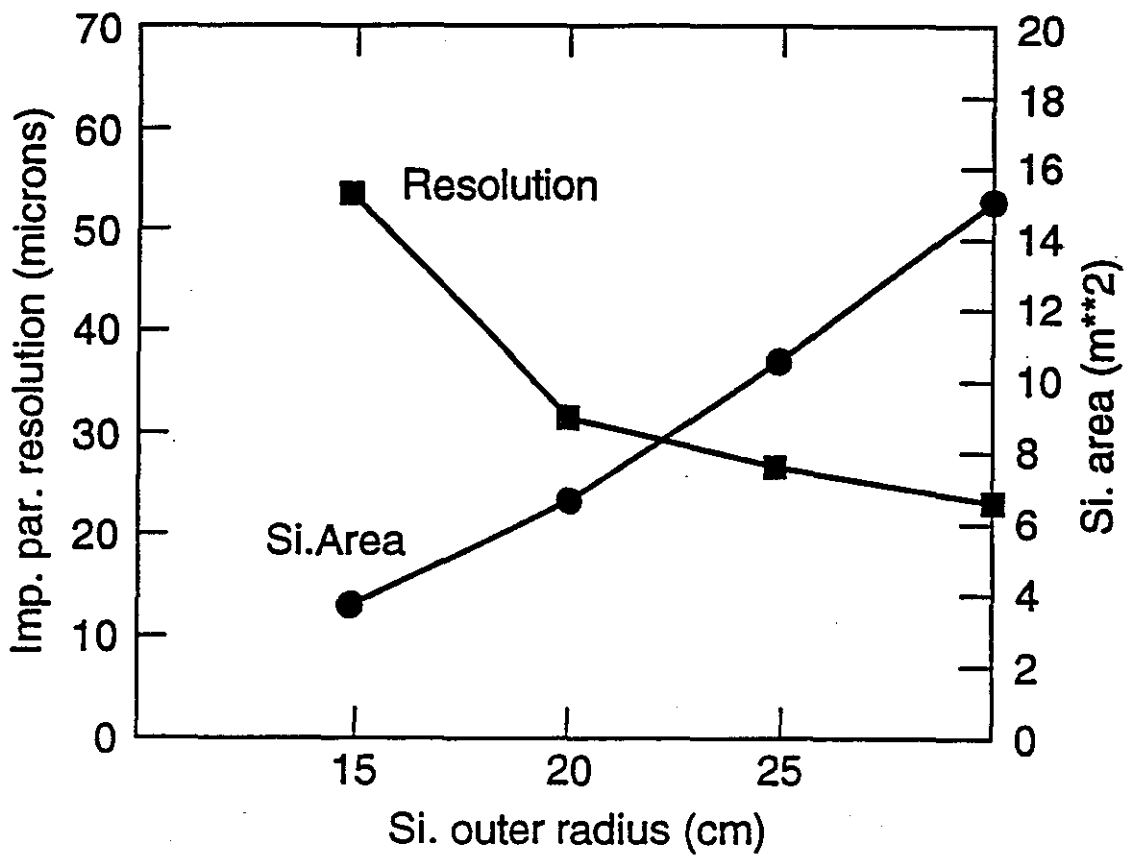

Figure 1-4 Impact parameter resolution and area of silicon detectors as a function of the outer radius of the silicon detector

c) Silicon microstrip pitch and strip length. The 50μ pitch of the present design is now quite standard for silicon detectors and provides adequate resolution and low occupancy. The silicon strip length was chosen to be 18 cm. This length simplifies the mechanical design; it allows the elimination of support rings near the center of the barrel, and allows all electronics to be at the ends of the barrel and the outside edges of the forward disk, with all the cooling and cabling on the outer edges as well. Strip lengths longer then 18 cm would not be practical because of signal to noise considerations.

d) Pad size and channel count in the IPC detector is determined by the requirements to keep the occupancy sufficiently low to allow the IPC tracker to operate at luminosities up to 10^{34} / cm^2 / sec. Previous experience with trackers indicates that the performance degrades significantly at occupancies above 10%. The pad sizes in this design, averaging $\Delta\eta\Delta\phi \sim 0.0007$ meet this requirement with some safety margin. These pad sizes lead to a total number of pads in the system in the vicinity of 400,000. Increasing the number of pads beyond this would be nice, but not necessary, and the increase of the cost of the electronics would be quite significant.

e) Outer radius of the Central Tracker. The magnetic field of 0.8T is determined by an optimization of the muon system and magnet cost vs. performance. At this fixed field the momentum resolution of the Central Tracker improves roughly like the square of the outer radius, R^2_{max}. From the point of view of the tracker, a larger R_{max} would be clearly better. If the number of layers and the electronics channel count were kept fixed as R_{max} increases the cost of the tracker would not increase very much. The cost constraint comes from the calorimeter cost, which increases very roughly by ~10M$ with a 25 cm increase in Tracker radius (see Figure 1-5). An inner radius of around a meter makes the EM calorimeter tower sizes at the chosen η and ϕ segmentation convenient from a mechanical point of view as well as appropriate in comparison with the Moliere radius of and EM shower. Thus, the tracker outer radius was set in large part by the optimization of the calorimeter.

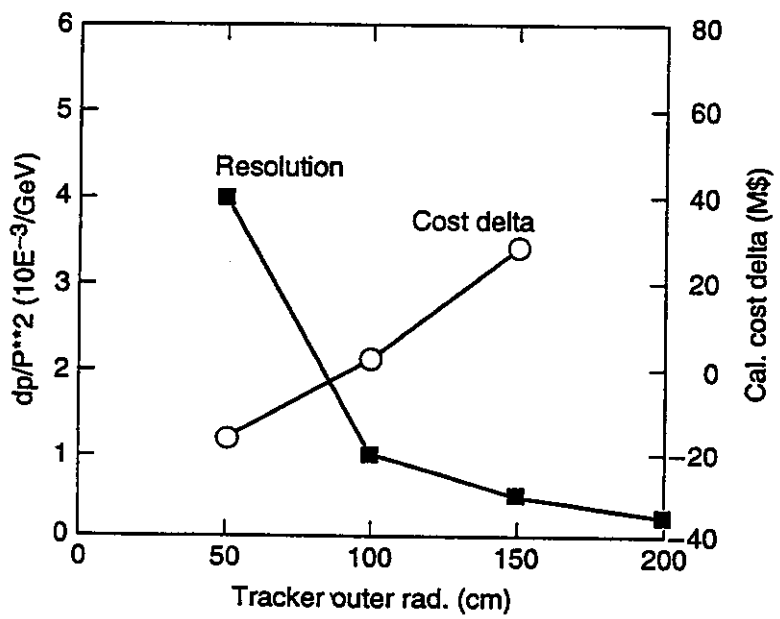

Figure 1-5 Momentum resolution and the incremental cost of the Calorimeter as a function of the Central Tracker outer radius

f) The number of layers of silicon and IPC's was set by the desire to have a reasonable pattern recognition efficiency. Much less than the 14 layers of this design would not allow acceptable track reconstruction efficiency in the high rate environment of the SSC. The momentum resolution improves like the square root of the number of layers, and the electron gamma separation also improves with more layers. Increasing the number of layers much over the present design would not be possible both because of space considerations and the significant increase in cost.

g) The stereo angles in the silicon and IPC Detectors. Larger stereo angles give better z resolution but also increase the probability of multi-track ambiguities. The present design of ± 5 mr in the silicon and ± 50 mr in the IPC is large enough to provide the required z resolution of around a millimeter (see Figure 1-12) while keeping the probability of multi-track ambiguities below ~1% at 10^{33} and below 10% in the IPC at $L = 10^{34}$.

1.5. Performance Parameters

The design parameters for the central tracker that will satisfy the physics goals outlined above are summarized in Table 1-1.

Table 1-1 Design parameters for the central tracker

Outer Radius	90 cm
Length	350 cm
Rapidity Coverage	$\lvert\eta\rvert \leq 2.5$
Magnetic Field	0.8 T
Occupancy	
at $L = 10^{33}\,\mathrm{cm}^{-2}\mathrm{sec}^{-1}$	$\leq 1\%$
at $L = 10^{34}\,\mathrm{cm}^{-2}\mathrm{sec}^{-1}$	$\leq 10\%$
Charge separation at 95% c.l.	$p \leq 600\,\mathrm{GeV}/c$
Momentum Resolution at high momenta(measurement limited)	$\Delta p / p^2 \sim (1.2) \times 10^{-3}\ (\mathrm{GeV}/c)^{-1}$
at low momenta (multiple scattering limited)	$\Delta p / p \sim 3.5\%$
Vertex Resolution	
along beam direction	$\delta z \sim 1$ mm
impact parameter	$\delta b \sim 25\ \mu$m above 10 GeV/c

Table 1-2 Design parameters for the central tracker

Silicon microstrips resolution/layer	10 μm
Silicon alignment stability	10 μm
Pad chamber resolution	50 μm
Pad chamber alignment stability	25 μm

A GEANT based Monte Carlo simulation program is now ready and running with a detailed description of the Central Tracker. The simulation includes our current best estimate of the amount of material in the silicon, the pad chambers, the support structures, the cooling loops, gas piping, the front end electronics, and cables. The amount of material, in units of percents of a radiation length, averaged over ϕ is shown as a function of η in Figure 1-6. The average amount of material before the outermost layer of the tracker at 90° is in the vicinity of ~15% of a radiation length.

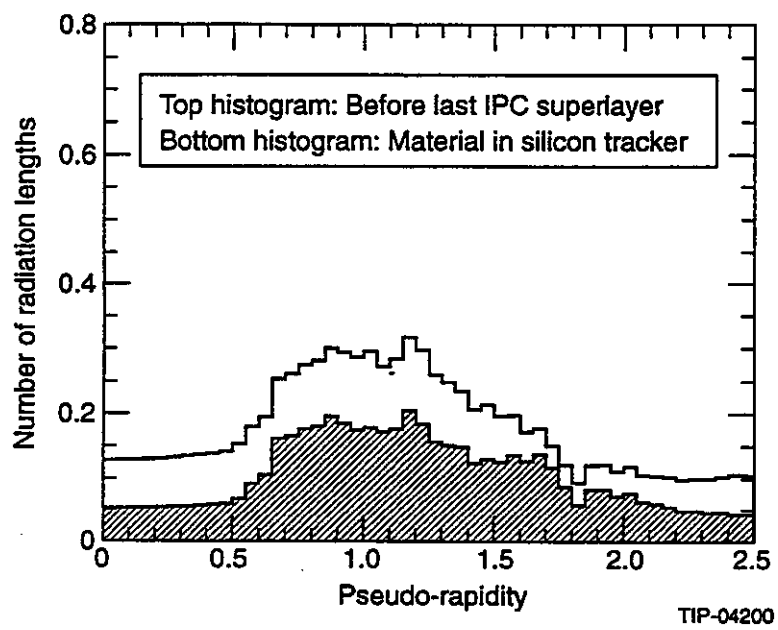

Figure 1-6 Material, in units of radiation length, in the Central Tracker.Bottom curve is the silicon detector only; the upper curve includes the IPC tracker up to the outermost detector layer.

This simulation assumes the chamber resolutions as shown in Table 1-2. With this input, and the amount of material discussed above, the momentum resolution of the tracker, given the 0.8 T field, was calculated. Figure 1-7 shows the momentum resolution at 90° as a function of momentum. For this curve it was assumed that a reconstructed vertex point from several tracks in each event can be used in the best fit for each track. For the highest momentum, the multiple scattering is negligible, and we see that the measurement error near 90° is $\Delta p / p \sim 1 \times 10^{-3} \times p(\mathrm{GeV}/c)$. The resolution at low momentum is dominated by multiple scattering, which limits the low momentum resolution near 90° to $\Delta p / p \sim 3.5\%$.

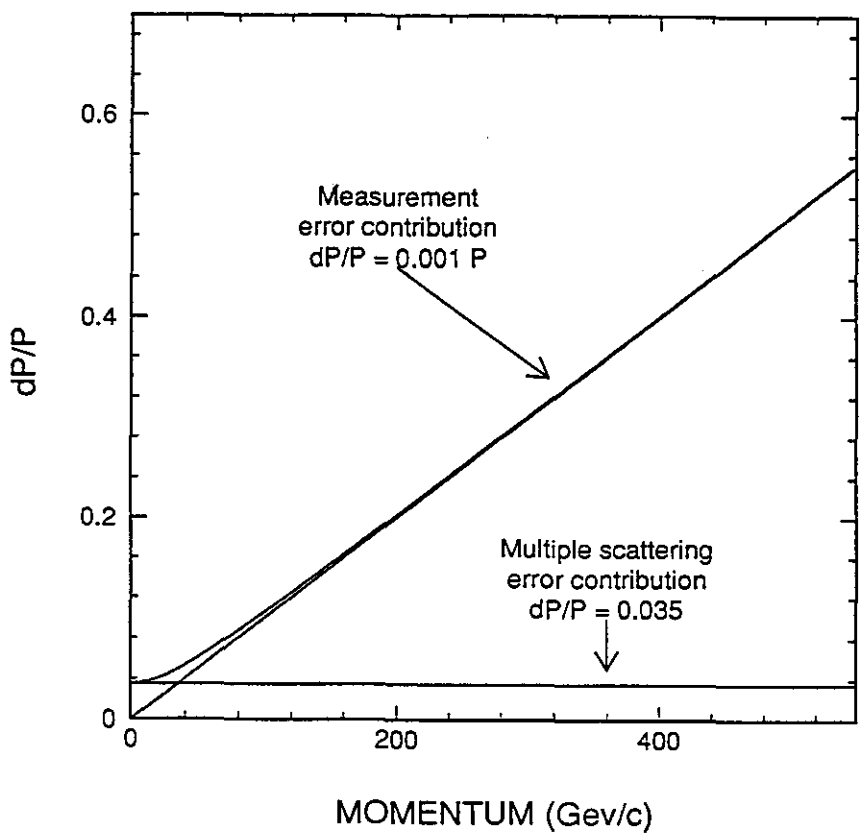

Figure 1-7 Momentum resolution as a function of momentum for the central tracker.

Figure 1-8 shows the momentum resolution as a function of η. The momentum up to which the sign of a particle can be determined to a 95% confidence level has been calculated and is shown in Figure 1-9 for both muons and electrons.

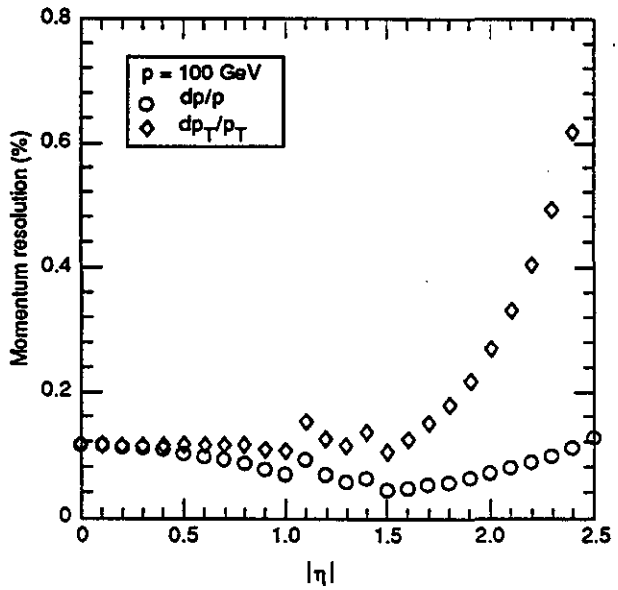

Figure 1-8 Momentum resolution for 100 GeV/c tracks as a function of pseudorapidity η.

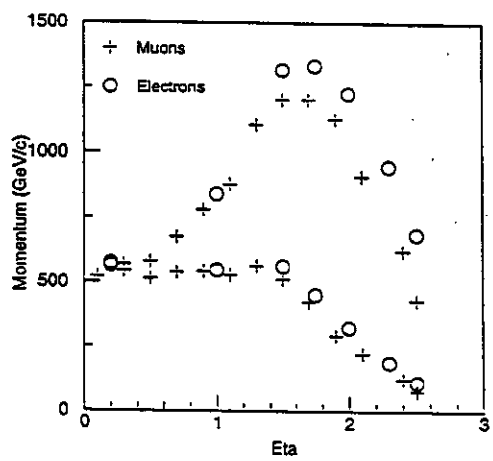

Figure 1-9 Momentum up to which the sign of the charge of muons and electrons can be measured with 95% confidence level. The upper curve is for total momentum P; the lower curve is for transverse momentum P_t.

Figure 1-10 and 1-11 show the impact parameter resolution as a function of momentum and rapidity, respectively. Figure 1-12 shows the Z-resolution at the vertex for a single track. The upper curve is for the IPC's alone, as will be the case at 10^{34} / cm^2 / sec. The determination of the vertex position will usually use many tracks so that the resolution will be correspondingly better.

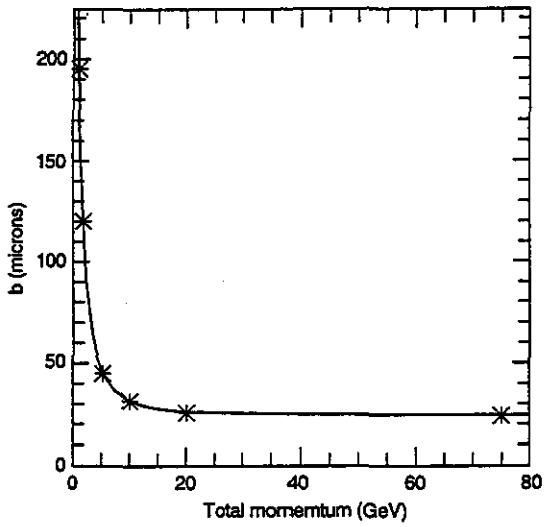

Figure 1-10 Resolution in the impact parameter b at the event vertex as a function of momentum.

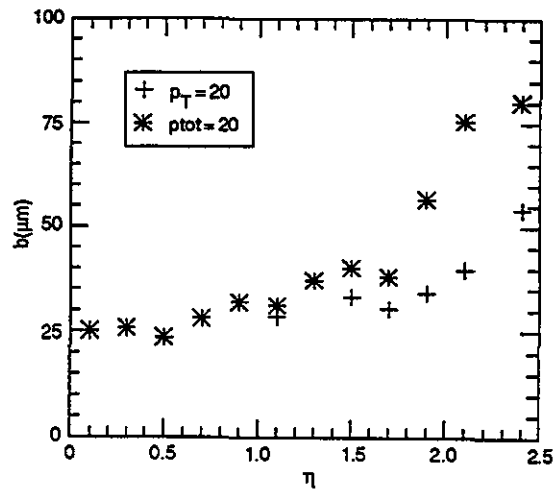

Figure 1-11 Resolution in the impact parameter b at the event vertex for 20 GeV/c tracks as a function of pseudorapidity η

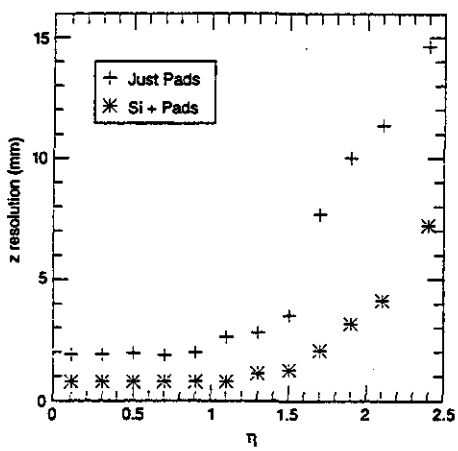

Figure 1-12 Resolution in the vertex intercept in the direction along the beams (z) for a simgle track.

The GEANT Simulation was also used to estimate the occupancy in various parts of the detector. These calculations included the primary tracks produced in the *pp* collisions as generated by PYTHIA (which agree quite well with $dn / d\eta d\phi \sim 1$ charged track per event) as well as secondaries produced in interactions, gamma conversions in the material of the tracker, and loopers i.e. low energy particles curling up in the magnetic field producing multiple hits in the tracker. In this calculation, it was assumed that the silicon detector integrates over one crossing only while the pad detector integrates over two crossings of the beams. Near 90°, the occupancy in the silicon is less than 0.1%, and in the pads it is around 0.4% per pad at a luminosity of $10^{33}cm^{-2}s^{-1}$ and around 4% at a luminosity of $10^{34}cm^{-2}s^{-1}$. We therefore expect that the pad detector would perform well even at the highest luminosities of the SSC.

2. DETECTOR SIMULATION AND PERFORMANCE

2.1. Tracker Parameters

2.1.1. Position Resolutions

The technologies chosen for the GEM Central Tracker (silicon microstrips and interpolating pads) must provide the position resolution necessary to achieve the overall momentum and other track measurement requirements. Silicon microstrip detectors are in widespread use with demonstrated resolutions of about 15 microns for normal incidence with 50 micron pitch detectors. This level of performance achieves the desired resolutions for momentum measurement and vertex reconstruction, as will be demonstrated in section 2.2 below. This performance is achieved without analog information on charge sharing between strips, although double strip hits for non-normal incidence can reduce the resolution to about 10 microns. In the GEM Central Tracker, the microstrip detectors are aligned with their microstrips running approximately axially. The longitudinal position is obtained by a small stereo angle between pairs of strips. The longitudinal resolution (δz) of two strips with a half-angle of ϕ between the two strips (called the stereo angle) and with a single strip transverse resolution σ, is

$$\delta z = \frac{\sigma}{\sqrt{2}\phi}$$

The ambiguity of paired strips increases with the stereo angle. Larger stereo angles increase the likelihood that a pair of tracks will cross strips with common partners and lead to an ambiguous matching of the strips. Therefore, one cannot arbitrarily increase this angle in the GEM environment. Nevertheless, based on the nominal occupancies in the GEM silicon tracker of roughly 0.001, a 5 milliradian stereo angle, resulting in longitudinal resolution of better than 2 mm per pair, allows an acceptably low ambiguity rate of less than a few %.

The position measurement in the interpolating pad system is achieved through charge division between the cathode pads. In this system, a transverse pad size of 2.5 mm must be converted into the design goal position resolution of 50 μm. This is done by measuring the induced charge on three to five adjacent pads with a signal resolution of about 1% of the total measured cathode signal. The GEM prototype has demonstrated this level of performance as described in section 4.1. The longitudinal position measurement from the interpolating pad system is achieved using the same technique as for the silicon: stereo strips. Since the resolution of the interpolating pad system is inherently worse than silicon, a larger stereo angle is required to achieve millimeter precision. The design calls for a more precise measurement from the outer tracker, since at the highest luminosities (10^{34}) the silicon will eventually fail, and the IPC system will be required to provide this measurement on its own. A goal of 1 mm per pad layer longitudinal resolution has been set. To achieve this, the pads must operate at a larger stereo

angle of ±50 milliradians. The performance of the pads will be somewhat degraded for tracks which are not of normal incidence. Such issues are under investigation as part of the R&D program.

2.1.2. Material Thickness

The GEM Central Tracker has been designed with the minimization of material as an important constraint on the overall optimization. Support structures are designed with composite materials, detector configuration choices are made to minimize the paths of services, and other trade-offs are evaluated with material minimization in mind. Such concerns are important as the material within the tracking volume limits the low energy momentum resolution of the tracker and degrades the GEM high precision electromagnetic calorimeter performance through the conversion of γ's within the tracker and the bremsstrahlung radiation from electrons. The silicon microstrip length choice is an example of a design choice which has been made specifically to address this issue By increasing the strip lengths to 18 cm (through bonding of 3 microstrip detectors together) the inner material in the form of electronics, cabling, and cooling services has been reduced. Figure 1-6 has presented the profiles of the material found in the central tracker.

2.1.3. Occupancy

In the design and optimization of the GEM Central Tracker, occupancies have been a major concern. The silicon subsystem has inherently small occupancies ($\approx$0.001 at 10^{33} luminosity) due to the very small cell sizes which result from the 50 μm strip pitch. While not characterized by quite such small occupancies, the interpolating pad system does nearly as well due to the small pad sizes and limited region of induced signal. The pads typically achieve occupancies better than 1% at 10^{33} luminosity and are better than 10% at 10^{34}. The occupancies have been calculated using a PYTHIA generator with a full GEANT simulation of the material in the tracker, and include the effects of secondary interactions, γ conversions and knock-on electrons, and low energy particles curling up in the magnetic field. Table 2-1 presents the occupancies in the silicon and Table 2-2 shows the pads occupancies.

Table 2-1: Occupancy in the Silicon Detectors

	Occupancy at $L = 10^{33}$ / cm^2 / sec per strip in %	
Barrel Layer	**Min. Bias Background**	**Min. Bias + Higgs Event**
1	0.16	0.35
2	0.13	0.27
3	0.09	0.19
4	0.07	0.15
5	0.06	0.12
6	0.05	0.10
Forward Layer		
1	0.04	0.09
2	0.04	0.09
3	0.04	0.09
4	0.04	0.09
5	0.04	0.09
6	0.05	0.10
7	0.05	0.10
8	0.05	0.10
9	0.05	0.10
10	0.05	0.10
11	0.05	0.10
12	0.06	0.11
13	0.06	0.11
14	0.06	0.11

Table 2-2: Occupancy in the IPC Chambers

	Occupancies per pad in %	
Barrel Layer	$L = 10^{33}$ / cm^2 / sec	$L = 10^{34}$ / cm^2 / sec
1	0.4 - 0.6	4 - 6
2	0.4 - 0.5	4 - 5
3	0.4 - 0.5	4 - 5
4	0.3 - 0.4	3 - 4
Forward Layer		
1	0.6 - 0.5	6 - 5
2	0.6 - 0.5	6 - 5
3	0.6 - 0.4	6 - 4
4	0.5 - 0.4	5 - 4

2.2 Tracker Intrinsic Performance

2.2.1.Detector Resolutions

Momentum Resolution

The GEM Central Tracker momentum resolution is limited at low momentum by the multiple scattering in the tracker and at higher momenta (above ≈30 GeV/c) by the measurement errors of the tracking detectors, the magnetic field of the GEM solenoid, and the overall tracker volume. As discussed above in section 2.1.2, the design has been constrained to reduce material in the tracking volume in order to minimize the multiple scattering effects and optimize

performance at low momentum. A multiple scattering limit of about 3.5% momentum resolution has been achieved. The measurement limited resolution is constrained by the 0.8T field of the GEM solenoid. The tracking volume is constrained by technical and financial constraints on the calorimeter and the muon systems. The tracker radius has been optimized through a thorough review of the trade-offs between the subsystems, and as a result the tracker outer radius increased somewhat in a final iteration of GEM. The result is a configuration which gives a measurement limited momentum resolution of 0.00115 p_T. Figure 2-1 illustrates these features. This figure presents the momentum resolution at 90 degrees ($\eta \approx 0$) as a function of momentum. The points indicate the results of a full GEANT simulation of tracking through the GEM tracking system followed by reconstruction. The solid curve is a parametrization of the resolution in the form

$$\frac{\sigma}{p} = \sqrt{(0.00115p)^2 + (.0035)^2}$$

The resolution versus pseudorapidity for fixed transverse and total momenta has been presented in Figure 1-8.

There we see that the basic performance remains uniform out to about $\eta = 1.5$, beyond which the track lengths in the transverse plane are truncated by the end of the tracker volume.

As GEM moves to operation at the highest luminosities, the tracking reconstruction will depend more and more on the pad system alone, as the silicon subsystem gradually degrades. The upper curve on Figure 2-1 shows the momentum resolution for the pad system alone compared to the resolution of the full system including silicon. The pad system alone respresents the expected performance at the highest luminosities (10^{34} cm^{-2}sec^{-1}) where the silicon system is expected to fail.

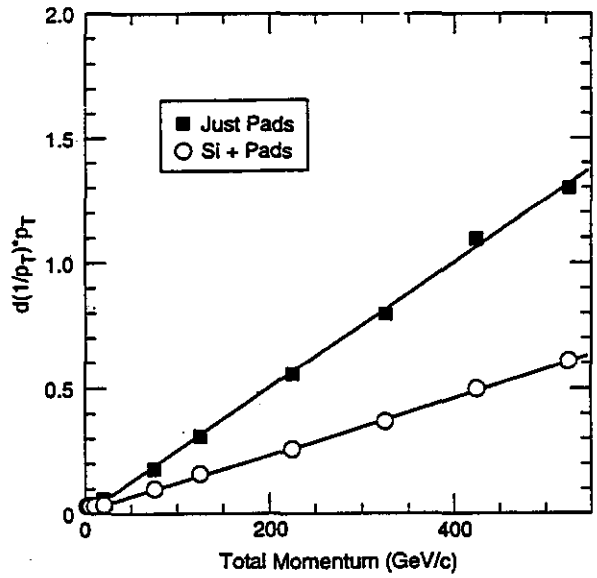

Figure 2.1 Measurement limited momentum resolution at η=0 as a function of momentum for the full tracker (relevent for 10^{33} luminosity) and for the interpolating pad tracker (relevent for 10^{34} luminosity). The data points are shown with the functions $\frac{\sigma(\text{full})}{p} = \sqrt{(0.0015p)^2 + (0.035)^2}$ **and** $\frac{\sigma(\text{pads})}{p} = \sqrt{(.0025p)^2 + (0.035)^2}$

The momentum measurement of electrons is complicated by the loss of energy by the electron through bremsstrahlung as it passes through the tracker. However, the tracker represents about 15% of a radiation length of material in the barrel and only a few percent of the tracks have secondary electrons produced. The result is reasonably good reconstruction of electron tracks. Furthermore, the effect of the bremsstrahlung is to add curvature to the track, improving charge determination. Figure 2-2 presents the distribution of reconstructed momenta for muons and electrons at 1, 10, and 100 GeV. The peak of the electron distribution is slightly offset to lower momenta due to the bremsstrahlung (this offset can be corrected for) and several percent of the tracks are significantly mismeasured. The one-sided tail on the electron distribution is evident. Nevertheless, the width of the central portion of the electron distribution, neglecting the tail, is very similar to that of the muon distribution and the isolated electron efficiency is 98%.

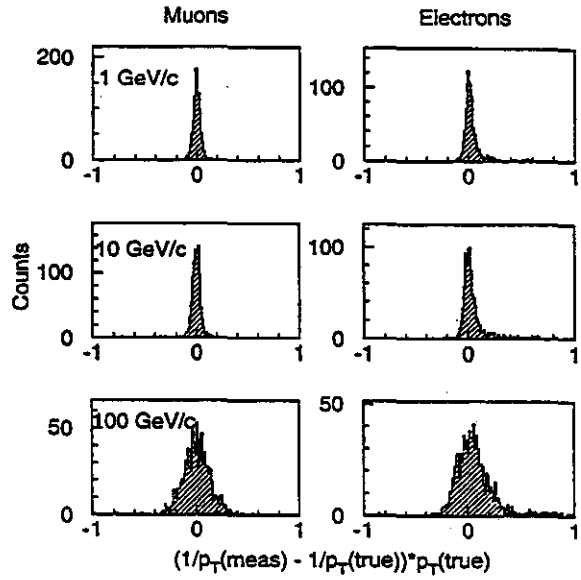

Figure 2.2 Momentum resoltuion distributions for 1, 10 and 100 GeV/c electrons and muons at η=0. Bremsstrahlung shifts the electron peak to lower momenta and the asymetric tails show that several percent are significantly mismeasured. The widths of the central region of the distributions are the same as for the muons.

Impact Parameter Resolution

The GEM Central Tracking system provides secondary vertex measurements through detection of tracks which have measurable impact parameters when projected back to the beamline. This capability is important for the heavy quark physics goals of GEM. Figure 1-10 presented the impact parameter resolution at 90 degrees ($\eta \approx 0$) as a function of momentum and Figure 1-11 showed the resolution versus pseudorapidity for fixed transverse and total momenta. At 90°the resolution is well described by the function

$$\sigma_b = 24\sqrt{1+\frac{70}{P^2}}\mu m(P \text{ in GeV}/c).$$

2.2.2. Pattern Recognition

In order to demonstrate the track reconstruction capabilities of the GEM tracking configuration, a prototype pattern recognition algorithm has been developed and applied to GEANT simulated events. The effects of expected detector inefficiencies and the geometrical dependence on detector coverage have been included. Figure 2-3 shows the number of tracking layers crossed by tracks emerging from the interaction region (with σ = 5 cm along Z) as a function of pseudorapidity (η). In the barrel (η < 1) there typically are 14 layers hit (6 double layers in the silicon system and 8 pad layers in the pad system). Due to the detailed geometry of the tracker, in some regions ($\eta \approx 1.2$) the number is lower and in some regions ($\eta \approx 2$) it is larger.

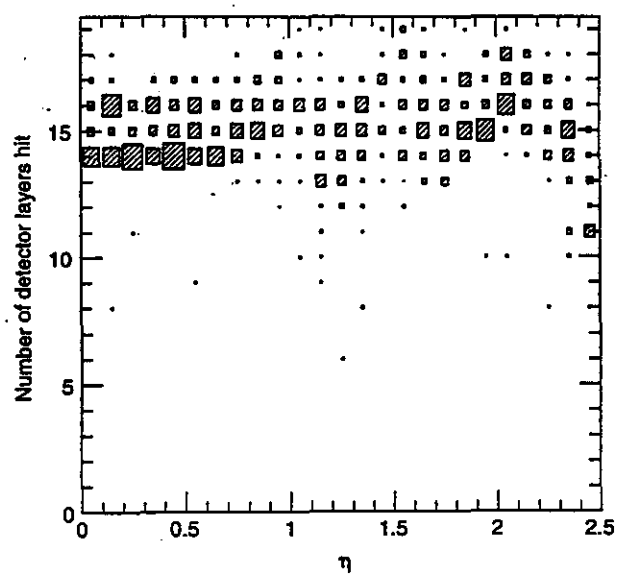

Figure 2.3 The number of detector layers hit by 500 GeV/c muons passing through the central tracker as a function of η. Vertex smearing has been included. The box size represents the number of entries. The effects of expected detector inefficiencies and geometrical acceptance have been included.

The track finding efficiency of the detector depends upon such things as the geometric efficiency, the detector efficiencies, track density, the dead time of the detectors, the number of layers and the placement of the layers in the detector, and the pattern recognition algorithm itself. All of these factors have been investigated. The pattern recognition algorithm in present use builds vector trees originating on an inner layer of the tracker. The tree is searched for best χ^2 sets of vectors. For the baseline configuration, the track finding efficiency has been found to exceed 95% for muons and electrons. Figure 2-4 presents the efficiency for muons from Higgs decay as a function of pseudorapidity. The overall efficiency for these muons with $|\eta| < 2.4$ is 97%. Figure 2-5 presents the efficiency for electrons from Higgs decay. For electrons the overall efficiency with $|\eta| < 2.4$ is 97%.

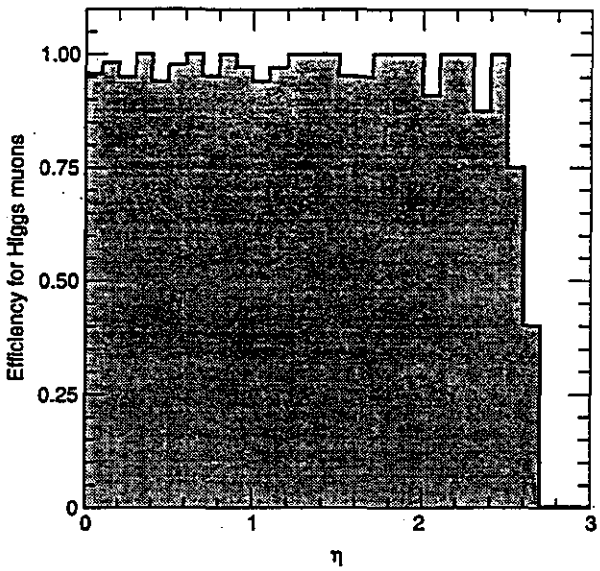

Figure 2-4 The fraction of muons from $H \rightarrow ZZ \rightarrow \mu\mu\mu\mu$, $\mu\mu ee$ decays that are found with the tracker pattern recognition program as a function of η. The efficiency is relatively constant at 97% out to η=2.

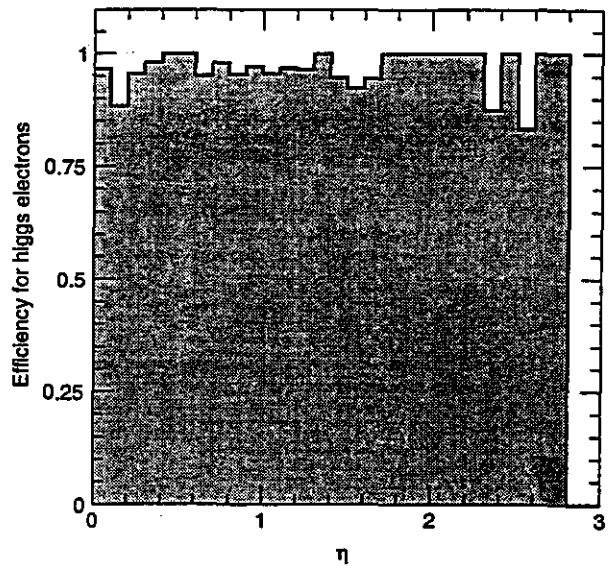

Figure 2-5 The fraction of electrons fro: $H \rightarrow ZZ \rightarrow eeee$, $ee\mu\mu$ decays that are found with tl tracker pattern recognition program as a function of η. Tl efficiency is very similar to that for muons, remainir constant at about 97% until η=2.

With time, the silicon microstrip detectors will develop increasing levels of electronic noise due to the increased leakage currents from radiation damage. In this case, inefficiencies due to deadtime can become important. A careful study including all of these effects has shown that reconstruction efficiency remains large (>97%) as long as the hit threshold is raised to about three times the noise, for noise levels up to 3,000 electrons.

For most of the physics goals of the Central Tracker, such as e/γ or e/hadron separation, full pattern recognition is not required; we need only look for the number of hits in a road extrapolated into the tracker from the calorimeter or the mon system (see discussion in Section 2.3.2., for example).

2.2.3. Multitrack Resolution

The ability of the GEM tracker to do multitrack finding is very important for charge identification of a lepton inside a jet, to reduce backgrounds in electron identification from γ conversion and Dalitz pairs, for eventual total reconstruction of a heavy quark jet, for t reconstruction, for τ identification, and simply for signal tracks of interest that have a minimum bias track very close to them. Multitrack resolution in the silicon tracker are excellent due to the 50 μm pitch of the microstrips. The equivalent figure in the interpolating pad system is 2.5 mm, and multitrack separation becomes a process of disentangling the analog signals which are mixed in neighboring strips. Multitrack resolution in the IPCs has been studied using a simulation

program written by Cherniatin and Chikanian at BNL.[1] The program incorporates test data collected using Cathode Strip Chambers running in CO_2CF_4.

IPC One Track Resolution

The single track resolution was estimated by generating the induced charge from a track passing through a pad at a given position and then fitting the resulting charge distribution to the function best describing charge induced on pads by Mathieson, *et al*, [2-5]:

$$q(x(i)) = 2.\frac{Q_{TOT}}{\pi}\tan^{-1}\left(\frac{\sinh\left(\pi\frac{W}{4L}\right)}{\cosh\left(\pi\frac{(x(i)-x(0))}{2L}\right)}\right)$$

where w = pad width, x is the distance from the center of the pad, and L = anode/cathode spacing. The resultant resolution is shown in Figure 2.6 as a function of position across the pad.

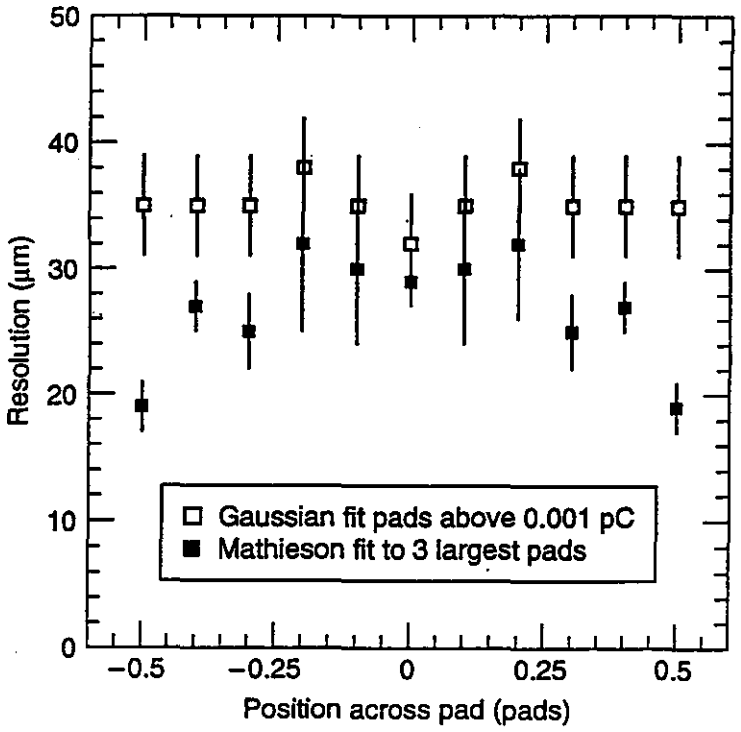

Figure 2-6 Single track resolution for simulated tracks traversing an IPC layer as a function of the position across the pad of the incident track. Two different functions are fit to the charge distribution. The one due to Mathieson, which better describes the induced charge distribution, gives a better resolution than a Gaussian fit.

IPC Two Track Resolution

When two tracks are separated by more than one pad width in the outer tracker, the pattern is easily recognizable: two peaks are observed in the charge distribution. However, when the tracks cross the same pad, it is only possible to recognize them as such by looking at the average total charge, as shown in Figure 2-7, which has been obtained at the SSCL using data taken with the Cathode Strip Chambers of similar geometry to the outer tracker chambers. In the top figure, the total charge for one layer is shown, while in the bottom figure the average over 8 layers is displayed. Once the signature of two tracks has been established, it is possible to fit the charge distribution to the Mathieson function for two tracks (essentially adding the charge from another track to the first one) and fitting for three parameters: the two positions and the ratio of the induced charges. The result of the two track resolution is shown in Figure 2-8 where only good fits are selected by a $\chi^2<2$ cut. The resulting efficiency is also shown. Tracks separated by more than 0.5 mm can be clearly resolved.

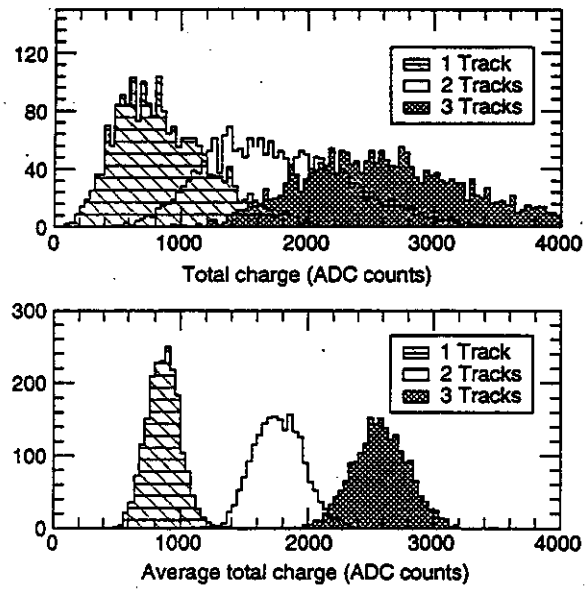

Figure 2-7 Total charge deposited by one, two and three tracks in a layer of IPCs (top figure). The bottom figure shows the total charge averaged over eight layers for one, two and three tracks. There is a clear separation between one and two tracks with <0.2% confusion when making a cut a 1300 ADC counts, and between two and three tracks <2% confusion when making a cut at 2160 ADC counts.

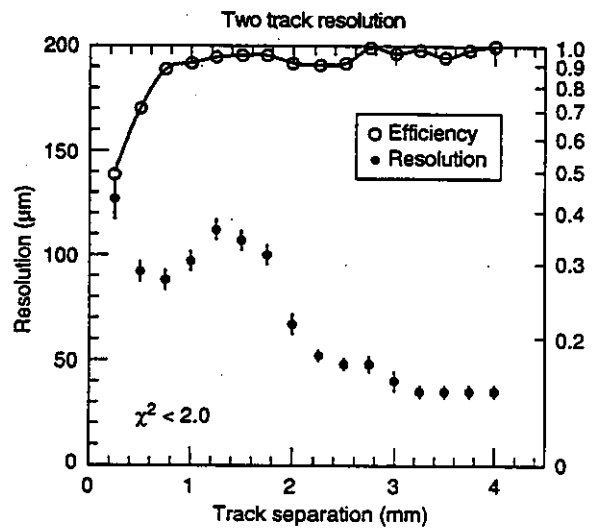

Figure 2-8 A simulation of the IPC two track resolution as a function of distance between the two tracks as found by fitting two Mathieson functions to the charge distribution. The efficiency for the fit passing a chisq cut<2.0 is also plotted.

IPC Three Track Resolution

For three tracks crossing one pad, it is not possible to resolve the 3 peaks in the induced charge distribution. However, the total average charge can be used to determine that 3 tracks are present. As the maximum separation (the distance between the two furthest tracks) is increased to two pad widths, three tracks can be resolved; and Figure 2-9 shows the average position resolution of the three tracks as a function of separation between the two CLOSEST tracks for a maximum separation of the 2 pad widths (the third track is randomly distributed between the two outer ones). The resolution is less than 100 μm for tracks with 6 mm or more of maximum separation.

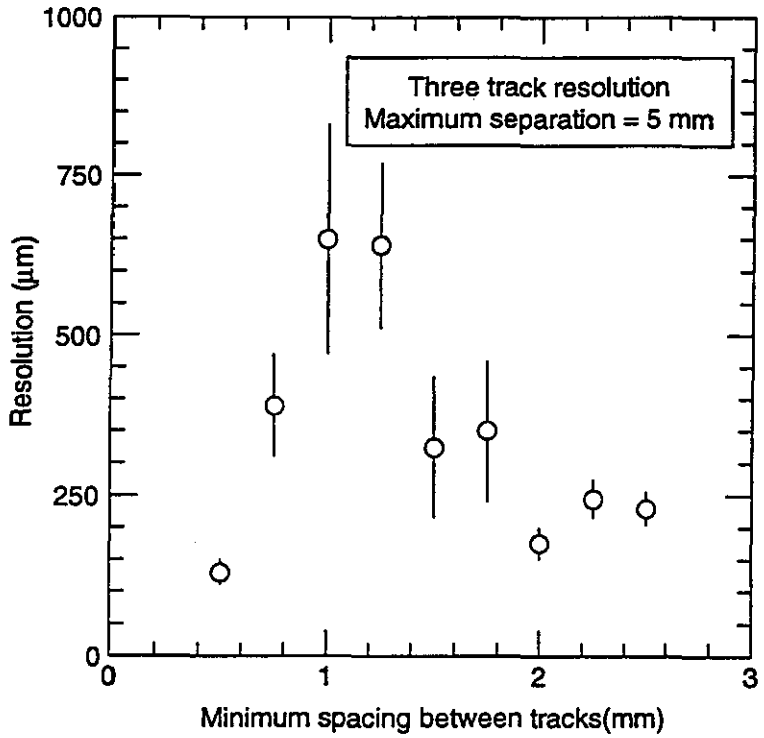

Figure 2-9 IPC three track resolution as a function of the distance between the closest two tracks (minimum spacing) for a set separation between the farthest two tracks of 5.00 mm. A resolution of 250 μm can be achieved when the minimum spacing is >2 mm, or approximatley one pad width.

2.2.4. Vertex Z Resolution

The measurement of the longitudinal position (z) of the primary vertex along the beamline is an important responsibility of the GEM Central Tracker. Accurate momentum vector reconstruction of neutral showers in the electromagnetic calorimeter depend on this, as well as separation of multiple events in the beam crossing. The longitudinal vertex position resolution from individual tracks at 90 degrees ($\eta \approx 0$) is 0.8 mm for tracks with momenta of a GeV or more. It must be realized that the vertex position resolution for an event will be improved from this performance by the many tracks emerging from the vertex, all of which give independent measurements of its position. The vertex position resolution for the pad system alone from single tracks at 90 degrees was shown in Figure 1-12, along with the full silicon-pad resolution. This plot demonstrates that the GEM tracking system operating at the highest luminosities of the SSC, after the silicon subsystem has ceased to contribute to track reconstruction, will still provide good vertex position measurements.

2.3. Physics Performance

2.3.1. Vertex Z Resolution and γ Direction Measurements

The GEM Central Tracker measurement of the direction of γ momentum vectors by locating the primary vertex is an important function. For example, the search for the decays of a Standard Model Higgs into two photons relies on a primary vertex reconstruction by the tracker. For this search, the z coordinate of the H^0 vertex must be determined to within 5 mm in order to obtain the mass resolution necessary to identify a Higgs.[11] The Higgs is produced with a substantial amount of transverse momentum which is balanced by particles recoiling against it. The tracker can count high p_T charged particles associated with each interaction in a given time slot and determine the vertex with the highest probability of being the origin of the Higgs.

Figure 2-10a shows the p_T spectrum for tracks that have survived cuts selecting high-p_T isolated charged tracks. Signal and minimum bias interactions are shown separately. In Figure 2-10b the multiplicity for both signal and minimum bias interactions are shown. Higgs interactions contain on average many more tracks with higher P_T than minimum bias interactions. From these tracks the vertex can be determined. Figure 2-11a shows the difference between the z coordinate of the estimated Higgs vertex and the z coordinate of the true Higgs vertex. The percentage of events in which the estimated vertex lies within 5 mm of the true Higgs vertex is shown in Figure 2-11b as a function of the H^0 mass and luminosity. These results are not very dependent on the isolation requirement for track selection. The vertex tagging efficiency is approximately 95% at nominal luminosity and 75-80% at high luminosity. The observed tagging efficiency is independent of the H^0 mass.

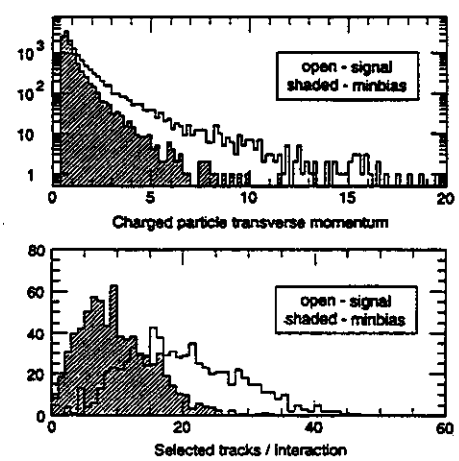

Figure 2-10 (a) The transverse momentum spectrum for p_T >0.5 GeV isolated charged tracks from standard model Higgs production (open histogram)for M_H=120 GeV, and minimum bias events (hashed histogram) produced using the PYTHIA Monte Carlo. (b) The number of these tracks per event from standard model Higgs production (open) and minimum bias events (hashed).

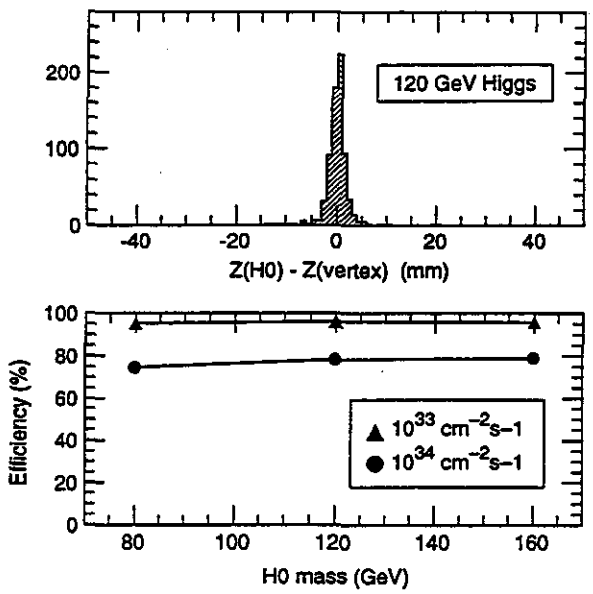

Figure 2-11(a) The difference in mm between the z coordinate of the true H^0 production vertex and the reconstructed primary vertex selected by choosing the vertex made up of tracks with the highest $\sum p_T$ for a 120 GeV standard model Higgs (b) Vertex tagging efficiency as a function of the standard model Higgs mass and luminosity.

2.3.2. Electron/Gamma ID

One of the most important functions of the GEM Central Tracker is the separation of electron and gamma showers in the electomagnetic calorimeter. This function is subdivided into identifying a gamma signal and rejecting electrons, and identifying an electron signal and rejecting γ and π^0's. We consider each of these separately in the following discussion.

a) Identifying signal gammas and rejecting background electrons. One example of this situation is the search for $H^0 \rightarrow \gamma + \gamma$ decays. For Higgs masses near the Z^0 mass one of the most severe backgrounds $Z^0 \rightarrow e^+e^-$ decays, with the $e^\pm$ showers faking γ's. One of the functions of the Central Tracker in GEM is to distinguish eletromagnetic showers induced by gammas and electrons by detecting the absence or presence of a charged track pointing to the shower in the electromagnetic calorimeter.

To study the rejection factors for electrons in the Central Tracker a sample of $H^0 \rightarrow \gamma + \gamma$ and $Z^0 \rightarrow e^+e^-$ decays were generated in a full GEANT Simulation of GEM. Electromagnetic showers were selected by the following calorimeter cuts:

i) E_T of shower $\geq$ 20 GeV

ii) (E in E.M. Cal)/(E in EM Cal +E in Had Cal) $\geq$0.95

iii) Isolation Cut ($\Sigma_{R\leq 0.3} E_T - E_{shower}) \leq 10$ GeV

These cuts select showers from γ's and e's with similar efficiency. At this point information from the Central Tracker was introduced:

i) the location of the interaction vertex was found from other charged tracks in the event in the Central Tracker. (See Section 2.3.1. above) to a precision of ~1 mm. The shower position is measured from the calorimeter to ~1mm precision.

ii) A road was defined in the tracker around a straight line joining the event vertex and the shower, with a width of 1.5 cm in both coordinates transverse to the center line of the road.

iii) The number of hits in this road were counted (the sum of the silicon and the pad chamber hits).

iv) A cut on the number of hits in the road was used to separate γ's and e's. A tighter cut (i.e. insisting on a smaller number of hits) improves the rejection of electrons, but results in a lower efficiency for retaining γ's.

The result of this study is shown in Figure 2-12, where the fraction of electrons rejected is plotted versus the gamma efficiency. The variable along the curve in this figure is the number of hits used in the cut. From this figure we see that as much as 99.5% of the electrons can be rejected (i.e. a rejection factor of 200) with acceptable γ efficiency. This results in a rejection factor of 4×10^4 against $Z \rightarrow e^+e^-$, which is quite sufficient considering that the cross section for $Z \rightarrow e^+e^-$ is expected to be around 160 pb/GeV, and the $H \rightarrow \gamma\gamma$ cross section is ~0.14 pb/GeV.

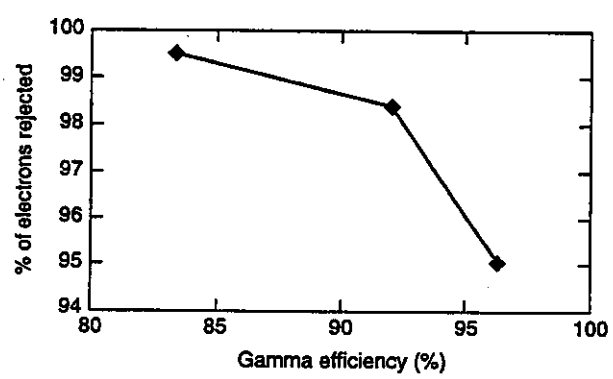

Figure 2-12 Fraction of background electrons rejected vs. the gamma efficiency for identifying γ's in $H^0 \rightarrow \gamma + \gamma$ events for M_H=80 GeV. For the tightest cut on the number of hits in the road, a rejection efficiency of 99.5% can be achieved with a corresponding γ efficiency of 83%.

b) Identifying an $e^{\pm}$ signal and rejecting a γ or π^0 background. An example of this situation is the search for $H^0 \rightarrow Z + Z^* \rightarrow e^+e^-e^+e^-$ or $e^+e^-\mu^+\mu^-$ decays. Electromagnetic showers from γ's, $\gamma \rightarrow e^+e^-$ conversions and π^0 decays present a severe background that has to be reduced by the Central Tracker by looking for the presence of a charged track pointing to the shower, and also by detecting the $e^{\mp}$ pair to the $e^{\pm}$ from γ conversions, and thus vetoing γ's and π^0's.

To study the rejection capability of the Central Tracker a sample of $H^0 \rightarrow 4$ leptons (with M_H=150 GeV), with background γ's and π^0's from a two jet event sample, was generated and run through a full GEANT simulation of GEM. Electromagnetic showers were selected using calorimeter cuts similar to those described in the $H^0 \rightarrow \gamma + \gamma$ study in section a) above. Similarly a road in the tracker was defined for each shower. However, to improve to the γ rejection further, electrons were required to have at least 6 hits in the road, and the momentum of the electrons were reconstructed in the tracker. A cut was then imposed requiring the agreement between the momentum form curvature in the tracker with the energy of the shower of the calorimeter. This resulted in a rejection factor of 100 against γ's and π^0's. Essentially all of the remaining background is due to γ's (or γ's from π^0's) that converted to and e^+e^- pair in the volume of the Central Tracker or Dalitz pairs from π^0's, and the electromagnetic shower was due to an actual $e^{\pm}$. This background can be further reduced by detecting the partner $e^{\mp}$. If the e^+e^- pair separates by more than a pad width the tracks can be reconstructed with an efficiency ~97% (see Figure 2-7). If the e^+e^- pair does not separate and stay within the same pad, we can identify them as multiple tracks with good efficiency (see Figure 2-5). Thus, we should be able to reduce the γ and π^0 background by another factor of ten, obtaining a rejection factor of ~1000 or better. (See Table 6.2-3.) This factor comes in at least squared in $H^0 \rightarrow Z + Z^* \rightarrow e^+e^-e^+e^-$ or $e^+e^-\mu^+\mu^-$ events. We thus believe that the Central Tracker has the capability of reducing the γ and π^0 backgrounds to a manageable level.

2.3.3. Electron/Hadron Separation

The electron identification capability of GEM and the rejection of hadrons depends both on the calorimeter (distribution of the shower energy between the electromagnetic and hadronic calorimeters) and the Central Tracker (matching the position of a charged track with the shower position and the comparison of momentum from curvature with the energy in the calorimeter). An example where this capability is essential is in the reduction of QCD jet backgrounds in the search for $H^0 \rightarrow z + z^* \rightarrow e^+e^-e^+e^-$ or $e^+e^-\mu^+\mu^-$. The background from jets can be due to jets fragmenting into high P_T γ's or π^0, which were discussed in the previous section, or jet fragmentation into high P_T charged hadrons (mostly $\pi^{\pm}$) which are the subject of this section.

To study the hadron and jet rejection capability of the Central Tracker, combined with the calorimeter, the sample of $H^0 \rightarrow 4$ leptons and the sample of 2 jet background events discussed in the previous sections have been used. The same calorimeter selection criteria for

electromagnetic showers were used, and the same analysis using the Central Tracker was done, i.e. looking for hits in the road pointing to the shower, matching the position of the charged track to the shower position, and the E/P comparison. The results of this analysis are shown in Table 2-3. The rejection of charged hadrons and jets are sufficient for the requirements of the Higgs search, as discussed in more detail in the Physics Section of the GEM Technical Design Report.

Table 2-3: Probabilities of misidentifying γ, π^0, $\pi^\pm$, and jets as electrons in GEM

Background	Probability of Misidentification as Electron
γ	10^{-3}
π^0	10^{-3}
$\pi^\pm$	8×10^{-4}
jet (non-isolated)	2×10^{-4}
jet (isolated)	1×10^{-5}

2.3.4 Muon Identification and Measurement

The GEM Central Tracker contributes to the GEM muon performance in a variety of ways.

a) Improvement in muon identification by comparing the momentum measurement in the Central Tracker with the momentum measurement in the muon system for a muon candidate track. The backgrounds to muons in the muon system (punchthrough backgrounds) consist of i) hadrons that decay into muons in the Central Tracker volume or in the calorimeter before interacting and ii) hadrons, typically secondaries produced by hadrons interacting in the calorimeter, which penetrate into the outer muon system. These backgrounds can be significantly reduced by requiring that the momentum and angles measured for these tracks in the Central Tracker agree with the momentum and angles measured in the muon system.

A quantitative study of this background reduction has been carried out[8] by generating a sample of $t\bar{t}$ events (using M_t=250 GeV)

$$t+\bar{t}\rightarrow W^+bW^-b\rightarrow e^\pm\mu^\mp+\mu_{incl}+x$$

where the $e^\pm\mu^\mp$ are isolated but the μ_{incl} is in a b-decay jet. A significant background to this process comes from two jet events

$$p+p\rightarrow 2\text{ jets }\rightarrow e^\pm\mu^\mp+\mu_{incl}+x.$$

The selection criteria used in this study were

i) $|\eta_{e,\mu}| \leq 2.5$

ii) Isolated $e^{\pm}$ with an isolated $\mu^{\mp}$, both with $P_T \geq 30$ GeV/c

iii) A non-isolated muon with $P_T \geq 30$ GeV/c

This produced a sample of $t\bar{t}$ events with a 50% background surviving due to the punch through background. For a clear study of this process the background should be $\leq 10\%$, requiring a further background reduction of a factor of five. To achieve this, the muon candidate tracks were extrapolated into the Central Tracker; the correct matching track was found for 90% of these tracks. A X^2 was formed for these tracks

where ΔP and $\Delta\sigma$ are the differences in the momentum and angles of the track as measured in the muon system and the Central Tracker, and δ_p and δ_σ are the corresponding errors. The X^2 distribution is shown in Figure 2-13.

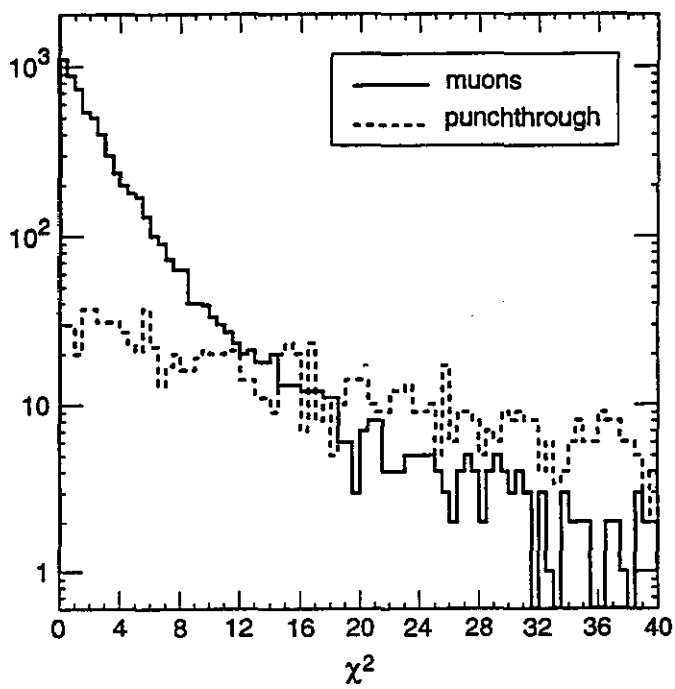

Figure 2-13 Distribution is χ^2 describing the agreement between the muon momentum vectors measured in the muon system and the central tracker. A cut at and angles measured in the muon system and the Central Tracker. χ^2>10 reduces the punchthrough by a factor of 5 and keeps 95% of muons.

A cut at $X^2 \leq 10$ keeps 95% of the true muons but reduces the punchthrough background by a factor of 5, which is what was needed to get a clean $t\bar{t}$ signal.

To study what requirements this background rejection places on the momentum resolution of the Central Tracker, this analysis was repeated, varying the Central Tracker momentum resolution $\frac{\delta P}{P^2}$ from 0.001 to 0.05. The resulting rejection factor of fake muons versus $\frac{\delta P}{P^2}$ is shown in Figure 2-14. We can see that we do need to be in the vicinity of $\frac{\delta P}{P^2}$~0.001, which is where the Central Tracker as designed now is, to get the required rejection factor.

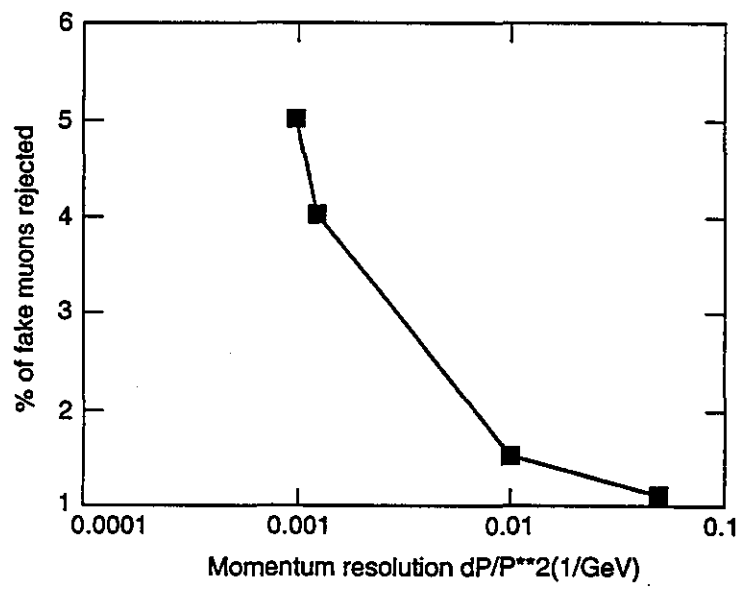

Figure 2-14 The rejection factor for punchthrough hadrons as fake muons from a χ^2 cut on the momentum vector agreement between the central tracker and the muon system as a function of the central tracker momentum resolution.

b) Improvement in muon momentum measurement at high momenta by providing the position of the vertex from the Central Tracker. A study of this effect[9] shows that the inclusion of the vertex constraint from the Central Tracker in the muon momentum analysis will result in an improvement across the whole angular region of 10 to 30% for muon momenta above 1 TeV.

c) Improvement in the muon momentum measurement at low momenta. The muon system momentum resolution degrades significantly below P_T~20 GeV/C due to fluctuations in the energy loss in the calorimeter; the resolution rises to about 6% at 10 GeV/c, where the Central Tracker resolution is ~3.5%. By combining the measurements from both systems, an improvement can be achieved[10], as is shown in Figure 2-15.

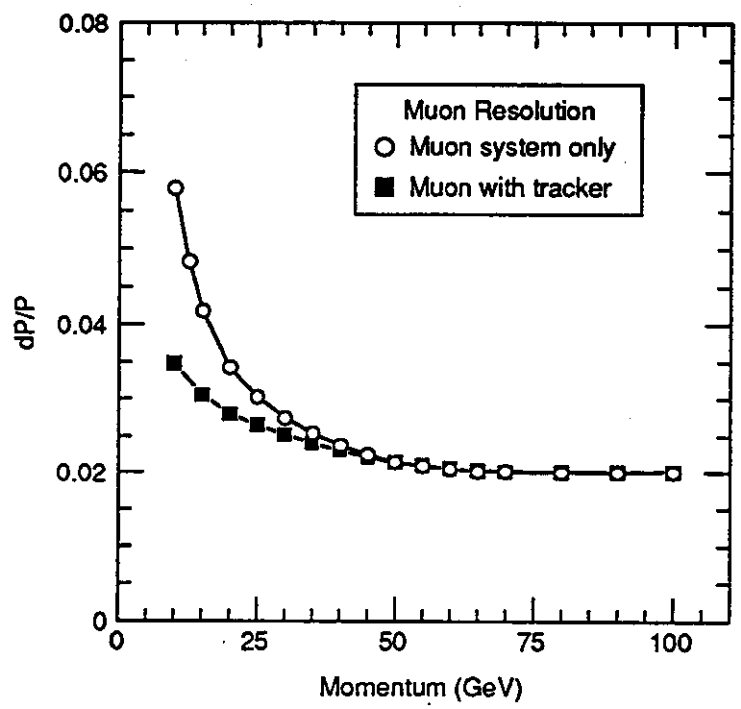

Figure 2-15 Improvement in the momentum measurement of low energy muons from taking the weighted averages of the central tracker information and the muon system measurement.

2.3.5. Charge Sign Determination for Electrons

The GEM detector can measure the charge sign of muons to very high p_T (≈ 2 TeV/c) using the excellent resolution of the muon system. Electron charge sign determination is provided solely by the Central Tracker. This capability is important, for example in testing lepton universality in new physics. The intrinsic capability of the GEM Central Tracker is 95% charge separation up to 600 GeV/c transverse momentum. However, electron charge sign determination is affected by the bremsstrahlung of the electron as it passes through the Central Tracker. In fact the curvature of the track in the tracker increases with energy loss, slightly enhancing the tracker's ability to separate charge. Nevertheless, the event is not as clean. The confusion from delta rays and converted gammas is a potential problem. For about 95% of the electron tracks, the bremsstrahlung resulting from the material of the tracker presents no

difficulty in measuring the tracks. For a few percent, however, significant confusion results. Figure 2-16 shows the efficiency for correct sign determination by the central tracker as a function of electron transverse momentum. The onset of degradation is evident, but is primarily limited by the tracker radius, magnetic field, and resolution, not bremmstrahlung. Figure 1-9 showed the 95% confidence level charge separation momenta determined from Figure 2-16.

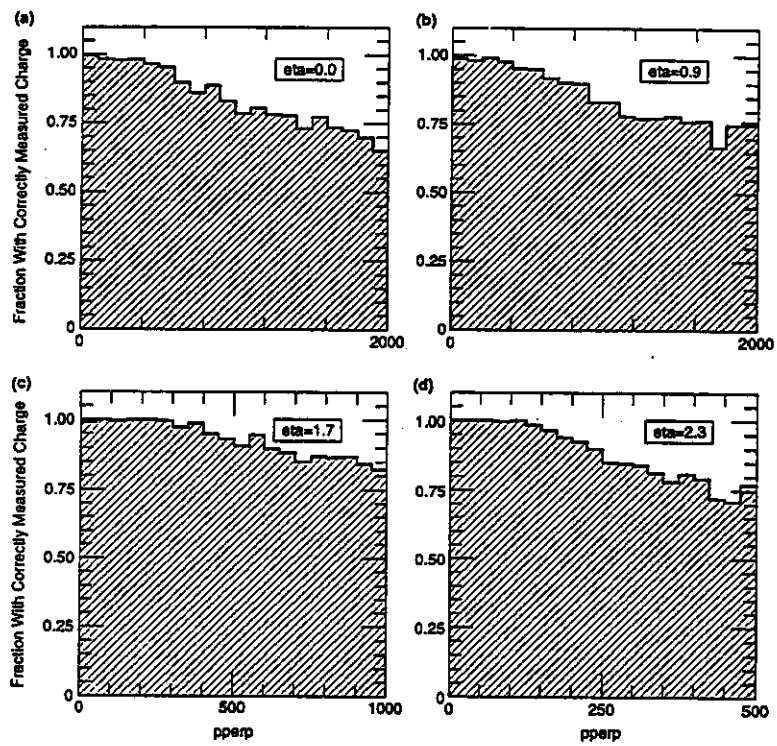

Figure 2-16 Efficiency for correct sign determination by the central tracker as a function of electron transverse momentum.

An example of a process where electron sign separation could be important is in the study of W-W scattering. This process could be of crucial importance if no light Higgs boson is found. Strong W-W scattering would manifest itself in an anomolously large cross section for the process

$$P + P \rightarrow W^{\pm} + W^{\pm} + x \rightarrow l^{\pm} + l^{\pm} + x$$

The isolation of this process depends on detecting the two isolated final state leptons. The background in opposite sign pairs, $W^{+}W^{-} \rightarrow l^{+}l^{-}$ appears insurmountable, but appears to be manageable for like sign pairs $W^{\pm}W^{\pm} \rightarrow l^{\pm}l^{\pm}$. The sign of the muon charge is well determined

in the muon system. Both electrons and muons could be used if the sign of the electron charge can be measured in the Central Tracker, which would increase the number of events by a factor of four over the $\mu^{\pm}\mu^{\pm}$ final state. Since the event rate for this process is pitifully small, this factor of four is crucial in being able to detect this process. The P_T spectrum of the leptons for this process has been calculated[15] for various model assumptions for the WW scattering process. These distributions are shown in Figure 2-17. As can be seen from this figure, electron sign determination up to 600 GeV/c covers most of the distributions for any of the three models.

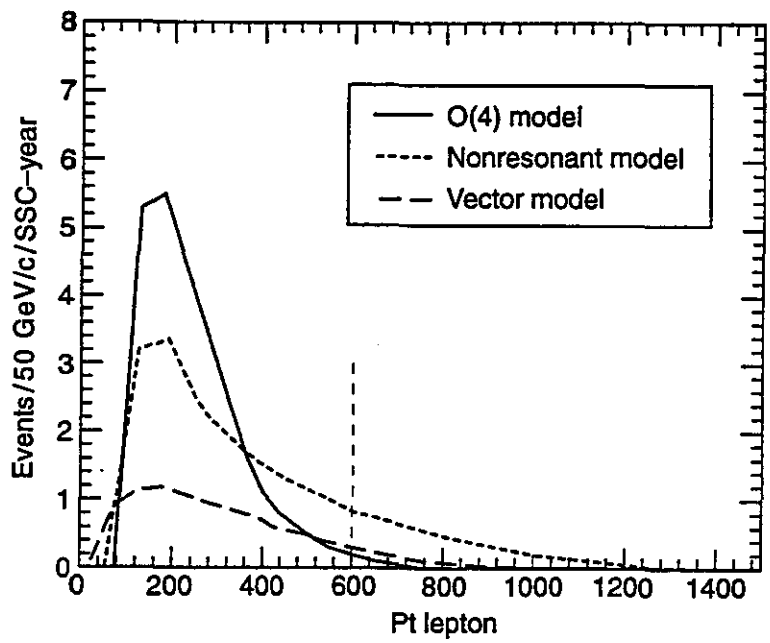

Figure 2-17 Transverse momentum distribution for the leptons in the W-W scattering $P+P \rightarrow W+W+X \rightarrow \ell+\ell+X$ for various models of W-W scattering. The solid line is non-perturbative Higgs 0(4) model, the dashed line is the Techni-rho model, and the dotted line is the non-resonant model. If a cut is enforced on the e^- of 600 GeV to ensure good e^- sign dtermination, a large fraction of the signal is kept.

2.3.6. Help with Isolation Cuts

Strategies for background reduction in physics measurements have been developed by GEM which rely heavily on isolation cuts in the calorimeter. The GEM Central Tracker has the capability to provide complementary isolation information. For example, in the search for Standard Model Higgs decays into two photons, the principal method for reducing the

overwhelming background from jets which fragment a large fraction of their energy into a tight cone of electromagnetic energy is to demand no associated energy in the calorimeter within the isolation cone. However, due to noise, the threshold on this criteria must be kept above several GeV. Few GeV tracks in the Central Tracker are easily detected and therefore allow a tighter cut on the isolation. An additional rejection of jet backgrounds by a factor of 2.2 over that achieved by the calorimeter isolation cuts alone looks feasible and is under study.

2.3.7. Tau Identification

Identification of τs is an important goal of the GEM Central Tracker. Testing lepton universality in any new physics could be an interesting issue. Full exploration of a Higgs will call for measuring branching ratios, with $\tau\tau$ being one of significant interest.

Figure 2-18 shows the GEM Central Tracker efficiency for measuring three prong τ decays as a function of p_T. Measurements require good separation of the three tracks at the outer pad layer. The 0.8 Telsa magnetic field aids in separation of the tracks and the very fine segmentation of the silicon microstrips ensures good track separation in the inner tracker. Good separation at the outer pad layer is defined as having the two tracks with largest separation separated at least 5 mm (2 pads) and those closest separated no less than 2.5 mm (1 pad). Figure 2-19 shows the distributions of these two distances for τ's with p_T = 150 GeV. These figures show that the separation between the two closest tracks is the most severe requirement, with most losses in Figure 2-18 resulting from failing this criterion.

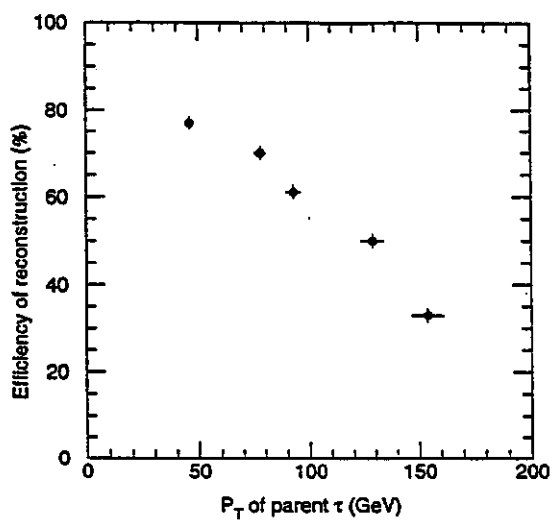

Figure 2-18 Efficiency for reconstructing all three tracks in the three-prong decay of a tau lepton as a function of the transverse momentum of the parent tau. As described in Section 2.2 in order to reconstruct all three tracks the separation between the two farthest tracks must be >2 pads (5 mm), and the distance between the two closest tracks must be >one pad (2 mm).

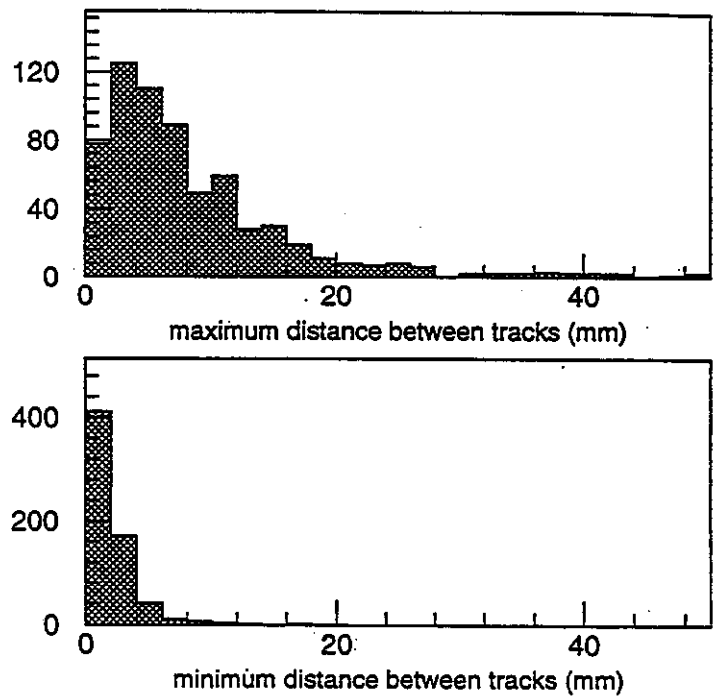

Figure 2-19 Distribution between the minimum and maximum separation at the outermost IPC layer between the trhee charged tracks from the decays of a 150 GeV/c τ

In the high p_T extreme where good momentum measurements are not possible due to the overlap referred to above, the Central Tracker can identify three prong decays by the very distinct pulse height information as described in section 2.2.3. Having identified the three track topology, the total energy can be measured in the hadron calorimeter. This measurement technique may be very useful in Z' studies, for example.

2.3.8. Secondary Vertex (b-tagging)

While the principal design goals of the GEM Central Tracker address the new high p_T physics expected at the high energy frontier of the SSC, the enormous rate of heavy quark production makes it an important subject of study for the tracker. With the very fine impact distance resolution ($\approx$ 25 μm) of the inner silicon subsystem, heavy quark studies will be done. Even though a fraction of the full phase space is lost in the forward direction, 60% of the B meson production at the SSC will occur for $|\eta| < 2.5$.[14] One of the most difficult obstacles to full utilization of this enormous sample ($\approx 10^{12}$ $b\bar{b}$/year at 10^{33}) is the development of an efficient trigger. The GEM muon triggers will be rate limited to about 20 GeV/c at full design luminosity, but early operation at lower luminosities may permit the trigger threshold to be reduced to the 10 GeV/c range, which will be desirable for this physics.

Interesting decay modes include $B_d^0 \to J/\psi\ K_S^0$. It is possible to construct a scenario in which several hundred of these decays are tagged as $J/\psi \to \mu^+\mu^-$ and $K_S^0 \to \pi^+\pi^-$ with the B_d decay vertex reconstructed.[13] This scenario could lead to a sensitivity of 0.15 in sin 2β where β is the CP violating phase of the $B\bar{B}$ asymmetry. B-jet tagging will also be important in top quark identification.

The *b*-jet tagging efficiency of the GEM central tracker is high due to the very good impact parameter resolution presented in Figures 1.10 and 1.11. Preliminary studies indicate that the efficiency for tagging the *b*-jet is between 30 and 40% for *b*-jets from top decay (with top mass of 140 GeV/c^2). Tagging algorithms have relied on identifying three large impact parameter tracks within a jet cone of ΔR=0.5. Each track is required to have an impact parameter in excess of three times the measurement error for its momentum and rapidity. Backgrounds have been investigated by studying light quark jets with similar p_T distributions and are found to fall below a 1% level of tagging. These results were derived from the full GEANT simulation of the central tracker. Thus, the GEM central tracker can enhance the heavy quark content of jets by a large factor.

2.4. Alignment and Calibration

The internal calibration of the central tracker is crucial to achieving the optimum position resolution and maintaining the required stability. This can be done continuously during data taking runs by using isolated muons produced in the pp collisions. A preliminary study has been performed to assess whether the alignment goals are realistic. Hits were generated inside tracking layers which had undergone shifts in their ϕ positions of a magnitude expected from the initial alignment errors. High-p_T muons whose *curvature* is known are then used to realign the tracking layers. Using information from the beam spot, which can be measured through an iterative procedure, residual errors of 5 μm in the silicon and 20 μm in the IPC's can be achieved. Figure 2.4-1 shows the final calibration error as a function of initial alignment for the silicon and the IPC's.

The main source of muons which can be used for this procedure (prompt and isolated) are from Ws and Zs and top events. At a luminosity of 10^{33}cm^{-2}s^{-1} the cross section for Ws and Zs predicts about 350 muons/hour/24° sector in each half of the tracker. For a top mass of 140 GeV and a 20% branching fraction to muons for one of the two tops in an event, a similar number of muons is obtained from top. The preliminary and conservative study shows that 50 high-p_T (p_T>30 GeV) muons will be sufficient to calibrate 24° sector of each half of the central tracker to sufficient accuracy. This number would be obtained in about six minutes running at this luminosity.

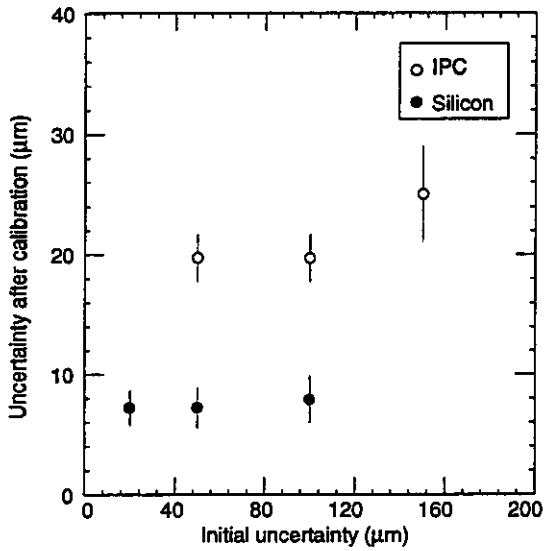

Figure 2.4-1: Remaining position uncertainty after calibration procedure as a function of initial uncertainty in the position of silicon and IPC layers.

2.5 References

[1] Cherniatin and Chikanian
[2] J.S.Gordon and E.Mathieson NIM 227(1984) 267-76
[3] E.Mathieson and J.S.Gordon NIM 227(1984) 277-82
[4] J.R.Thompson, J.S.Gordon and E.Mathieson NIM A234 (1985) 505-11
[5] E.Mathieson, NIM A 294 (1990) 121
[6] J.Thomas GEM TN-92-246
[7] A.Ostupchuck GEM TN-92-225
[8] B. Zhou, GEM TN-92-100
[9] L. Rosenson, GEM TN 92-97.
[10] GEM Collaboration, GEM T 92-231.
[11] H.Yamamoto and R.Zhu, GEM TN-92-126.
[12] I. Sheer, GEM TN-93-370 (1993).
[13] M. Strovink, Private Communication
[14] M. Botlo et al, SLAC-PUB-5795, 1992.
[15] J. Bagger, Private Communication
[16] Jaroslav-Antos, GEM TN 93-3XX (1993).

3 THE SILICON DETECTOR

3.1. Design Considerations

3.1.1. Design Parameters

The GEM Central Tracker has been divided into two subsystems to provide the different performance demands of the inner volume and the outer volume with different tracking technologies.The design parameters for the inner silicon subsystem of the GEM tracking are set by resolution, occupancy, and speed requirements of the Central Tracker system. Table 3.1-1 presents some of the important design goals relevant to this. These are the goals specific to the silicon subsystem, required to achieve the overall tracking goals presented earlier. The critical performance parameter of the tracker is the spatial resolution of 15 microns per layer in the azimuthal direction derived jointly from the momentum resolution and impact parameter resolution requirements.

Table 3.1-1.

Design Goals for the Silicon Subsystem	
position resolution	15 microns per silicon layer
	2 mm per silicon layer along the beam
rate	60 MHz
occupancy	approx .001 at 10^{33}
efficiency	>95% per silicon layer
material thickness	<6% radiation length at 90 deg
Lifetime	5-10 years

3.1.2. Choice of Silicon Microstrip for Inner Tracker

Silicon microstrip detectors are a natural choice for the inner tracking subsystem. The position resolution requirement of 15 microns azimuthally is achieved by the very fine segmentation of 50 micron pitch microstrips. The longitudinal position resolution (along the beam) is achieved by introducing a stereo angle into the system. The very fine segmentation leads to low occupancy. Silicon microstrip detectors are in broad use in high energy physics and can now be considered a mature technology. They provide a detector medium which is relatively radiation hard, an important consideration for the choice of the technology for the inner tracking regions where the charged particle dosages will be most hostile. Existing operational experience

has demonstrated that a system can be constructed which will withstand many years of running at the high luminosities of the SSC.

We have selected single-sided AC coupled silicon detectors as opposed to double-sided detectors as the baseline for the tracker design. Single-sided detectors have the advantages of cost, maturity in design, and multiple vendors. In addition, a baseline 18cm strip places stringent requirements on the capacitance. The n-side of the double- sided detector has too high a capacitance to be feasible.

The geometrical configuration of the silicon tracker was based on considerations of cost, radiation damage, tracking efficiency, and physics. The radius of the inner layers of silicon is primarily determined by lifetime limitations due to radiation damage. At 10 cm our projected lifetime is about 7 years. The silicon tracker outer radius is primarily determined by cost since the surface area of silicon and the electronic channel count increase rapidly with radius. The number of layers in the barrel section and disks in the forward sections was optimized by investigating the track finding efficiency for different numbers of hits per track. Our results indicate that to maintain track finding efficiencies above 95% the track should intersect at least 6 layers. Inefficiencies on each layer due to dead regions, deadtimes, or noise can be tolerated by requiring 4 or more good hits per track. Position information along the beam is accomplished by introducing either a +5 or -5 milliradian stereo angle on the two layers. Simplicity of design led us to chose 18 cm ladders.

3.1.3. Microstrip response

Optimization of the silicon microstrip detectors for use in the GEM tracking system requires a careful study of induced currents in the microstrips in the specific environment of the Super Collider. The GEM microstrip detectors will be operated in a 0.8 Tesla magnetic field, and tracks will be crossing the detectors at angles in excess of ten degrees in the transverse plane. Both effects potentially cause the deposited charge in the detector to be shared by two or more microstrips, thereby reducing the induced current in each strip. Figure 3.3-1 illustrates the physics of the charge collection process in the silicon microstrip detectors. Electron-hole pairs are liberated alone the charged track according to the Landau distribution with a most probable rate of 80 pairs per micron. These electrons and holes drift to opposite electrodes with an angle to the normal determined by the Lorentz Force and their drift velocities. Induced currents in the microstrips are due to the motion of the holes and electrons in the detector. The goal of the optimization is to maximize the signal in the microstrips by a proper design of the silicon tracker.

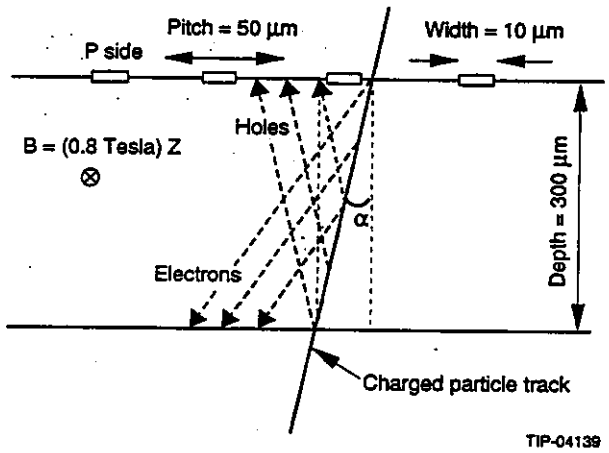

Figure 3.3-1 Microstrip Detector

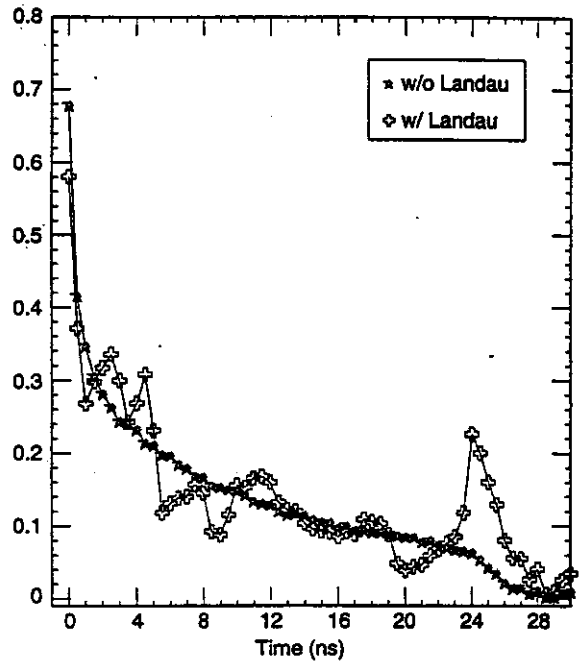

Figure 3.3-2: Strip Detector Waveforms

To study the dependence of the induced signal on the motion of electrons and holes, a calculation was done by using the Santa Cruz code [3.1.1] This code uses the weighting-field concept based on the reciprocity theorem of electrostatics [3.1.2]. For single-sided microstrip detectors reversed biased in an n-substrate, the microstrips on the p-n junction side are primarily sensitive to the drift of the holes in the detector. Simulations for the GEM configuration shows about eighty percent of the induced current comes from the drifting holes, and most of the induced current from the electrons is generated by electrons originating near the anode (the n-p junction). Two calculated waveforms from the detector is shown in Figure 3.3-2 . One waveform includes Landau fluctuations and the other assumes charge uniformly distributed through the silicon. The Landau fluctuations will alter the pulse shape and therefore introduce time walk.

To correct for the sharing of charge by the Lorentz drift it is desirable to tilt the silicon detector at the correct Lorentz angle (6 degrees for electrons, 1.4 degrees for holes). This can only be partially effective since the individual detectors are wide enough (3.2 cm) and close enough to the interaction point(IP) (10 to 22 cm) that a stiff (high momentum) track from the IP often will cross the detector at a large angle in the transverse plane. The Santa Cruz code was used to determine the sensitivity of the efficiency on the detector tilt angle. Figure 3.3-3 shows this dependence. Tilt angles out to 5 degrees are clearly possible. We have used 5 degrees in our baseline design since this allows us to take advantage of the existing research in the cooling rings.

An additional important effect resulting from charge sharing between adjacent strips has implications for the timing resolution of the detectors. Figure 3.1-4 shows the induced waveform on two adjacent strips for the situation in which a charge track crosses near the interface and induces charge on both strips. Since the induced signal on

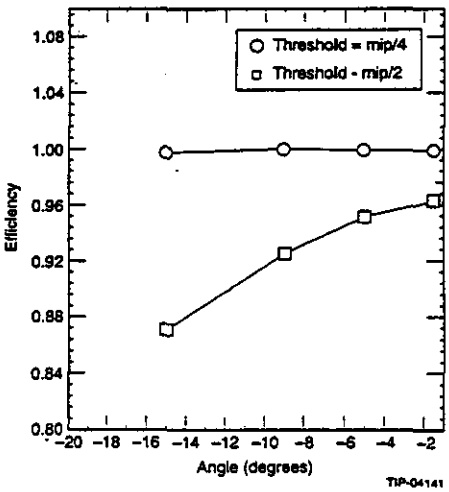

Figure 3.1-3 Dependence of efficiency on tilt angle.

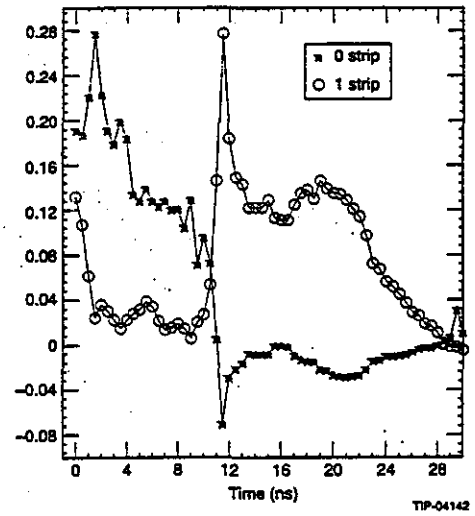

Figure 3.1-4 Pulse waveforms for track passing between strips.

each strip comes from charge deposited either near the p-n or on the n-side away from the p-n junction, there is a time lag in the signal for the strip with charge closer to the n-side. This effect is being carefully considered in the design of the front-end electronics.

3.1.4. Strip Length Considerations

It is desirable to make the microstrips as long as possible to minimize channel count and subsystem complexity (and therefore cost). Additionally, long strips make it possible to remove all electronics and associated services from within the barrel of the central tracker and to remove them from the tracking volume in the forward regions . However, increased strip length may degrade performance because of decreased signal-to-noise causing strip inefficiencies and pattern recongnition problems due increased occupancy.

Ultimately, detector performance depends on strip capacitances and strip length resistances. Strip capacitance drives the front-end electronics noise and must be held small to achieve best signal to noise performance. The strip capacitance is dominated by inter-strip capacitance and is weakly dependent on strip width (ref 3.1.3) . Strip widths should be maintained in the 10-15 micron range for 50 micron pitch strips. The speed of response of the strip will be determined by the combined RC time constant of the strip. Inter-strip capacitances

typically are 1.2 picofarads/cm, although recent results indicate these values may be engineered to somewhat lower values.(ref 3.1.4.).

Strip length resistances are presently under research and development by GEM to improve on the microstrip performance. Since 18 cm microstrip capacitances are less than 22 pF, to maintain an RC time constant for the strip of less than 10 nanoseconds, the strip resistance should be less than 25 ohms per centimeter. To accomplish this the present development work involves attempting to increase the strip cross section to a height of about 2 microns, with a width of 10-15 microns.

The combined effect of capacitance, resistance, and strip length is to introduce dispersion and attenuation into the ideal strip line. Coupled with reduced signals due to radiation damage to the silicon detector and the amplifier, the response of the microstrip will be less than the ideal 24000 electrons due to minimum ionizing particles. Noise and reduced signals directly lead to strip inefficiencies and therefore track finding inefficiencies. To understand what limits are placed on the noise level (and also the strip characteristics) by the need to maintain track finding efficiencies greater than 95%, detailed simulations were performed. The simulations included strip deadtimes due to previous hits (10 crossings), increased equivalent noise due to attenuation and radiation damage, noise on the signal, and noise hits due to all physics processes during the crossing of interest as well as the previous crossings. Figure 3.1-5 shows the track finding efficiencies for various noise levels with a fixed threshold. Clearly, to maintain good track finding efficiencies a threshold to noise level at least 3/1 is needed. Figure 3.1-6 shows the track finding efficiencies for a fixed noise to threshold of 3/1 as a function of noise. An equivalent noise charge (ENC) greater than 3000 electrons leaves no margin for channel to channel variations in gain or threshold values. An ENC of 2500 will give us some margin. The efforts on improving the microstrip response are directed towards reducing the ENC to levels less than or equal to 2500.

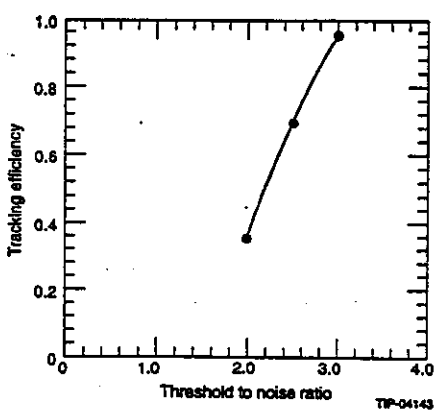

Figure 3.1-5: Track finding Efficiencies versus Threshold

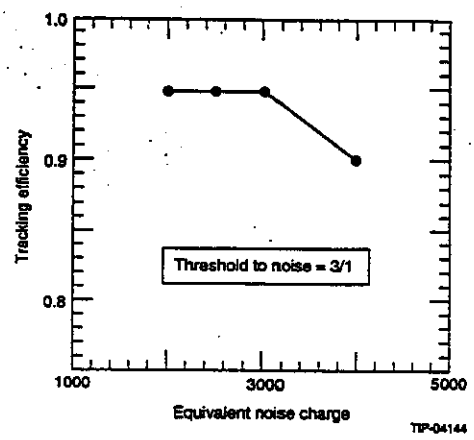

Figure 3.1-6: Track finding Efficiencies versus Noise Level

3.2. Silicon Tracking System Mechanical Design

The Silicon Tracking System (STS) baseline design shown in Figure 3.2-A contains 10,836 silicon strip detectors which are distributed radially and axially about the accelerator interaction region. Our current tracker design has an overall length of 2.1 m and an outside radius of .38 m. The silicon microstrip detectors are arranged in the volume into three distinct groupings in the tracker; the central or barrel region and two forward planar regions. The total number of detectors in the central region is approximately 2,484, with approximately 4,176 wafers in each forward region. The Tracker specifications demand that each of these wafers be precisely located relative to each other and located relative to the interaction region. It is also imperative that the alignment of the wafers relative to each other be exceptionally stable over long periods of time. Figure 3.2-B shows the STS baseline design. The central region contains six layers of silicon ladder assemblies, extending 180 mm axially on each side of the interaction region.

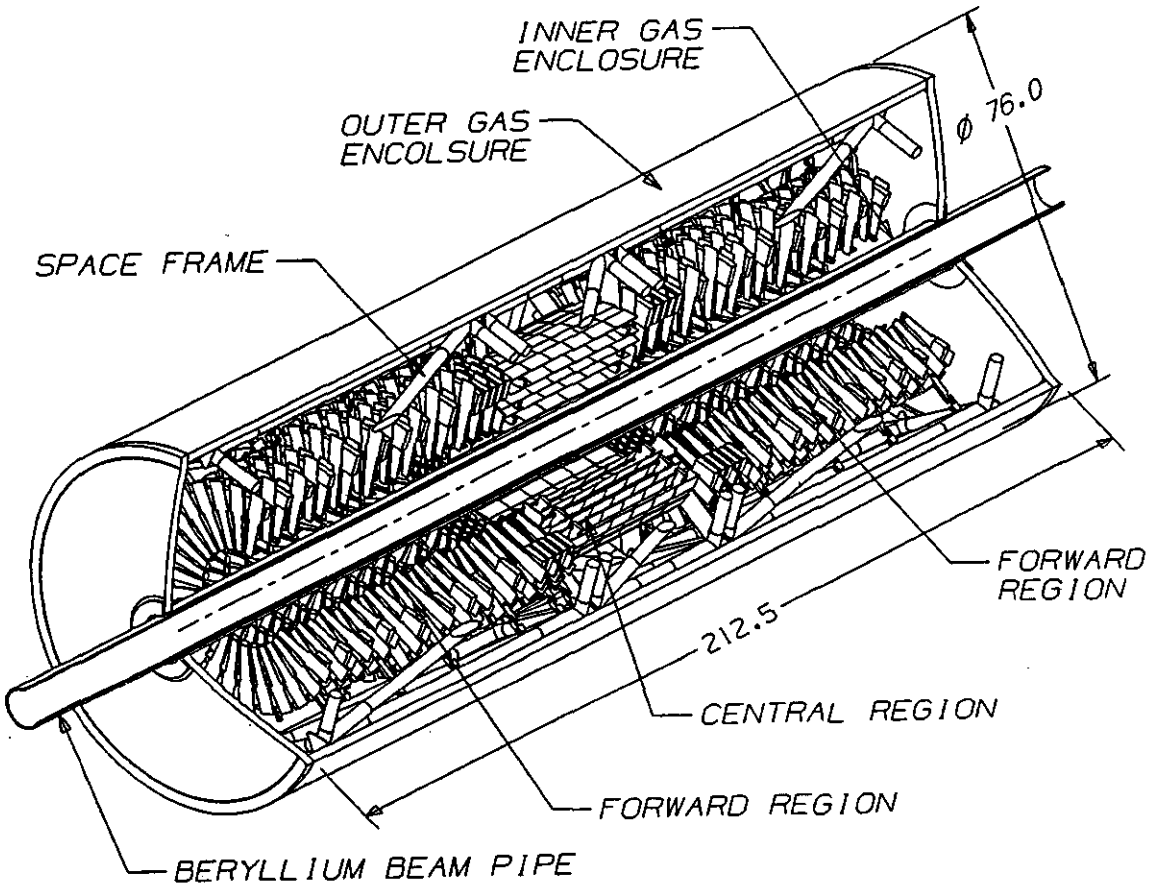

Figure 3.2-A: Cut-Away of STS Assembly

The baseline silicon detector ladder specifications are shown in Table 3.2-1. The specifications highlight the differences between the central and forward regions of the silicon tracker.

Table 3.2-1

Item	Central region	Forward region
Shape:	Rectangular	Rectangular / Trapezoidal
Active detector width:	3.2 cm max	3.2 cm max
Number of channels:	1280 (640 per side)	1280 (640 per side)
Number of wafers	2484	8352
Stereo angle:	10 mrad (+/- 5 per side)	10 mrad (+/- 5 per side)
Module heat load:	2.97 W	2.97 W
Number of modules:	414	1528
Module heat flux:	1.3 W/cm^2	1.3 W/cm^2
Operational Temperature	0°C	0°C
Temperature Control	+/- 0.1 °C	+/- 0.1 °C
Lorenz angle:	0°	0°

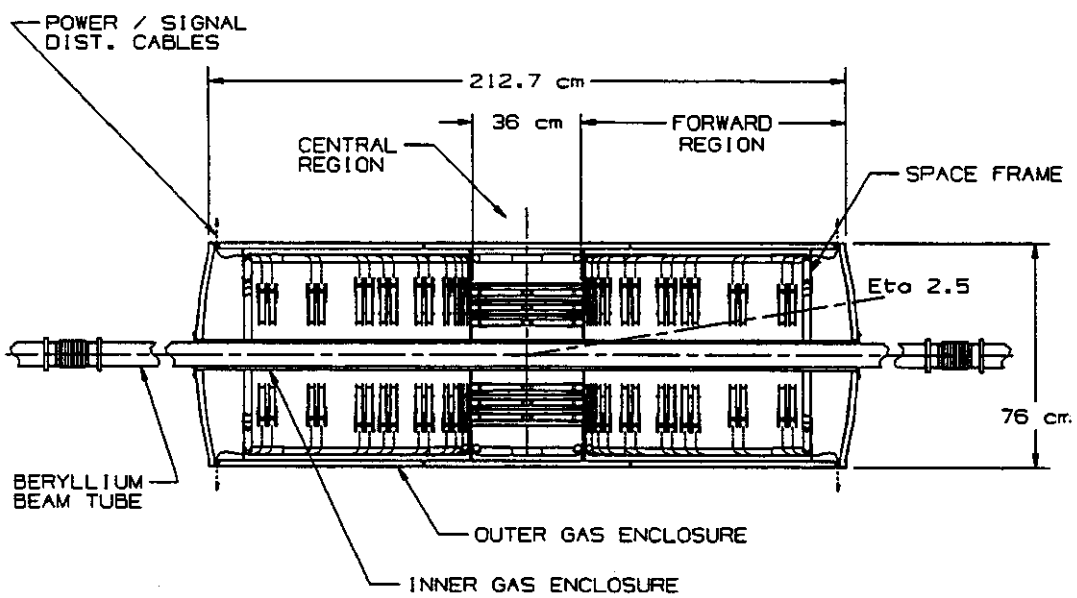

Figure 3.2-B: Side View of STS Assembly

The barrel region radii of each layer as ranges from a minimum of 100 mm to a maximum of 221 mm. The forward region contains fourteen similar silicon ladder assembly layers at each end. The central and forward region layers are placed so that a single trajectory from the interaction region will intercept six layers down to an eta coverage of 2.5.

A dimensionally stable metal matrix composite (MMC) space frame will provide structural support for the central and forward regions. Ultrahigh elastic modulus, immunity to moisture-induced distortions, and tailorability of coefficient of thermal expansion (CTE) motivated this selection. Aluminum and magnesium matrices, combined with P120 fibers @ 60 v/o are candidates. These yield axial modulii of 485 GPa and 485 GPa with CTEs of -0.25 ppm/°C and -0.6 ppm/°C, respectively.

An ultralightweight G/CE sandwich construction enclosure contains evaporated butane vapor and provides transfer of STS mechanical support loads. This shell and its end cover plates have an areal density of only 1.2 kg/m^2. Experimental quasi-isotropic (OI) panels of 250 μm material thicknesses have been constructed from P75 graphite and 1939-3 epoxy and irradiated using protons at a fluence of 10^{15} particles/cm^2, representing 10 operational years. Out-of-plane mechanical distortions were measured to be less than 5 μm, instilling confidence in the general material selections and contruction approach. A 1.0-mm-thin beryllium inner liner will complete this stiff, low-mass structure. All of the signal cables, power cables, and cooling lines will penetrate the enclosure at the ends, between the cylinder and the endcap enclusres.

The silicon ladders are bonded to structural rings made from G/CE to form the silicon shell superlayer assembly, which provide structural support, and a passage for an internal heat pipe wick. The detectors in the central region are canted at an angle between 0°(the current baseline) to 5° (the original baseline), as shown in Figure 3.2-C1 (the original baseline). Heat from the electronics flows through the thin-walled composite faceted cooling ring surface, onto which the detector is mounted, and evaporates the cooling fluid medium.

The two forward regions are each composed of 14 silicon annular disks. The detector ladders in the forward region are not canted, which significantly simplifies the cooling ring design. Individual detectors in the central region are arranged circumferentially around the beam axis. The forward ladders are in the shape of a trapezoid in order to fit as individual arc sectors. Circumferential hermeticity is preserved by overlapping adjacent trapezoidal modules. Further simplification of the cooling and structural ring construction is provided by having adjacent modules in one disk on alternating sides of the cooling ring as depicted in Figure 3.2-C2. A more complete description of this geometry is discussed in a subsequent section.

The preferred technique for cooling the forward region silicon ladders will be evaporative as previously discussed. Cooling and structural rings which support the trapezoidal-shaped modules must track the silicon wafer contraction or they may introduce distortion. The module support interface will have built-in compliance to allow for a minor material coefficient of thermal expansion (CTE) mismatch.

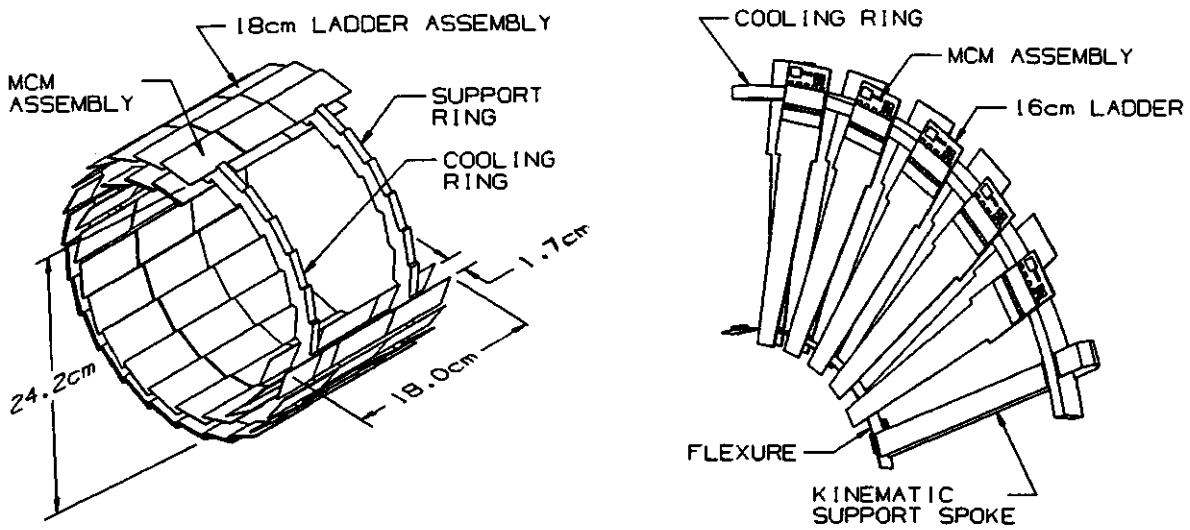

(1) (2)

Figure 3.2-C: Silicon detector barrel and forward modules

The gas enclosure is configured to safely contain the butane vapor of the cooling system. Introduction and removal of Butane into and out of the containment vessel will be accomplished in a manner imposing only slight differential pressures (0.1 atms) across the containment vessel wall. Any pressure differential excursion outside the 0.3 atms limit will be automatically vented under controlled conditions.

Kinematic mounts will be used to support the internal space frame to the outer containment vessel wall. Since the Butane vapor pressure is controlled by the condenser pressure, large internal pressure excursions are not expected. Slight outside pressure excursions (up to 0.1 atms) will result from barometric pressure variations (e.g. Texas thunderstorms). At the points where the space frame mounts with the end of the gas enclosure, "hard points" will be embedded into the gas enclosure to minimize deflections due to pressure differentials across the enclosure. Nonetheless, the internal kinematic mounting of the space frame will be configured to ensure that the STS axis does not become misaligned to the outer support structure (OSS) reference frame.

Design concepts chosen to achieve the STS performance goals are presented in the following sections. The design effort has concentrated on addressing the stringent stability, positional accuracy, radiation exposure, and radiation length limits required for this high resolution tracking system.

To meet the high resolution requirements, the individual ladder must meet the following mechanical location tolerances shown in Table 3.2-2,

Table 3.2-2

Silicon Ladder Tolerance	Circumferential	Radial	Longitudinal
Assembly Placement Tolerance	100 μm	200 μm	250 μm
Assembly Optical Inspection Precision	10 μm	25 μm	50 μm
X-Ray Calibration Measurement Precision	3 μm	25 μm	50 μm
Long Term Relative Stability Tolerance	10 μm	80 μm	250 μm

The assembly placement tolerance is the requirement for assembling the ladders into a subassembly. Each ladder will then be inspected to the assembly optical inspection precision requirements. The entire tracker assembly will be mapped with a highly collimated x-ray source to the x-ray calibration measurement precision listed. In order to maintain a high resolution the tracker subassemblies must meet the long term relative stability tolerance. At this point, long term is not well defined. The tracker will be built with a 5-10 year operational life, but occasional recalibrations are planned throughout its life. These calibrations may be in situ or utilizing stiff tracks, done on a predetermined schedule.

3.2.1. *Material Considerations*

The demanding design requirements for the STS call for the need of specialized high performance materials (Ref. 1, 2, 3). The construction materials must have the following characteristics: high radiation length, high stability, compatibility with Butane and radiation, low CTEs, and insensitivity to moisture effects. Achieving the design goals will require the application of state-of-the-art material composites with high stiffness-to-weight ratio construction techniques.

In order to maintain the tight stability requirements, ultrahigh modulus materials with long term stability and radiation compatibility are required. Listed in Table 3.2.1-1, are potential material candidates based on high stiffness. The primary candidates are beryllium, G/E composites, and aluminum MMCs based largely on ease of fabrication and affordability. Dimensional stability in the G/E composites may be achieved by using a hydrophobic cyanate ester (CE) binder matrix. Beryllium is nearly transparent to particles and impervious to moisture and butane. Unfortunately, it has a large CTE, is very costly, and requires complicated machining procedures. G/CE materials are a good compromise, having more favorable particle interaction characteristics than monolithic metals and more favorable CTE, cost, and fabrication characteristics than beryllium. The STS' environmental factors required special consideration because the performance of G/CE exposed to a combination of butane and ionizing radiation is

not well known. For this reason, a mechanical testing program was undertaken. Mechanical tests were performed before and after environmentally conditioning the coupons in a butane filled container, and irradiating them with a cobalt gamma ray source. These results are shown in Table 3.2.1-2.

Table 3.2.1-1 Material Candidates

Material	Elastic Modulus E (GPa)	Density ρ (g/cm^3)	Specific Stiffness E/ρ (10^8cm)	CTE α (ppm/K)	Thermal Conductivity k (W/m-K)	Specific Heat C_p (J/g-K)	Radiation Length (eff.) L_{Re} (cm)
			Material Candidates				
Beryllium	290.0	1.84	16.08	11.60	146.0	1.88	35.43
Boron Carbide	448.2	2.52	18.15	4.73	43.0	0.90	19.90
Carbon/Carbon[a]	152.0	1.90	8.16	0.10	246.0	1.00	18.80
Graphite/Epoxy[b]	311.7	1.68	20.00	−1.13	46.2	0.92	25.00
Mg-MMC[c]	190.3	2.03	9.56	−0.35	412.0	1.00	16.80
Al-MMC[c]	196.5	2.39	8.39	0	409.0	1.02	13.22
			Reference Materials				
Silicon	**131.0**	**2.33**	**5.74**	**2.60**	**129.0**	**0.70**	**9.37**
Aluminum	68.9	2.70	2.59	23.58	168.0	0.90	8.89
Boron	344.7	2.34	15.03	8.30	1.0	1.29	22.52
Fused Silica	73.0	2.20	3.39	0.50	1.0	0.92	12.30
Copper	117.2	8.91	1.34	16.90	400.0	0.39	1.44
SiC	325.0	3.00	11.05	2.30	200.0	0.89	8.52

[a]Unidirectional properties.
[b]Graphite Fiber (P75)/Epoxy matrix (1939-3), unidirectional, ~60% fiber.
[c]Graphite Fiber (P120) MMC-Metal Matrix Composite, quasi-isotropic, ~60% fiber.

Table 3.2.1-2 Mechanical Properties Test Results for P75s/954-3 Laminates Normalized to 60% Fiber Volume Fraction

Mechanical Property	Test Institution	Specimen Description Neat	0°	90°	QI
Elastic Tensile Modulus (GPa)	LANL	3.7	323	6.9	100
	LANL*	3.4	321	6.6	110
	CONV	3.8	324	6.4	96.5
Elastic Compressive Modulus (GPa)	NDE	3.7	280	8.1	97.5
	LANL	3.7	300	6.7	81.3
	LANL*	3.5	283	6.8	81.3
	CONV	3.4	270	6.2	77.2
Elastic Shear Modulus (GPa)	LANL	1.2	4.5	1.7	--
	LANL*	1.1	4.8	1.7	--
	CONV	1.2	4.0	1.6	--
Poisson's Ratio	LANL	0.38	0.25	0.0043	0.28
	LANL*	0.37	0.25	0.0031	0.31
	CONV	0.40	0.32	0.0063	0.33
	NDE	0.40	0.32	0.0060	0.33
Ultimate Tensile Strength (MPa)	CONV	60	1000	23.4	294
Ultimate Tensile Strength (MPa)	CONV	--	337	41.7	131

*Denotes results for specimens environmentaly conditioned by 10 Mrad and Butane

LANL and one independent testing organization used similar, conventional (CONV) load frame- and load cell-based tests. A third organization used nondestructive evaluation (NDE) methods-scanning electron microscopy and scanning acoustic microscopy to determine the elastic properties of specimens. The data generated by all institutions and methods were comparable and closely matched published data including manufacturer's specifications. The overall conclusion of the mechanical properties test program is that the P-75/954-3 materials system is now mechanically fully qualified and is acceptable for achieving STS baseline performance objectives.

Radiation length limits are another primary specification of any construction material to be used in the tracker. Figure 3.2.1-A shows the thickness of various material candidates which meet 2% of a radiation length. From a radiation length stand point beryllium clearly stands out as an advantage, with G/E as the next optimum. G/E composites offer the advantage over Be of being able to have a variable CTE. Where G/E composite structures are bonded to dissimilar

materials it is important to match the CTEs to avoid thermal stresses. In other structural applications it is important to minimize the total thermal distortions with zero CTE materials.

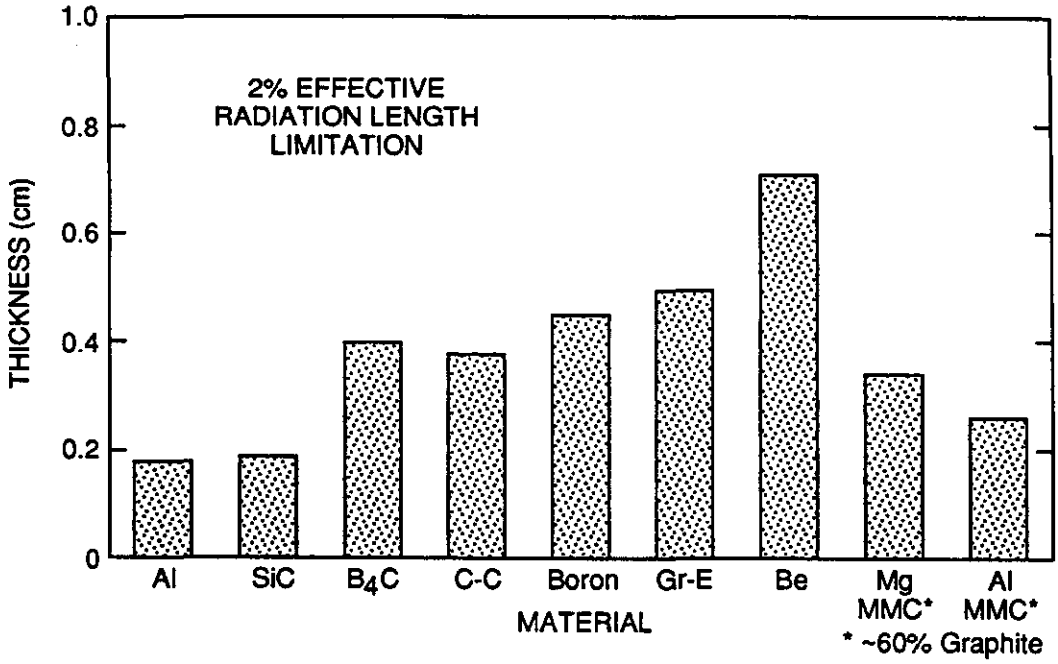

Figure 3.2.1-A Material Comparison: 2% Radiation Length

3.2.2. *Gas Enclosures*

A gas enclosure system will be required to contain the butane vapor and prevent external gases from contaminating the butane coolant. Unlike the space frame, the gas enclosure will be designed for strength and dimensional stability. The space frame attachments will attach directly to the mounting bulkheads. Figure 3.2.2-A shows the enclosure design that must meet the radiation length requirements and be capable of withstanding the range of external or internal pressure.

Analysis indicates the cylinder will withstand an external buckling pressure of 1.3 atmospheres gage. Under operating conditions the pressure may vary by as much as ± .1 Bar (1.5psig). Relief valves and controls will be added to the system to ensure the pressure does not exceed the enclosure working pressure of 5 psi.

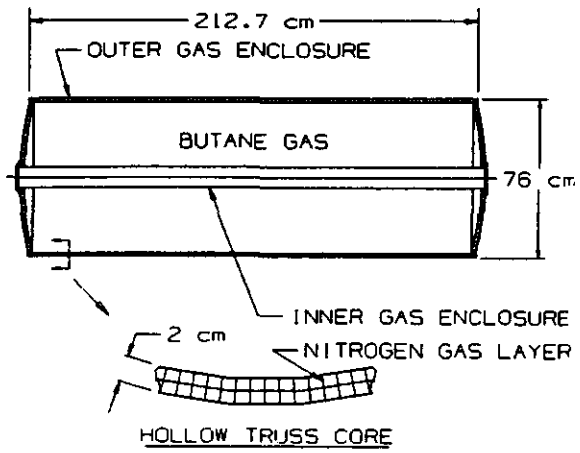

Figure 3.2.2-A: Gas Enclosure Design for the STS

The outer shell enclosure will be constructed of a double wall truss core design to maximize the stiffness, with G/E materials to meet the radiation length requirements. The inner enclosure will be constructed of beryllium to minimize the radiation . Removable ends will allow access to the ends of the tracker where the utilities and signals pass through the gap between the cylinder and endcap.

The gas enclosure is designed as a buffer zone for any potential butane gas leak. The double wall truss core design will allow for a layer of flowing nitrogen gas that will contain a hydrocarbon sensor. Any butane will be sensed in this area. Active control of the thermal boundary will be accomplished by controlling the nitrogen temperature through a heat exchanger.

Structural analysis of the inner beryllium enclosure has begun with emphasis on understanding how to minimize the overall radiation length. Configuration and fabrication studies with different combinations of stiffening ribs are being investigated. Figure 3.2.2-B shows the baseline inner enclosure with a 1 mm wall and optional ribs at about 40 cm spacing.

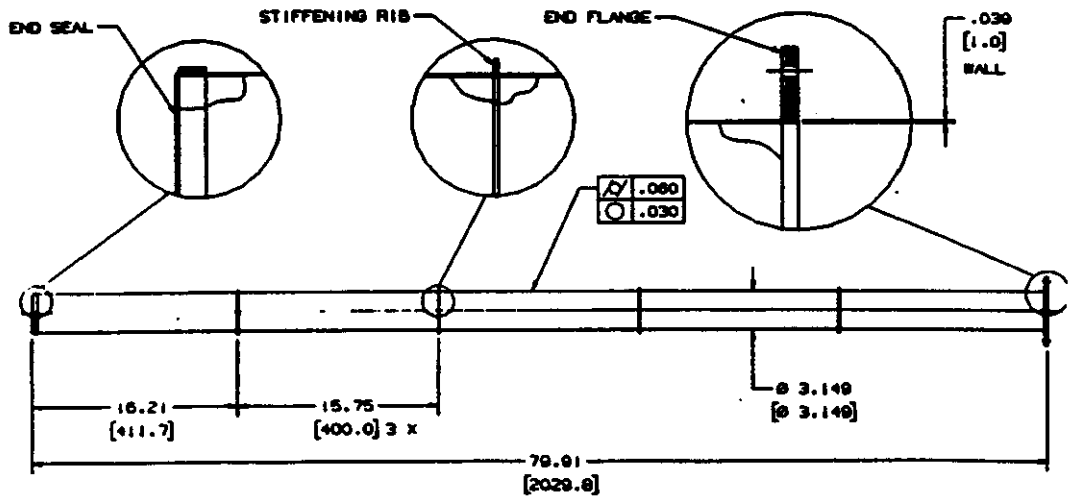

Figure 3.2.2-B Inner Beryllium Enclosure

Figure 3.2.2-C shows the results of a series of buckling analyses demonstrating the effect of wall thickness, radius and rib spacing on buckling pressure. The two sets of curves are for .015", and .020" wall thickness with either 8 or 10 cm Ø. The inner gas enclosure has been increased to 10 cm Ø to accommodate a larger vacuum beam pipe. As spacing between the ribs is varied from 12.7 cm (5") to 203 cm (80") the buckling pressure increases below 30 cm lengths, allowing for a thinner tube wall. The two added points are FEM solutions along with plots showing the buckling mode shape. The lower of the points has a value of 33 psi which is too low if out of roundness is taken into account. The higher point of 76 psi, is obtained by adding ribs at a 40 cm (16") spacing.

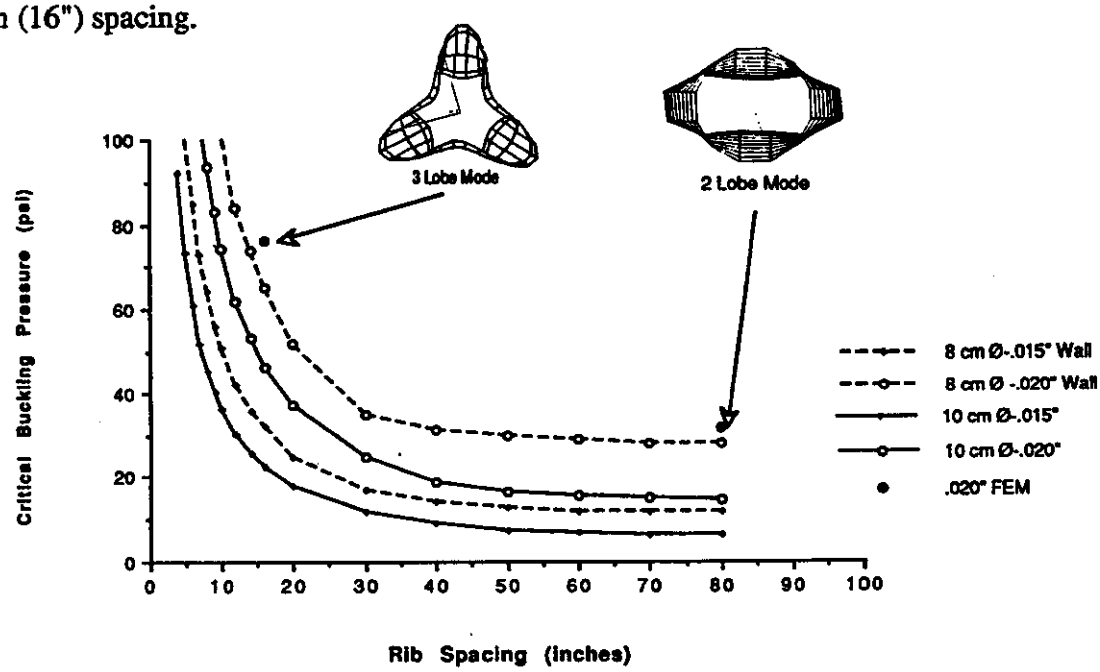

Figure 3.2.2-C Critical Buckling versus Rib Spacing

Figure 3.2.2-D is a plot of radiation length vs Eta for a .020" wall tube with ribs and a .040" thick wall tube. The thinner tube including the thickness of the ribs is clearly an advantage from a radiation length standpoint.

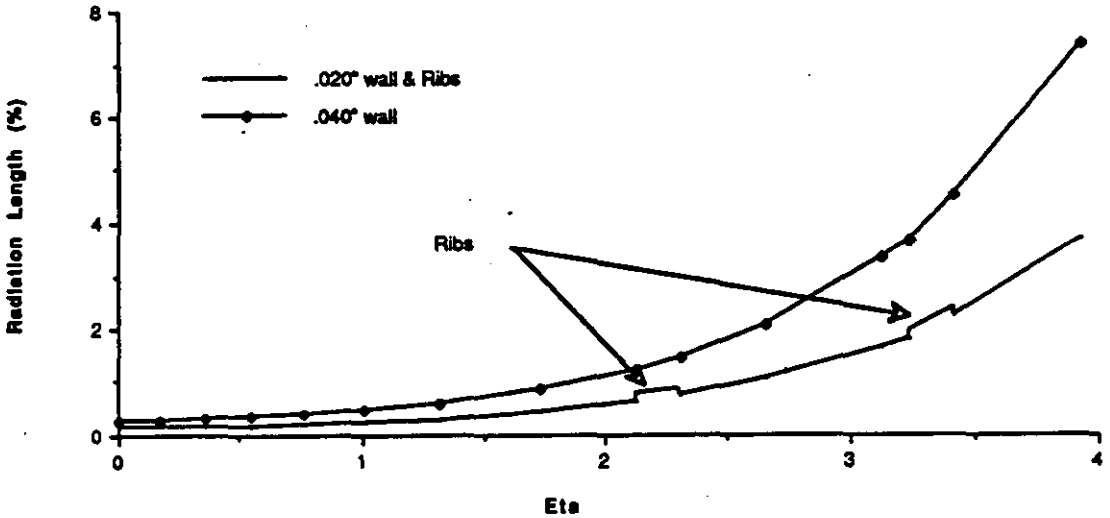

Figure 3.2.2-D Radiation Length versus Eta

To minimize the radiation length of the beryllium gas enclosure will require very tight quality control in manufacturing the vessel. Both wall thickness variation and out of roundness can have significant effects on the critical buckling pressure. Figure 3.2.2- E shows the calculated results of out of roundness vs buckling pressure. For a .020" thick wall and an out of roundness of .030"R the pressure could be off by 50 %.

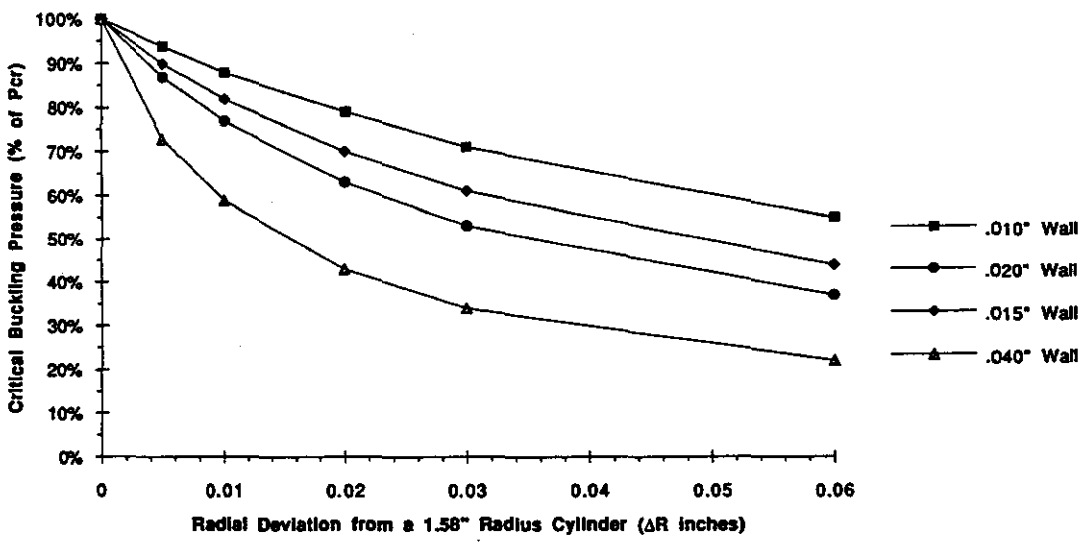

Figure 3.2.2-E Buckling Pressure vs. Out-of-Roundness

Detailed discussions with manufacturers have identified fabrication steps or techniques that may lead to these conditions. Proposed fabrication techniques include extrusion, rolling and welding, and forming and brazing. Each technique has its own tradeoffs with proposed solutions to meet the design requirements. At this time no specific fabrication technique has been chosen.

3.2.3. *Space Frame*

The central and forward planar subassemblies will be installed into a low mass, highly stable space frame that is capable of maintaining their relative alignments for long periods of time. The design requirements for this space frame include: butane vapor compatibility, radiation compatibility, thermal stability, low creep, ease of assembly and installation. Aluminum MMC material adequately meets the requirements. The material has a high elastic modulus with an acceptable radiation length. It has no moisture sensitivity, and can be modified to a near zero CTE. Figure 3.2.3-A shows the design concept for the space frame. The central detectors will be supported between the two spiders. The forward region detectors will be directly attached to the frame.

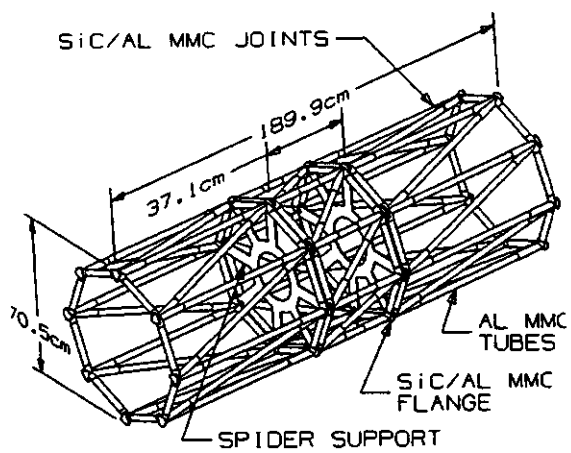

Figure 3.2.3-A: Space frame for the STS

The design is an open frame with octagonal cross-sections interconnected by longitudinal and diagonal stringers. The frame is constructed of .76mm thick 25.83mm diameter tubes bonded into composite connectors made of aluminum metal matrix / silicon carbide particulate (SiCp/6061). The modular design will include the ability to assemble and disassemble the frame for maintenance access to the center of the detector. Frame modularity was considered by incorporating positioning/repositioning pins to accurately relocate the three modular frame sections for precision assembly.

A near zero CTE frame is required to minimize the thermal deformation due to the cool down of 20° C from assembly (alignment) to operation. This will minimize the relative displacement of the central and forward subassemblies. In addition, the forward subassemblies will be kinematically mounted to the frame to isolate them from any externally induced thermal deformation. The central region support cylinders are kinematically mounted to one of the spiders, which are attached between the central and forward sections of the space frame. Power and signal cables, coolant lines, and fiber optic cables will enter along the central region spider, as can be seen in Figure 3.2-B.

3.2.3.1. Space Frame Analysis

The modal analysis of the space frame included the weight of the power and signal cables, coolant lines, and fiber optic cables which are to be supported along the length of the longitudinal stringers of the forward sections of the frame. Figure 3.2.3.1-A shows a plot of natural frequency versus the weight of cabling added to the space frame. The baseline weight for copper cabling is 130lbs. The cabling weight has a very strong impact on the overall natural frequency of the STS. Currently a redesign of the cabling to lower its mass and radiation length is underway.

The design guidelines for the space frame are to attain a stiffness which results in the fundamental frequency of the STS above 45 Hz. The selection of 45 Hz results from a "quiet" region between the 30 and 60 Hz acceleration/displacement peaks. It is desireable to be somewhere between 45 and 55 Hz for the fundamental frequency.

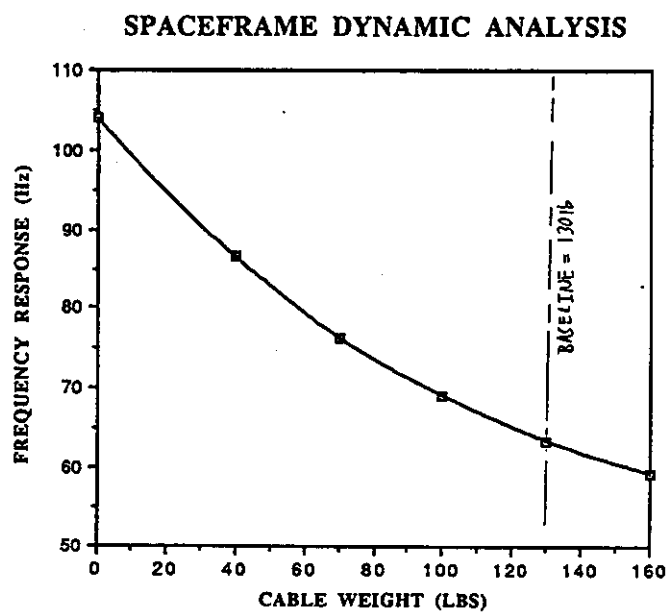

Figure 3.2.3.1-A: Natural Frequency versus the Weight of Cabling

Figures 3.2.3.1-B illustrates the effect of a variable tube modulus of elasticity on static deflection. Figure 3.2.3.1- C shows the modal analysis for the frame vs. tube modulus with zero cabling weight.

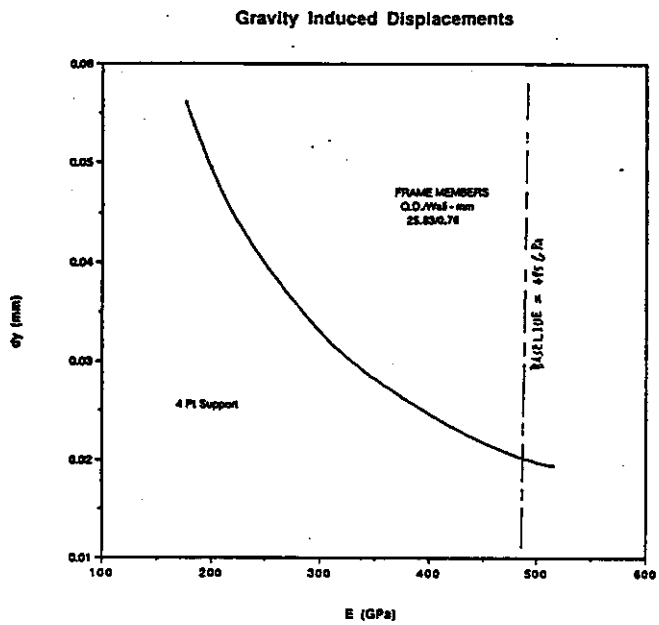

Figure 3.2.3.1-B: Static Analysis for the Space Frame with Zero Cabling Weight

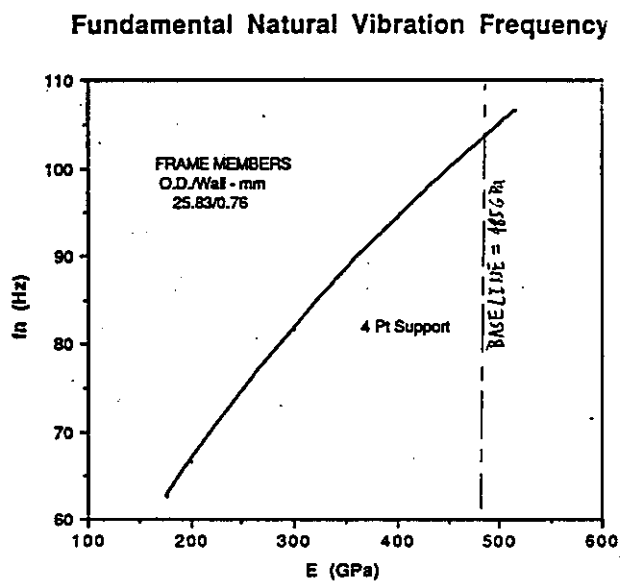

Figure 3.2.3.1-C Modal Response for the Frame with Zero Cabling Weight

Space Frame Joint Analysis

A finite element structural analysis was completed on the joints for the silicon tracking system (STS) space frame. The purpose of this analysis is to compare the stiffness of a joint/mounting flange assembly of a modular space frame to a non-modular space frame.

The original concept for the STS space frame envisioned a non-modular design which would minimize the material, thereby minimizing the associated radiation length. The problem

with this type of design, however, is that it would be difficult or impossible to install or service the central region of the STS without complete disassembly of the entire STS, including both forward regions. The STS will be the last detector out when being serviced, and consequently will be under the most serious time constraints to make quick maintenance turnaround. Such problems necessitated the design of the current three module space frame which allows for parallel assembly and maintenance ease. Each region is supported by its own frame, and the three frames are pinned together at the joints.

The original joint concept is shown in Figure 3.2.3.2-A. The advantages with this design are the radiation length, as previously stated, stiffness, and lower manufacturing costs.

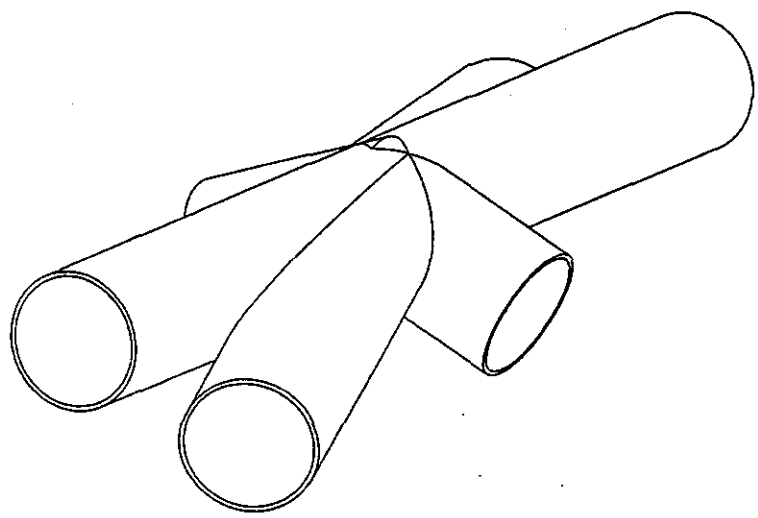

Figure 3.2.3.2-A: Original non-modular STS space frame joint concept

The current joint concept, consisting of a joint bonded to a triangular flange, as shown in Figure 3.2.3.2-B The joint/mounting flange assembly is attached to a second assembly with three fasteners. The addition of the fasteners, mounting flanges, and extra joint material amounts to an increase in radiation length, a definite concern to this design. It is a more complex design, requiring slightly more time to develop, with more components, and will be more expensive to manufacture. The modular joint is also not as stiff as the non-modular joint, an important fact for the stiffness of the entire STS space frame. It is therefore necessary to undertake detailed finite element analyses to determine the difference in stiffness between the two designs and suggest a way to minimize this difference.

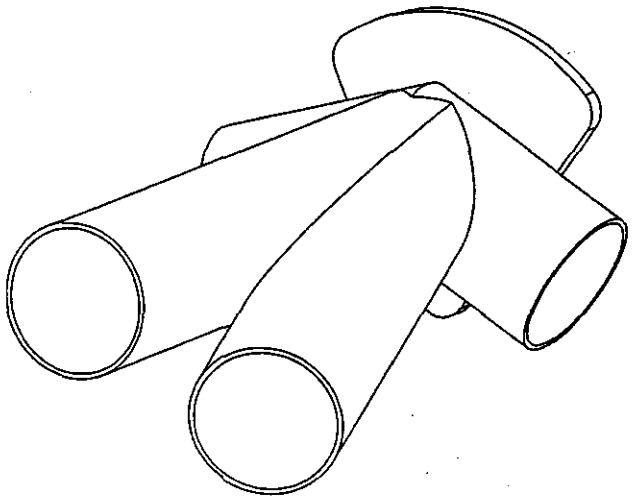

Figure 3.2.3.2-B: Current modular STS space frame joint concept

One method that can be used to increase the stiffness of the modular joint is the addition of stiffeners (gussets). Figure 3.2.3.2-C shows a preliminary design that will also be analyzed using a finite element code and compared to the previously mentioned joint designs.

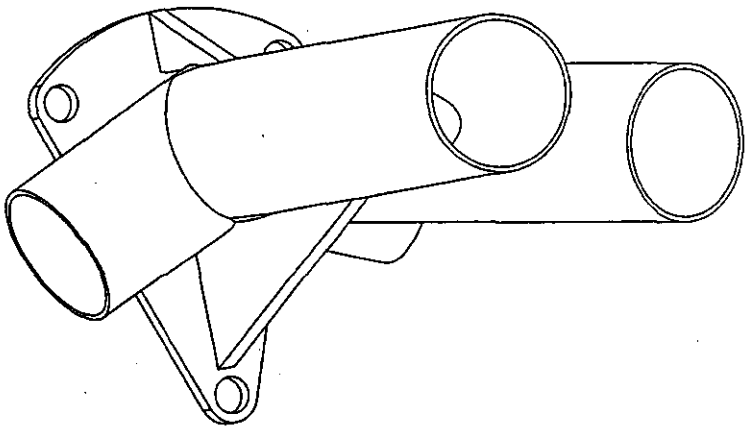

Figure 3.2.3.2-C : Preliminary modular STS space frame joint with gussets concept

The FEA compares the engineering stiffness (k) of a modular joint (Figure 3.2.3.2-D) with that of a non-modular joint (Figure 3.2.3.2-E), and a modular joint with gussets (Figure 3.2.3.2-F) when subjected to a longitudinal load as shown. The models were constructed to develop ideas on how to construct the joint to provide equivalent stiffness to the non-modular joint.

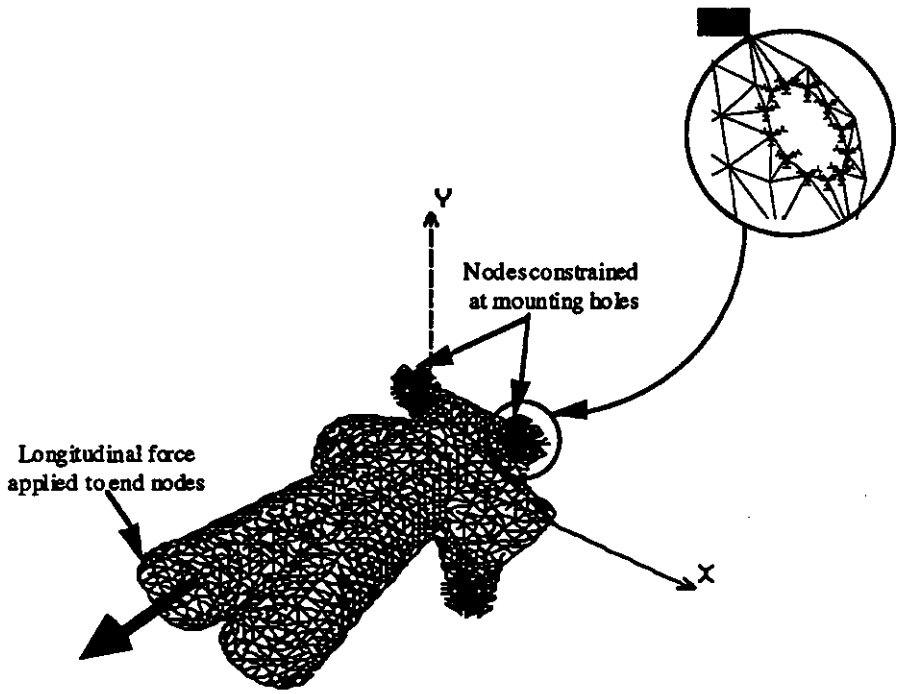

Figure 3.2.3.2-D : Finite element model of a modular space frame joint without gussets

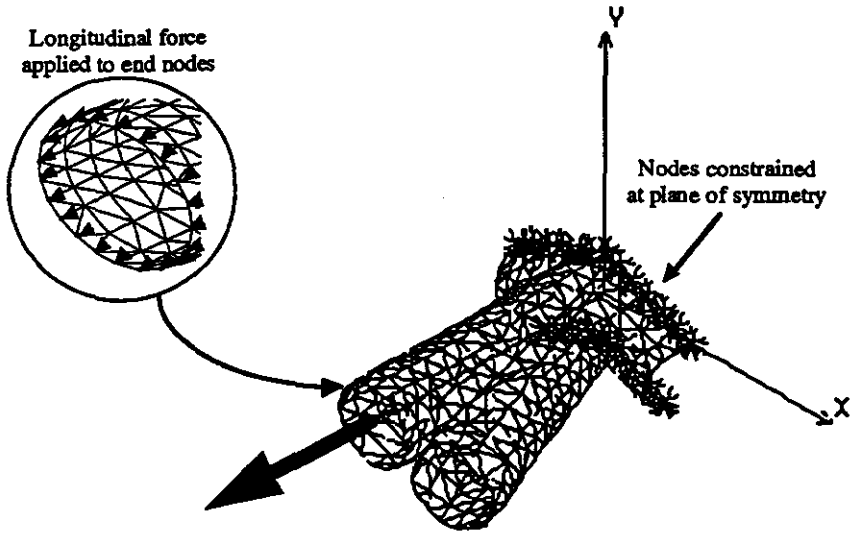

Figure 3.2.3.2-E: Finite Element Model of a Non-Modular Space Frame Joint

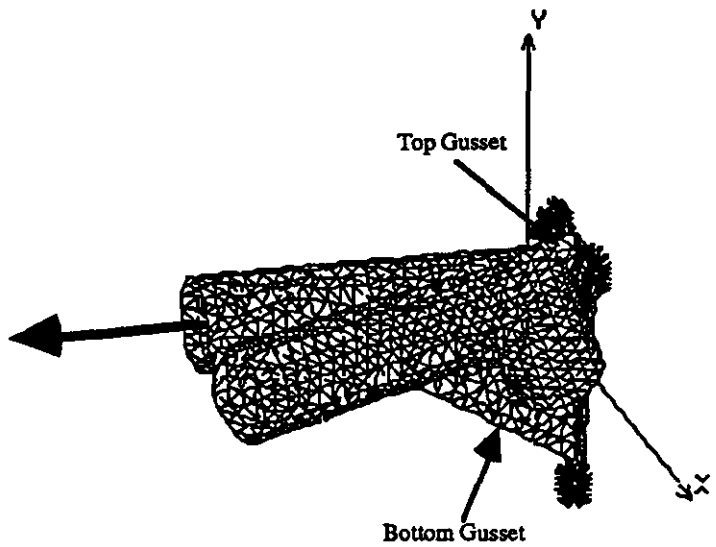

Figure 3.2.3.2-F: Modular Space Frame Joint with Gussets

The important material property in this analysis is the elastic modulus which is listed for the joint, mounting flange, and gusset in Table 3.2.3.2-1.

Table 3.2..3.2-1 - Moduli of Elasticity for Joint Components

Component	Material	Modulus of Elasticity (GPa)
Joint	Al-MMC (unidirectional)	485
Flange, Gussets	Al-MMC (quasi-isotropic)	197

The geometrical dimensions of the components have not been finalized at this point and depend largely on the results of this analysis. Flange thickness will be varied in this analysis, while the gusset thickness will remain constant at 3.175 mm with the joint wall thickness at 2.00 mm.

As shown in Figure 3.2.3.2-G there is a large discrepancy between the non-modular and modular models in longitudinal stiffness. The result is improved with the addition of a top and bottom gusset and the thickening of the mounting flange.

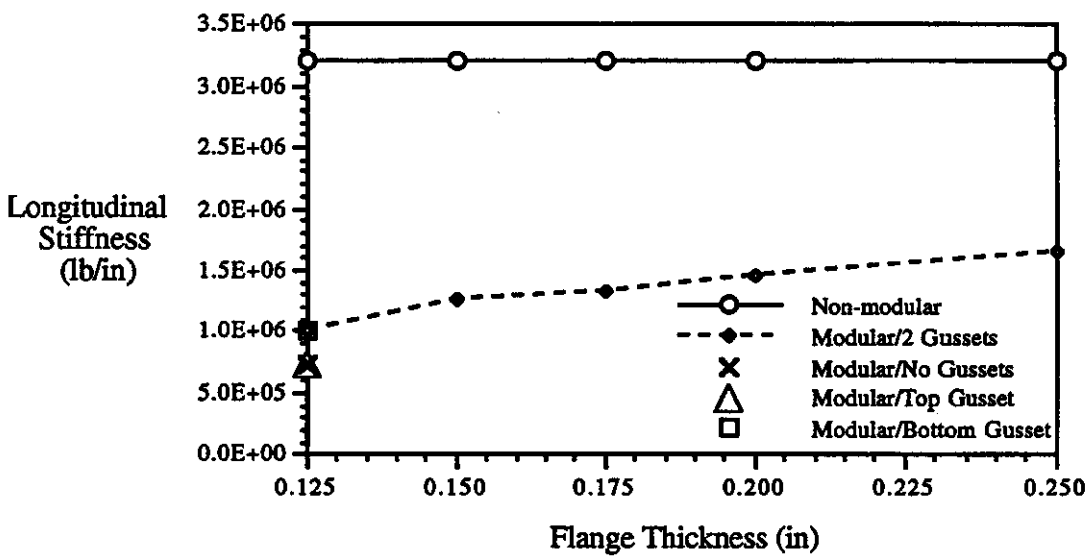

Figure 3.2.3.2-G: Plot of finite element output from the STS space frame joint analysis

At this point in the analysis the material properties assumed are those of graphite and aluminum metal matrix, even though it is realized the fiber is SiCp not graphite. Later analyses will put the lower properties into the model. The current geometry optimization is more sensitive to the present material properties, and hence will be easier to solve.

To date a modular (flanged and bolted) type space frame joint does not exhibit the stiffness of a non-modular type. The modular joint has been shown to have 22% of the stiffness of a non-modular joint. This value can be improved to 53% by adding gussets and increasing the

thickness of the mounting flange, but radiation length is sacrificed in the process. Because an equivalent higher stiffness does not seem attainable at this point, future finite element analysis performed on the STS space frame should take into account the lower stiffness of a modular joint. The overall space frame model will need to be refined further to include a reduced joint stiffness. This analysis will be required to ensure that we can maintain the structural stiffness in a region which results in the STS fundamental frequency in the 50Hz range.

3.2.4. *Central Region*

The silicon ladder assemblies are grouped into superlayers consisting of two ladder layers. Each superlayer is segmented into 36-cm long ladder assemblies. By standardizing the components, the additional cost of custom sizes is eliminated. There are a total of six ladder assemblies: two forming the inner superlayer, two forming the middle superlayer, and two forming the outer superlayer. One half of the central region superlayer is shown in Figure 3.2.4-A. Both ends of the 36-cm long ladder assembly is mechanically bonded to the inside and outside diameter of G/CE cooling rings. In addition to providing the mechanical support for the ladders, the hollow cooling ring provides the passage for the wick coolant distribution.

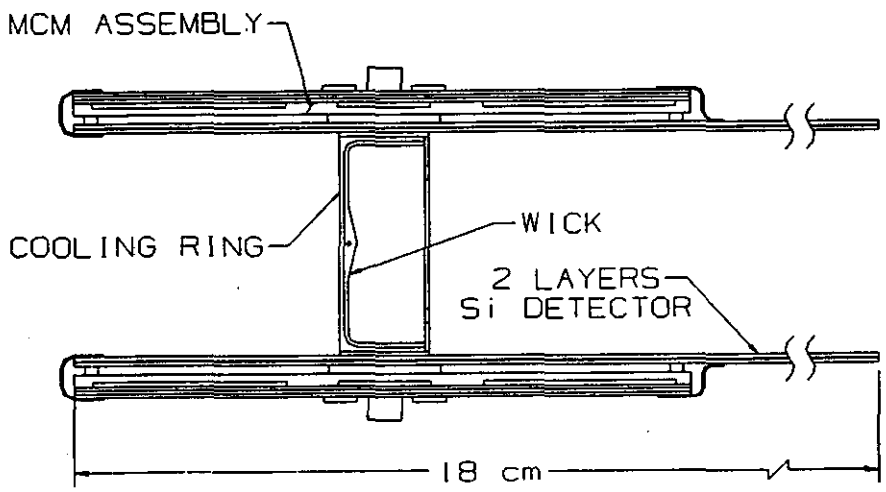

Figure 3.2.4-A: Central Region Superlayer

The decision to go from a 12 cm ladder to 18 cm ladder has resulted in substantial changes in the central region. Previously, the shorter ladder necessitated the electronics have cooling/support rings every 12 cm. The longer ladder design allows the electronics to now be all mounted outboard, away from the I.P. and spanning the entire 36 cm as shown in Figure 3.2.4-B. By stiffening the ladder assembly appropriately the central support cylinders can be entirely removed which frees up more than half the radial space, resulting in substantial design and radiation length improvements.

The cooling ring wall thickness and cross sectional height must be minimized from a radiation length consideration, and must be structurally stiff enough to provide adequate stability to the ladders. The cooling ring material of choice is G/CE for many reasons. The material provides high stiffness at low radiation lengths and is reasonably priced. Fabricating the rings by compression molding with a short chopped fiber is one method of producing this complicated, high precision, multi-surfaced geometry. Compression molding of cooling rings is difficult with the thin wall thickness required to minimize radiation length, and the very convoluted geometry. Due to additional difficulties in manufacturing the baseline wick (one piece circumferentially continuous) a change in the baseline cooling/structural ring design was made.

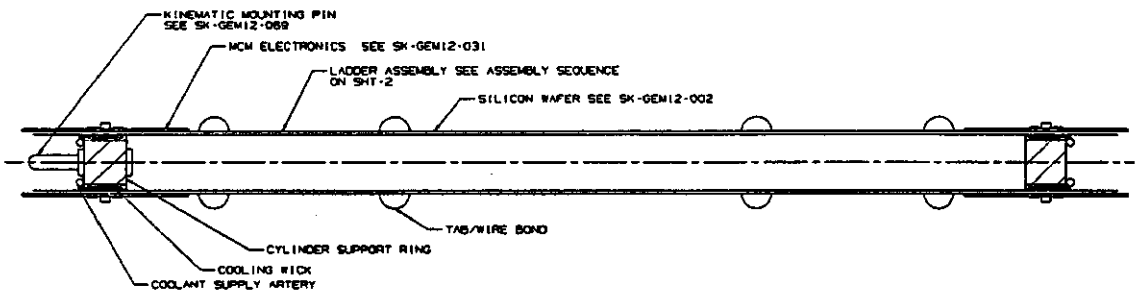

Figure 3.2.4-B Superlayer Cross-Section

The current design approach will be to use a "geartooth" layout as shown in Figure 3.2.4-C1 that uses a laminated honeycomb core fabrication. This design has the ladders at a 0 ° Lorenz angle alternating in height to achieve overlap. Figure 3.2.4-C2 is a design using a 5° Lorenz angle with ladder overlaps producing a "sawthooth " shape. The segmented "geartooth" ring improves several areas : 1) the cooling ring no longer has to be compression molded, 2) the wick can be made in small segmented pieces. The facets are no longer to be fabricated as an integral part of the ring but will now be a separate piece which can be bonded after the ring has been fabricated and machined.

Figure 3.2.4-D shows the entire central region with ladders at a 5 ° Lorenz angle. The support spokes which are used to support and tie all the central region superlayers together can be seen. The superlayer support material and the support spoke are made of the same material to match the CTE's to prevent thermally induced strains. The ladders are bonded to the top and bottom of the cooling ring and overlapping at the edges. The minimum edge to edge overhang is set by overlapping the inactive regions of the wafer, the inactive region due to the stereo strips, and 5 strips to assure detector coverage. The minimum overlap is 3.8 mm. The actual overlap will be established for each layer by keeping the nominal wafer width constant.

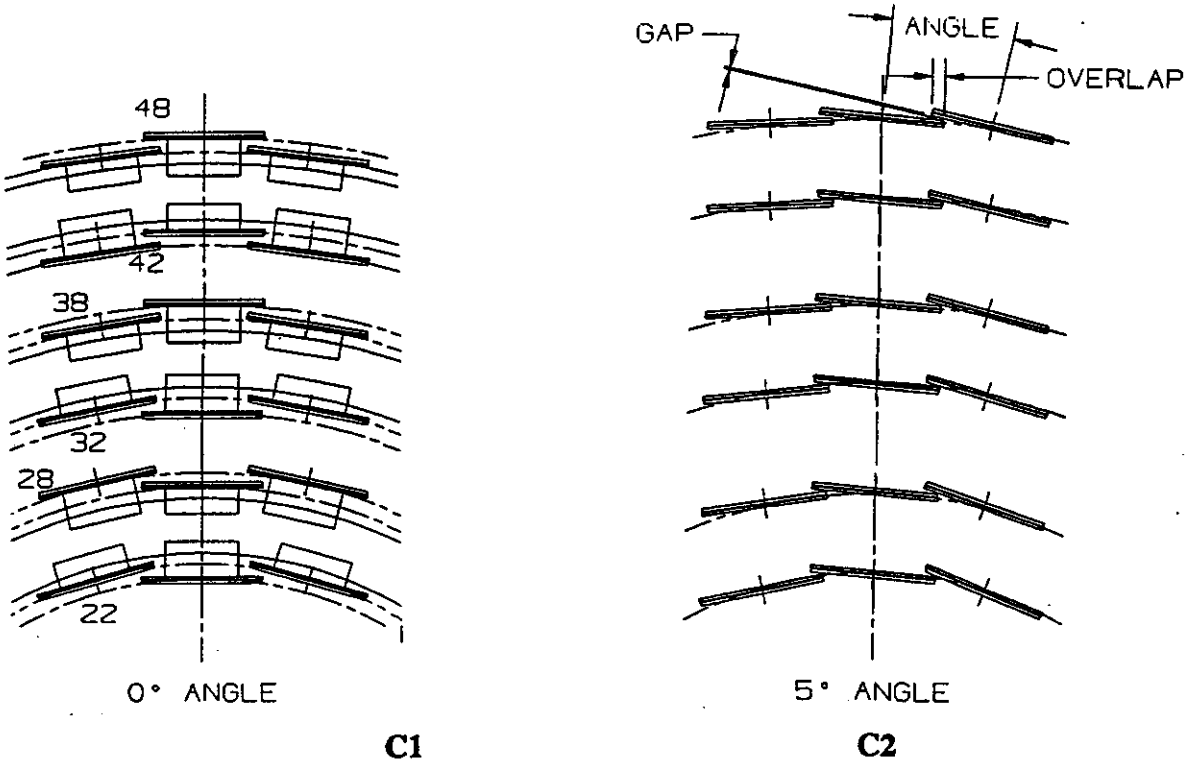

Figure 3.2.4: Proposed Central Region Geometry, Previous Geometry

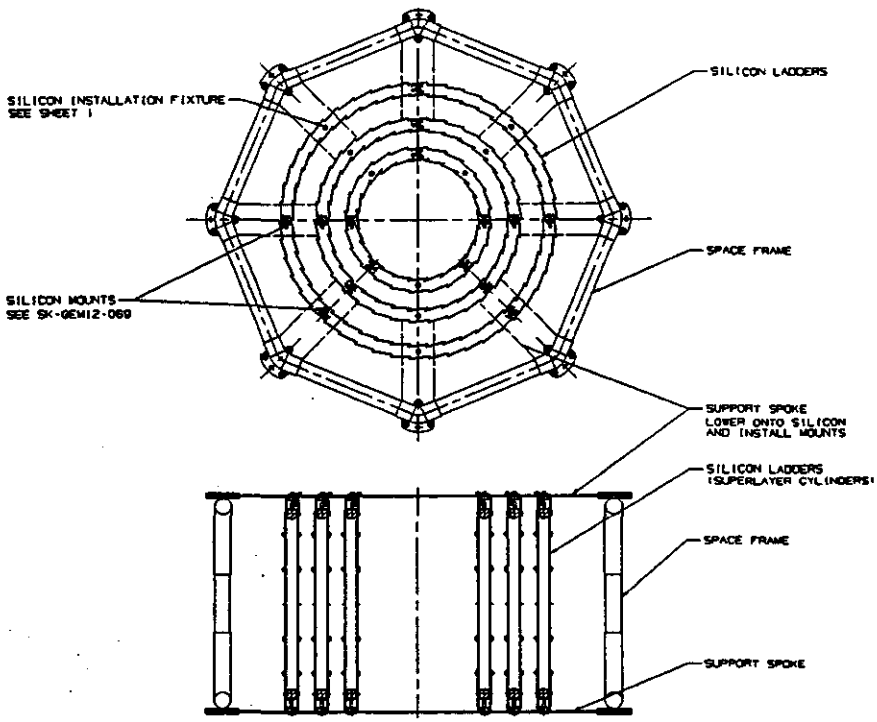

Figure 3.2.4-D Central Region assembly

Each superlayer shell assembly is attached to three of the spokes with kinematic mounts to isolate the cooling rings from strains induced through web. 3 mounts are attached at one end, and two mounts are attached at the opposide end. Figure 3.2.4-E shows details of two types of proposed mounts.

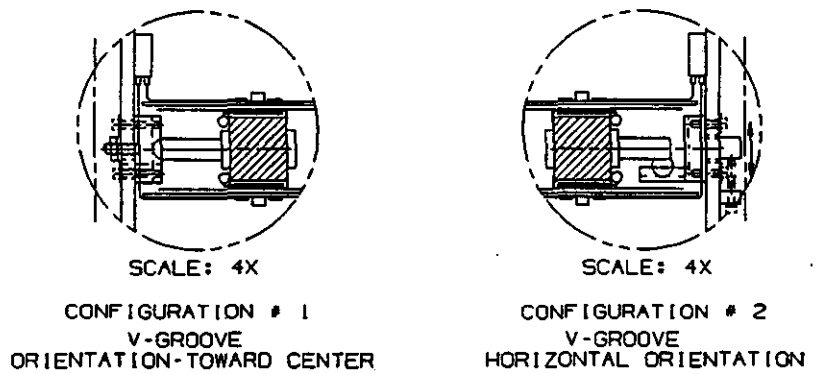

Figure 3.2.4-E: Central Region Kinematic Mounting

The cables will be mounted to the central region support spokes which come down between the forward and central region space frames. This small area will contain the 2 - 5 volt electronics power supply, 50 volt wafer bias supply, LED power supply, digital and trigger signals, thermal instrumentation, transmitting and receiving FO cables, in situ alignment FO cables, and grounding plane and shielding. The ribbon cables attached to the ladder electronics will be routed down and connected to the power bus. The design of the ribbon cable to bus connector will require substantial R&D to develop a low radiation length, multi-connector, detachable connection.

The current baseline design incorporates the use of one LED per MCM assembly. The minimum bend radius for a 250 μm Ø fiber optic cable might be as high as 5 cm R., which will require a series of gradual bends from the LED into the cooling ring.

3.2.5. *Forward region*

Design details of the forward region planar subassemblies shown in Figure 3.2.5-A. The design specifications for ladder stability, operating temperature, ladder overlap, signal and power cable routing are basically the same, so a similar design philosophy will be incorporated. The ladder will be tapered from a maximum of 33.4-mm wide down toward the centerline, with a ladder length of 14 or 16-cm. Identical electronics packages are mounted at the readout end of the ladders. Structural support for the ladders will come from an inner and outer ring with three interconnected spokes at 120° apart. Kinematic mounts would be installed as shown in Figure 3.2.5-B.

The forward region assemblies are grouped into superlayers in a similar manner as the central region. A minimum number of different inner and outer radii are preferable to minimize the construction costs. The axial placement is established to maintain three superlayer intercepts by any ray originating at the interaction region. Ladders would be alternately bonded to the cooling rings front and back with a nominal five strip overlap at the edges. The outer edges of the ladder assemblies would be bonded over the cooling ring in much the same manner as the central region ladders. However the inner edges would be attached to small radially flexible members that would allow for differential thermal expansions due to small mismatches in CTE.

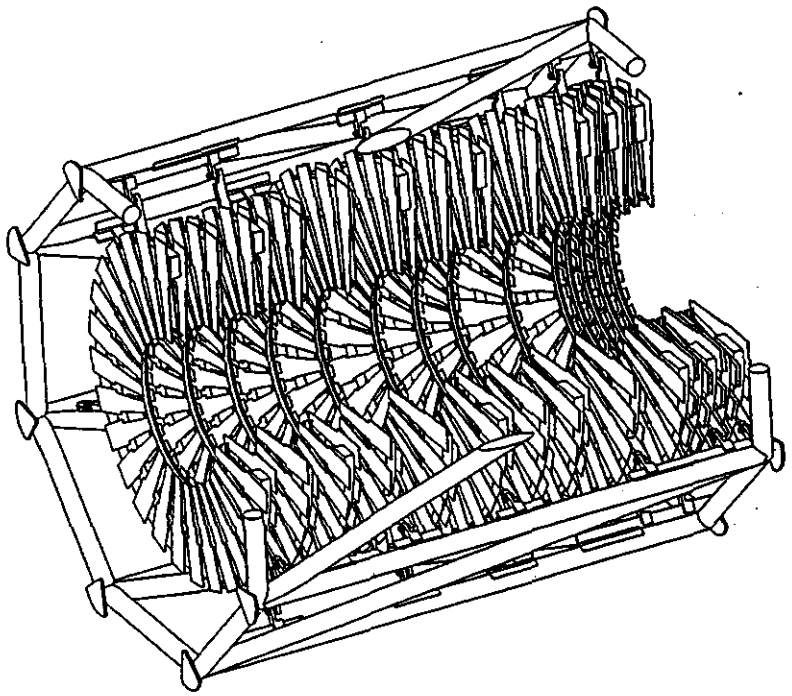

Figure 3.2.5-A: Forward Region Assembly Cut-Away

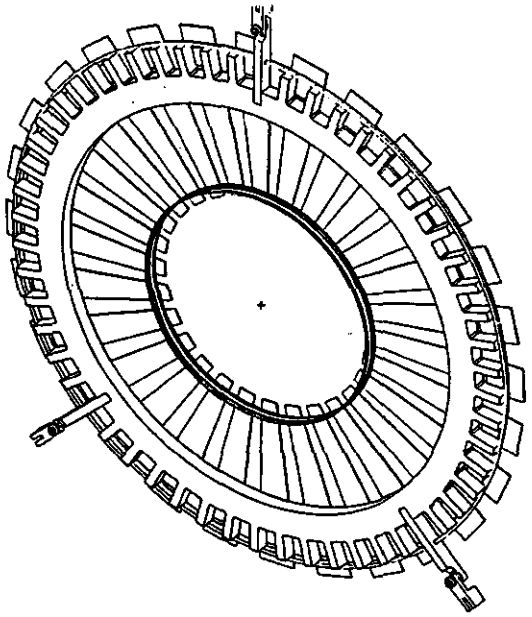

Figure 3.2.5-B: Forward Region Planar Assembly

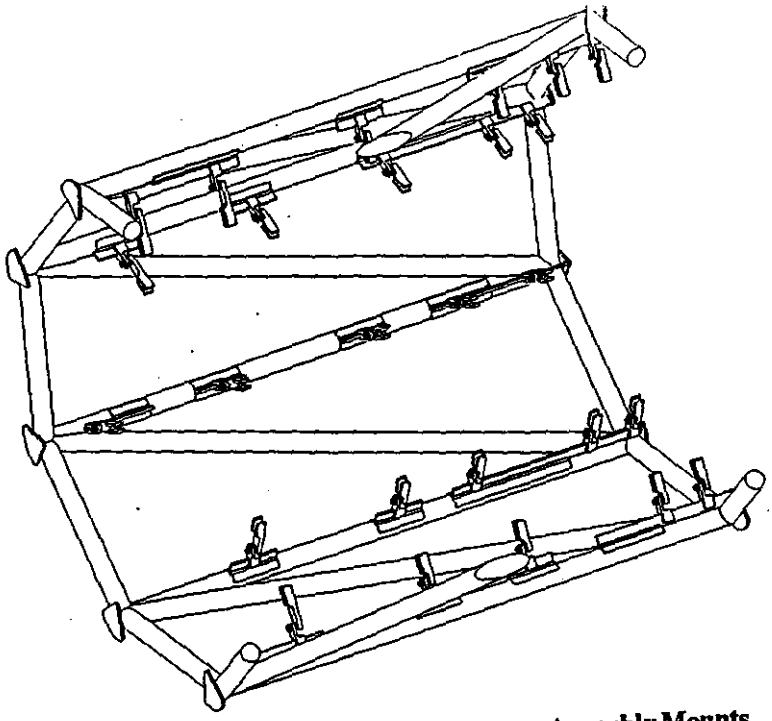

Figure 3.2.5-C: Forward Region Planar Assembly Mounts

3.2.6. Cooling system

The silicon tracker contains over 1942 MCM assemblies each generating about 3.5 W of thermal energy or a total heat load of 6.8 kW. Heat generated in the central region subassembly is extracted through 6 cooling rings of 3 different diameters. A total of 1.45 kW of heat is generated in the central region as follows:

Cooling Ring	# MCM/Ring	Heat Load/Ring	# Rings
Inner layer	48	168 W	2
Mid layer	69	242 W	2
Outer layer	90	315 W	2

The forward region contains 28 cooling rings extracting 5.35 kW of heat distributed as follows:

Cooling Ring	# MCM/Ring	Heat Load/Ring	# Rings
16 cm disk assy	56	196 W	20
14 cm disk assy	51	179 W	8

The local heat fluxes at the MCM / cooling ring interfaces may be as high as 1.5 W/cm^2. A maximum operating temperature of 0°C has been selected to minimize the detector leakage current which has a strong temperature dependence. The mechanical stability requirements call for precise thermal control over the entire assembly with a minimal thermal gradient. In addition, the system should operate as close to atmospheric pressure as possible to minimize the need for structural mass in the gas enclosure.

These requirements have led to the development of a baseline cooling system which uses an evaporative phase change system to isothermally cool the detector assembly. Evaporative systems offer several advantages over other systems. Evaporative cooling systems are characterized by high local heat transfer rates which yield lower thermal gradients and greater isothermalization over large areas. Coolant flow rates are much lower, requiring lower liquid inventories, and thereby lowering the radiation length. A closed loop thermo-siphon system is passive in operation, with temperature stability self regulating. A phase change system also provides uniform pressure distribution throughout the containment system.

Cooling alternatives are being evaluated that include: forced convection of air or nitrogen gas, and forced convection of either a water-glycol or water-methanol mixture. Forced convection with gases would produce thermal drifts and gradients as well as dynamic pressure conditions. The cooling rate at the detector surface for a gas cooled system is well below demonstrated cooling rates of an evaporative system. Directional flow associated with gas

convection can also produce large thermal gradients from inlet to outlet producing nonuniform thermal displacements. A forced flow gas convection system will require high flow rates generating high pressure gradients and turbulence induced vibrations. Large gas inlet and return lines are also required to support the high flow rates. These cooling characteristics cause a gas cooled detector to have generaly poorer dimensional stability.

Forced liquid convection cooling is being investigated as an option to 2 phase cooling to develop a quantitative comparison of the mass flow rates, thermal gradients, and total radiation length. Figure 3.2.6-A shows a optional water cooling loop for a forward and central region cooling ring. Each ring contains a single pass coolant loop that enters one side of the ring and flows evenly around each side to a return line that exists at the end.

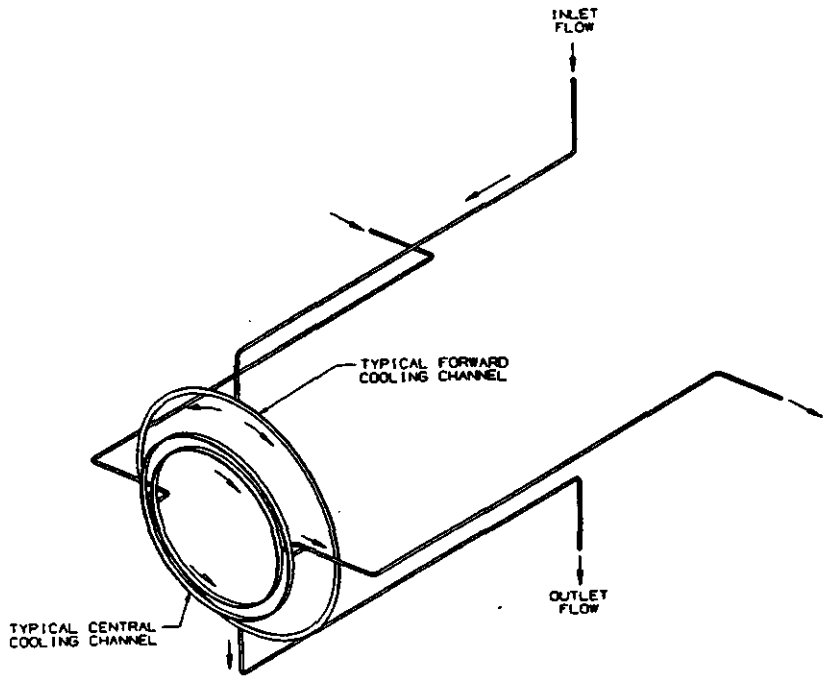

Figure 3.2.6-A Typical Liquid Coolant Loop.

The coolant channels could be located inside a honeycomb core cooling ring as shown in Figure 3.2.6-B. The channel would be located directly under the MCM, centered in the middle. Thermal calculations have been done with a baseline channel 1 cm wide and .2 cm high, with an Aluminum wall 100 μm thick. Complete system pressure calculations, which have yet to be accomplished, will determine the wall thickness required for dimensional stability. A draw back to this configuration is the mismatch in CTE between the channel and silicon ladder assemblies. An alternate design might be to have short lengths of rectangular channel interconnected with flexible joints that would mechanically decouple the channel into many small segments. This would lead to many connections and potential leak sources as well as pressure losses at each bend and connection.

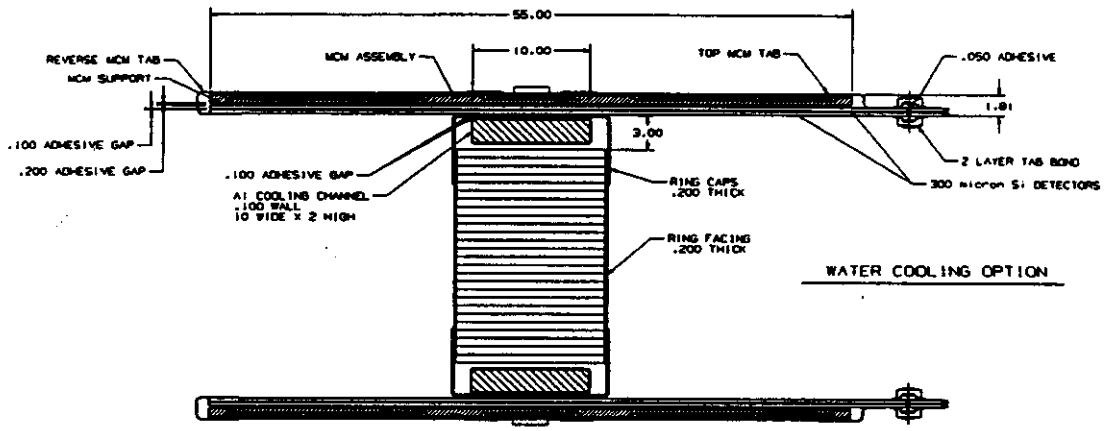

Figure 3.2.6-B Water Coolant Channel

Liquid coolants considered so far include water-glycol and water-methanol mixtures to keep the water from freezing at an operating temperature of 0 °C or slightly lower. The freezing point of the solution can be controlled by the ratio of the liquids as shown in Figure 3.2.6-C. Due to thermal line losses and convection film gradients the coolant could be at -10°C or colder, so -20°C was chosen as a safe initial specification. Both 40 volume percent methanol and ethylene glycol give freezing temperatures below -20 °C.

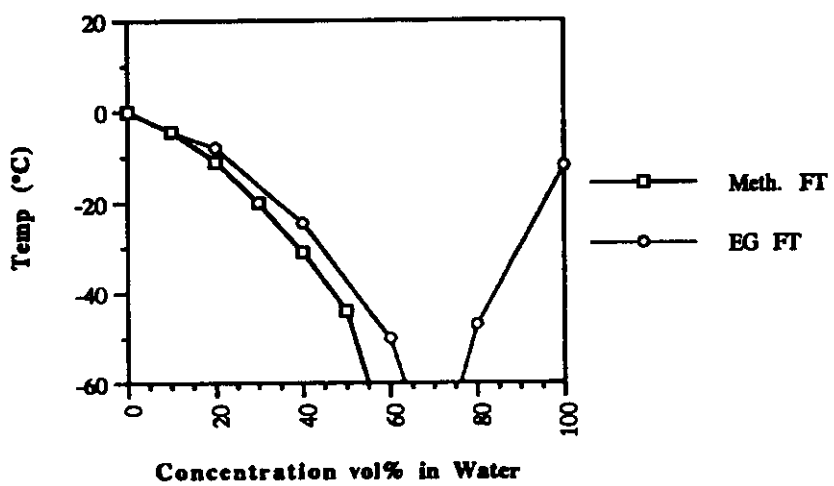

Figure 3.2.6-C Coolant Freezing Temp. vs Concentration

Coolant viscosity is a very important property which will determine our pressure losses in the system. It is highly desirable to operate at a suppressed pressure less than atmospheric to meet a leakless specification. This would guarantee that any system leak would not expel coolant out of the channel onto the electronics causing damage. For this reason we desire the lowest coolant viscosity. Figure 3.2.6-D shows the coolant viscosity with varying concentrations

of methanol, ethanol and ethylene glycol. The data shows that at 40 volume % concentration and a temperature of -20 °C, methanol is the additive of choice. An even lower viscosity can be obtained with increased methanol concentration, however a flammable mixture is reached at 60 volume percent.

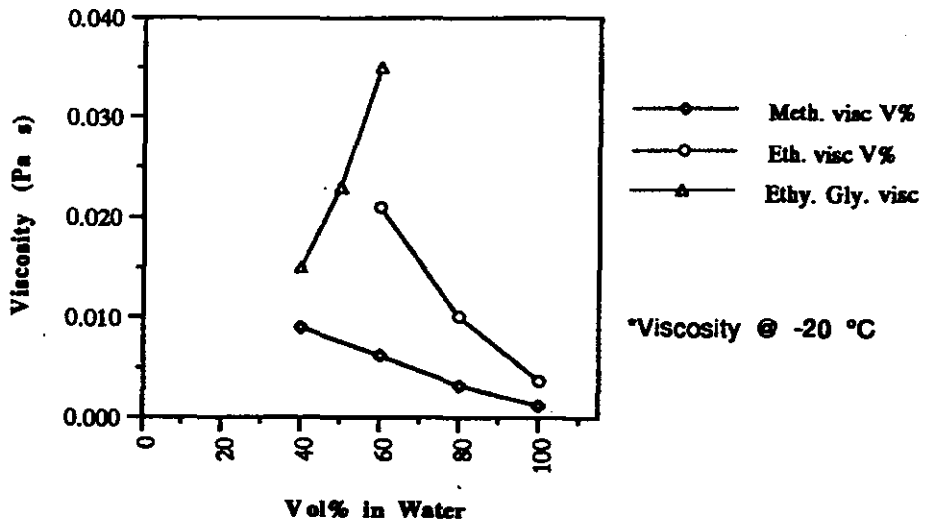

Figure 3.2.6-D Coolant Viscosity versus Concentration.

The surface heat transfer coefficients for water cooled systems are better than gas systems, but are less than that of an evaporative cooling system. This would result in a larger thermal gradient than an evaporative system, for a given heat flux. Preliminary calculations on this coolant line cross section yield a convective heat transfer of about .075 W/cm^2 °C, compared to .3 W/cm^2 °C for an evaporative system. The area would be larger for a coolant tube due a larger perimeter area however the heat fluxes are not constant due to conductive gradients in the side walls. Figure 3.2.6-E shows the effect on convective heat transfer coefficient and film ΔT due to varying channel aspect ratios. Low aspect ratios have very high heat transfer coefficients that produce low film temperature gradients, but produce high pressure losses. For our channel parameters with an aspect ratio of .2, a uniform heat flux would give a film ΔT of 4.5°C. A more detailed calculation shows a variable heat flux producing a ΔT of 7 °C. This temperature can be lowered by increasing the tube conductive wall thickness by at a radiation length penalty.

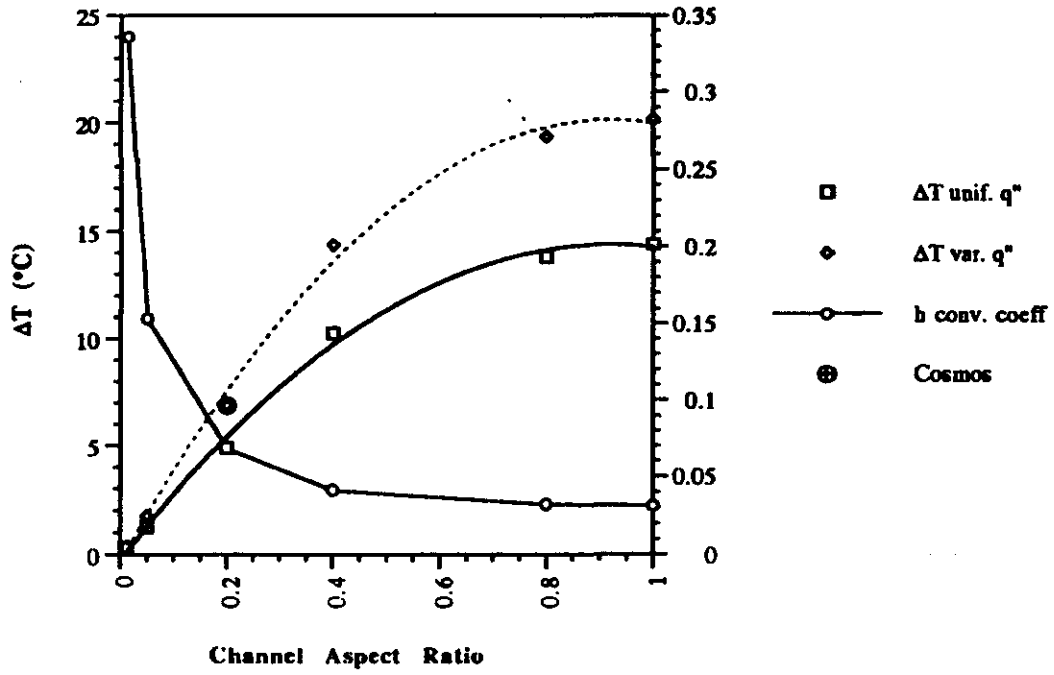

Figure 3.2.6-E Coolant Film ΔT versus Aspect Ratio.

Thermal gradients are also produced along cooling lines with distributed heat sources, developing a coolant temperature increase by as much as 5°C. These gradients can be minimized by using short multiple parallel cooling lines but at a substantial radiation length penalty. Figure 3.2.6-F shows a more complete system layout of half of the tracker. Each cooling ring contains a single pass coolant tube with a supply and return line to the end of the enclosure. The supply and return lines are distributed azimuthally to smear the added radiation length.

Where thermal transfer efficiency is required, as in the rings, the line is rectangular in geometry and where mass transfer efficiency is required, as in the supply and return , circular lines would be employed. From a mechanical stability aspect the flow conditions are designed to be laminar throughout to avoid turbulent vibration. With such high viscosities this is hard to avoid and not a major issue. This gives us the opportunity to investigate high flow rates in the supply and return tubes to keep the radiation length down, but causes an increase in pressure drop down the lines. At this point a more detailed system design would be required to establish the total system pressure drop.

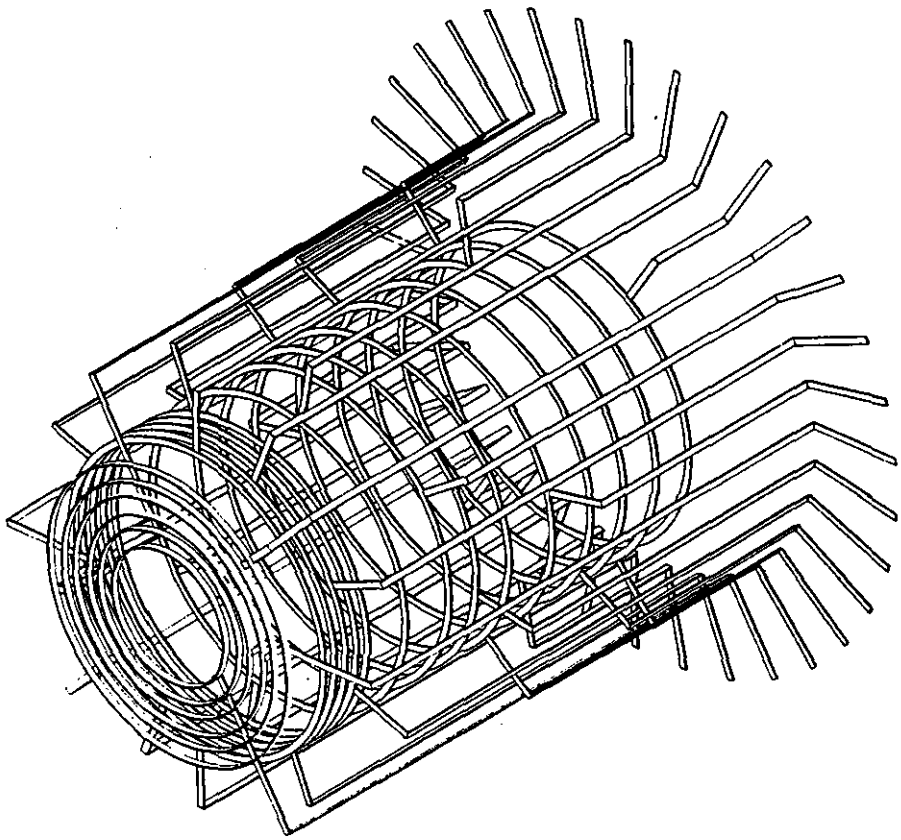

Figure 3.2.6-F Liquid Coolant Supply System.

Meeting the challenging design goals of minimizing both radiation length and thermal strain, and maximizing the mechanical and thermal stability may be easier to achieve with a phase change cooling system.

Phase change mediums with near 0°C boiling points at atmospheric pressure include fluorocarbon refrigerants such as R-12 B1 and R-114. Fluorocarbons refrigerants are undesirable for this application due to the decomposition in a radiation environment producing fluorine and chlorine radicals which can damage the silicon detectors. Both refrigerants are toxic and R-114 is a known carcinogen. Several amines, which are also flammable, have been considered as potential working fluids, but they decompose under radiation to form ammonia. Table 3.2.6-A is a list of fluids with boiling temperatures near 0°C.

Table 3.2.6-A Two Phase Fluid List

Fluid Name	Composition	$T_{boiling}$°C	Compound	Class
Dimethylamine	C_2H_7N	6.9	Am	F
cis-2-Butene	C_4H_8	3.8	HC	F
Bromomethane	CH_3Br	3.5	HC	T
R 114	C2F4Cl2	3.0	FC	NF
Trimethylamine	C_3H_9N	2.9	Am	(F)
trans-2-Butene	C_4H_8	0.9	HC	F
n-Butane	C_4H_{10}	-0.4	HC	F
R 12 B1	CF2BrCl	-3.7	FC	NF
1,2 Butadiene	C_4H_6	-4.4	HC	
Sulfur Dioxide	SO2	-4.6	Ac	T
R C318	C4F8	-5.8	FC	
1-Butene	C_4H_8	-6.3	HC	F
Methylamine	CH_5N	-6.4	Am	T(F)
R 142b	C2F2H3Cl	-9.1	FC	NF
iso-Butane	C_4H_{10}	-11.9	HC	F
R 506	(mix)	-12.3	FC	NF
Dimethylsilane	C_2H_8Si	-20.1	HC	
Cyanogen	C_2N_2	-21.1	HC	T
Dimethyl ether	C_2H_6O	-24.8	Eth	F

The abbreviations listed under class are F - flammable, NF non-flammable and T - toxic. Butane has a normal boiling point at 0°C, is stable under radiation, non-toxic, and chemically compatible with silicon; however, it is flammable with the appropriate oxygen mixture.

For butane in air, the lower and upper explosive limits are 1.9 and 8.5 percent by volume, respectively. The butane system will always be enclosed in a secondary gas enclosure filled with nitrogen gas as described in an earlier section. This will always allow for a control over the butane gas mixture in the event of a leak. If butane were to leak out, it would be diluted into the secondary flowing nitrogen gas. If a leak occurred with a lower internal pressure the nitrogen would flow into the butane environment, not air. More detailed safety features are described in the GEM Conceptual Safety Analysis Report (CSAR).

The MCM heat generating sources will be mounted on top of the cooling rings as shown in Figure 3.2.6-G.

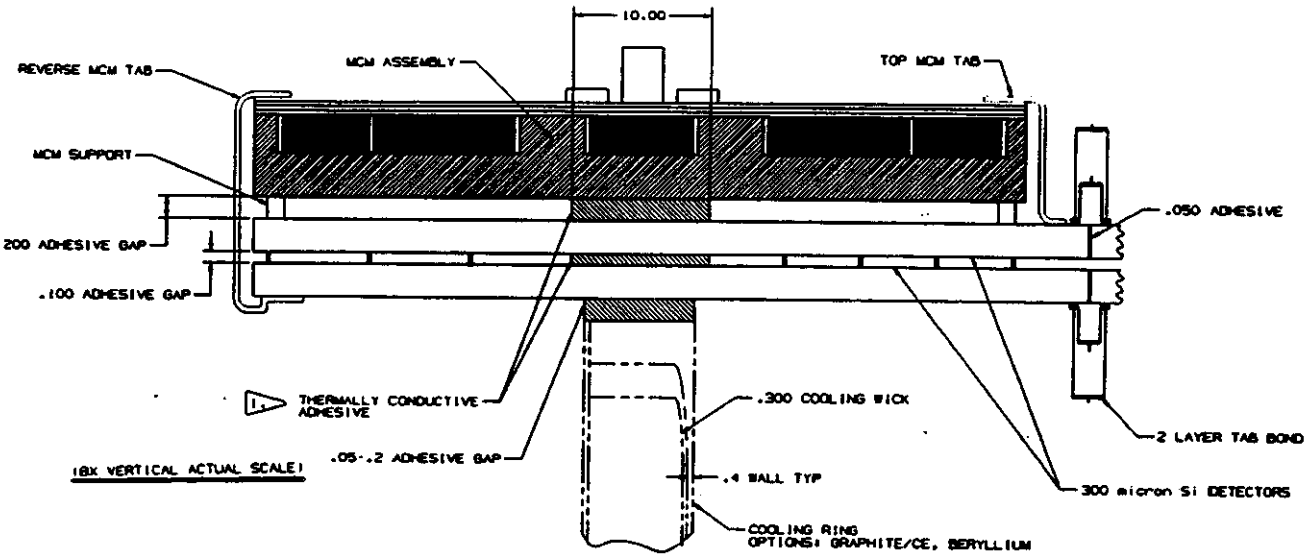

Figure 3.2.6-G Cooling Ring Cross Section.

The evaporative wicks could be mounted inside the cooling ring as shown, or mounted on the Ladder assembly outside of the cooling ring. The liquid in the wicks evaporates due to the electronics heat load. The fluid loop is closed by transporting the resulting vapor to a condenser driven by the small pressure differential that exists between the silicon tracker containment vessel and the condenser. The condensed liquid is fed back to the detector array through a liquid distribution system. Butane or isobutane will be used as the coolant because of the desire to operate the silicon at near 0° C and at 1 atmosphere pressure.

In the interest of minimizing system mass, the design goal is to supply the circumferential artery with liquid from the liquid distribution system at a single point. Thus, the gravitational pressure drop is a major contribution to the total pressure difference between the liquid and vapor. Figure 3.2.6-H shows a 2 phase coolant liquid supply system with evaporative wicks. The circumferential wicks could be segmented and individually mounted in the ring or on the ladder. A minimum of 4 supply lines would supply the coolant to the wicks from above as shown or from the underside to minimize the pressure drop.

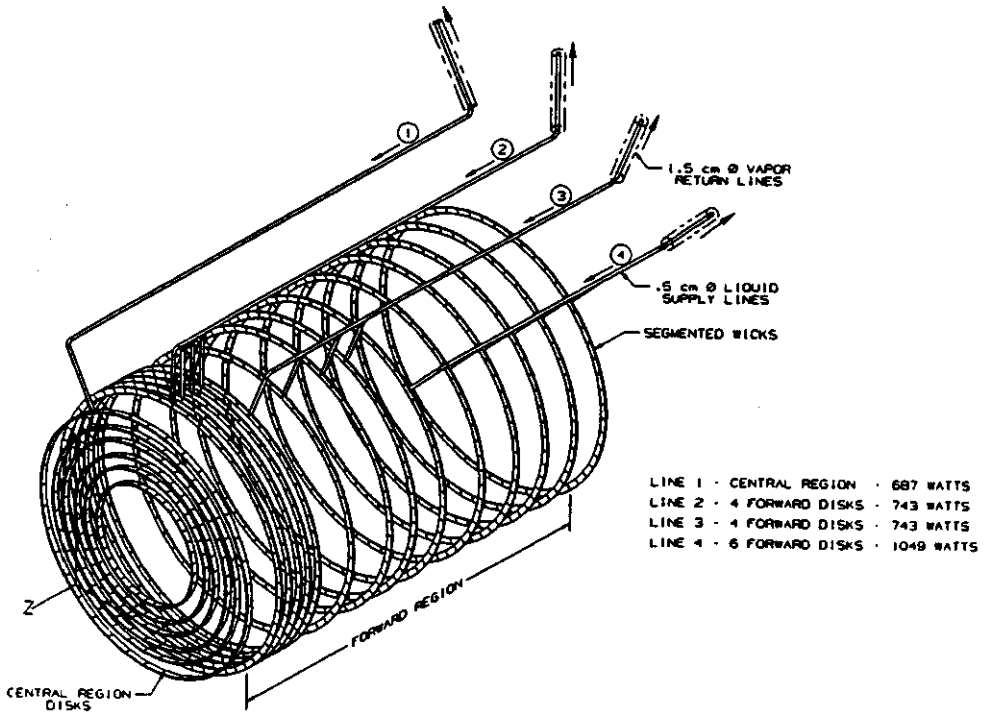

Figure 3.2.6-H Two Phase Coolant Supply

This total pressure drop must be sustained by the capillary pumping capability of the wick structure. A large pore size will lead to uncontrolled bleeding from the wick, however smaller pore sizes lead to higher wick thermal gradients and reduced permeability. Figure 3.2.6-I shows some recent data from the SDC R&D for three different wick materials. Most of the tests to date have been conducted with polystyrene wicks over a range of porosity in an effort to find an optimum point. The data shows a temperature decrease with larger pore sizes, but resulted in uncontrolled bleeding. A higher thermal conductivity wick is required at small pore sizes to lower the temperature to an acceptable level. Both porous beryllium and porous graphite wicks have been fabricated and tested. As shown on the plot, beryllium offers very low temperature gradients with graphite being a bit higher. At this point not enough samples have been tested to develop a full curve of the relationship.

There are additional pressure drops that must be overcome by the capillary pumping capacity of the wick structure. These are power and power density related in that they are dependent upon the mass flow rate due to the evaporation. They are also dependent upon the allowable wick thickness, which is limited by the allowable radiation length. If the wick permeability is too low a "dry out" condition can develop leading to locally high temperatures.

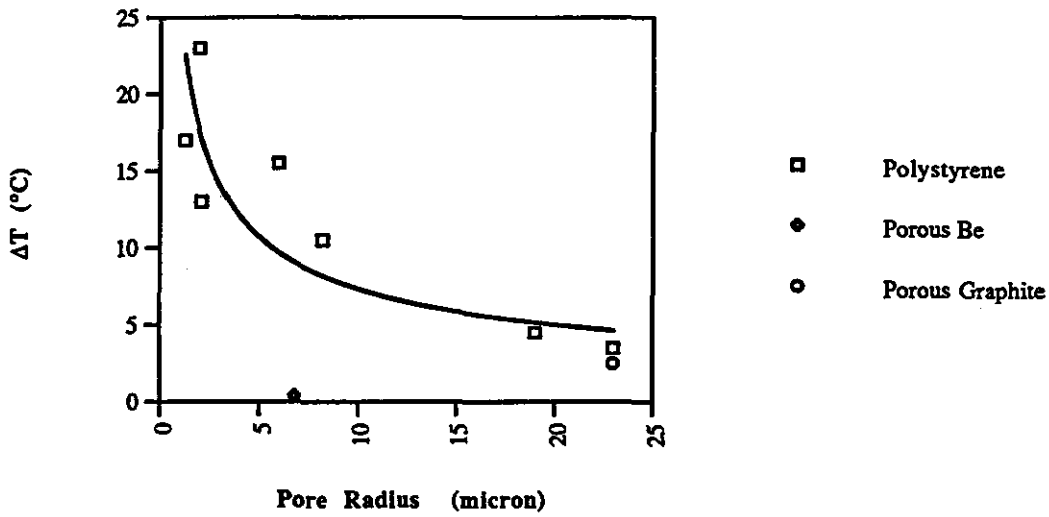

Figure 3.2.6-I Wick ΔT vs Pore Size.

Figure 3.2.6-J shows a design proposal for a two phase system that breaks up the functionality of a single wick into several components that that can be more easily optimized. This design would require a thermally isolated supply artery to prevent the formation of vapor in the arteries. The system would operate under a hydrostatic pressure as apposed to pure capillary action. This would ensure positive wetting of the wicks preventing vapor build up and dry out. The wick would serve to uniformly distribute the coolant against the surface with the heat flux. A large pore sized graphite wick would keep the film temperatures reasonable and have a high enough permeability to ensure adequate wick supply. A selective surface with a small pore size would be required to prevent uncontrolled the bleeding. The right combination of proper microporous film material and coolant could produce a nonwetting surface that will not bleed but still allow free vapor passage.

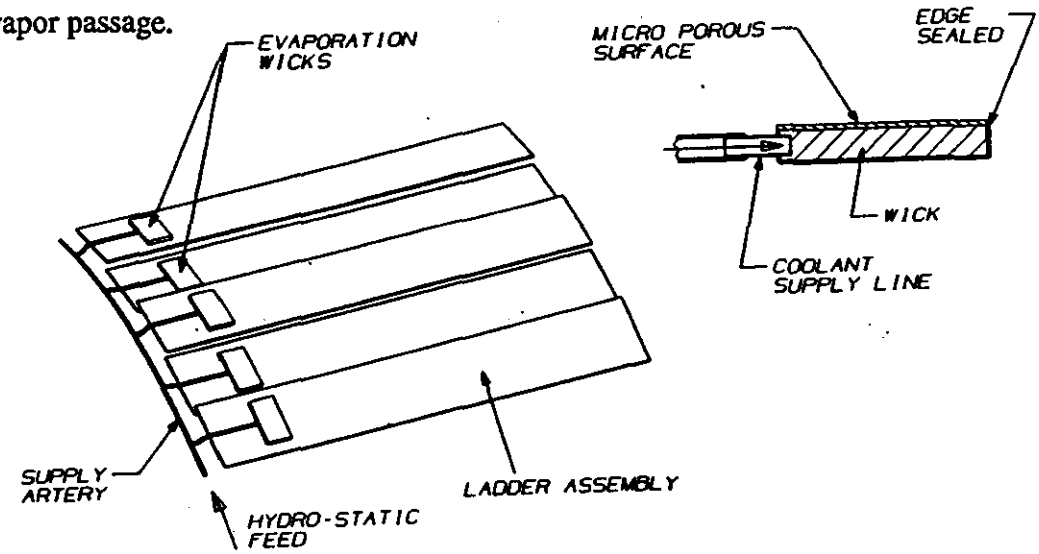

Figure 3.2.6-J Segmented Evaporation Wicks.

Design details hinge in part on the development of the optimum wick structure for liquid distribution and design options that improve the thermal coupling between the electronics and the wetted wicks. A suitable wick structure must be developed and incorporated, liquid and vapor line sizes must be finalized, the condenser must be designed, a suitable start-up and shut-down procedure must be developed, and system component testing must be performed.

3.2.7. *Silicon Alignment and Detector Monitoring Systems*

Mechanical design, alignment systems and assembly procedures must be closely coordinated to build a high resolution STS. Concepts for GEM detector alignment/assembly procedures have just been started. The difference between actual placement tolerances and knowledge of position need to be carefully separated and considered. The tolerances requirements will determine where the most effort is placed, either in assembly or in calibration and stability monitoring. The most difficult tolerance will most likely be the circumferential positioning of parts, subassemblies and detectors. Even the easiest tolerances will be quite demanding, probably too demanding for manual placement.

Next, six distinct alignment/assembly steps need to be defined and planned. Assembly/alignment procedures depend on a definition of: 1) a stable assembly reference system, 2.) an assembly procedure, alignment system and mechanical placement machine to attach silicon ladders to support rings and planer arrays, 3) an assembly/alignment procedure to attach shells and planer array subsystems to a space frame, 4) a method to place the assembled detector onto the SSC beam line, 5) alignment monitors to follow alignment changes during assembly, transport, installation and use, and 6) a calibration procedure to be used for the installed detector. Trade off's between these steps will influence the cost, assembly time and difficulty of building the detector.

In addition to the alignment/assembly procedures some testing, most likely on prototypes, should be planned to establish the stability of completed subassemblies. A dependable alignment monitoring system will relieve some burden on the mechanical stability of the assembly, but monitoring systems only monitor a few points on the structure; subassemblies are treated as rigid bodies. TV holography is a test procedure with the required resolution and field of view for testing the stability of completed subassemblies. The technique is basically an optical interferometer for non-optical surfaces. A state of the art system can measure quantitative and qualitative information about object shape, shape changes induced by mechanical or heat loading, mechanical resonance frequencies and resonant Q. State of the art TV holography systems are not available commercially. They have to be custom built to carry out these important tests.

Critically important and challenging is the alignment monitoring system for the calibrated detector. A useful alignment system should monitor detector alignment shifts after assembly, during transport and installation, and between calibration runs. The resolution of the monitor should be sufficient to determine when another calibration is needed. If the rigid body assumption about the subassemblies is valid, and if the alignment monitor has sufficient dynamic range, then after an initial calibration run, the monitoring system can be used to correct particle track information and eliminate the need for continuous time consuming calibrations .

A concept for a continuously monitoring system is shown in Figure 3.2.7-A. The 3-D positions of one subassembly relative to another, and the position of the silicon detector to the outer detectors, are monitored with a rad-hard, compact non-intrusive fiber optic motion sensor. As shells are attached to the space frame, fiber optic motion sensors will also be attached to every rigid body subassembly to monitor the internal relative 3-D positions and changes to each other. Additional monitors will provide the same information on the tracker reference system to a reference outside the detector. At the present stage of development of fiber optic motion sensors, a motion sensor is needed for each degree of freedom to be monitored.

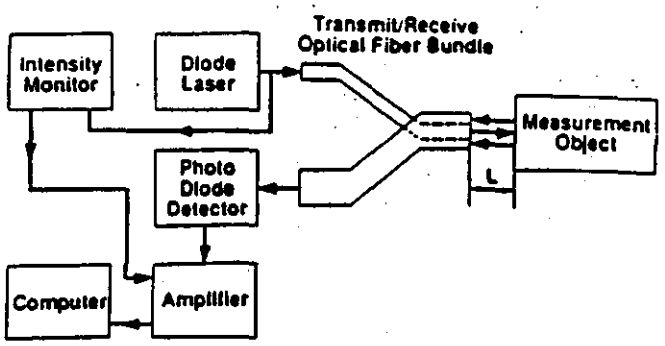

Figure 3.2.7-A: Subassembly Alignment Monitoring System

With five monitors on a rigid assembly, as shown all motions except translation along the beam axis are monitored. If the motion sensor is reflected off of spherical surface, all 6° of freedom can be monitored with a seven fiber bundle assembly shown in Figure 3.2.7-B. Using this technique, detector alignment status can be continually monitored from initial assembly through transport and installation, and during operational use between calibrations.

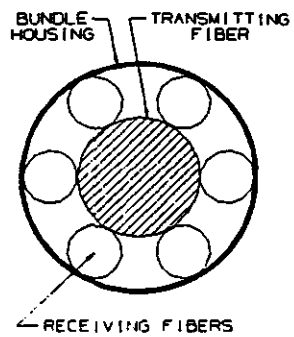

Figure 3.2.7-B: 7 Fiber Bundle Assembly

A simplified schematic for a motion sensor system is shown in Figure A with typical response curves. For a few mm between fiber and object the response is on the order of 8 mv/μm. The measurement resolution is .05 microns. The response curves are linear on the leading and trailing parts of the curve, either of which are suitable regions for operating points. With automatic gain control any variations in the light output from the diode laser can be monitored and compensated. Calibration can be carried out on a test fiber away from the detector.

Installation should be relatively easy, if it is planned into the detector from the beginning. Since all the active hardware is outside of the detector volume, the system will be very robust. The several mm spacing between fiber and object used for published results is smaller than needed for detector applications, but similar results for 2.5 cm spacing and 1 micron resolution, and many mm of dynamic range have been demonstrated. The response curve shape is similar for the larger spacing between the fiber and object. The position of the peak response can be adjusted by choosing an appropriate receiver fiber diameter.

The fiber optic motion sensor is now a research device, not commercially available; research is needed to develop the concept for the detector application and test and calibrate it during prototype tests. Other than this technique there is no known, easy technique to continuously monitor the alignment status of the detector during transport and between calibrations.

3.2.8. *Silicon Ladder*

Two silicon detectors are bonded edge to edge to form an 18 cm long ladder that will be read out at one end. An 18 cm length ladder has advantages of reduced cost, channel count, and power consumption and provides options for simplifying the assembly. The two stereo layers will be bonded back to back producing an included angle of 10 milliradians as shown in Figure 3.2.8-A.

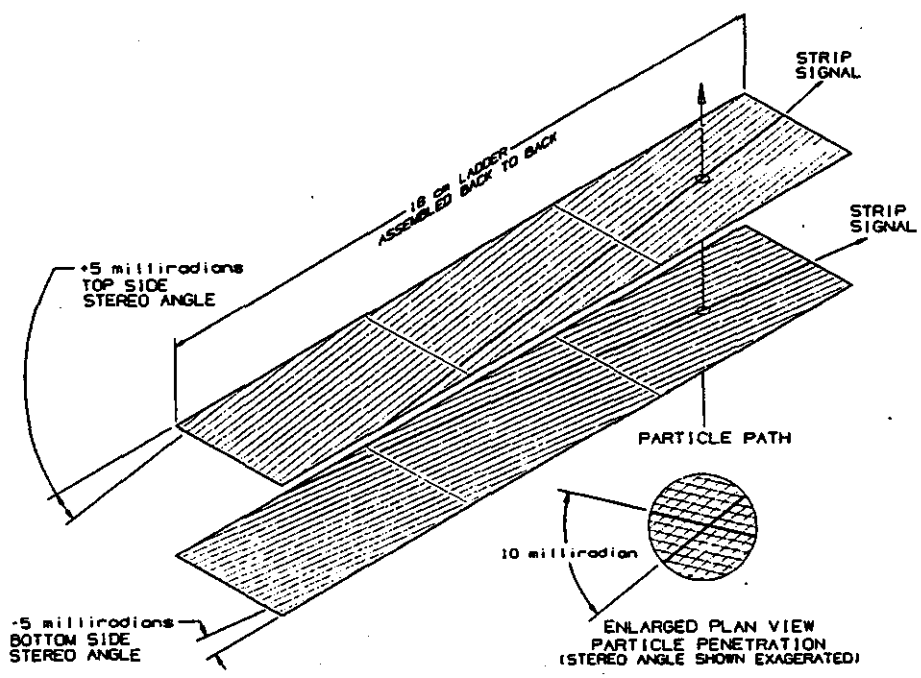

Figure 3.2.8-A Stereo Angle.

A large single MCM is mounted on the top of the ladder over the cooling ring end as shown in Figure 3.2.8-B. It is critical to maintain a low profile compact ladder assembly in order to achieve compact packaging of the ladders onto the cooling rings.

The edges of the silicon ladder are structurally reinforced with thin G/E rails to increase the transverse stiffness of the assembly. Fundamental to this design, is the plan to carry the fabrication, assembly, and testing of the individual components in parallel as far as possible. This will provide a little relief in the schedule since these are in the critical path, but most importantly this will allow for individual component testing prior to final assembly commitment.

The first step in the assembly is to perform the end to end mechanical bonds of the 18 cm ladder, and then proceed to either tab or wire bonding. The silicon wafer strip surfaces are expected to be very thin and delicate. This drives us to consider doing the wire bonding prior to bonding back to back, otherwise the wire bonding pressure could be transferred to the lower facing causing potential damage.

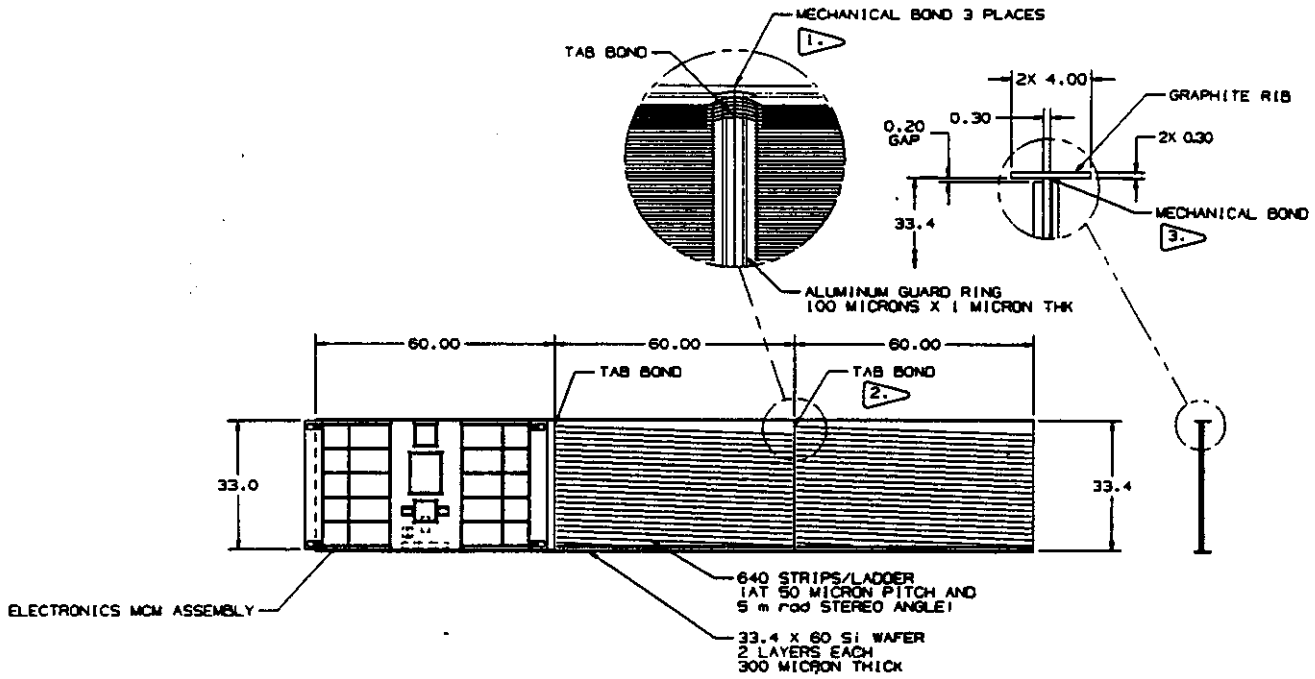

Figure 3.2.8-B Ladder Assembly

In parallel, the electronic MCM would be fabricated and qualified through testing prior to being committed to the wafer assembly. Mounting the MCM assembly directly on the face of the wafer presents a possibility of damaging the very thin (1 μm) SiO_2 coating. Prototype tests will have to conducted during the R&D phase to develop procedures and techniques for the assembly step. This assembly will also contain the ribbon cable which delivers the electronics power, timing and calibration signals, and bias voltage for the wafer.

Once the MCM assembly has been qualified, it will be mechanically bonded to the wafer assembly and wire bonded to the strip pads. At this stage of the assembly there is the opportunity for additional systems tests before proceeding to the back to back assembly. The back-to-back assembly will require accurate lateral positioning of the two stereo layers. Several techniques will be investigated during the R&D phase, along with prototype assembly tests and evaluation.

Details of the MCM are shown in Figure 3.2.8-C. The major components of each electronic subassembly are: ten 128 channel analog bipolar chips, ten digital CMOS chips, 1 controller CMOS 2D chip and CMOS 2A, one TDM chip and an LED and driver, all mounted on a hybrid substrate.

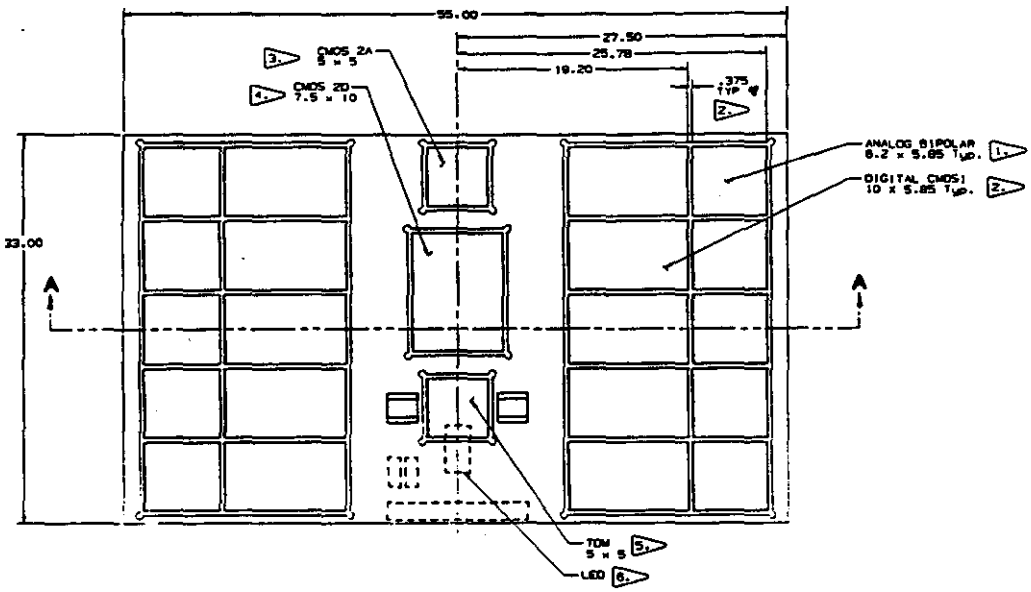

Figure 3.2.8-C MCM Assembly

Listed below are some of the required thermal and structural design specifications:

Maximum ladder assembly distortion	< 100 μm
(including gravitation effects, thermal distortion and externally induced strains)	
Maximum electronics CMOS operating temp.	35° C
Maximum bipolar operating temp.	25° C
Maximum detector temp (at commissioning)	5° C

Sources of heat generation are the analog IC, digital IC, controller IC, TDM and LED. The specifications for the heat sources are :

Analog thermal load*	1.2 mW/channel	1.536 watts total
Digital thermal load	.3 mW/channel	.384 watts total
CMOS 2D	250 mW	.250 watts total
CMOS 2A	50 mW	.05 watts total
TDM	250 mW	.250 watts total
LED	500 mW	.500 watts total
Total MCM heat load		3 watts

*Additional power requirements to increase the signal : noise will drive the heat load up to possibly 3.5 watts.

Cooling ring power density 3.5 W / 2.23 cm^2 = 1.57 W/cm^2

The material selection of the hybrid on which to mount the electronic components is strongly driven by the need for good thermal conduction to the heat sink. Material options for the MCM substrate include Alumina, Beryllium Oxide, Aluminum Nitride and Silicon. Radiation length and CTE mismatch to the ladder are also important properties in the proper selection. Beryllium Oxide is not a strong candidate since Texas Instruments would prefer to not work with the oxide. The table below lists the materials and relevant properties:

Material	Th. Cond. (W/cm °C)	Rad Le (cm)
Al_2O_3	.35	10
BeO	1.6	31
Si	1.3	9.36
AlN	2.0	25

Figure 3.2.8-D is a plot of thermal conductivity times radiation length which gives a magnitude of thermal conductance normalized to radiation length for various materials. Aluminum nitride which has both a good conductivity and radiation length is the material of choice from a technical point of view.

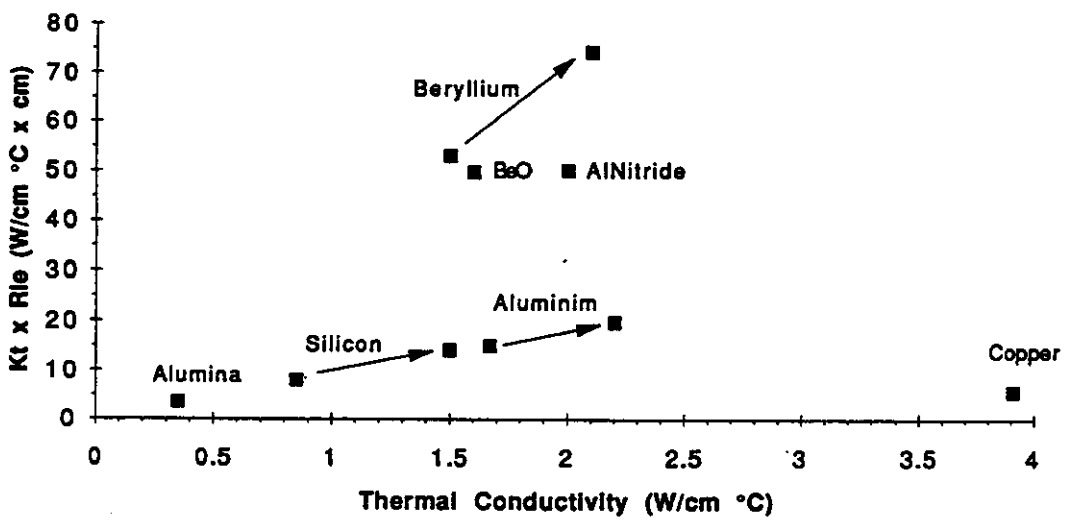

Figure 3.2.8-D MCM Substrate Material Comparison.

Figure 3.2.8-E shows the mechanical design that was modeled to understand the thermal profile throughout the MCM assembly (the vertical scale has been increased 8x for clarification). The thermal loads for the chips and LED are distributed on the top surface of the integrated

chips, and the MCM is thermally coupled to the cooling ring through the adhesive layers to the cooling ring.

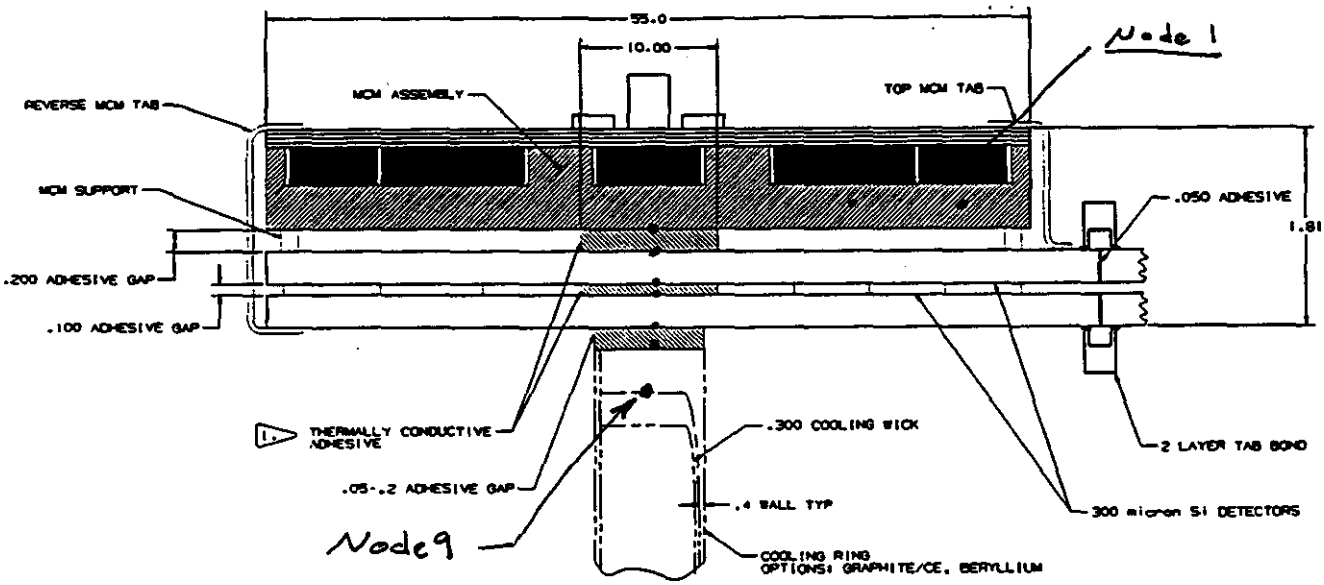

Figure 3.2.8-E MCM Thermal Model

Figure 3.2.8-F shows calculated thermal profiles through the MCM from the analog IC (node 1) to the evaporative wick interface (node 9). A maximum of 14 °C is achieved in the analog IC and the detector is at about 6 °C. The right hand figure is a bar chart representation of the temperature drop between nodes. Additional calculations for a range of MCM thicknesses and material composition are summarized in Figure 3.2.8-G.

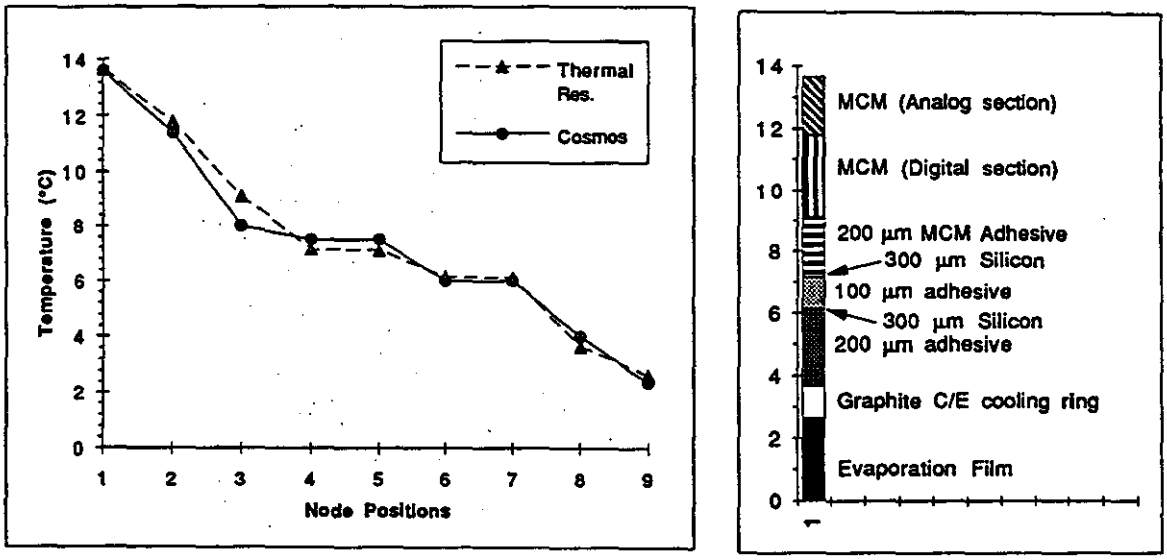

Figure 3.2.8-F MCM Thermal Profile.

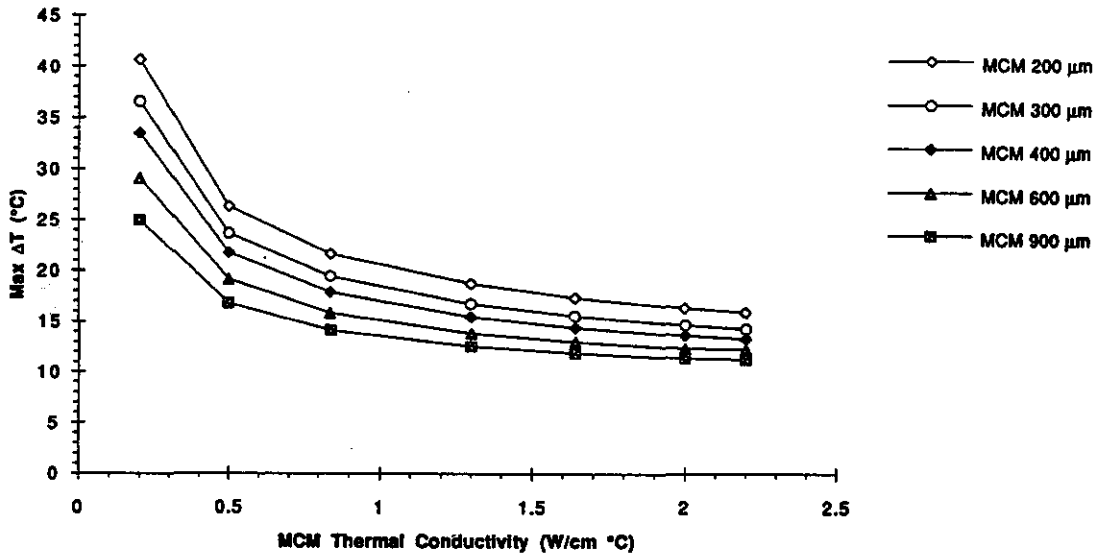

Figure 3.2.8-G Max Temp versus Conductivity & Thickness

The calculations indicate that an MCM substrate with a thermal conductivity less than .5 w/cm °C (Al_2O_3) produce unacceptably high temperatures in the Analog IC (> 25°C). These temperatures can be lowered by increasing the substrate thickness up to 900 µm, but the radiation length becomes quite high. The current baseline design proposal is to use Aluminum Nitride at 350 µm thickness, which is cost effective production thickness For Texas Instruments.

To minimize the lateral deflection and increase the natural frequency, several options for stiffening the wafer in the transverse direction have been considered. Small thermal gradients, gravity, cooling ring induced strains, and external vibration are potential sources that contribute to the wafer distortion. Figure 3.2.8-H shows two designs that have been investigated; side rail stiffeners and top rail stiffeners.

Figure 3.2.8-H Ladder stiffening options.

The ladder assembly stiffness will be increased by the addition of thin G/E side rails, which will be edge bonded to the wafers. The G/E rails may be as high as 4 mm with a thickness of .4 mm, and bonded the full length of the ladder except at the cooling ring attachment. Wafer deflection and natural frequency vs. length are shown in Figure 3.2.8-I for various ladder parameters. The first curve shows the deflection of a single 300 µm thick detector simply

supported at the edges. Our baseline design calls for two 300 μm thick detectors bonded back to back. Curve 2 shows a factor of 4 decrease in deflection due to the increased bending stiffness. The further decrease in deflection due to the addition of the rails is shown in curves 3 and 4. It should be noted that the two layer wafer configuration deflects more than the single wafer since the additional weight is distributed in such a manner that it does not greatly contribute to the lateral stiffness. The rails will be constructed of G/E matrix with a closely matching CTE to that of silicon, and will be structurally symmetrical about the neutral bending axis to minimize unbalanced thermal distortion of the wafer. Side rail interference with adjacent wafers may occur in packaging the wafer and electronics on the cooling ring at small Lorentz angles, particularly in regions of the wire bonding. This may necessitate the use of lower height rails or placing the rails on top of the ladders as shown above. Figure 3.2.8-J shows the effect of rail height on the wafer deflection for rail heights up to 4 mm, for a simply supported 16 cm long assembly. At rail heights of less than 1.5 mm, the increase in bending stiffness is not substantial.

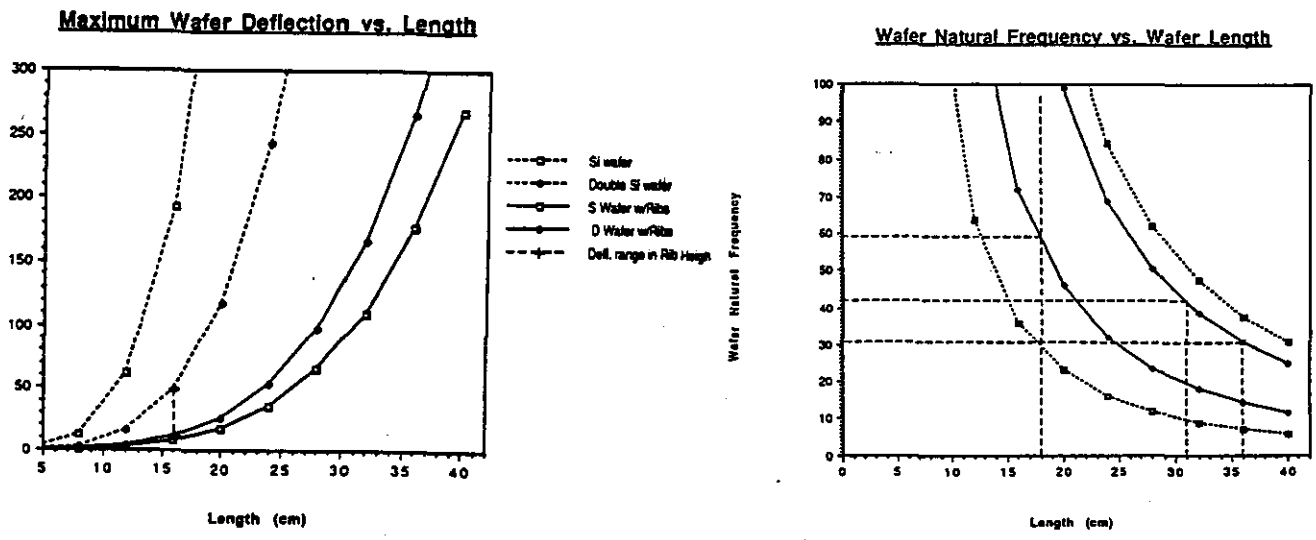

Figure 3.2.8-I Deflection & Natural Frequency

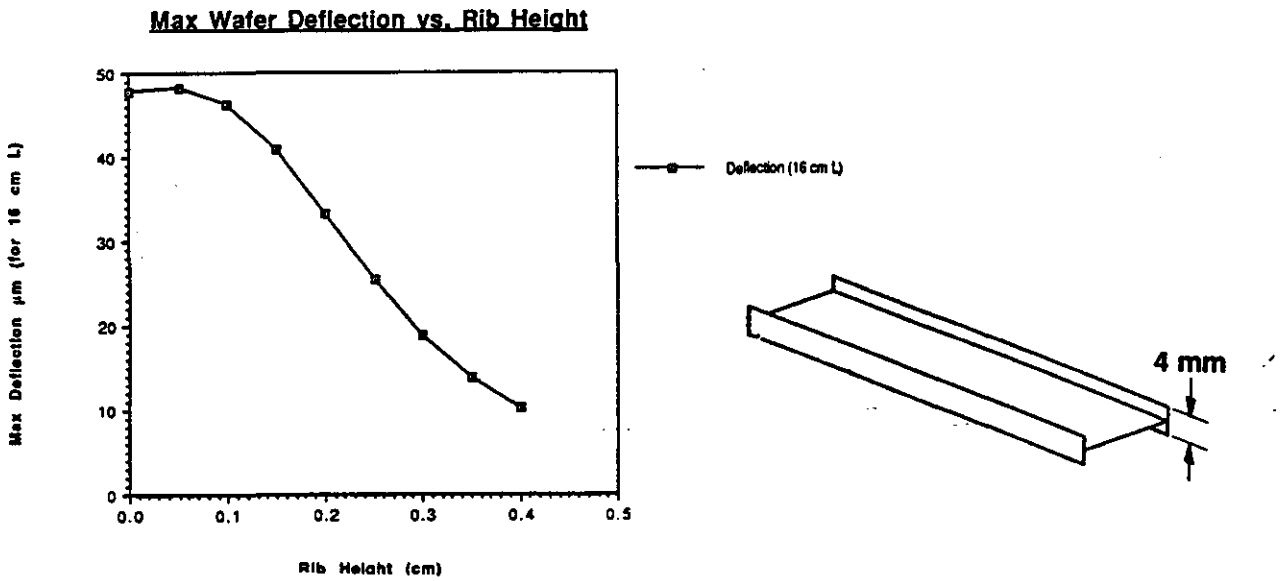

Figure 3.2.8-J Deflection vs. Rib Height

Using the top rail configuration allows us the detectors to be overlapped at lower Lorentz angles. Since they overlap only at the edges, this leaves the entire center open for structural stiffening. Figure 3.2.8-K shows how the stiffener would be placed on an 18 cm long ladder.

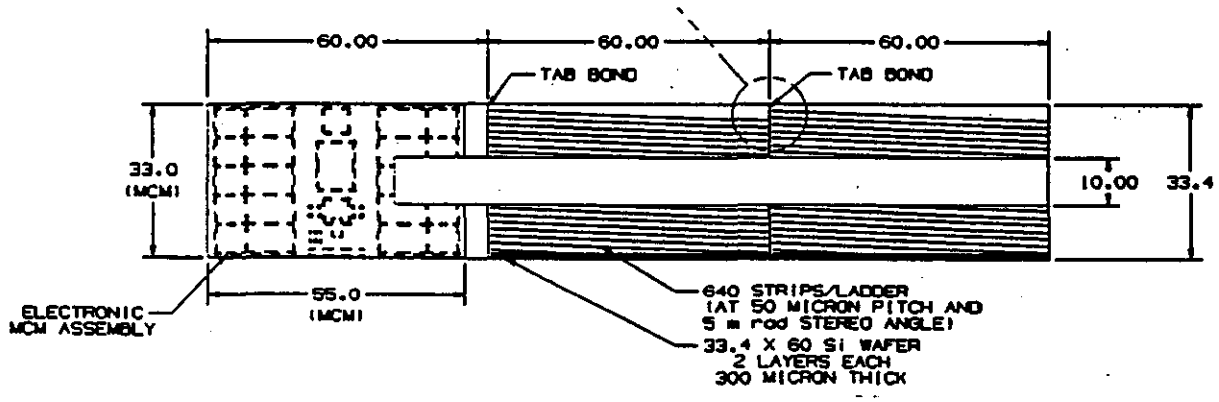

Figure 3.2.8-K Top Rail Stiffener.

Several parameters of the top rail design effect the ladder stiffness and have been individually investigated as well as in combination. The parameters identified and analyzed so far include:

Parameter	Range
Stiffener spacing (foam)	.15 cm - .5 cm
Stiffener thickness	100 μm - 400 μm
Stiffener width	.5 cm - 2 cm
Stiffener modulus	8 E6 psi - 30 E6 psi

The design goal is to raise the ladder natural frequency well above 60 Hz with plenty of design margin. Radiation length, assembly and packaging are system level design issues that also must be taken into account. Figure 3.2.8-L shows the structural frequency versus ladder length for various modulii. The geometry of the top rail has been optimized as follows; thickness - 100 μm to minimize the radiation length, width 1 cm for ease of assembly, spacer thickness - .5 cm for ease of assembly over the MCM and structural efficiency.

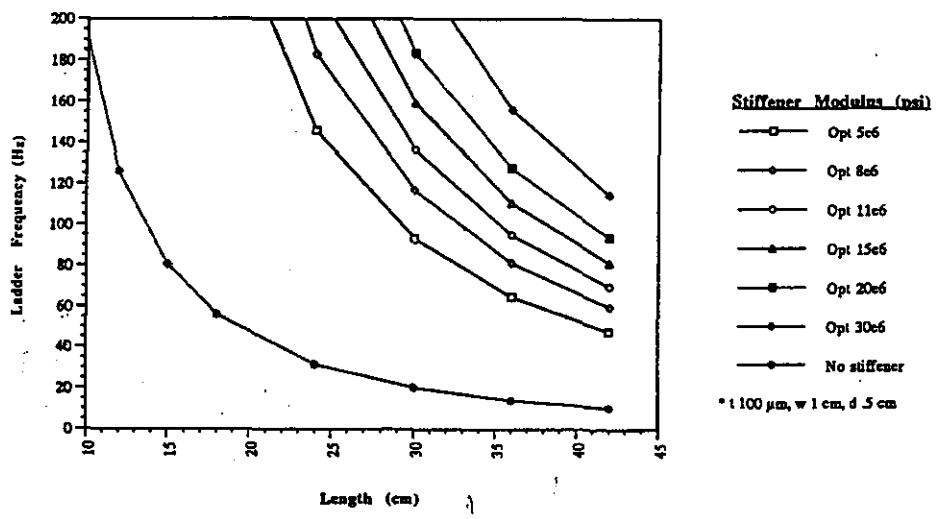

Figure 3.2.8-L Ladder frequency vs. Length and Modulii.

The plot indicates that frequency with these parameters can easily be pushed over 60 Hz for ladder lengths up to 36 cm long. This gives us the option to eliminate the middle structural support rings and graphite/epoxy support cylinders to simplify the design. Additional design and analysis must be done before this design is fully embraced. The foam spacer will inhibit free convection cooling of the ladders due to leakage current. This will only become a problem later

in life after several years of irradiation. Central region layouts with the new cooling ring design and ladder overlap will have to be completed to verify the .5 cm thickness can accommodated during assembly.

At this point we have not developed a final ladder design to fully meet the thermal and structural specifications. Continuing design studies and detailed thermal and structural analysis are in progress to develop an optimum design. Prototype design, assembly, and testing will be conducted throughout the R&D phase to more closely evaluate the options.

A nominal wafer size of 33.4 mm x 60 mm was chosen to maximize the use of a 10 cm diameter silicon wafer. Two such wafers will be produced from one 10 cm diameter disk. The baseline design at this time is two layers of single sided A/C coupled totally depleted silicon microstrip detector with the following specifications:

Active Dimensions:	58.8 mm x 32 mm
Thickness:	300 μm ± 15 μm
Flatness:	8 μ
# of Strips:	640
Strip Pitch:	50 μm
# of Readouts:	640
Readout Pitch:	50 μm
Substrate:	n type, high resistivity silicon, 4-8 KΩ
C(interstrip):	> 5 x C(backplane) < 1.5 pf/cm
C(coupling):	> 10 x C(interstrip)
Depletion Voltage:	60 Volts max. prior to irradiation
	140 Volts max. after 5 MRads of irradiation
Break Down Voltage:	150 Volts min. prior to irradiation
	180 Volts min. after 5 MRads of irradiation
Leakage/Strip:	10 nA max. prior to irradiation
	90 % strips ≤ 2 nA prior to irradiation
Leakage/Wafer:	3.5 μA max. prior to irradiation (assume 90% @ 2 nA + 7% @ 10 nA + 3% @ 100 nA)
Metalization:	Aluminum
Polycrystalline Si Res:	< 500 KΩ (max 5% change after 5 MRad irradiation)
Radiation Hardness:	5×10^{13} neutrons/cm^2 ; 5 Mrad
Strip faults/Wafer:	Maximum of 3% of the strips (19 strips) due to a combination of Capacitive coupling faults or P-N Junction faults. No more than 3 faulty strips in 10 adjacent strips.

Each wafer will contain 640 strips at a 50 μm pitch tilted at a 5 milliradian stereo angle.

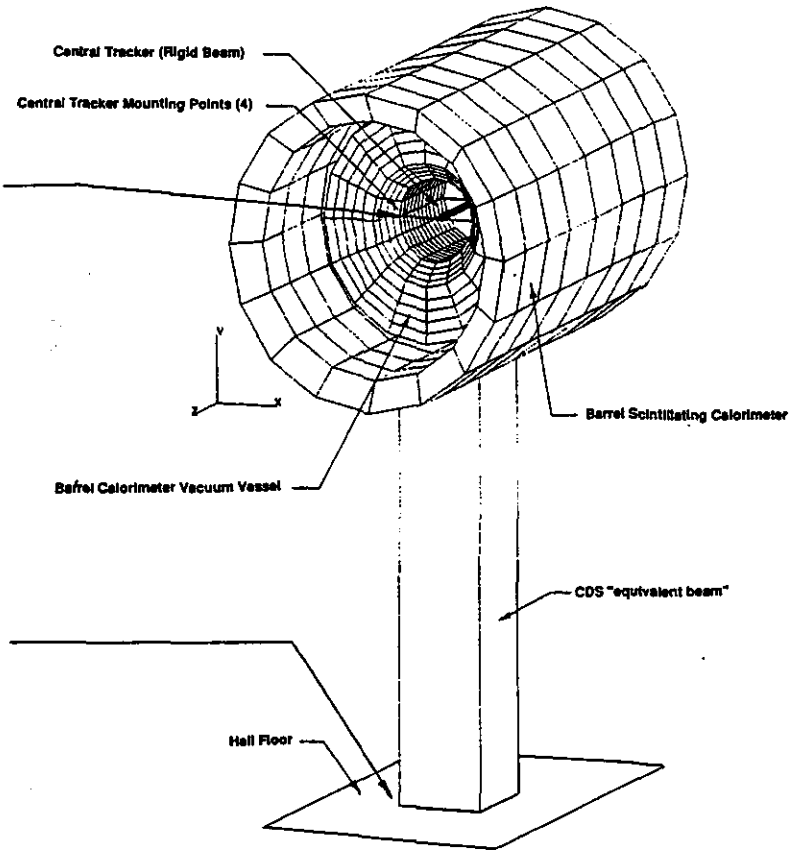

Figure 3.2.9-B Finite Element Model

The scintillating calorimeter was modeled as a rigid body between the two full-length stainless steel cylinders of the central detector housing. The two end cap calorimeters were modeled as lumped masses (with rotary inertia), each supported on four stanchions attached to the inner cylinder of the scintillating calorimeter. The barrel calorimeter was modeled as a rigid body, supported on four stanchions attached to the barrel calorimeter's vacuum vessel. The vacuum vessel was rigidly attached to the inner cylinder of the scintillating calorimeter and contacted the barrel calorimeter at 16 points (along 2 concentric circles) on each of the vacuum vessel's flat sides. The tracker was suspended inside of the inner cylinder of the barrel calorimeter's vacuum vessel at four attachment points. The outer detector housing was connected to ground through a beam. This beam had properties capable of representing the primary modes of the central detector support, which in turn were estimated by other FEM models of this structure. The stanchions were modeled as beams, having axial and bending stiffness properties calculated from the actual multiple-plate design. The orientation of the stanchions was handled carefully (the stanchions have a much greater stiffness in one transverse direction than in the other direction, and the orientation of the strong and weak axes is not parallel to the global coordinate system of the model).

The tracker itself was modeled with beam elements, and was not intended to simulate the elastic behavior of the tracker, but only to represent its mass distribution. The tracker was connected to the inner vacuum vessel cylinder at four points, as shown in Figure 3.2.9-C.

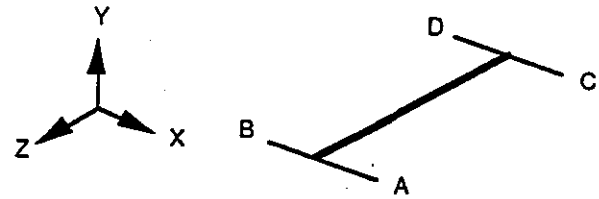

position A	y, z
position B	x, y, z
position C	y
position D	x, y

Figure 3.2.9-C Central Tracker rigid beam model

The tracker mass was taken as 607.8 kg (1340 lbm). An additional mass of 907.2 kg (2000 lbm) was added to the central portion of the barrel calorimeter vacuum vessel's inner cylinder to simulate the 5 cm-thick polyethylene liner.

The excitation used in this analysis was a random base motion excitation and was applied in each of the three coordinate directions (i.e., parallel to the x, y, and z axes) independently. The power spectral density envelope that was used is shown in Figure 3.2.9-D. The envelope has a constant acceleration PSD magnitude of 1.0e-08 g^2 / Hz from 0.1 - 100.0 Hz, thereafter decaying at a rate of 6 dB per octave. The constant acceleration portion of the PSD is equivalent to a displacement PSD that decreases at a rate proportional to 1/f^4. The rms value (0.1 - 1000.0 Hz) of the displacement PSD was 0.000453 m, and of the corresponding acceleration PSD 0.00138 g. The plot also includes displacement PSD's from the Los Alamos Ground Test Accelerator (GTA) facility and a PSD of non-cultural subterranean ground vibration taken from [1].

The response of one end (the end with the positive z coordinate) of the tracker was computed based on the modal properties of the lowest 12 modes and the base motion PSD described above. A damping ratio of 2% was used for all modes. The response calculated was the relative displacement, i.e., the displacement of the end of the tracker relative to the base (floor). The rotation of the tracker was also calculated. The rotations may be understood as absolute rotations since the base was not assumed to rotate.

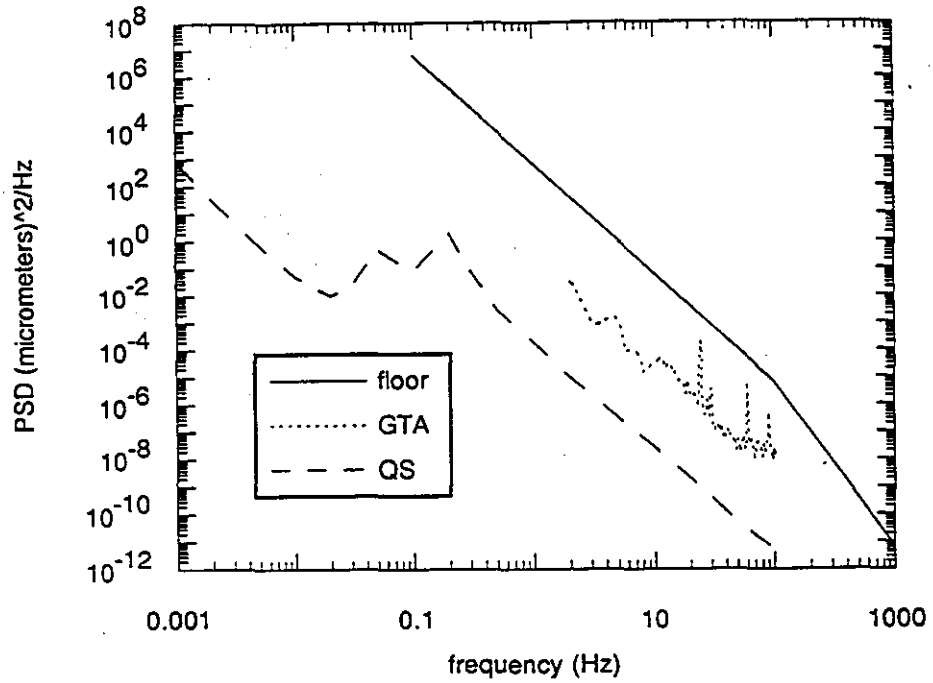

Figure 3.2.9-D Base excitation PSD envelope

The table below lists the rms values of the relative displacement in each direction (x, y, and z) and the rotations about each axis, for each of the 3 excitation directions.

Excitation direction	Output direction					
	x	y	z	rx	ry	rz
x	12.95	~0	~0	~0	.041	~0
y	.521	1.68	.015	~0	~0	~0
z	.022	17.4	145	17.42	.023	~0

A strong coupling between z-direction excitation and y-direction response was observed. Mode #1 gives the strongest example of the reason: the central detector support rotates about the x-axis as it sways in the z-direction. This x-axis rotation causes the y-direction motion of the ends of the tracker. The rms displacement in the y direction and the rms rotation in the rx direction caused by z-direction base motion were nearly identical. The y-direction response of the end of the tracker was dominated by the tracker's rotation about the x axis (the y-direction response to y-direction base input was comparatively small). Since the length of the tracker was exactly 2 meters, the y-direction displacement at the end of the tracker (in meters) was numerically equal to its x-axis rotation (in radians).

As this was a linear analysis, the PSD response for a different input PSD of identical shape (i.e., a PSD differing only in magnitude from the one used) is directly proportional to the

PSD responses calculated here. The rms values of response would scale as the square root of the proportionality factor (i.e., the rms value of a given response would be 0.7071 times the corresponding value from the table for a base motion PSD of 1/2 the magnitude of the PSD used in this analysis).

Since the design of the central support structure and calorimeter are still at a conceptual stage, a sensitivity study was conducted over the expected design range. The stiffness of the central detector support was varied to change the frequency ± a factor of 2 and the calorimeter stanchions reduced 1/5th. The plot below (Figure 2.3.9-E) shows how the RMS displacement of the Central tracker assembly would increase if frequencies were reduced.

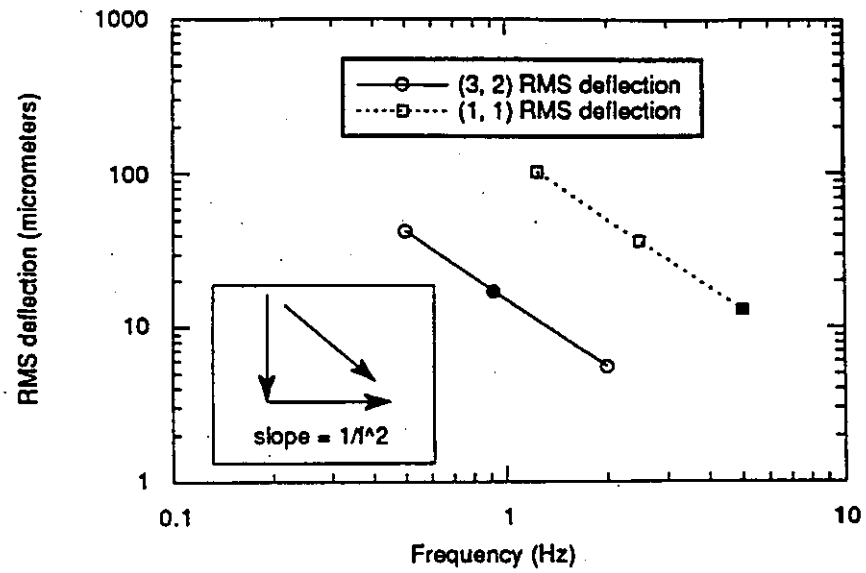

Figure 3.2.9-E Tracker response to 2 mode frequency changes

Plot (3,2) shows how the y displacement can increase up to 50 μm as the central detector support frequency drops to .5 Hz. Plot (1,1) shows how the x displacement can increase up to 100 μm as the stanchion frequency drops to near 1 Hz. These are two identified modes that could possibly cause large displacements of the central tracker if they are ignored. We will continue to develop structural models as the design evolves and provide input to the structural design to maximize the trackers' stability.

3.3 The Silicon Tracker Electronics

3.3.1 Introduction

This section concentrates on the design of the electronics associated with the silicon strip detectors. The scheduling and R&D efforts associated with the silicon tracker electronics are discussed in the Central Tracker section of this report. There are nearly 2.5 million individual

PIN diode strips in the system, each channel requiring an individual amplifier plus readout chain. The channels are grouped into sub-units called 'ladders', such that a whole ladder corresponds to a physically separate mechanical unit. Electrically, each ladder is divided into two 'half-ladders', each of which can be identified with its own readout system. The readout system for a half-ladder resides physically on a Multi-Chip Module (MCM) which is bonded to the SSD sensor of the half-ladder and which provides the readout for 1280 PIN diode strips. With 1946 MCM's in total, the channel count in this system is very high, so that a careful design is needed in order to

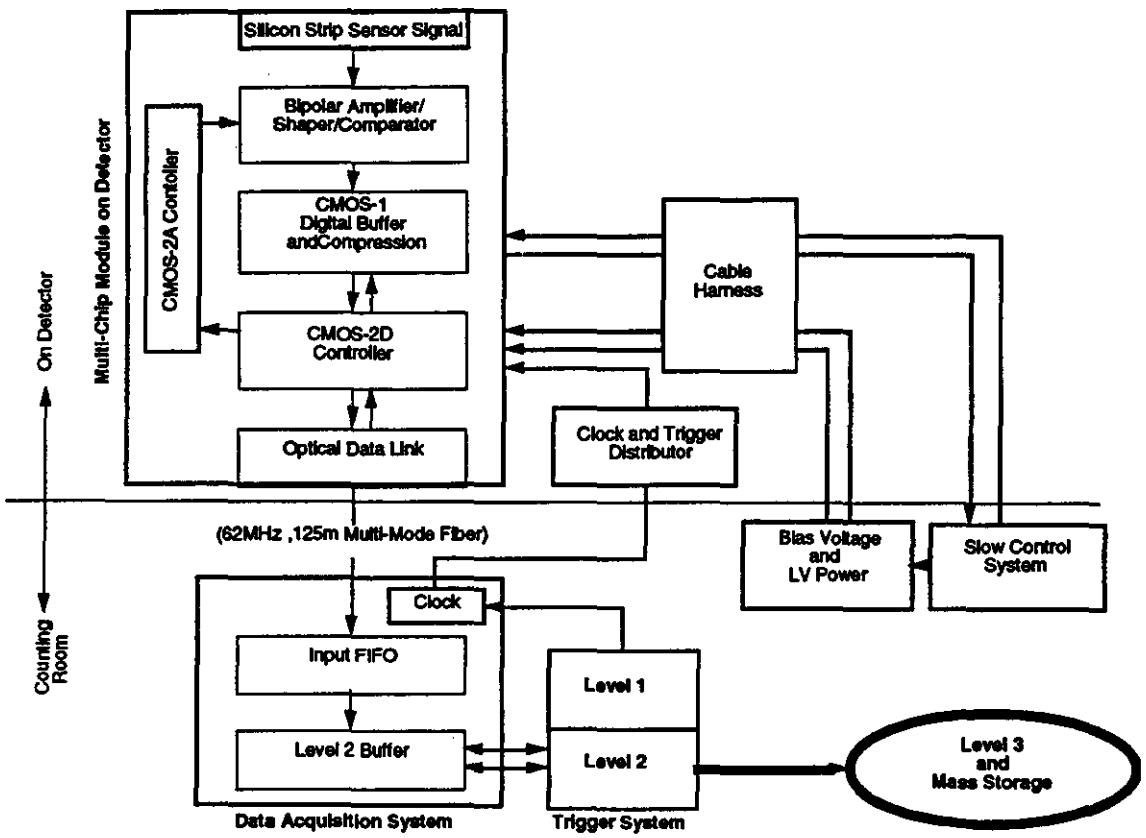

Figure 3.3-1 Silicon Tracker Electronics ArchitectureFunctional - schematic of the silicon tracker electronics system.

Input Signal

The input amplifier current pulse produced by a charged particle traversing the silicon strip detector is highly dependent upon the structure of the silicon strip detector and will be considered later. The response of silicon detectors to minimum ionizing tracks has been

Table 3.3-3. Input Signal Characteristics (one strip)

Input Signal (normal incidence)	4fC (24,000e)
Charge Collection Time	25ns
Strip-to-Strip Coupling Capacitance per unit length of strip	1.0pF/cm
Lorentz Drift Angle (holes)	1.5 degrees
Post Radiation Leakage Current (0 _C)	~1.0mA
Rate from Charged Tracks($10^{33}cm^{-2}s$)	20-60kHz

Amplifier and Comparator (BIPOLAR)

The choice of a radiation hardened bipolar design is based upon the superior noise and power performance. Bipolar amplifiers out-perform CMOS amplifiers in noise-power product for capacitances in the range of above 6pF and for amplifier rise times of 20-30ns. Equivalent noise levels in the range of 1500e can be achieved for lumped input capacitance of 15pF. The actual noise figures as determined by simulation will be discussed in a later section.

The effect of the comparator threshold on track finding efficiency has been studied. The study included the effects of comparator latency, full event simulation via the GEANT code system, and track finding efficiencies. The study revealed that, for an single amplifier, the threshold should be set 3.0s RMS above the pedestal value for good track finding efficiencies. Channel -to-channel fluctuations in the gain and pedestal values, and other system noise sources will require a somewhat higher setting of 3.5s RMS noise above pedestal in order that the noise hit rate, and hence channel inefficiency, be comparable to the intrinsic inefficiency due to charged particle rate in the SSC environment. An amplifier noise level of 2200e would imply a 7700e threshold setting that is still reasonably efficient for the expected distribution of signal sizes.

The Digital Data Processing Architecture

The proposed digital architecture consists of an event-driven latch, data storage and compressor. The data latch accepts a non-synchronized (relative to the system clock) analog pulse of random duration and generates a single, synchronized 16-ns digital pulse. Information is then stored for the duration of the LEVEL-1 trigger extraction cycle (2-4 microseconds) using a

data driven architecture. Triggered data is then passed on for data compression using either the clustering or 8/16 algorithm and transmitted out through a fiber optic link. The SSC inner-detector strip occupancy is sparse and the trigger attenuation is high, allowing for both time and data compression. Based on this expected sparse strip occupancy (0.1% to 1.0%), a maximum trigger rate of 100 KHz and a compression efficiency of 25X - 5X, the architecture will require a mean data bandwidth of 5-30 MBits/sec/1280 strips.

3.3.2 Electronics Design

As discussed earlier, the GEM silicon-tracker electronics architecture is an optimized system-level design composed of the following subsystems: (i) Analog amplifier, waveshaper and discriminator. (ii) Digital storage, compression and control. (iii) Optical readout and clock and trigger distribution (iv) Multi-chip-carrier (MCM).. The system design balances and distributes design complexities and costs evenly amongst the above subsystems. The issues and requirements considered in our design optimization, in addition to specifications and cost, include ease of realization, assembly complexity and testability. A design description of (i) - (iv) follows:

<u>The Bipolar Analog Chip Design</u>

Design Considerations:

Baseline design requirements such as radiation-hardness levels, noise performance, discriminator time-walk as well as power consumption are well established by various studies including SDC's . The circuit designs and fabrication alternatives, however, has yet to be optimized. Additional design considerations unique to the Silicon Tracker environments need to be addressed further to achieve the optimal design. Some of the design issues concerning analog bipolar ASIC design are:

- Thermal environment, where the temporal fluctuation may be quite small, but the thermal gradient over the entire tracker volume may not be.
- The rate of radiation damage as a function of relative location of the electronics, and, consequently, uneven gain changes of the transistors throughout the Silicon Tracker volume, causing non-uniform bias point shifts .
- Testability and controllability of each channel, while considering the enormous number of channels to scan.
- Protection of each input line from most transient surges or spikes.
- Fluctuation of the bias points of the circuits due to process variation.

- Cost of production which is a strong function of die yield.

A thorough description of the design of this circuit has been made elsewhere[1].

Design Baselines and Goals:

The input current of the preamplifier is positive (hole-current) since GEM Silicon Tracker is using single-sided detectors only. It is important to minimize the input capacitance of the strip detectors for good noise performance. Signal charge is AC coupled to the preamp input, thus no separate HV blocking capacitance is necessary. The amplifier input, still, require some protection from any accidental presence of large voltage spikes.

The most fundamental design goals are shown in Table 3.3-4. These goals are to be balanced in final design to achieve the optimum performance.

Table 3.3-4: Performance Goals for the Silicon Electronics Analog Chip

Power Consumption:	1mW/Channel (+/-1.5V, 3.3V supplies)
Equivalent Noise	1200e B-O-L
(for 15pF lumped input capacitance)	1500e E-O-L
Double Pulse Resolution:	100ns
Time Walk (1fC to 8fC):	less than 16ns

Prototype Circuit Design:

Figure 3.3-2 shows the prototype circuit which includes the preamplifier, amplifier, shaper with a baseline restorer and a level discriminator. The preamplifier is a traditional cascode arrangement with emitter follower buffer. A charge conversion capacitor of 0.2pF is used in parallel with 120 KW for 24ns charge integration time, which is dictated by the charge waveform from the strip detector. A larger feedback resistor with smaller conversion capacitance will increase the conversion gain and lower the input equivalent noise. It is, however, at the expense of larger fluctuation of the DC bias point at the preamplifier output since the feedback resistor provides the base current of the input transistor. Any change in transistor gain from process

[1]S. Hahn et al, IEEE 1992 Symposium on Instrumentation in Nuclear Physics , Bipolar Amplifier and Comparator Circuit for the SSC, to be published

variation, radiation damage or temperature drift will result in larger DC bias shift with increased feedback resistor. The input circuit node has a protection diode with a 50-ohm current limiting resistor and calibration injection capacitor. The noise contribution of the current limiting resistance is insignificant compared to other noise sources.

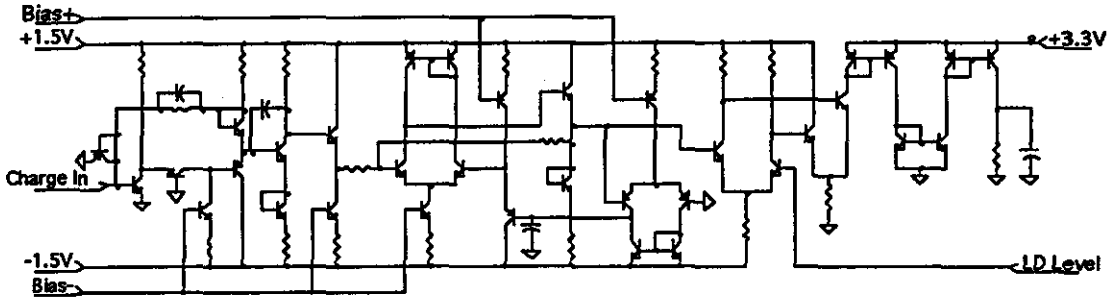

Figure 3.3-2 Silicon Tracker Amplifier and Comparator Design

Preamp/Shaper/Discriminator Schematic Used for SPICE Simulation

The preamp output is fed to an emitter degeneration amplifier with a gain of approximately 3.5, which was determined from the bias drift consideration of the direct-coupled stages. Gains larger than 3.5 result in approximately too much DC shift for the base-line restorer when the transistor gain drops by one half.

The third stage amplifier not only amplifies and shapes the signal, but also maintains the output quiescent point near zero through a base-line restorer amplifier which feeds back an error signal through a low-pass filter. The pole of the low-pass filter should be at a sufficiently low frequency not to significantly attenuate the signal. The closed loop gain, including the gain of the main differential amplifier, of the baseline restorer should also be kept within the gain margin for stable operation.

The DC restored signal output is discriminated against the reference voltage at the differential inputs of the comparator. The comparator has two differential gain stages followed by three current-gain stages using current-mirrors. The current output is converted to voltage signals through a load resistor.

Simulation Results:

Amplifier Operation

Component model libraries from Harris (UHF-series) and AT&T (CBIC-U, U2, V series) were used to simulate the circuit operation. Both companies are in the forefront of bipolar fabrication technology and produces multi-GHz complementary transistors for custom and semi-custom ASICs. Of the two vendors, AT&T transistors with higher DC gains and cut-off frequencies have somewhat better performance over Harris'. Due to the high frequency operation

of the transistors and passive components, these models incorporate distributed parasitic elements as well. A typical waveform at the input of the comparator is shown in Figure 3.3-3 for various input charge amounts, where the shape of the input charge pulse is typical for a silicon strip detector.

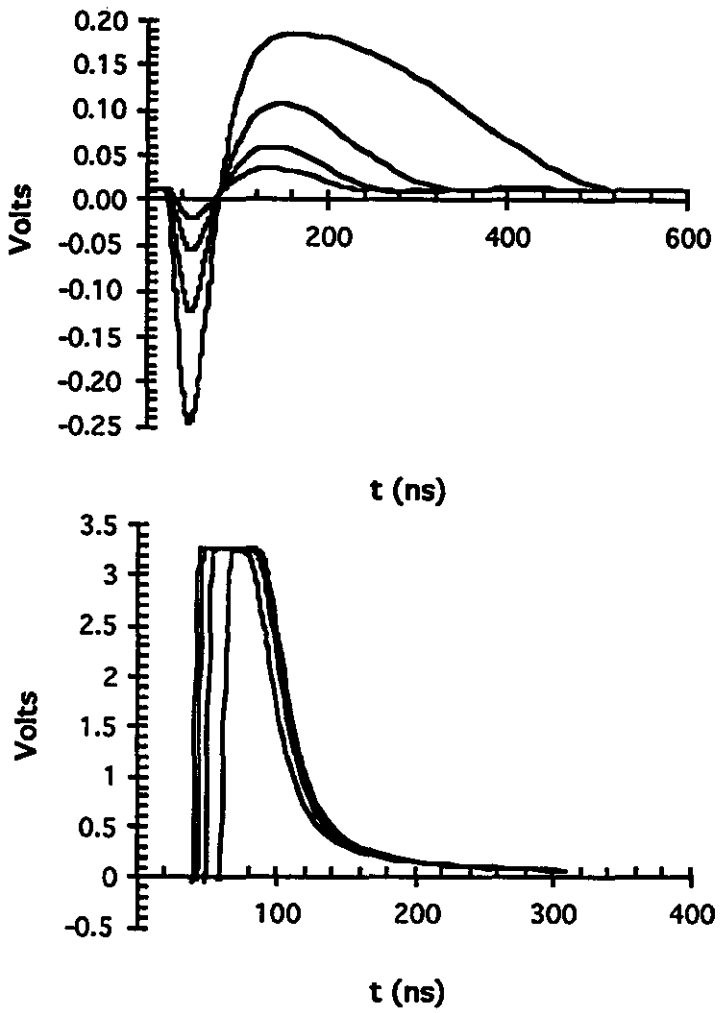

Figure 3.3-3 Silicon Tracker Amplifier Response

Shaper and Comparator Output Waveforms for 1, 2, 4, 8 fC Input Charges. Note the delayed time of the smaller comparator output pulses due to time walk. The double pulse resolution is determined by the comparator reset time which is of order 150ns.

The shaper output as shown in Figure 3.3-3 has a stable DC bias level which is within a few millivolts of the ground potential. It has a bipolar swing due to the differentiating effect of the baseline restorer, which essentially cancels the low frequency component of the signals at the

shaper input. Typical waveforms at the level discriminator output node show the time-walk due to varying input signal amplitudes.

The GEM design with 18 cm strip detectors challenge detector and electronics design and performance. Charge sharing among neighboring channels due to inter-strip capacitances and time dispersion of the propagated signal must be minimized. For a given preamplifier charge collection time the charge collected per pulse and the resulting signal-to-noise ratio is limited by the total strip capacitance and resistance. In addition, adjacent amplifiers with non-ideal strip-line termination interfere reactively and can cause oscillatory operation of the amplifiers.

To overcome these undesirable effects, it is imperative to use detectors with the lowest inter-strip capacitance and metalization resistance. When the equivalent strip resistance is reduced from 50 ohms/cm to 20 ohms/cm, the equivalence noise for a far-end charge injection decreases by up to 10%. Lowering inter-strip capacitance from 1.2 pF/cm to 0.8 pF/cm also lowers the noise by 15%.

The following simulation results, listed in Table 3.3-5, were obtained with AT&T CBIC-V series transistor libraries. The 18cm detector length is simulated with a range of distributed capacitance and resistance values, while the charges were injected at either far or near end. To better simulate the strip detector operation, five strips were arranged in parallel with the middle three channels connected to the amplifiers and the outer two channels terminated with a 100 ohm//100pF combination. In each of the simulations, the detector charge waveform with Landau effect was used. Thus, the equivalent noise charge is quite a realistic estimate of the detector plus electronics performance.

Table 3.3-5: ENC as a Function of Linear Strip Resistance and Capacitance

Equivalent Noise for Far(Near) End Charge Injection for 18cm strips			
Noise vs Capacitance		Noise vs Resistance	
(20 W/cm)		(1.0 pF/cm)	
0.6 pF/cm	1948(1916)	10 W/cm	2191(2180)
0.8 pF/cm	2122(2092)	20 W/cm	2276(2233)
1.0 pF/cm	2276(2233)	30 W/cm	2356(2272)
1.2 pF/cm	2432(2371)	40 W/cm	2431(2303)
1.4 pF/cm	2664(2579)	50 W/cm	2501(2327)

When the Level Discriminator is set at 6,000e, a time walk of 29ns results by comparing the arrival times for the discriminated signal from 8,000e and 48,000e input pulses. This represents the extreme case of maximum time walk and we expect that a large majority of the signals will fall within the 16ns time window of the digital section of the electronics.

These simulation results however do not include the worst case operation of the front-end electronics, which is expected at the end of the lifetime, when the transistor gains are expected to drop to less than half of the beginning of life values. Nor does it measure any degradation in noise from increased detector leakage currents, which is expected to be near 1uA per strip. Other effects such as interference noise from the logic circuits located on the same multi-chip modules, and worst-case analysis due to manufacturing process variations are still to be performed.

Digital Architecture

The digital data processing architecture, shown in Figure 3.3-4, comprises the unit digital circuit per MCM. The digital architecture processes the analog hits from the "top" 640 channels and "bottom" 640 channels for a total of 1280 channels. The digital architecture is composed of 10x128 channel CMOS-1 chips, 1xCMOS-2D, 1xTDM and 2xLED. The CMOS-1 latches, buffers and compresses the incoming hits from the analog comparator. CMOS-2D interrogates the ten CMOS-1 chips, encodes the data and drives the Time-Division-Multiplexer (TDM). In addition, CMOS-2D operates the slow control and test system. The TDM time-division-multiplexes the 31 MBits/sec "top" and 31 MBits/sec "bottom" into a single 62 MBit/sec channel and provides the necessary drive current levels to the LED. The TDM chip can also be run in a mode which will provide a 2x31MBits/sec "top" plus 2x31MBits/sec "bottom" for a 124MBits/sec data bandwidth. Note that two independent optical channels provide additional reliability and bandwidth. A description of the digital architecture follows.

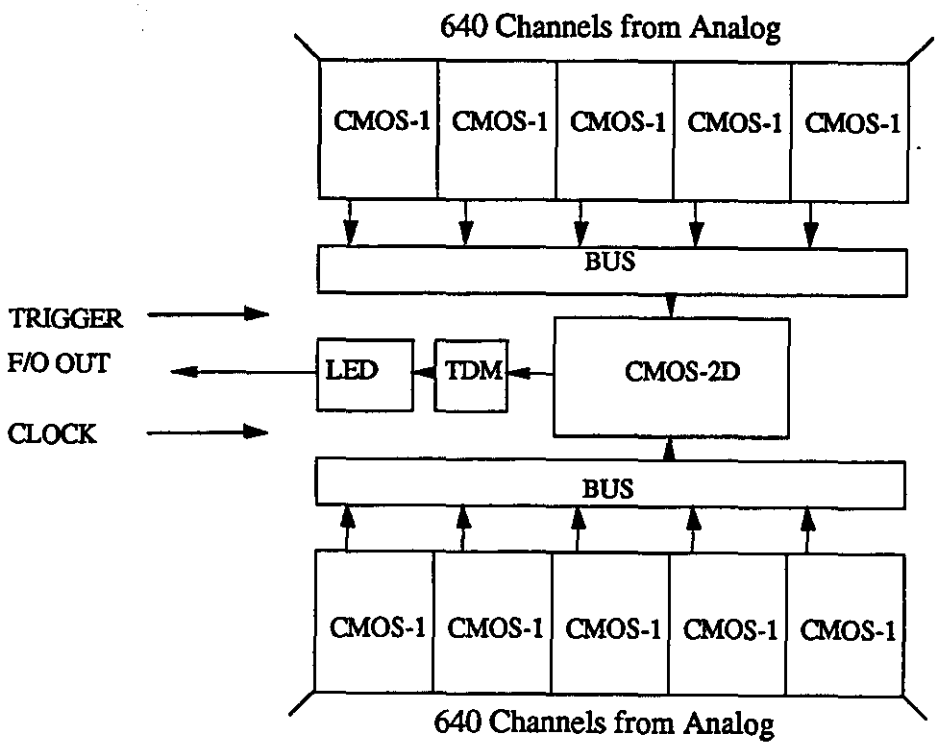

3.3-4 Digital Architecture Design

The processing architecture of the digital data storage (DDS) on the CMOS-1 chip for the Silicon Tracker.

Data Latch:

When a strip detector is hit by a particle, the resulting charge generated is collected, amplified and wave-shaped by the analog amplifier. Variations in the time and amplitude envelope of the charge waveform due to particle type, trajectory and position can produce a time jitter (time walk) at the output of the amplifier. Hence, the total time delay involved in a particle traversing a strip to when the analog stage produces a digital output is represented by a fixed delay plus a random component (time jitter). In addition, the same time and amplitude variations in the charge envelope produces a strong return-to-zero time-jitter (several beam crossings) at the

output of the analog stage. Therefore, the requirements expected of the latch are the generation of a single, synchronous (relative to the system clock), pulse independent of the rise and fall time jitter of the analog stage. The latch can be programmed to trigger on rising or falling analog edge. Note that by only triggering on edges, shorted amplifier and strip detector channels do not influence the data stream.

Data Storage (Concurrent Pointer Tracking):

The storage algorithm makes use of the sparse nature of the data. The expected SSC inner-detector strip occupancy is very low, allowing for the implementation of data driven storage[2,3,4]. In data driven storage, only the hit channels initiate the data processing. In addition, since the relative processing activity in a good data driven storage architecture is directly proportional to the strip-detector channel occupancy, a significant reduction in data processing volume is expected. A reduction in the data processing volume leads to lower power dissipation and eases some of the problems involved in high speed integrated circuit (IC) chip design. Indeed, in the architecture presented major portions of the chip circuitry are dormant because only hit strips are processing and power is dissipated only during data shifts and pointer increments (discussed below).

A brief description of the algorithm follows. Referring to Figure 3.3-5, when an analog rising or falling edge is detected and latched, the current count of COUNTER is copied into the register pointed to by WRITE (REG6 in this case). WRITE is then incremented to the next register (REG7) for the next latched edge. Simultaneously, the count of COUNTER and the contents of the register pointed to by READ (REG3 in Figure 3.3-5) are continuously compared (note that the contents of REG3 and the counter always lag by 2n, where n is the number of counter bits and 2n X 16 ns is the trigger delay). When the contents are equal and a trigger is present, OUT=1 and READ is incremented to the next register (REG4). If the contents are equal and no trigger is present, OUT=0 and READ is still incremented to the next register.

---

[2]V. Cook, P. M. Mockett, "A Precision Vertex Chamber For EMPACT," Symposium on Detector R&D for the SSC, Fort Worth, Texas, Oct 15-18, pp. 136-138.
[3]O. Barkan, E. L. Atlas, W. L. Marking, S. Worley, G. Y. Yacoub, G. Kramer, J. F. Arens, J. G. Jernigan, S. L. Shapiro, D. Nygren, H. Spieler, M. Wright, "Development of a Customized SSC Pixel Detector Readout for Vertex Tracking," Symposium on Detector R&D for the SSC, Fort Worth, Texas, Oct. 15-18, 1990, pp. 142-144.
[4]R&D Report on Double-Sided Silicon Detectors and Associated Electronics, Sept. 1990, 62-78.

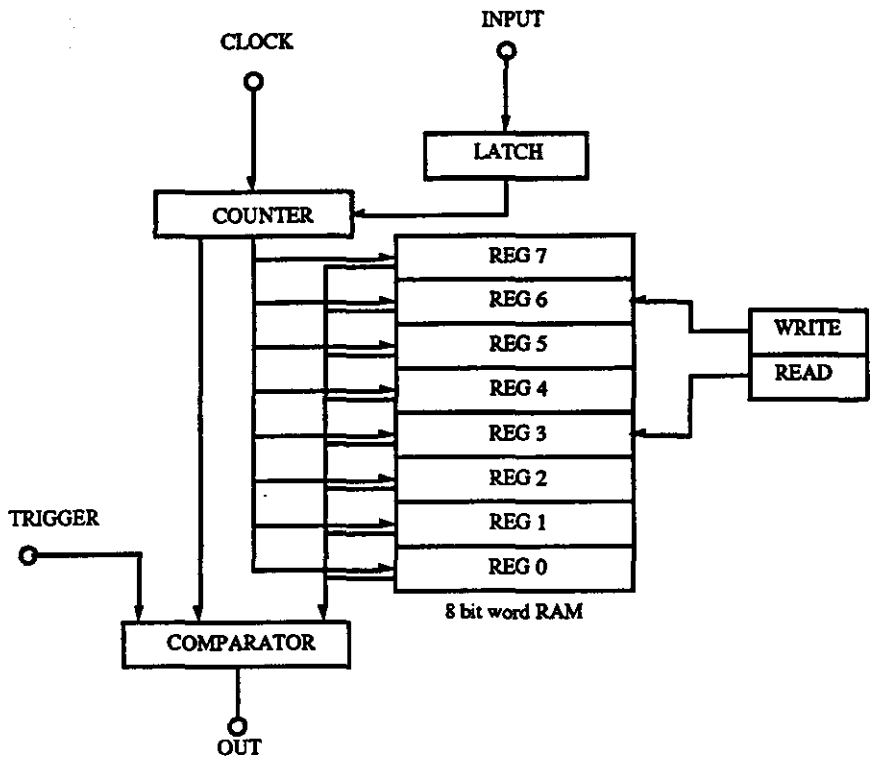

Figure 3.3-5 Silicon Tracker CMOS-1 Data Driven Memory

Data driven memory unit for one channel of the CMOS-1 chip is shown. The operation is centered around the Read and Write pointers as described in the text.

Of primary importance is the constant updating of the read pointer so that prompt readout of the appropriate tagged-hit is initiated in the event of a matching trigger. The key to the success of this data driven storage technique is that the read pointer is guaranteed to point to the address of the only possible event candidate when the corresponding trigger is processed. This requires that all read pointers are concurrently updated by the counter and trigger relative to the pointers contents, and relative to the write pointer. This technique is called concurrent pointer tracking. Note that the read pointer is always trying to "catch" up to the write pointer. It should be noted

that the read pointer value can only be equal-to or less-then the write pointer and action on a read pointer is always delayed one cycle (clock) behind the write pointer action for a given position on the ring. In addition to the above mentioned restrictions, a read pointer location is current only until the COUNTER value equals the tag pointed to by the read pointer. When this occurs, the read pointer is advanced to the next location (provided that it does not pass the write pointer). If no events have recently occurred and the write pointer has been idle, the circuit goes dormant (empty buffer) until a hit arrives. Under the empty buffer condition (READ=WRITE), incoming triggers are ignored.

Other features are:

i) Only the relative clock phasing between the system clock and any other counter (like COUNTER) is important (note that 250,000 - 500,000 counters will be distributed throughout the architecture). If a phased clock is used (in GEM this represents 256 counts X 16 ns), the trigger is always timed to arrive 256 counts later (relative to an event) independent of the contents of COUNTER. This implies that the trigger can be sent down a single fiber as a pulse and system-clock resets are not required.

ii) Each single-bit circuit (i.e. Figure 3.3-5) is a self-contained autonomous cell, that is errors tend to be confined to a single or few cells (each cell represents a single bit). The cells can also be made to be self-correcting in the event of a single-event-upset (SEU) of logic 'glitch'. This is possible due to the concurrent pointer technique combined with sparse data and the 100 KHz trigger rate (on average, COUNTER will normally cycle through all the 'garbage' and re-align READ and WRITE well before the next hit or trigger occurs).

iii)The trigger aperture can be adjusted.

iv) The cell is event driven and goes dormant and dissipates very little power when no hits are registered.

Data Compression:

The trigger latches the 128-bit data vector out of the data storage and initiates the data compression cycle. Two compression algorithms are under investigation, clustering and 8/16. The clustering algorithm is the more efficient but the 8/16 is easier to implement. It appears that a hybrid 8/16 clustering algorithm will be the most optimum solution.

Clustering: Data compression through clustering is accomplished by transmitting both cluster and single hit information. The algorithm proceeds as follows: The uncompressed data retrieved from storage is edge-detected for either single hit or cluster edges. Then, the relative position offsets of the edge boundaries are found. The resulting compressed data vector is then composed of the number of edges and the position offsets of each edge (relative to the CMOS-1 boundary

in this design). The clustering algorithm is useful only for sparse single-hit/clustered data. The GEM data set is extremely sparse even at high luminosity (see specifications above) and hence, is suitable for edge compression. The combined 5 X CMOS-1 and CMOS-2D architecture produces the following transmittable vector:

[01234][XXXXXX...][XXXXXX...][XXXXXX...][XXXXXX...][XXXXXX...]

or,

[HITS][EDGES0 ....][EDGES1 ...][EDGES2 ...][EDGES3 ...][EDGES4 ...].

where 0,1,2,3,4 represent the five 128-Bit segments of the 5 X CMOS-1 chips. The header is composed of 5 bits containing hit information (hit segments). The remaining data stream consists of segment data. If a segment contains hits, the first 6 bits sent represents the number of edges, followed by the bit steam of #edges X 8-Bits.

8/16: 8/16 data compression is accomplished by dividing the 128-Bit segments into 16, 8-Bit words. The 16 words are independently logic OR-ed. If an 8-Bit word contains a hit, that particular word is sent up. Each 128-Bit segment contains a 16 bit segment header indicating which 8-Bit word is hit. Data transmission and bus control are identical to that described above for clustering. The combined 5 X CMOS-1 and CMOS-2D architecture produces the following transmittable 8/16 vector:

[01234][XXXXXXXXXXXXXXXX...] ... [XXXXXXXXXXXXXXX...]

or,

[HITS][SEG0 ....][SEG1 ...][SEG2 ...][SEG3 ...][SEG4 ...].

where 0,1,2,3,4 represent the five 128-Bit segments of the 5 X CMOS-1 chips. The header is composed of 5 bits containing hit information (hit segments). The remaining data stream consists of segment data. If a segment contains hits, the first 16 bits sent contains segment header data, followed by the bit steam of 8-Bit words.

Cluster-8/16 Compression Efficiency: A Monte Carlo simulation for both the cluster and 8/16 compression efficiency shows that the clustering algorithm is 40-50% more efficient that the 8/16 algorithm over the occupancy ranges expected at the SSC. While clustering is more efficient in compressing data, the 8/16 appears to be easier to build, runs faster and may be more reliable then clustering. It is hoped that a hybrid scheme will be the most optimum

Data Transmission:

Fiber optic data links connect the Front-End Electronics with the external world, and consists of two separate links; one for the data readout and another for clock/trigger inputs. There are two data readout link per MCM, but each clock/trigger link serves up to 8 MCM's. The high-bandwidth items of interest to this section are the fiber-optic readout, clock distribution and trigger distribution. The optical readout is the MCM's dedicated data link that transmits hit information. The clock and trigger are brought onto the MCM through micro coax from a central optical receiver.

Optical Readout:

The discussion in this section primarily focuses on the design issues up to the detector/amp assembly (primarily in terms of optical compatibility and noise/error rates). The design calls for an 850 nm optical link which employs a rad-hard Honeywell LED. It employs the use of a large numerical aperture fiber (ID = 200 microns), a surface mount LED and a TDM driver.

A large diameter fiber allows for lower-loss insertion (more light is couple from the diffused LED source into the fiber) and cheaper fiber connections (cleave & weld, bulk connector, etc.) for both matched and unmatched fibers (from Ensign-Bickford), then do lower diameter fibers (ID < = 50-100 microns). The larger fiber size (OD = 500 microns) also provides easier handling characteristics then do smaller fibers. A great deal of the optical-link costs are found in the assembly phase (primarily in the fiber interconnects). Inexpensive bulk-head connectors can be manufactured by drilling 500 micron holes into matched Lucite blocks in the case of the larger fibers. The blocks are bolted together to form the connections (losses from fiber positional mismatch and coupling are minimized due to the large diameter of the fiber).

The Time-Division-Multiplexed (TDM) chip not only provides the multiplexing between the two CMOS-2D channels but also provides the appropriate buffering. The circuit is fairly common and an appropriate off-the-shelve part should be available. Note that driving a device with high-current requirements at 31 MHz (let alone 62 MHz) with straight CMOS circuitry without bipolar buffering is very difficult. If the incoming clock (see below) needs buffering, an additional buffer can be provided on the TDM chip.

Clock and Trigger Distribution:

The clock and trigger are carried on the same fiber by phase locking the clock. The clock is fed into a phase-locked-loop (PLL) and distributed to the MCM assemblies through micro coax. The trigger is signalled by the absence of a clock tick, i.e. when a clock pulse is deliberately left out. When the PLL generates the missing pulse (and hence detected) a trigger pulse is generated and distributed through a second set of micro coax. An important observation

is that the signal to noise ratio of the optical link remain high enough to maintain the integrity of the trigger. GaAs PLL clock distribution chips are available from both Vitesse and Tri-Quinn. The PLL/distribution chip and receiver/amplifier pair are mounted on the inside of the cooling ring and metal 50-100 ohm microcoax are used to distribute the signal. A similar packaged circuit from Honywell is available also (with their DMUX chip replaced with the PPL/distribution chip).

Multi-Chip Module (MCM) Design

The base assembly unit is composed of two 640-channel silicon strip detectors bonded together back-to-back to form an 18 cm half ladder. A single MCM will provides the interface electronics for both the top 640 and bottom 640 channels. A schematic of the MCM is illustrated in Figure 3.3-6. The role of the MCM is dual in that it provides an efficient electro-mechanical interface between the electronic and mechanical systems. The MCM is supported by the strip-detector wafer through a thermally-conductive spacer, while the strip-detector itself is mounted (glued) to the cooling ring. Note that all mechanical contacts in this design straddle the thermal symmetry axes in order to minimize position drifts due to thermal expansion and contractions. Power and the digital-slow-control-bus are connected to the space frame cabling through an edge connector, while the clock and trigger are brought in through 100-ohm micro-cables from the 1:8 phase-locked optic to coax distribution modules situated on the cooling ring. Data from the MCM is transmitted through the fiber optic link that also runs through the space frame.

The single MCM assembly represents a self-contained modular unit. The modularity is due to the integration of the digital control circuits (CMOS-2) and Input/output (slow control bus and optical driver) with the main analog and digital signal processing circuits. Advantages of modularity include improved electronic system integration, reduction in assembly labor and, of great importance, a significant increase in reliability and testability (through on-board automated testing). Because of the increased testability, the amount of time, labor and equipment required to test the system are significantly reduced.

The MCM circuit (Figure 3.3-6) consists of ten pairs of custom integrated circuits, two custom CMOS chip common to all ten pairs, a pair of LED optical transmitters, along with multiple discrete components. Each pair of custom integrated circuits handles 128 channels of the strip detectors for a total of 1280 channels, and is composed of a Bipolar analog processing chip and a CMOS-1 chip for data buffering and compression. The two controller chips, called CMOS-2A and CMOS-2D serve all ten CMOS-1 chips for control of data flow and also provides the housekeeping function of the MCM requiring both analog and digital circuits inside the chip. The MCM also includes decoupling and current limiting circuits for detector biases and the IC chips.

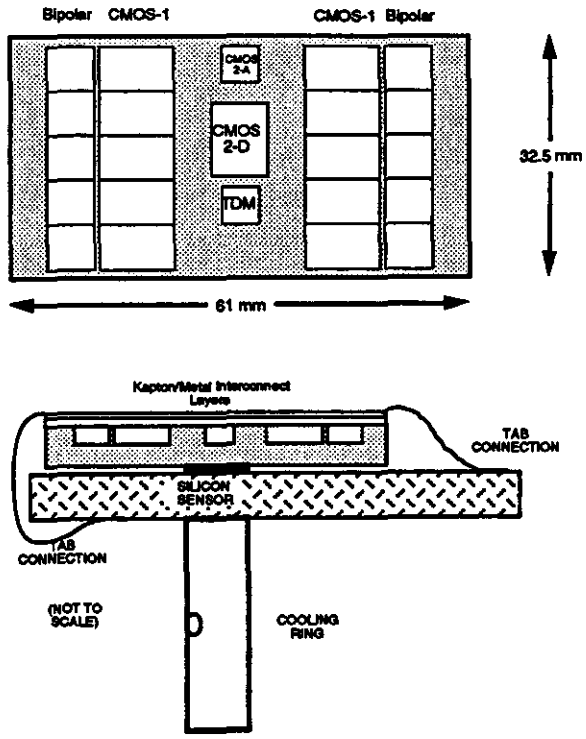

Figure 3.3-6 Silicon Tracker MCM Unit

Arrangement of VLSI Circuits on MCM and the mounting of the MCM to the ladder assembly for the Silicon Tracker.

The technology implemented utilizes the General Electric/Texas Instruments High-Density-Interconnect (HDI) process. The process imbeds the IC chips into the substrate and builds the interconnect layers above the chips. This technology maximizes heat transfer from the chip to the MCM and from the MCM to the cooling ring and minimizes spurious radiation due to digital switching and power supply coupling by maintaining quasi-TEM modes in its signal paths. A complete layout has been designed at this time.

4.1 The Interpolating Pad Chamber Outer Tracker

4.1.1. Interpolating Pad Chambers

An Interpolating Pad Chamber (IPC) is a multi-wire proportional chamber with one cathode plane consisting of a array of electrically isolated regions, or 'pads'. These pads sample the induced charge on the cathode plane due to an avalanche at the anode initiated by ionizing radiation in the chamber volume. The centroid of the induced charge distribution, determined from the pad signals, defines the ionizing particles's transit position.

Several techniques have been developed over the years for reading out segmented cathode MWPCs. These include resistive charge division, capacitive charge division, and geometrical charge division. The resistive charge division technique, which employs resistive strips running under each anode wire with periodic readout points, is not favored for large area applications, due to the difficulty in maintaining a uniform resistance. The geometrical charge division technique is the most straightforward, using a separate readout channel for each pad. Capacitive charge division is an extention of geometrical charge division in which the pads are made narrower, and one or more pads are skipped between readout pads. In this scheme, the induced charge on the intermediate pads are coupled to the nearest readout pads via the inter-pad capacitances. Its major advantage over the simple geometrical approach is a reduced capacitive load on the readout amplifier input, which results in lower electronic noise, at the expense of position linearity. Optimization studies of the cathode readout are now underway, and will be used to evaluate the tradeoffs between the geometric and capacitative readout techniques. The current GEM Outer Tracker design and the IPC prototypes constructed to date employ the geometric charge division technique. Changing to a capacitative charge division readout scheme would not affect any aspect of the IPC design other than the physical layout of the chamber cathode.

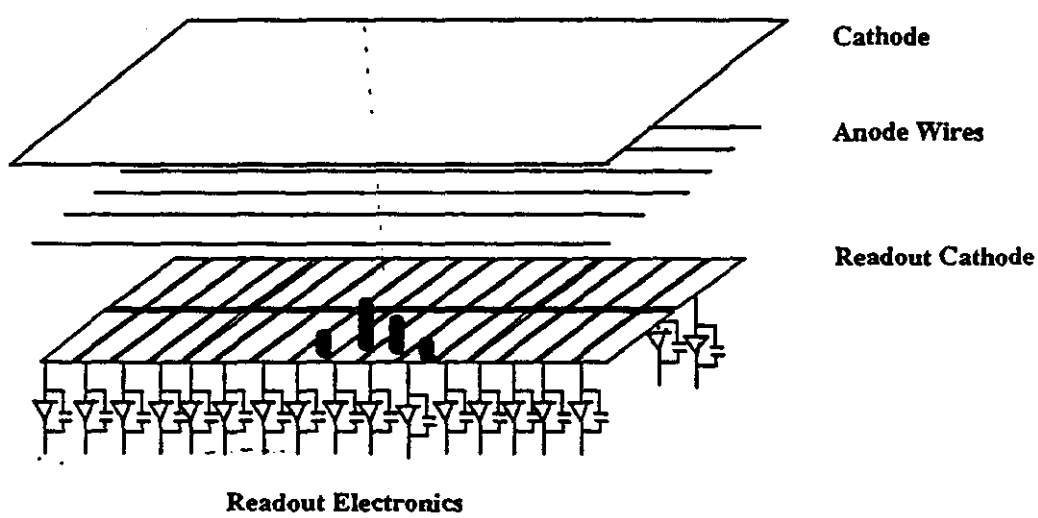

Figure 4.1-1 Geometric Charge Division

4.1.2. Geometrical Charge Division

For IPC readout by geometric charge division, the transit position of an ionizing particle

Table 4.1-1

Design Constraints	
Beam Crossing rate	62 Mhz
Charged Track Density/ Min Bias Event	dN/dhdf=1.2
# Min Bias Events / Crossing @ $10^{34}cm^{-2}s^{-1}$	16
Tracks/Sec-mm Wire @ $10^{34}cm^{-2}s^{-1}$	1×10^4 $s^{-1}mm^{-1}$
Integrated Charge/Yr-cm Wire @ $10^{34}cm^{-2}s^{-1}$	0.85 C/cm-Yr
Level 1 Trigger Rate	10 Khz
Level 1 Trigger Latency	2 ms
Design Goals	
Occupancy @ $10^{34}cm^{-2}s^{-1}$	<10%
Design Goal Position Resolution/Layer - r/f	50 mm

can be obtained from the equation

$$x = \sum Q_k x_k / \sum Q_k$$

where x_k are the position of the pads, and Q_k are the signals induced on each pad. Typically, the effective extent of the induced charge spans 3-5 pads, depending upon the chamber geometry. It is desirable from the standpoint of occupancy and channel count considerations, discussed below, to keep the number of pads associated with a given particle transit low. In practice, the number of pads used to calculate the particle position from the charge centroid is always finite, leading to a non-linearity in the relationship between the true and reconstructed position. For this reason, a fit of the pad signals to the known spatial distribution of the induced charge distribution for the chamber geometry used is generally superior to the centroid method of determining the avalanche position.

The position resolution obtained from the centroid measurment is directly related to the signal to noise ratio of the readout chain. A simple error analysis of the equation for the centroid position shows that the position resolution obtained is given by

$$\sigma_x / w = \sqrt{n}\sigma_{Q_k} / \sum Q_k$$

Where w is the pad width, and n is the number pads used in the measurment.

4.1.3. Design Parameters

The design parameters of the IPC system are set by the resolution, occupancy, and speed requirements imposed by the physics goals of the Central Tracker. In this section we discuss the optimization of these parameters under the operational constraints and design goals summarized in Table 4.1-1.

Table 4.1-2

Wire spacing	2 mm
An.-Cath. spacing	2 mm
Wire Diameter	20 microns
Voltage	3000 V
Gas	50-50 CO_2-CF_4

4.1.4. Chamber Geometry

The chamber geometry is set by the requirement of a fast electron collection time and reasonable mechanical tolerances. A large anode to cathode distance would result in an unacceptably long electron collection time, while separations less than 2 mm would result in unacceptably tight mechanical tolerances, due to the large chamber capacitance.

The chamber gain is given approximately by

$$M = ke^{(CV_0)}$$

so that a large chamber capacitance results in a more rapid increase in gain for a given voltage change, with correspondingly larger sensitivity to mechanical tolerances. It can be shown that

$$\Delta M / M = (\Delta Q / Q) \ln M$$

$$\text{and,} \Delta Q / Q = (C / 2\varepsilon_0) \Delta a / a$$

$$\Delta Q / Q = (Cl / 2\varepsilon_0 s) \Delta l / l$$

where $Q = CV_0$ is the charge per unit wire length, M is the chamber gain, a is the wire radius, l is the anode/cathode spacing, and s is the spacing between wires.

The geometry specified in Table 4.1-2, corresponding to the present IPC design, has a capacitance of 7.6 pf/m. For this geometry, a 2 mil variation in the anode/cathode spacing results in a 10% variation in the gain of the chamber.

4.1.5. Occupancy

The design goal for occupancy in the IPCs is set by the desire for robust operation at a beam luminosity of 10^{34} $cm^{-2}s^{-1}$. The IPC design parameters which affect the occupancy are

the number of pads having a significant signal associated with a single track, the pad length, and the length of time during which a subsequent hit on a pad would result in serious degradation in position resolution due to pileup.

The most conservative estimate of occupancy assumes that three pads are needed to reconstruct a position, and multiple tracks with separations less than this are not analyzable. However, studies conducted by the Tracker Group, described in detail in Section 2-7, have shown that the positions of two tracks separated by a small fraction of a pad width can be determined with minimal loss of resolution, and one can expect to do better that this worst case estimate in practice. The real two track resolution will be measured as part of the GEM Central Tracker test beam program.

A fast detector response is a critical aspect of the Central Tracker IPC system. A deadtime of 40-50 nsec (3 bunch crossings) is desirable in order to achieve the IPC occupancy specification. The deadtime of this system is given by the time taken for the shaped output of the front end amplifier to return to a level such that it can be subtracted from the subsequent pulse without significant loss of resolution. A lower limit to the shaping time which can be used is given by the characteristic time for collection of the ionization electrons at the wire. Integration times shorter that this will result in a large reduction in the observed signal, large event to event differences in the peak signal, and a strong dependence of the peak signal on the shaping time. A operational requirement of the IPCs, therefore, is that they have an electron collection time of order 20 nsec. At the same time, the Lorentz angle of the gas at 0.8 kG must be kept under 15 degrees, as the chambers must be canted at this angle with respect to the magnetic field to minimize the position resolution degradation due spreading of the induced signal along the cathode, and mechanical constraints make an cant angle larger that 15 degrees difficult. A gas mixture suitable for Central Tracker use in the IPCs must, therefore, be relatively fast, with a small Lorentz angle. Suitable gas mixtures do exist which satisfy our requirements. An example are CF_4 - CO_2 mixtures, the properities of which the GEM Central Tracker Group at Indiana University have been investigating using a chamber designed to make precision drift velocity and Lorentz angle measurements. Results show that these gas mixtures are relatively fast, and exhibit Lorentz angles below 10 degrees at 8 kG over a wide CF_4 concentration range. The results of these gas studies have been used in a simulation of an IPC chamber using the wire chamber simulation program GARFIELD. The critical operational parameters used in this simulation are listed in Table 2. The contours of equal electron drift time obtained in the simulation are shown in Figure 4.1-2. The contours are at 5 ns intervals. It is apparent from this figure that the maximum delay between the traversal of the particle and the arrival of the first electron at the wire is less than 20 ns, as is the spread in arrival times for electrons coming from a given particle track. The distribution of .arrival times of the first electron at the anode is shown in Figure 4.1-3 for an ensemble of random trajectories through the chamber. This represents the major contribution to time jitter in the system, and demonstrates that it will be possible to assign virtually all hits to the proper crossing.

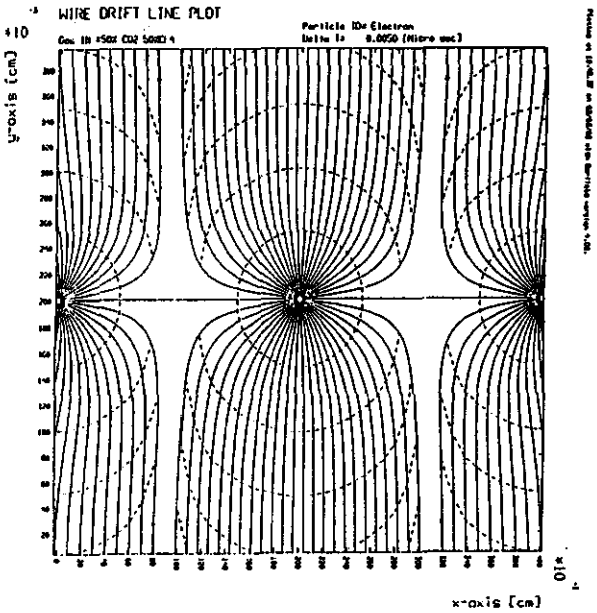

Figure 4.1-2 Equal Time Contours

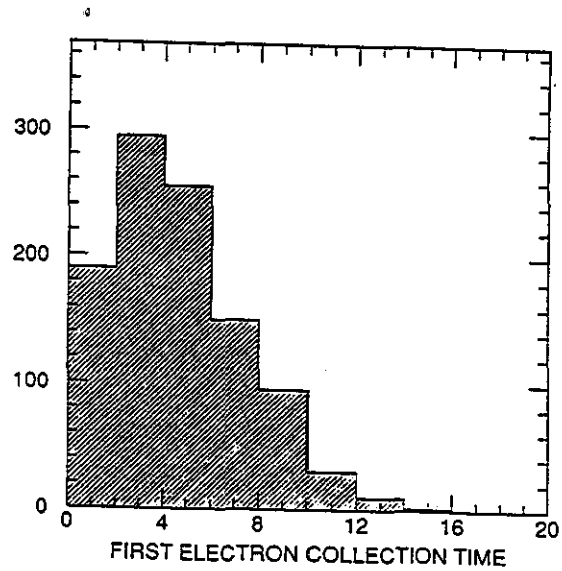

Figure 4.1-3 First Electron Collection Time Dist.

4.1.6. Position Resolution

As stated earlier, the position resolution is determined by the signal to noise ratio of the readout chain. The design goal of the tracker calls for 50 micron resolution, corresponding to 2% of the pad width. Refering to the relationship between position resolution and signal to noise ratio, this requires a signal resolution of about 1% of the total measured cathode signal. The gas gain , which determines the signal ampliitude, is, therefore, constrained by signal to noise considerations. Figure 4.1-4 shows the measured position resolution in an prototype IPC chamber versus the gas gain, while Figure 4.1-5 shows the distribution of event positions at a single source position. These measurements were made on a chamber with the same geometry as the baseline IPC design, a fast gas mixture, and a front end amplifier with a peaking time of 20 ns, and demonstrate that the 50 micron requirement is achievable under real conditions At low values for the gas gain the resolution is measurement error dominated, and hence varies roughly as the inverse of the gas gain. Under the operating conditions used to generate the data in Figure 4.2-4, the position resolution of the chamber under study approaches an asymptotic value at a gas gain of 2×10^4. The gas gain above which the chamber resolution is dominated by irreducible effects is determined by the noise in the front end readout electronics, normally expressed in

equivalent electrons. The dominant noise component, due to the input transistor of the preamplifier, can be expressed as

$$\sigma_q \propto C_{in} / (g\sqrt{t_{shaping}})$$

This component of the amplifier noise increases with the inverse square root of the shaping time, and is proportional to the input capacitance. This capacitance includes the mutual capacitance between pads, along with the capacitance between a pad and the readout lines, ground planes, etc. The present design of the cathode calls for readout lines lying on the opposite side of a 0.5 mm thick sheet from the pad plane, with no ground plane between the readout and pad layers. Measured values of the total capacitance for 0.2 cm wide rectangular pads plus readout lines are in the range 2-25 pf for the range of pad lengths encountered in the IPCs.

Based the performance of monolythic preamplifers fabricated as part of the GEM R&D program, and described in detail in the electronics section of the TDR, it is reasonable to expect a noise figure of 1300 electrons for an input capacitance of 25 pf, with a peaking time of 20 ns. Using this value for the expected noise in the readout chain, we require a total cathode signal of roughly 1.3×10^5 electrons to obtain a total signal to single channel noise ratio of 100. This value can be used to determine the gas gain required to achieve the 50 micron position resolution design goal. The number of ion pairs produced in a 4 mm gap of 50-50 CO_2-CF_4 is 60. The measured signal on the cathode is smaller than $60 \times G$ as a result of two factors. First, the induced signal is shared between the two cathodes and the adjacent wires, so the induced signal on a given cathode is roughly one half the total. Second, the shaping amplifier filters out all but the initial portion of the induced signal. For the baseline chamber geometry and known values for the ion mobilities of CO_2 and CF_4 the fraction of the total charge seen at the output of the shaping amplifer is 20% for a 20 ns peaking time. Combining these factors, and requiring a cathode signal of 1.3×10^5 electrons, we find that the gain required would b 20,000 if electronics noise were the only contribution to the position error. Results of the position resolution measurments in IPC prototypes, shown in Figure 4.1-4 and Figure 4.1-5, indicate that irreducible effects, such as diffusion, also contribute to the position error, requiring that a slightly higher gas gain than this value be used.

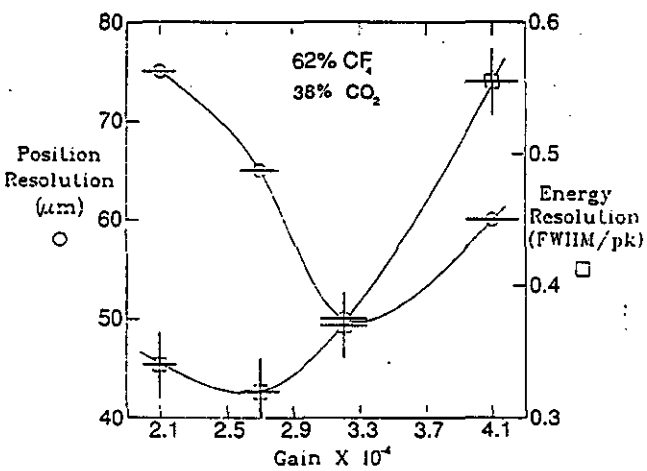

Figure 4.1-4 Position Resolution vs Gain

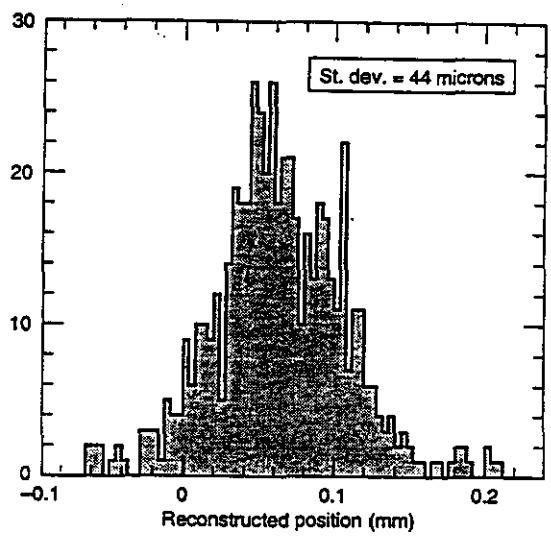

Figure 4.1-5

4.1.7 Position Resolution Degradation Due to Non-Normal Incidence

The preceding discussion of the position resolution was for particles at normal incidence. When particles cross the pad chambers at non-normal incidence, the resolution is somewhat degraded.

a) For a track crossing a barrel chamber at an angle ϕ from normal, the charge hitting the anode wire is spread over a length

$$\Delta W = d \tan \phi$$

were d is the cathode-to-cathode thickness of the chamber (4mm in our case), as shown in Figure 4.1-6.

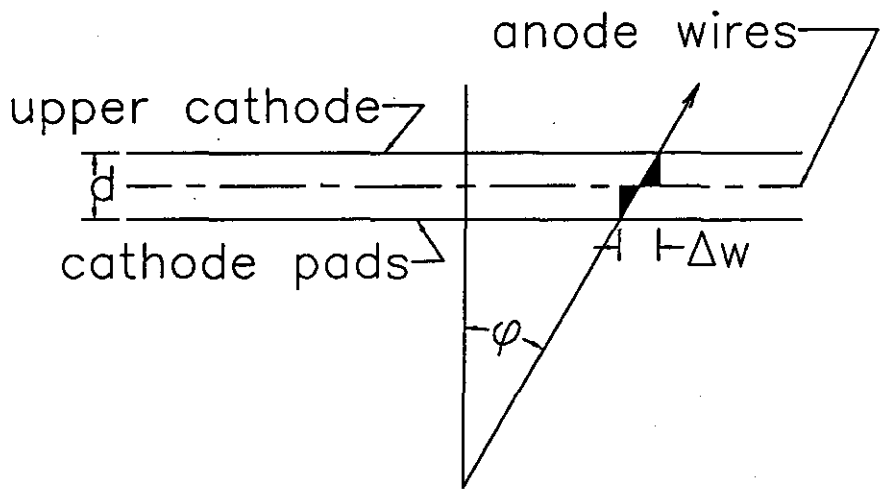

Figure 4.1.6 Cross Section of IPC chamber module looking along the beamline

If the charge were spread uniformly over this region ΔW, the interpolation of the pad signal would give the position of the center of this region. However, due to fluctuation of the charge deposition along the track crossing the chamber, there will be an uncertainty in the measurement of the center of the region ΔW. A monte carlo simulation of this situation indicates that a resolution smearing of an amount δ results from this where

$$\delta = 0.08 \times \Delta W$$

The resultant resolution then is

$$\sigma = \sqrt{\sigma_0^{\,2} + \delta^2}$$

where σ_0 is the resolution at normal incidence.

It is the consideration of this effect that determines the number of barrel chambers around the circumference of a barrel layer. To keep δ to be not larger than σ_0 implies that the ϕ range in a chamber be kept to less than $\pm 9^\circ$, which leads to 20 chambers per layer. The resultant resolution as a function of ϕ across a barrel chamber is shown in Figure 4.1-7.

The resultant resolution as a function of ϕ across a barrel chamber is shown in Figure 4.1-7.

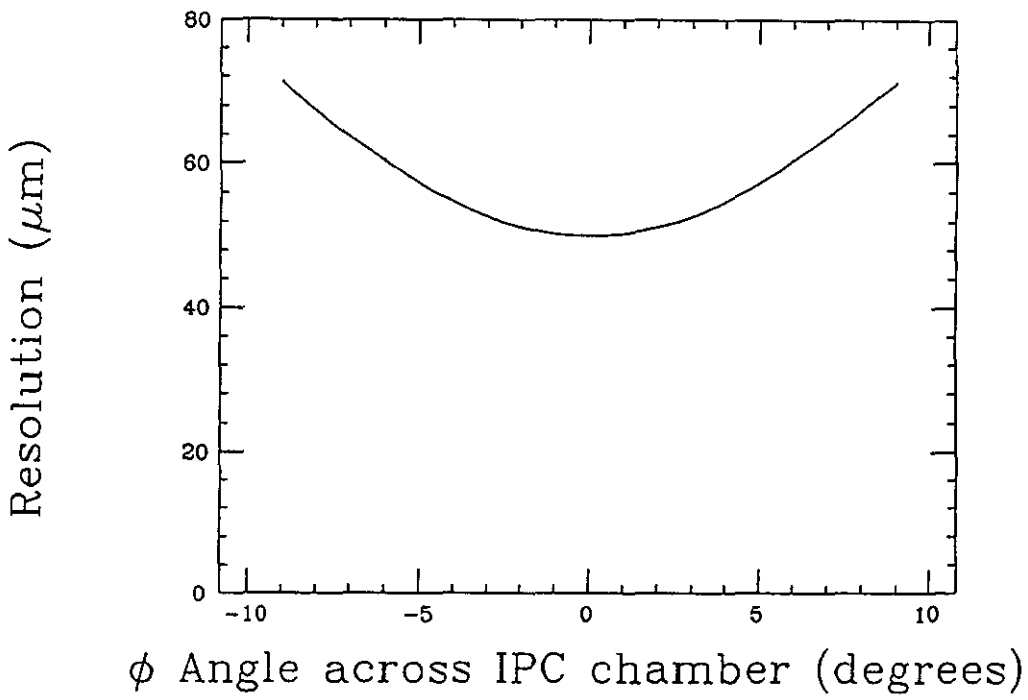

Figure 4.1-7 Resolution across a barrel IPC chamber as a function of the angle of incidence of tracks in the azimuthal (ϕ direction)

b) Non-normal incidence in the "θ" direction causes a track to deposit charge on several anode wires along a distance $\Delta\ell$

$$\Delta\ell = d \tan \psi,$$

where $\psi = 90^\circ - \theta$ as shown in Figure 4.1-8. If the long dimension of the pads, which is much larger than the wire spacing, were exactly perpendicular to the wire direction, there would be no resolution degradation due to this. However, the pads are rotated by the stereo angle θ_{stereo} from this position; this leads to a resolution smearing

$$\delta = 0.08 \times \Delta\ell \times \theta \text{ stereo}$$

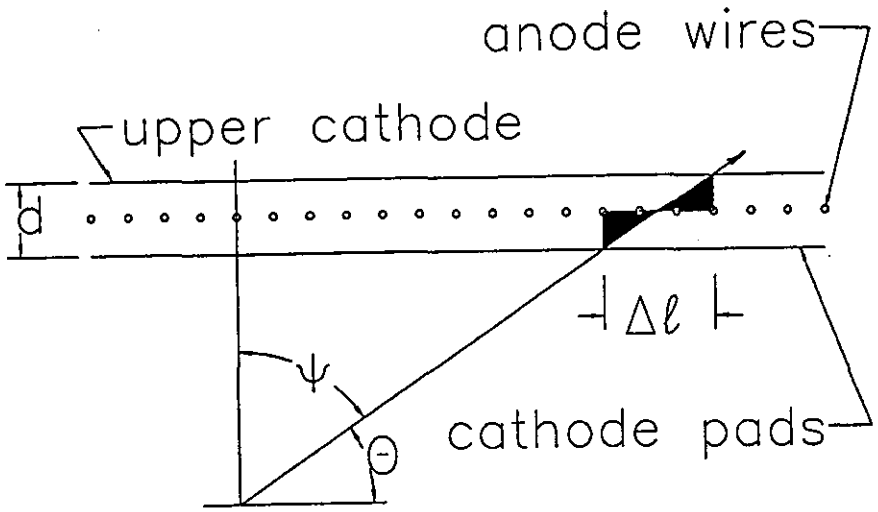

Figure 4.1-8 Cross section of IPC chamber mocule looking along the anode wires in the chamber

The resultant resolution as a function of Z along the barrel chambers is shown in Figure 4.1-9 for the innermost and outermost layers of the barrel.

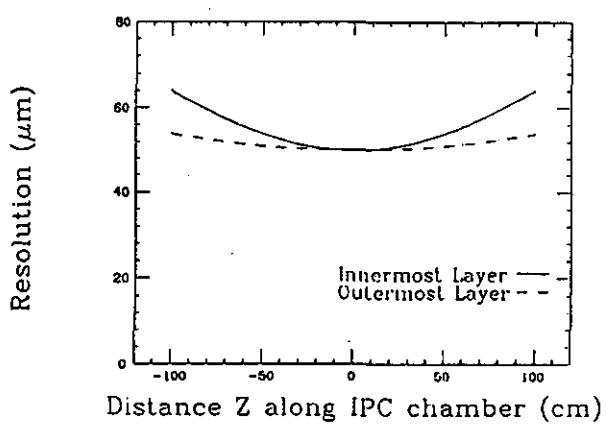

Figure 4.1-9 Resolution along a barrel IPC chamber along the Z (beam) direction for stiff tracks coming from the center of the interaction region for the innermost and the outermost layers of IPC chambers.

Combining these effects produces the resolutions in the extreme corners of the innermost and outermost layers of barrel chambers shown in Figure 4.1-10.

82	71	82
64	50	64
82	71	82

a) Resolutions in the innermost IPC layer

74	71	74
54	50	54
74	71	74

a) Resolutions in the outermost IPC layer

Figure 4.1-10 Resolution in μm at various points of a barrel IPC chamber for stiff tracks coming from the center of the interaction region.

c) Similar effects apply to the endcap chambers. The desire to keep the resolution smearing due to non-normal incidence to less than σ_0 led to a design with 10 trapezoidal chambers around a forward disk. The resultant resolutions in the extreme corners of the endcap chambers are shown in Figure 4.1-11.

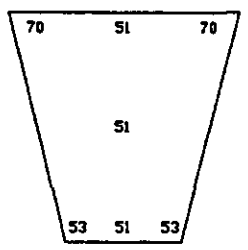

a) Resolutions in the endcap IPC layer closest to the interaction point

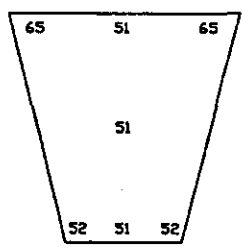

a) Resolutions in the endcap IPC layer farthest from the interaction point

Figure 4.1-11 Resolution in μm at various points of an End Cap IPC chamber for stiff tracks coming from the center of the interaction region.

d) The above discussion has neglected the effects of the Lorentz force due to the 0.8 Tesla magnetic field that the tracker is immersed in. This effect can fortunately be corrected for by tilting the barrel chambers in "ϕ" by the Lorentz angle. The endcap chambers will remain in the plane perpendicular to the beams but the anode wires will be strung tilted in the "ϕ" direction by the Lorentz angle. Thus the Lorentz force will not cause any degradation in the resolution. The above discussion about resolutions at non-normal incidence holds, except the angles of incidence in the "ϕ" direction discussed in a) above change by the Lorentz angle.

All of these effects affecting the IPC resolutions have been taken into account in the GEANT calculations of the momentum and vertex resolutions presented in sections 1 and 2 above.

4.1.8. Rate Effects

The effects of the high rate SSC environment on IPC performance falls into two categories. These are chamber aging, and the effects of space charge on chamber gain. Chamber aging refers to a gradual decrease in the gas gain in the chamber due to a buildup of deposits on the electrodes, resulting in narrowing operating plateau and eventual chamber breakdown. This effect is directly proportional to the integrated charge collected per unit length of wire. At a luminosity of $10^{34}cm^{-2}\ s^{-1}$ the amount of charge collected per SSC year per cm of wire in the IPCs, assuming a gas gain of 30,000, is 0.85 C/cm at a radius of 30 cm. For a given integrated charge, chamber aging depends primarily on gas composition. Measurements have been carried out on chamber aging for CF_4-CO_2 mixtures. For a 50-50 mixture the measured decrease in the operating current of a test chamber was found to be

$$(I - I_0)/I_0 = 0.07 C^{-1} cmYr$$

This result confirms the expectation that these gases should exhibit very small aging effects. It is well known, in fact, that Freon can be used to recover a chamber which suffers from aging.

The conclusion is that at the gas gain required from signal to noise requirements, the chambers should be able to operate for a number of years at $10^{34}\ cm^{-2}s^{-1}$ while suffering minimal aging effects.

The buildup of space charge in the IPCs will result in a decrease in gain of the chamber at sufficiently high ionization rates. At a luminosity of $10^{34}cm^{-2}s^{-1}$, the charged track rate in the IPCs is $2x10^9\ s^{-1}$ in each IPC, or $1x10^4\ s^{-1}$ mm wire $^{-1}$ in the innermost layer of IPCs. Measurements conducted on IPC prototypes running CF_4-CO_2 mixtures and exposed to a high intensity x-ray source generating local ionization levels in excess of this amount indicate little if any space charge induced reduction in gain at these ionization levels. To confirm this, a critical

part of our R&D plan during the coming year is an investigation of space charge effects on chamber operation at high particle fluences using minimum ionizing particles.

4.2 IPC Tracker Mechanical Design

4.2.1 Introduction

The following sections describe the mechanical design of the interpolating pad cathode (ipc) portions of the GEM central tracker subsystem. These sections are intended to supplement the GEM Technical Design Report with more detailed information.

Figure 4.2-1 is an isometric view of the interpolating pad cathode tracker array. The support structure is omitted for clarity. There are two chambers per superlayer module for both endcap and barrel sections. In addition, there are twenty barrel modules per superlayer for the barrel section and ten modules per superlayer for each endcap section. The barrel and endcaps each have four superlayers. Table 4.2-1 summarizes the design parameters for the interpolating pad cathode subsystem.

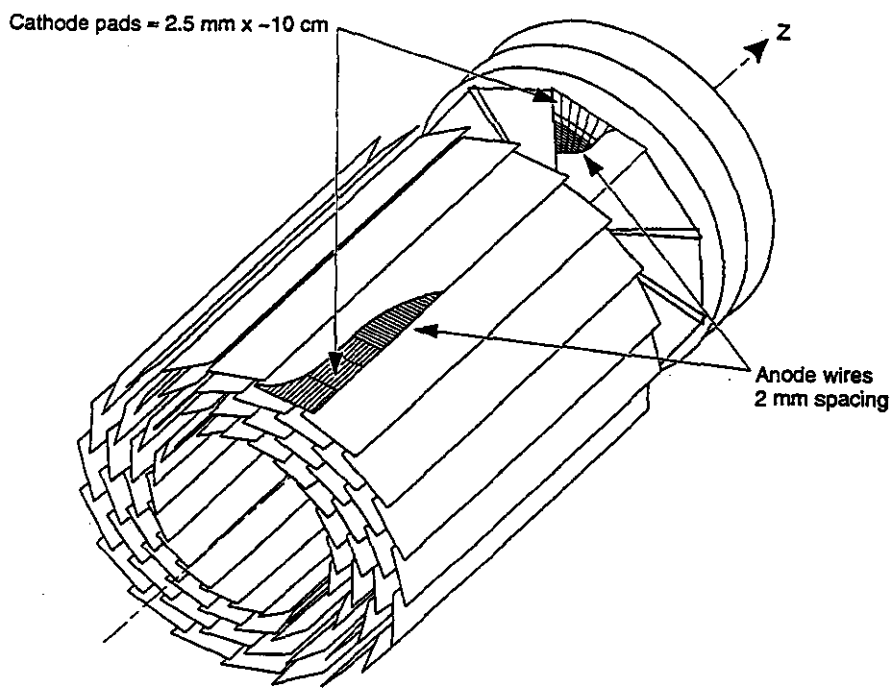

Figure 4.2-1 IPC Tracker Array - Isometric View

Table 4.2-1: GEM IPC Array Design Parameters

Parameter	Quantity
Lorenz angle	12.5 degrees
Number of sectors - barrel superlayer	20
Number of sectors - endcap superlayer	10
Number of superlayers - barrel and endcap	4
Number of chambers per superlayer	2
Chamber depth (cathode to cathode)	4 mm
Anode wire diameter	$20 \leq$ diam. $\leq 40\mu$
Anode wire potential	3 Kv
Barrel IPC superlayer length	200 cm
Barrel IPC array inner radius boundary	39 cm
Barrel IPC array outer radius boundary	88 cm
Endcap IPC minimum axial boundary	112 cm
Endcap IPC maximum axial boundary	170 cm
Number of barrel pads	204240
Number of pads (each endcap)	93540
Electronics power dissipation - barrel	12.5 Kw
Electronics power dissipation - each endcap	5.7 Kw

Ideally, the GEM ipc tracker mechanical support would occupy no volume and would have zero mass. However, real-world considerations dictate otherwise. On the one hand, physics limitations (e.g. radiation length, etc.) require use of low density, low Z materials; on the other hand, mechanical requirements demand extremely stiff and stable materials. The geometric arrangement of these materials is important in minimizing their use. Table 4.2-2 summarizes the long term mechanical stability requirements for the ipc tracker.

Table 4.2-2: GEM IPC Array Stability Requirements

Parameter	Quantity
Between superlayer modules in ϕ	25μ
Between superlayer modules in z	100μ
Between endcaps and barrel in ϕ	25μ
Between endcaps and barrel in z	100μ
Module transverse flatness	160μ
-or-	20μ over adjacent pads

A further requirement is relatively simple removal and replacement of superlayer modules. Physical access to the GEM central tracker will be infrequent (annual) and there will undoubtedly be intense competition for the time available. Modules must be removed and replaced quickly. The modularity features will be discussed in a later section.

In summary, the materials trade-offs will be discussed first. Structural design will be discussed next, followed by module gas flow and on-board electronics cooling. Finally, superlayer module assembly will be discussed. The ipc/silicon support structure and the ipc endcap structure mechanical designs will be covered in separate sections.

4.2.2 IPC Barrel Superlayer Module Design

Materials Considerations

Table 4.2-3 shows densities, Young's moduli, specific stiffnesses (ratio of Young's modulus to density), and radiation lengths for an assortment of materials. Organic matrix composite materials have a clear advantage here. In addition, unlike isotropic homogeneous materials (e.g. aluminum, steel, etc.), mechanical properties can be "engineered" by altering fiber volume fraction, number of plies and specific ply orientation.

Table 4.2-3: Properties of Selected Materials

Material	Density (ρ) g/cm^3	Modulus (E) GPa	Spec. Modulus (E/ρ) 10^8 cm	Rad. Length cm
303 st. steel	8.03	187.30	2.38	1.76
Copper	8.94	113.72	1.30	1.43
6061 aluminum	2.71	66.89	2.52	8.9
Mylar	1.39	2.67	0.20	28.7
G10/FR4	1.70	12.7	0.76	19.4
Graphite/epoxy (P75/1939-3)	1.68	109.2	6.63	25.0

High modulus graphite fibers in a cyanate ester matrix provide the greatest specific stiffness, coupled with relatively high radiation resistance and low moisture absorption. The negative factor is the higher cost relative to lower performance composites (e.g. G10/FR4) and most metals.

Graphite/cyanate-ester composites work well for most structural support requirements within the GEM central tracker. However, the interpolating pad cathode modules contain high voltage components (anode wires and associated circuitry). Graphite is a semiconductor (volume

resistivity of 10^{-3} ohm-cm); materials with volume resistivities in the order of 10^{14} ohm-cm are required for the high voltage standoffs and for the ipc printed circuit board substrates. Kevlar (aramid), high-purity quartz and ordinary glass fibers exhibit resistivities of this magnitude.

Materials to be used in the GEM ipc tracker are expected to be exposed to a high radiation (1 Mrad/year), high magnetic (0.8 Tesla) environment over a lifetime of ten years without significant degradation. In addition, hygrothermal conditions could be factors during construction materials storage, component manufacture and transportation to the SSC site. The ipc modules will be installed within an inert gas atmosphere during operation. Cyanate ester has been shown to have greater radiation resistance and lower moisture absorption than epoxy counterparts. Of the insulating fibers mentioned previously, Kevlar exhibits the highest Young's modulus. Both Kevlar and ordinary glass fibers (as used in G10 or FR4) exhibit potential hygrothermal problems.

High purity quartz (>99.9 % SiO_2) fiber has excellent electrical, mechanical and hygrothermal properties. The coefficient of thermal expansion is about 0.5 ppm/^{o}C, as compared to ordinary glass, which is about 8.5 ppm/^{o}C. There is a precedent for using this material for printed circuit board substrates. However, quartz/cyanate ester laminates cost significantly more than G10 or Kevlar.

Table 4.2-4 summarizes some typical electrical and mechanical properties for an assortment of composite materials. Note that the data for the quartz laminate is based on a single sample from manufacturers' literature. Tests will be required to determine properties for project-specific fiber/resin combinations. This data will be included within subsequent editions of the progress report. Table 4.2-5 outlines materials selected for use in the ipc tracker array and their respective locations within the array.

Table 4.2-4: Physical and Mechanical Properties of Selected Composite Materials

Material	Density (ρ) g/cm^3	Modulus (E) Gpa	Specific Modulus (E/ρ)-10^8cm	CTE (α) ppm/^{o}C	Moisture Absorption (%)	Volume resist.-cm	Dielect. const. (ε)
G10	1.7	12.7	0.76	11	0.2	4.4×10^{12}	3.8
Kevlar/ epoxy(a)	1.36	35.45	2.66	3.3	1.8	5×10^{15}	4.1
Quartz/ epoxy(b)	1.82	26.16	1.47	6.4*	**	6.76×10^{14}	3.6
Graphite epoxy(c)	1.68	109.2	6.6	-0.43	**	10^{-3}	

Notes: (a) Kevlar 49 (181 fabric)/5208; (b) FMI HPQY-102 (300 2/2 fabric)/Hexcel F253 epoxy; (c) P75/1939-3 quasi-isotropic lay-up; * Data for this lay-up configuration; value is expected to be reduced for optimized lay-up; **Data not available; independent testing to follow

Table 4.2-5 : Material Selections for IPC Components

Location	Material
IPC superlayer module- pad cathode printed circuit board	High purity quartz/cyanate-ester composite
honeycomb core	Nomex or graphite/cyanate-ester
anode wire supports	Quartz/cyanate-ester
anode wires	Gold-plated tungsten
cathode plane supports	Quartz/cyanate-ester
cathode plane	Copper-coated Mylar or Kapton
gas window supports	Graphite/cyanate-ester
gas plenums	TBD
IPC doublet unit-struts	Graphite/cyanate-ester
support tube	Graphite/cyanate-ester (filament-wound)
endplate	Graphite/cyanate-ester
IPC endcap support structure-	Graphite/cyanate-ester
Si/IPC support structure (LANL)-	Graphite/cyanate-ester

IPC Barrel Superlayer Module Structural Considerations

The GEM ipc tracker array must remain stable both from a short- and long-term point of view. The ipc tracker array mechanical design group is engaged in detailed structural analyses of both the barrel superlayer modules themselves and the overall ipc/silicon tracker support structure which will be discussed in a subsequent section.

Short-term stability could be adversely affected by dynamic inputs from systems external to the central tracker. Specifically, these are the liquid krypton calorimeter (0 to 10 Hz) and various vacuum pumps and other rotating machinery (30 Hz spike, which corresponds to 1725 rpm AC electric motor). Since GEM does not yet exist, data is currently being gathered from other accelerator facilities to permit rough order-of -magnitude calculations. As the dynamic model for the entire GEM detector becomes more refined, more precise inputs to the tracker will be used.

The current barrel IPC modules are designed to reach first bending mode resonance at frequencies greater than 43 Hz (30 Hz * $\sqrt{2}$). Figure 4.2-2 shows a cross-section of a typical ipc barrel module which is 2 meters in length. The individual superlayer modules reach the first bending mode between 25 and 30 Hz, depending on width. The first bending mode is directly proportional to the honeycomb thickness between the ipc printed circuit boards. Overall module thickness is limited by geometric considerations.

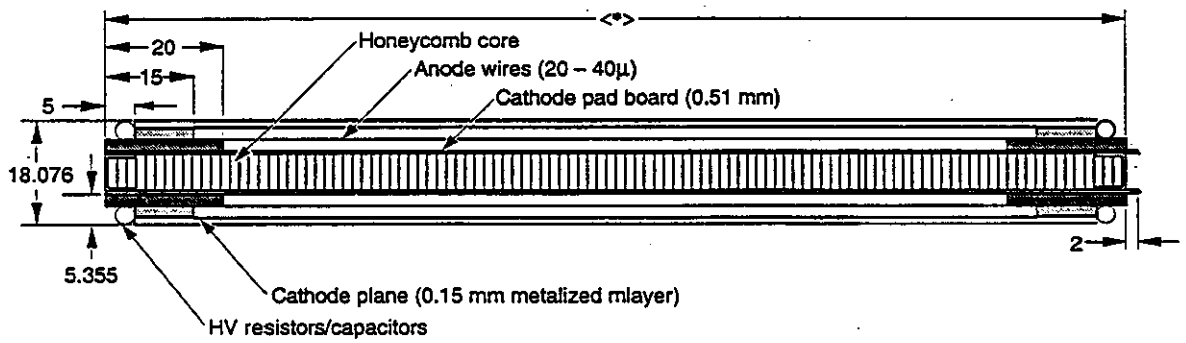

Figure 4.2-2 Cross Section of a Typical IPC Barrel Module

The most effective way to push the first bending mode above 43 Hz is to connect together two modules from adjacent superlayers to form "doublets." Struts at the quarter, half and three-quarter points link the modules together. In addition, a 6.3 cm diameter graphite/cyanate ester filament wound tube is installed between the modules to provide additional rigidity and to support the on-board electronics packages. Figure 4.2-3 shows the concept as described.

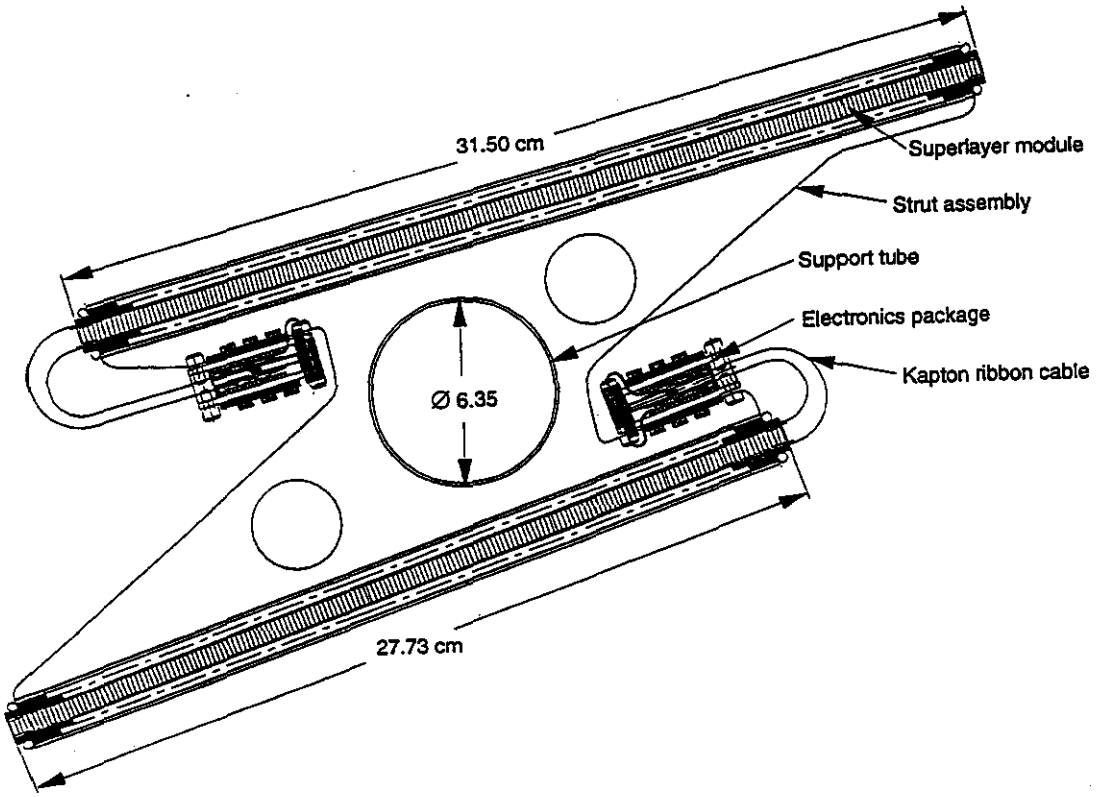

Figure 4.2-3 (a) End View - IPC Barrel Doublet

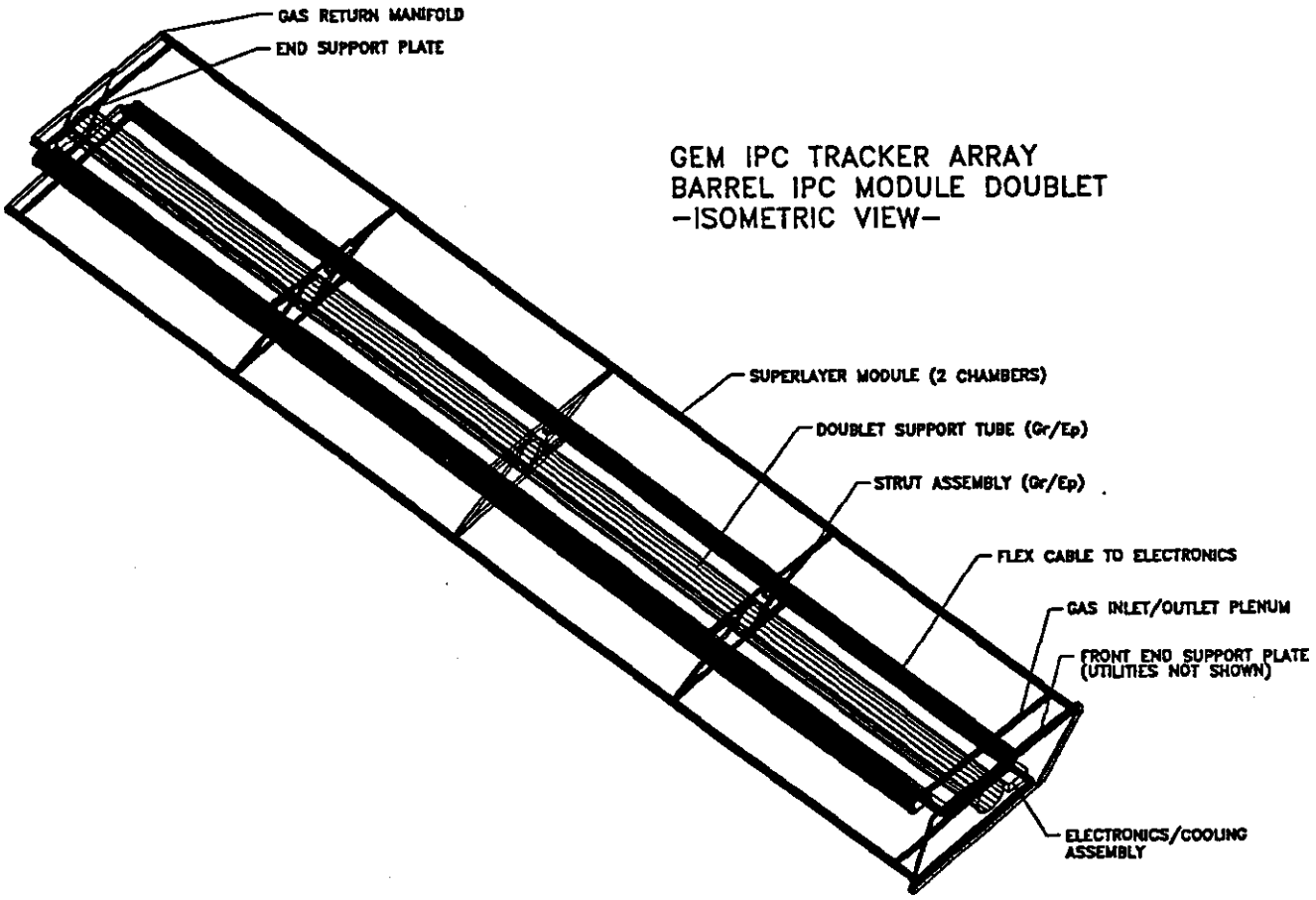

Figure 4.2-3 (b) IPC Isometric View - IPC Barrel Doublet

A finite element model has been developed to validate the doublet concept. The model consists of quadrilateral shell, solid and bar elements. Orthotropic properties are used where composite materials are employed. Figure 4.2-4 is a side view of the deformed model (first bending mode), where one end of the doublet is fixed and the other is simply supported. The first mode is at 55.6 Hz; the second bending mode is at 134.5 Hz.

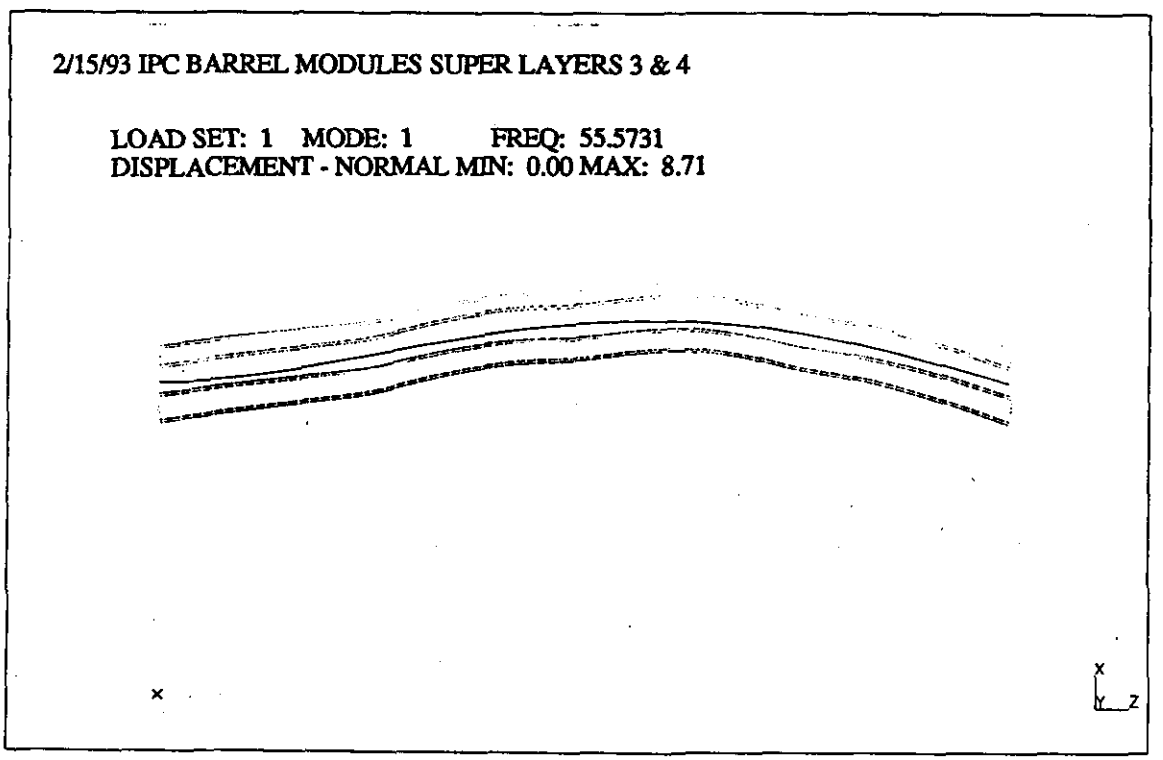

Figure 4.2-4 IPC Barrel Doublet Finite Element Model - Deformed

Verification of the finite element model was achieved by constructing a mechanical prototype with available materials and experimentally determining the modes of vibration. The model was modified to reflect properties of the available materials. Figure 4.2-5 illustrates the experimental setup. The prototype was suspended vertically from the ceiling with a "bungie" cord to isolate the structure and to eliminate the effect of gravity on transverse (bending) modes. A hammer with a load cell on the tip was used to provide an impulse and the quantitative data associated with it. Accelerometers were placed at the locations noted in the figure and a spectrum analyzer was employed to display the transfer function resulting from the impulse. The data were then displayed on a computer in the form of natural frequencies , associated mode shapes and damping levels.

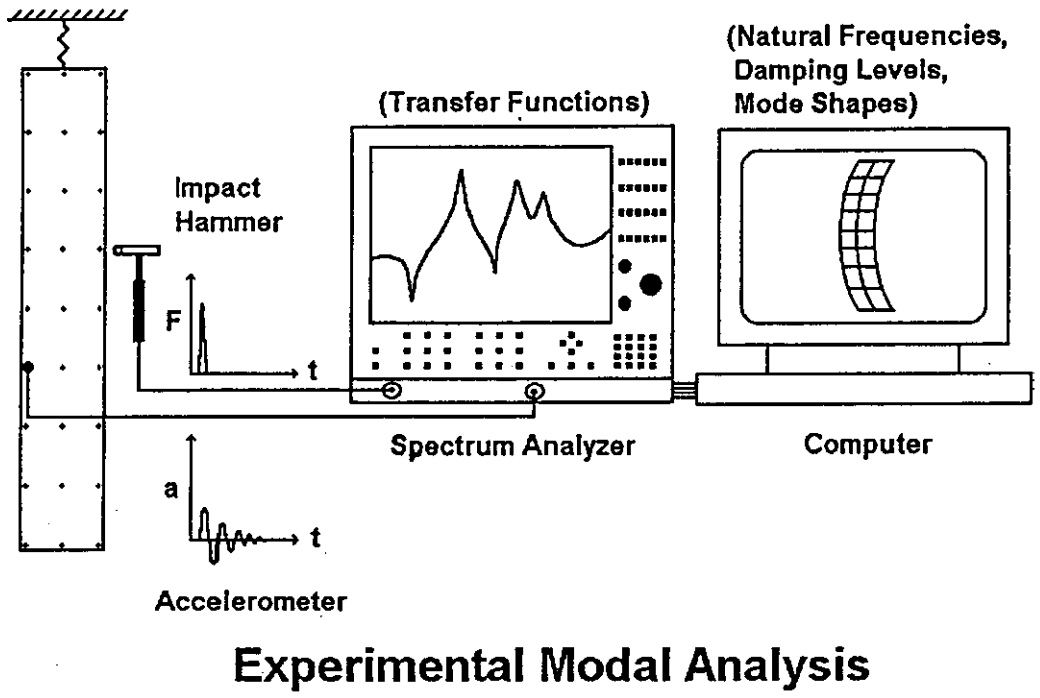

Figure 4.2-5 Modal Testing Apparatus

Table 4.2-6 provides a comparison between the finite element analysis (NASTRAN) and experimental results. Note that all frequencies are considerably lower than the equivalents in the proposed design due to use of available materials.

Table 4.2-6 Comparison of Experimental and Calculated Prototype Vibration Modes

Mode	Shape	Boundary conditions	NASTRAN results	Test results	Damping % critical
1	1st bending	free-free	65.8	66.7	0.53
2	2nd bending	free-free	170.5	161.5	1.89
1	1st bending	simple support/both ends	30.1	29.5	—

IPC Barrel Module Design Detail

Figure 4.2-6 is an isometric view of a typical ipc barrel module assembly. Figures 4.2-7 and 4.2-8 show details of the module, particularly the pad cathode printed circuit board, anode wires, cathode plane and gas window (both shown cut-away).

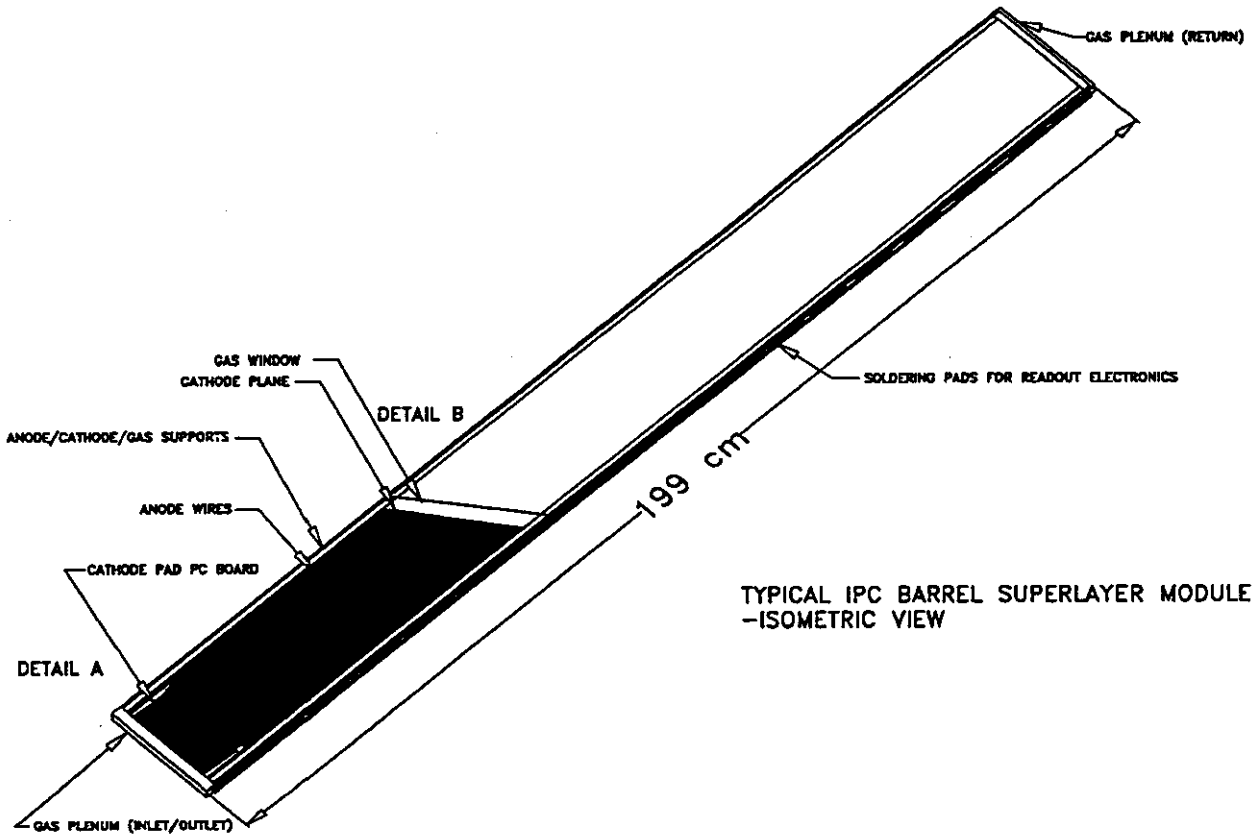

Figure 4.2-6 Isometric View of a Typical IPC Barrel Module Assembly

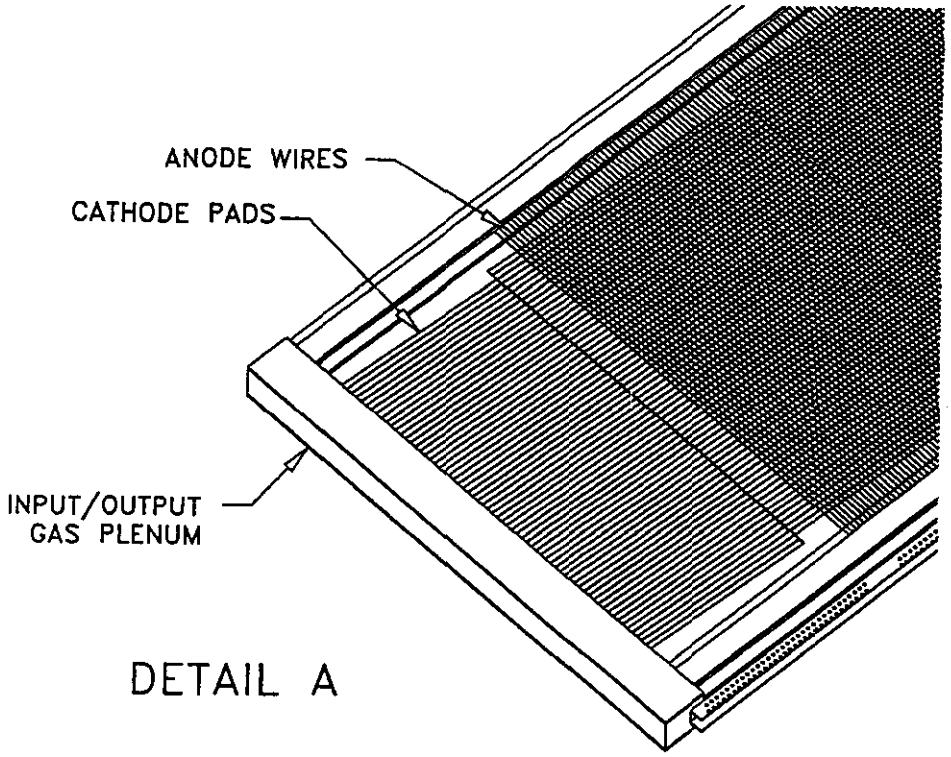

Figure 4.2-7 Details of IPC Barrel Module

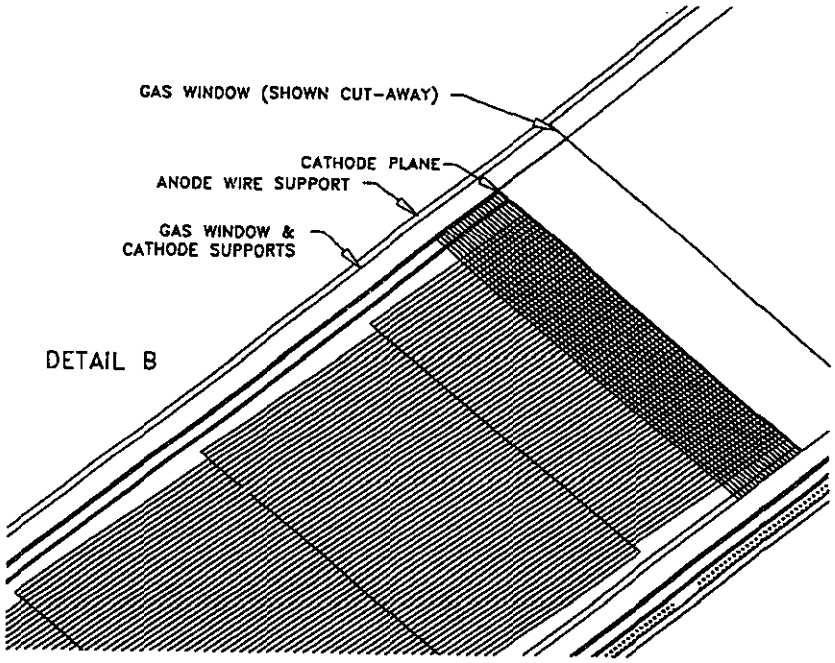

Figure 4.2-8 Further Details of IPC Barrel Module

Figure 4.2-9 is an exploded view of the module assembly with components labeled. The circled numbers on the left side of the figure are the steps of module assembly and are as follows:

Step 1: Prepare honeycomb core;

Step 2: Bond pad cathode printed circuit boards to core;

Step 3: Bond anode wire supports to core sub-assembly;

Step 4: Bond gas plenums to core subassembly;

Step 5: Wind anode wires onto core subassembly, solder wires and associated resistors and capacitors;

Step 6: Bond cathode plane supports to subassembly;

Step 7: Stretch and bond cathode plane to subassembly;

Step 8: Bond gas window supports to subassembly;

Step 9: Stretch and bond gas window to subassembly.

In addition to this assembly procedure, pairs of modules from adjacent superlayers must be assembled into doublets. On-board electronic packages are then installed, acceptance tests are performed and the finished units are shipped to the SSC site for installation.

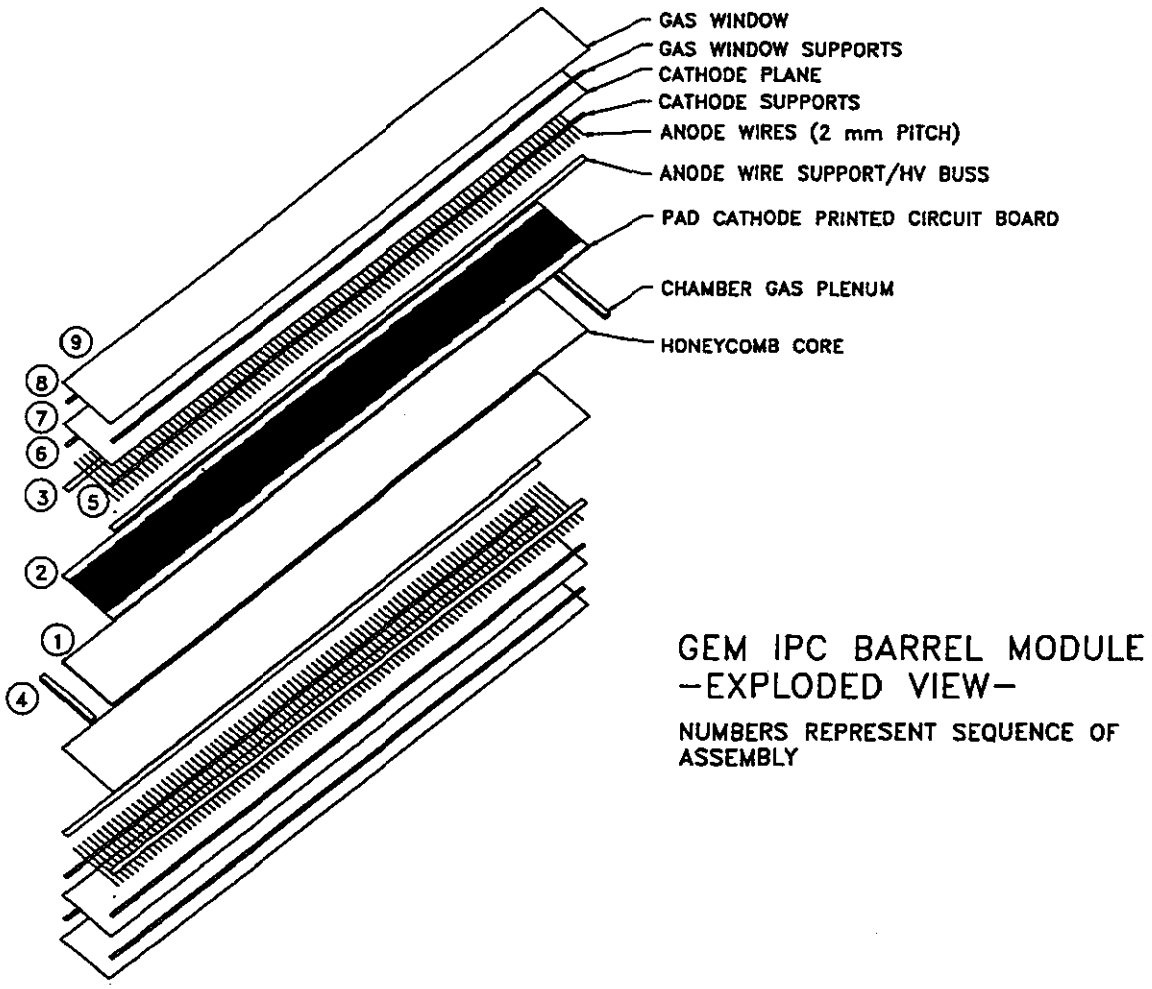

Figure 4.2-9 Exploded View of IPC Barrel Module Assembly

4.2.3 IPC Endcap Superlayer Module Design

The ipc endcap modules are trapezoidal in shape as shown in figure 4.2-10 and are one quarter the length of their barrel counterparts. Little time has been expended to date on their detailed design. However, the module cross-section and assembly procedures are expected to be similar those of a typical barrel module in that there are two chambers per module, separated by a honeycomb core. Electronics will be located around the outer perimeter of each endcap for accessibility and to avoid unnecessary radiation exposure.

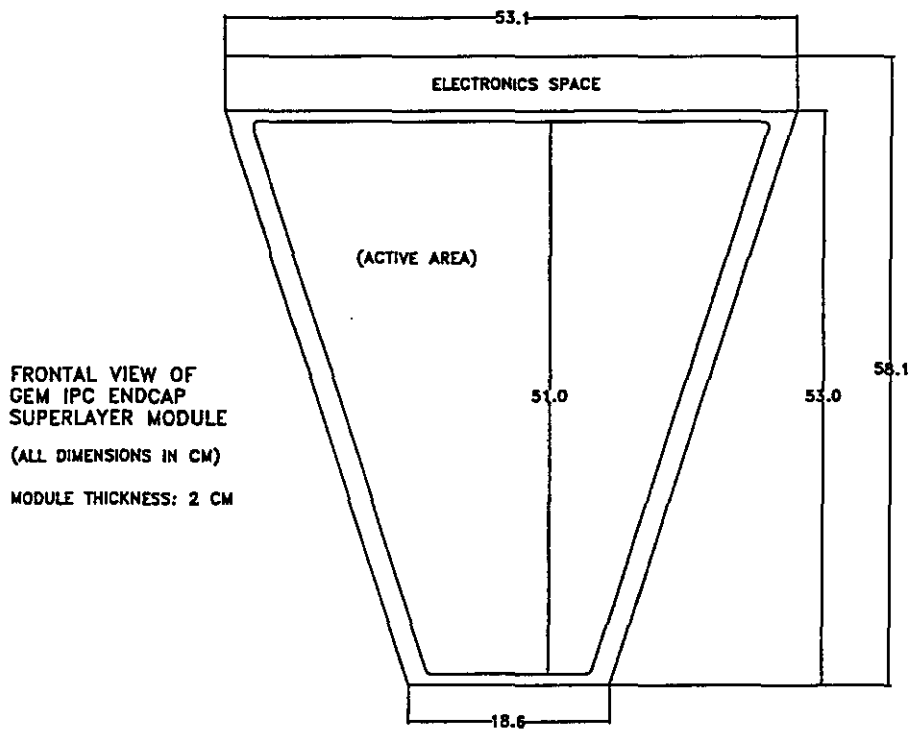

Figure 4.2-10 Frontal View - End Cap IPC Module

4.2.4 IPC Endcap Support Structure

The ipc endcap support structure design is in the conceptual stage at the time of this writing. The structure must serve a dual purpose similar to the silicon/ipc support in that it serves both as a mechanical support and as a gas enclosure. Figure 4.2-11 shows the support structure concept. The superlayer modules are attached to four graphite honeycomb composite annular disks (one per superlayer). The disks are kinematically mounted within the support structure, which consists of a central support tube, axial ribs, a fixed forward annular bulkhead, removable shear panels around the outer perimeter and a removable rear bulkhead.

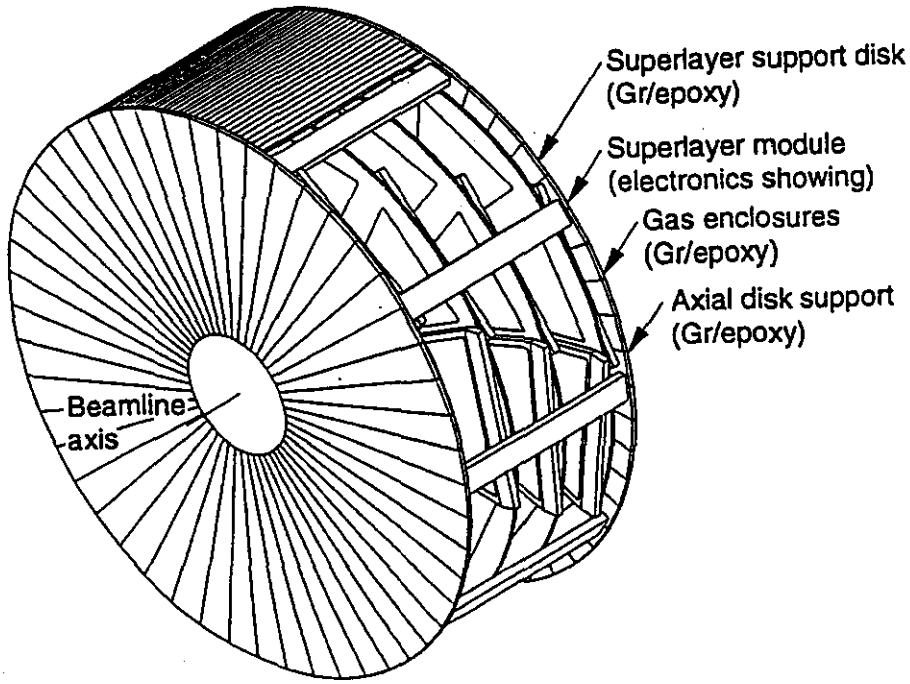

Figure 4.2-11 Isometric View - IPC End Cap Concept

4.2.5. OuterSupport Structure

The STS/IPC Outer Support Structure will be housing all of the GEM central detector. It is a structure that must be stable from the standpoint of vibrations, thermal expansion, and expansion due to moisture absorption. In order to achieve all of these requirements, the structure must be made entirely of graphite composites. Because of the importance of the stiffness of the structure, extensive finite element analysis has been performed on computer-generated models. This analysis and results from more than thirty Finite Element Method (FEM) computer runs will be discussed in detail.

The original support structure design called for a bulkhead with a 12.7 mm graphite/polyimide honeycomb core with 0.41 mm quasi-isotropic graphite/epoxy skins, shear panels of the same material and material thicknesses, and Y stringers with the dimensions of 3.18 mm x 12.7 mm constructed from unidirectional graphite/epoxy material. The current design concept is visually similar to the original design. The differences are that several of the thicknesses for panels and lengths of panels have changed. Despite these changes, however, the structure remains within the original envelope. The structure is shown in Figure 4.2.5-A and consists of two bulkheads, ten full length bonded shear panels, ten removable shear panels, ten Bulkhead interface shear panels, twenty shear panels that are bonded in place running between bulkheads, and forty "Y" shaped stringers running longitudinally at the points of the polygon between shear panels.

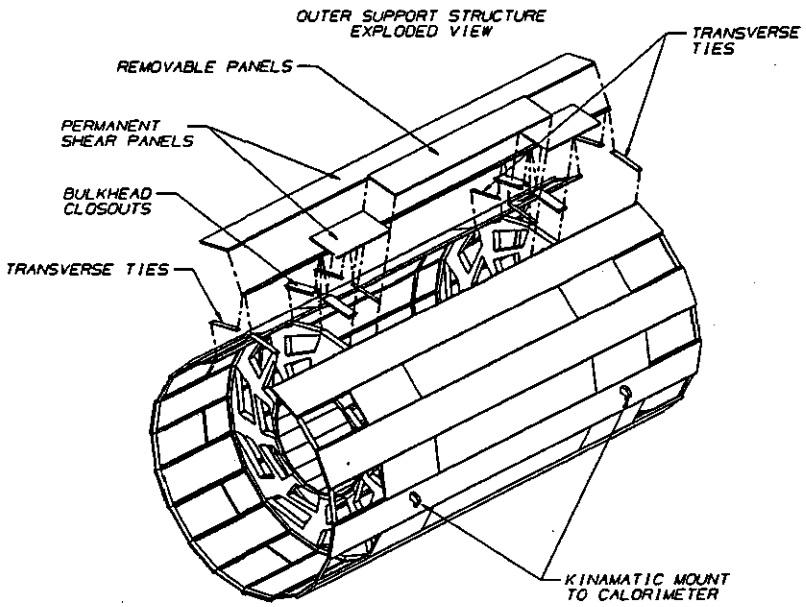

Figure 4.2.5-A: Outer Support Structure

When designing this structure several criteria were used. These criteria included: minimal overall radiation length, a fundamental frequency of 42 to 45 Hz, and minimization of dimensional changes due to temperature and moisture. Because of the fundamental frequency criterion, the design problem becomes stiffness instead of strength driven. The target frequency was achieved by varying the cross-sectional dimensions and the modulus of elasticity of the Y-stringers, the skin thicknesses of various panels and the core thickness of the bulkheads. The dimensional stability is minimized simply by using graphite composites with a cyanate ester resin system. Varying the thicknesses of the graphite skins and honeycomb core that make up this structure produced various radiation length results. These results are weighed against the associated radiation length to determine whether the benefit is worth the penalty.

One of the first design decisions made was to use a twenty sided polygon instead of a cylinder for the support structure. This was based on the shape and configuration of the hardware that will be installed between the outer and inner diameters, lack of space between the detector and the EM Calorimeter, accessibility to the detector hardware, and cost.

The analysis of this structure has been extensive due to the large number of iterations varying feature sizes and material properties. The base configuration was modeled and analyzed using the material properties of aluminum. Other aluminum models of single stringers (beams), single panels and single panels with stringers were subsequently run for purposes of verification. These models were then verified by hand calculations using closed form solutions. A separate model was constructed to predict the behavior of the bulkheads, and, thus, give an indication of the loss of stiffness caused by placing openings in the bulkhead for IPC module insertion. Analysis performed on with the verification models showed that the primary model was accurate. It also predicted a loss in stiffness due to the opening in the bulkheads of 10% to 15%. With the accuracy of the primary finite element model established, the bulk of the analysis could begin. The parameters varied in each iteration (run) of the analysis and their resulting effect on the modal frequencies of the structure.

Figure 4.2.5-B (below) shows that increasing the bulkhead core thickness caused the fundamental frequency (and therefore stiffness) of the structure to increase. It was also noted that the bulkhead moved axially at its fundamental frequency.

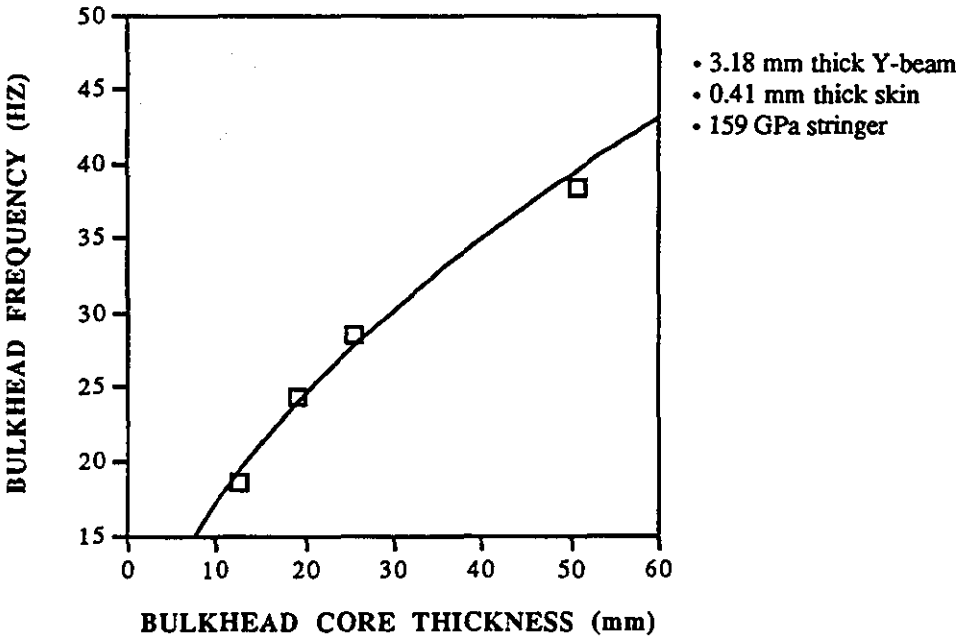

Figure 4.2.5-B: Variation of bulkhead frequency with bulkhead core thickness

The increase in bulkhead core thickness did not produce as large an effect on the stiffness as desired, however, especially since the model of the bulkhead by itself indicated that a frequency over fifty hertz was possible. This realization led to an attempt to stiffen the junction between the bulkhead and the outer and the inner diameters. This was accomplished by increasing the modulus of elasticity for the unidirectional graphite epoxy material comprising the Y-stringer. The effects of the increasing modulus on the analysis was minor as shown in Figure 4.2.5-C (below). Even when the bulkhead thickness was subsequently increased to 50.8 mm with the same modulus iterations the fundamental frequency of the bulkhead did not increase by a large amount.

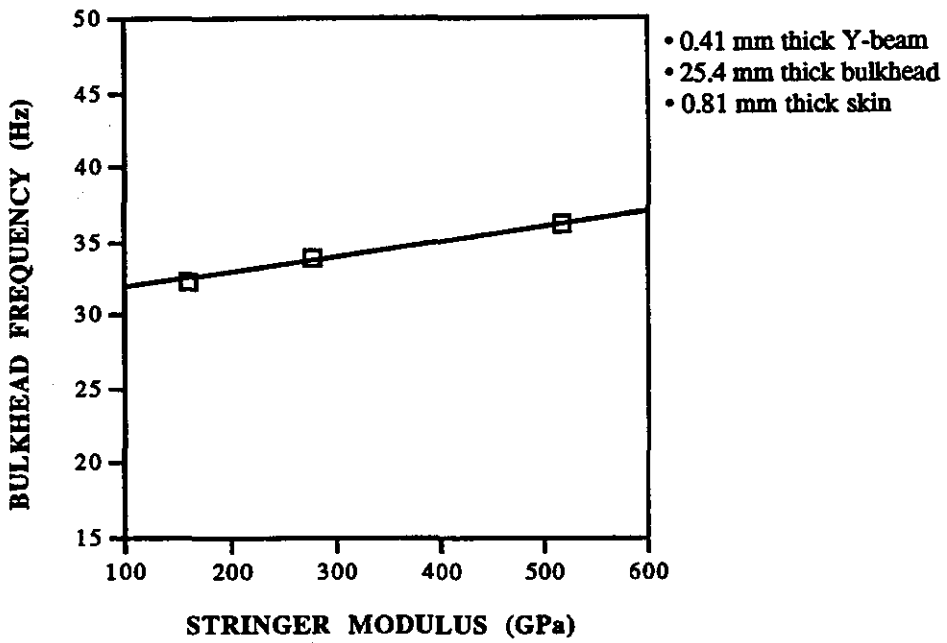

Figure 4.2.5-C: Variation of bulkhead frequency with stringer modulus

The Y-stringers with the 6.35 mm thick webs were abandoned in favor of the 3.18 mm versions due to the marginal gains and the higher radiation length. The 517 GPa modulus of elasticity version was abandoned due to manufacturing difficulties, high cost, and durability problems. The 276 GPa version was picked because it is the highest value that can be easily attained (i.e. no manufacturing or cost problems) and it demonstrated satisfactory stiffness.

The forward region of the structure has every other facet of the polygon open. This is helpful for cabling and cooling line routing and access, but reduces the stiffness of the structure. In an effort to stiffen the structure transverse stringers were added between the bulkhead and the outer most end (on each end). Results of the analysis, however, showed that only one hertz was gained by doing this.

Increasing the skin thickness of the bulkhead had the greatest effect on the iterations performed so far as can be seen in Figure 4.2.5-D (below).

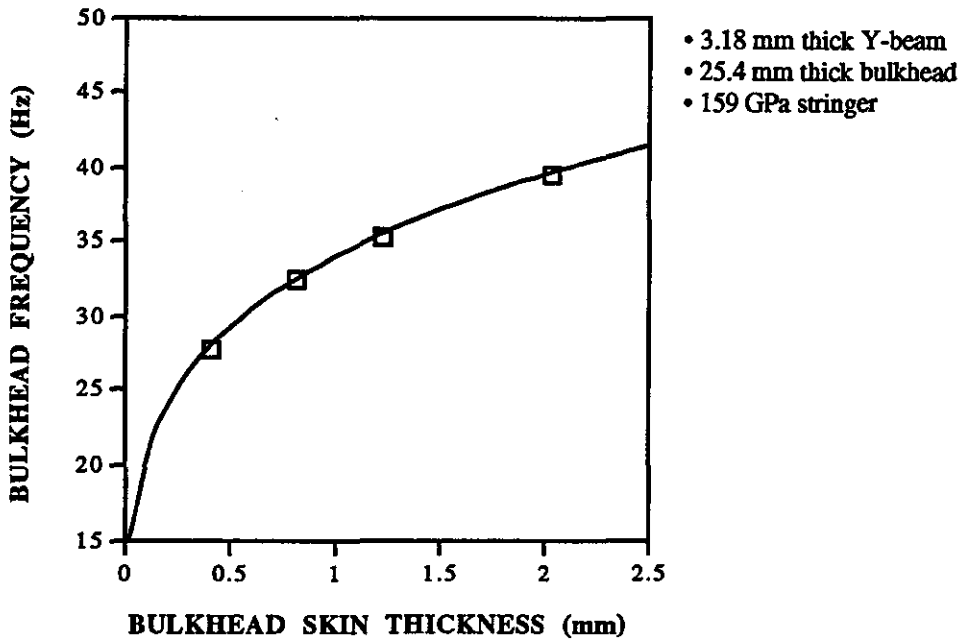

Figure 4.2.5-D: Variation of bulkhead frequency with bulkhead skin thickness

Figure 4.2.5-E (below) shows the effect increasing the shear panel thickness has on the bulkhead's fundamental frequency. The shear panel of 2.03 mm thickness demonstrated the best frequency value, but it was decided that continuing to higher thicknesses would lead to problems with high radiation lengths.

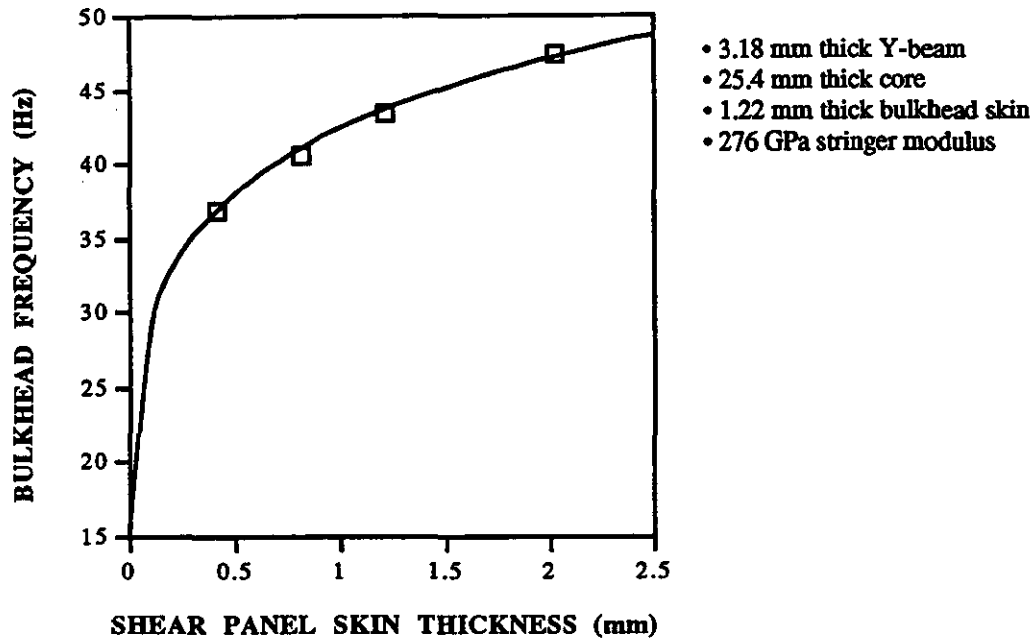

Figure 4.2.5-E: Variation of bulkhead frequency with shear panel thickness

Having analyzed all of the components where thicknesses could be increased to increase stiffness, other avenues had to be explored. Increasing the length of the small fixed shear panels that run in conjunction with the removable panels (reference the picture of the structure) so that they would extend past the bulkheads into the forward region is something that could stiffen the junction between the two. The model was therefore modified so that these panels extended past the bulkhead into the forward region by approximately 180 mm. This resulted in an increase in the fundamental frequency of the structure of 10%.

With the bulkhead core thickness at 25.4 mm, the best stiffness results were obtained when the skin was thickest. In the interest of decreasing the radiation length problem, the core (honeycomb) was increased to 50.8 mm. This would allow the skin thickness to be decreased and still produce a good overall stiffness for the bulkhead. Dropping the skin thickness down to 1.22 mm produced a higher frequency than the 25.4 mm core thickness / 2.03 mm skin thickness combination while favorably reducing the radiation length.

As a result of the analysis that has been performed, at this juncture the following configuration is recommended for the STS/IPC Outer Support Structure:

- Y-stringer web thickness of 3.18 mm
- Y-stringer modulus of elasticity of 276 GPa
- Bulkheads that have a 50.8 mm core and 1.22 mm thick skins
- Shear panel skin thickness of 1.22 mm
- The short shear panels extend into the forward region by at least 180 mm

There are still several more items that need to be developed or explored in the analysis of this structure before it can be brought to closure. These include adding the openings where the IPC Modules are inserted, looking closer at the critical junctions (like the bulkhead and the shear panels) in relation to realistic fabrication methods, and optimization analysis on how far the short shear panels should extend into the forward region from the bulkhead.

4.2.6. IPC Detector Gas System

Background and Requirements

The IPC ionization gas system has been designed to be reliable and cost effective and to meet demanding performance requirements. The requirements include providing remote control and monitoring of an equimolar mixture of CF_4 and $C0_2$ with 1/4 gas change per minute in the IPC's. The required flow rate is about 80 l/min through 4 mm ionization spaces and 1 mm gas windows (on the top and bottom of each IPC); the flow is contained by 0.15 mm thick mylar films. Less than 5 Torr pressure difference from atmospheric pressure across a mylar window is desired to preclude bursting the windows. Since detector operation is somewhat sensitive to absolute pressure, constant pressure will be regulated in the IPC'S. Gas flow will be measured and gas composition will be monitored to 1% accuracy for the major constituents and to several ppm for trace contaminants. The ionization gas system will include a gas scrubbing sub-system that will filter out water vapor, 0_2 , and total hydrocarbons to low ppm levels. The contamination levels will be continuously measured using gas analyzers. Radiation lengths for the system will be minimized by selection of low Z materials where possible. The system will account for luminosity induced heating of the ionization gas.

Because of the relatively large gas flow rate and the high cost of CF_4 , a recirculating gas system has been selected. As shown in Figure 4.2.6-1 the full up system consists of supply cylinders of high-purity CF_4 and $C0_2$ and a mixing pressure tank where the source gases will be mixed by partial pressures prior to charging the system. The driving potential for the flow will be provided by sealed metal bellows pumps, which will impart a one atmosphere pressure rise. The flow will be metered, controlled, scrubbed, and analyzed prior to distributing it to the IPC's. Flow distribution will take place from a manifold located in the annular space between the end

cap and barrel calorimeters via 1.59 mm stainless steel capillary tubes. These capillaries are designed to return the pressure to atmospheric over a length of about 2 m, which is sufficient to reach the IPC inlet connections from the manifolds. The large equal impedance of each of the inlet capillaries will equalize the flow of 1.2 l/min to each of the IPC's in the barrel region. The gas flow will be cooled by a liquid-gas heat exchanger to take out adiabatic compression heating because of pumping, as well as ionization heating of the gas in the IPC's. Most of the IPC ionization gas system hardware will be located at surface level in the gas mixing building and , therefore, will be easily maintained.

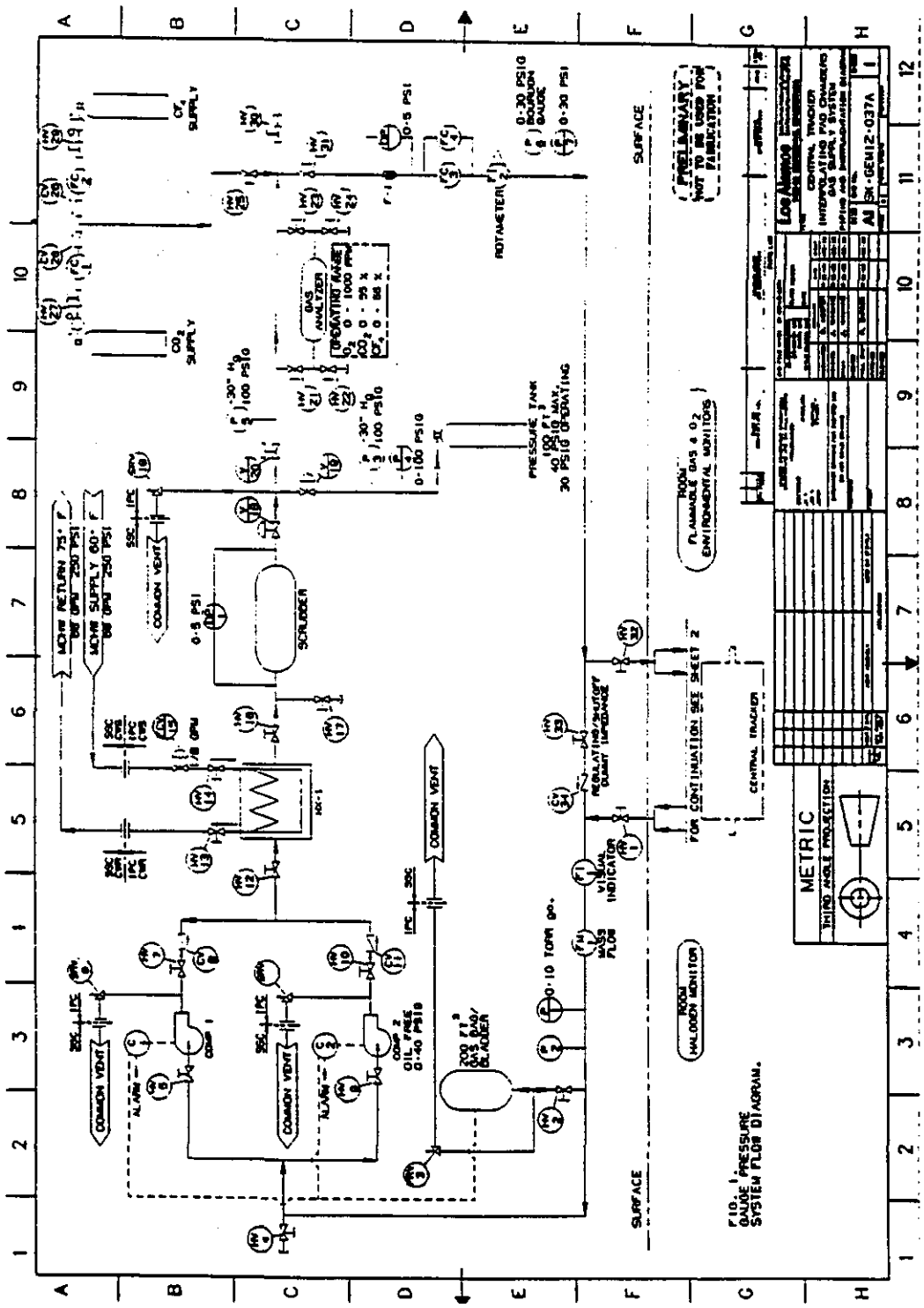
SURFACE
ROTAMETER
PRESSURE TANK
SCRUBBER
COMMON VENT
SURFACE
METRIC
THIRD ANGLE PROJECTION
FIG. 1
GAUGE PRESSURE
SYSTEM FLOW DIAGRAM.

Figure 4.2.6-1

Wire Chamber Aging

A number of lifetime limiting problems associated with the operation of wire chambers have been observed and are summarized in detail in Ref. 1. Such problems include loss of gain, reduction of plateau, loss of energy resolution, excessive currents, self-sustained current discharge, sparking, and others. Symptoms of wire aging usually include depositions of organic material as solid dendrite growths or thin films, or as liquid oily or grease-like matter on the anode or cathode wires. This process is referred to as "polymerization." It is believed that the source of hydrocarbon contamination material in the ionization gas can be breakdown of wire chamber materials in the radiation field or outgassing because of improper assembly or cleaning procedures. Not all wire chambers have exhibited such deleterious problems even after operation in relatively high radiation levels. However, some chambers have aged very rapidly. Ref. 1 (Kadyk, op. cit.) presents an overview of the parameters that can affect wire chamber aging and provides tabulations of good and bad materials for wire chamber construction as well as good and bad gas system materials and procedures. Previous experience with wire chamber aging has been incorporated in the design and fabrication of the IPC gas system prototype.

IPC Gas System Prototype

To insure fulfillment of SSC requirements, a prototype IPC gas system is being developed at Los Alamos. The original objectives of the prototype experiments at Los Alamos are to demonstrate recirculating flow with equal flow distribution in each IPC at atmospheric pressure, to gain familiarization with gas system equipment, to investigate the effectiveness of gas contamination control with a gas scrubbing system and monitoring, and to demonstrate gas mixing, system start-up, flow control, and pressure regulation.

A second set of objectives is also being pursued. Because the SSCL is planning to test three prototype IPC's in the Alternating Gradient Synchrotron beam facility at Brookhaven (BNL) during July 1993, Los Alamos is designing and fabricating the prototype gas system to be modular so that it can be shipped to BNL on portable panels and standard racks in time for the July tests. The IPC beam tests allow check-out of the recirculating gas system under realistic, albeit much lower beam strength, operating conditions. The BNL tests will provide data on contamination and allow assessment of the effectiveness of gas scrubbing components.

A. Flow Model and Components. The IPC gas system prototype flow model schematic diagram is shown in Figure 4.2.6.-2. From left to right there are three modular panels: pumping and mixing, gas supply, and gas scrubbing. Not shown to the extreme right in the diagram are two standard racks, one with the on-line gas analyzers and one with the computer data acquisition and control system. This system was designed to provide 3.6 l/min of recirculating gas flow to three IPC's and is being treated as an ultra-clean system. Starting in the lower left hand corner of the diagram, a Parker Metal Bellows Corp. MB 118 sealed metal bellows pump

delivers the gas flow with a pressure rise of 15 psi. Thus, the gas enters the pump at atmospheric conditions and exits at about 30 psia. The gas is pumped under laminar flow conditions through 3/8-in.-O.D., stainless steel, tubing and fittings with minimal pressure drop (10.8 Pa/m); all shut-off and metering valves are of the metal bellows type.

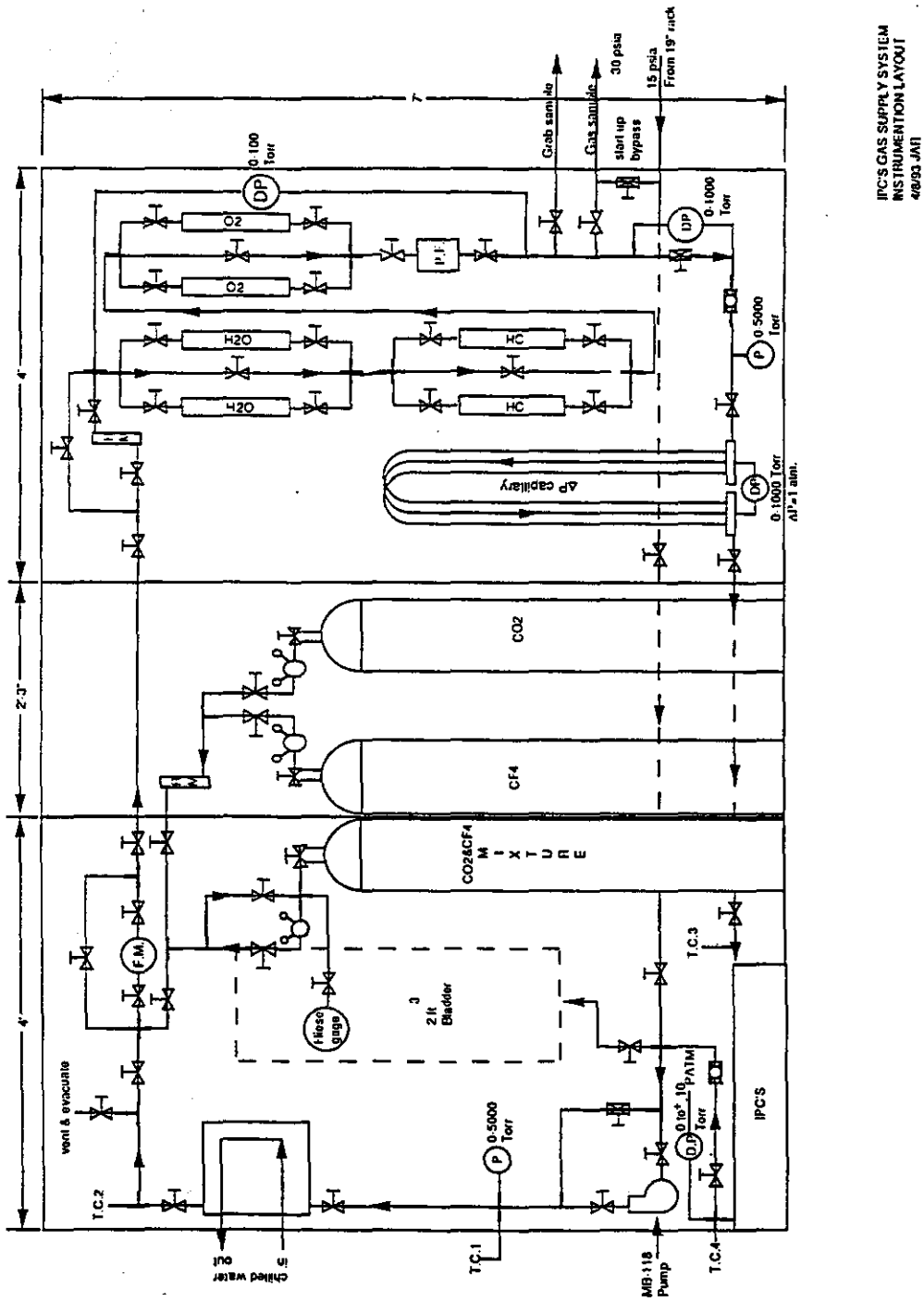

Figure 4..2.8-2

After pumping the gas is cooled by a simple constant surface temperature heat exchanger to remove the heat of adiabatic compression added by the pump, as well as any heating that may occur in the IPC's. Prior to the gas mass flow meter are the source gas and mixing stations. The source gases (CF_4 and $C0_2$) are of semiconductor industry grade purity with all contaminants certified to be in the few parts-per-million (ppm) range. As the gas enters the right-most gas scrubbing panel, it passes through a rotameter for visual flow confirmation and then enters a sequence of four flow filtration devices: moisture removal by molecular sieve, hydrocarbon removal by activated charcoal, oxygen removal by a copper-based getter, and finally particulate filtration.

In the lower right-hand corner of the diagram a "grab sample" port is shown. The purpose of this port is to allow sampling of the ionization gas at various times during operation for quadrupole mass spectrum analysis (both at Los Alamos and at BNL). Such analysis will be done to monitor the accumulation of hydrocarbons in the flow. Next in line is the "gas sample" and "start-up bypass" port. Dedicated analyzers will be used for on-line monitoring of moisture, oxygen, and carbon dioxide concentration. Moisture and oxygen contamination will be monitored in the ppm range while carbon dioxide will be measured for control at 50% within 1%.

During start-up the bypass metering valve will be wide-open while the main metering valve, which leads to the capillary tube manifold, will be fully closed until the pump start-up transient has passed. Gas flow will then be diverted from the bypass leg to the capillary leg by differentially closing (opening) the two metering valves. The line pressure is expected to be about 28 psia after the main metering valve (ahead of the capillaries). The 1/16-in.-O.D., 0.014-in.-wall-thickness, 2-m-long capillary tubes are specially designed to drop the pressure by frictional effects from 28 psia to atmospheric pressure prior to insertion in the IPC's. Thus, the capillaries serve a three-fold purpose: (1) drop pressure to atmospheric, (2) provide high flow impedance so as to equally distribute the flow, and (3) provide a flow distribution mechanism in tight quarters in the IPC tracker.

Finally, a relatively large (2 ft^3 = 56.6 l) flexible ballast volume is used to maintain atmospheric pressure downstream of the capillaries and ahead of the pump.

A 14.4 l stainless steel tank is used to simulate the capacitance of the three IPC volumes for testing at Los Alamos. This tank and the capillary manifold will be replaced during the BNL tests.

B. <u>Supporting IPC Gas System Calculations.</u> Table 4.2.6-1 presents a summary of key prototype system parameters calculated for three IPC'S and an equimolar mixture of CF_4 and $C0_2$.

Table 4.2.6-1: IPC Gas Prototype System Parameters

1. Mixture Properties
   a. M = 66 kg/kgmole
   b. R = 0.126 J/gK
   c. c_p = 0.759 J/gK
   d. k = 1.20
   e. m = 16.0 E-6 Pa.s
   f. r = 2.68 kg/m^3
2. IPC Volume Flow Rate and Re
   a. Assume 2 layers, 3 IPC's, 0.6 cm flow passage, 200 cm long, 20 cm wide
   b. V_3 = 14.4 l
   c. Q_3 = 3.6 l/min = 0.127 ft^3/min
   d. Re = 34 (<1400 => very laminar)
3. Cost of CF_4 plus CO_2 for BNL tests if discard: $10 k
4. Supply Tubing
   a. Select 3/8 in. OD, with 0.035 in. wall
   b. For Q = 3.6 l/min, v = 1.27 m/s, Re = 1649 (<2300 lam.)
   c. Dp/L = 10.8 Pa/m = 0.0016 psi/m
5. Capillary Tubing
   a. For 0.0625 in. OD SS tubing with 0.014 in. wall
   b. Dp/L = 9.17 psi/m (will vary L to vary Dp)
6. At Q = 3.6 l/min the MB 118 pump delivers Dp = 21 psig

C. Instrumentation, Data Acquisition, and Control. The IPC gas system prototype instrumentation package includes pressure, temperature, and flow sensors located as shown in Figure 4.2.6-2 to diagnose system performance and to control the system. Absolute pressures are measured on the high-pressure side of the pump and ahead of the capillary tubes. Differential pressures are measured across the scrubbing system, across the main metering valve, across the capillaries, and between the IPC's and atmospheric (for control of isolating solenoid valves). All of these pressure transducers are MKS Baratrons. A Heise bourdon gage measures the pressure in the mixture tank, and another Heise gage measures atmospheric pressure. Temperature measurements are made across the pump, across the cooler, and across the IPC's using compensated Type-K thermocouples. The gas mass flow rate is measured using a Teledyne Hastings-Raydist Model NALL mass flowmeter. Gas contamination is monitored on line using a Teledyne Model 316 oxygen detector and a Teledyne Model ZT-2 moisture detector. Gas composition is monitored to 1% on line using a Teledyne Model 235 $C0_2$ gas analyzer.

The data acquisition system consists of an Apple Quadra 950 computer running LabView software by National Instruments. The Quadra 950 controller communicates via GPIB with a Hewlett-Packard HP3852A data acquisition and control unit with scanner cards for voltage and temperature measurement. The differential pressure between the IPC's and atmospheric will be constantly monitored by the computer to lie between +10 Torr and -10 Torr; otherwise, the computer will close two solenoid valves and turn off the pump.

D. Cleaning and Assembly. All parts that come in contact with the ionization gas are cleaned using a four-liquid process: (1) acetone (to cut lubricants or oils), (2) Micro Liquid Laboratory Cleaner by International Products Corp., Burlington, NJ (low residue detergent), (3) de-mineralized water (to rinse), and (4) alcohol (methanol). Small parts are cleaned using these same four liquids, but with the acetone and Micro steps done in an ultrasonic agitator bath. Assembly after cleaning will be done using rubber gloves.

Schedule and Status

Table 4.2.6-2 summarizes the IPC gas system tasks and schedule.

Table 4.2.6-2: IPC Gas System Tasks and Schedule

1. Obtain CF_4 and CO_2 for developmental tests at Los Alamos.
2. Prepare test facility in Rm. 27, Bldg. 1, TA-46, Los Alamos.
3. Obtain sealed metal-bellows pumps suitable for 3 IPC's.
4. Obtain gas mass flowmeter.
5. Obtain gas bag bladder.
6. Obtain scrubbing system components.
7. Obtain capillary tubing.
8. Obtain other miscellaneous system components such as particulate filters, tubing, va etc.

(Items 1.--8. were accomplished by end of April 1993)

9. Obtain and check out gas monitoring equipment. (By May 14, 1993)
10. Plumb three panels. (By May 10, 1993)
11. Complete IPC tank and capillary manifolds and complete hookups. (By May 14, 1993)
11. Set up a data acquisition and control system using LabView and existing Apple Quadra 950 (By May 14, 1993)
12. Begin flowing gas and taking data at LANL. (May 14, 1993)
13. Prepare gas system for shipment to BNL. (June 15, 1993)
14. Ship to BNL. (June 18, 1993)
15. Familiarize BNL staff with the system and help set it up for the experiment. (End of June 1993)
16. Perform gas system check-out as needed and initial measurements. Obtain gas system data. (July 7, 1993)

4.2.7 IPC Detector Electronics Cooling System

Background and Requirements

The IPC detector electronics cooling system for GEM has been designed to fulfill IPC requirements of 48 kW total electronics heat generation, dimensional and positional stability in the range 25 μm to 100 μm, low vibration, low risk of water leakage, and low radiation length.

The baseline cooling concept selected is a "leakless" chilled water cooling system. Future studies must consider the force and vibration levels associated with the water flow, corrosion in the aluminum cooling channels, modeling of heat transfer from the multichip modules and other powered components, and the design, operation and control of the leakless system. The IPC electronics cooling system will be prototyped to confirm its performance.

Baseline IPC Electronics Water Cooling System Design

As shown in Figure 4.2.7-1 , the IPC electronics water cooling system consists of two unconnected loops, one containing high-purity de-mineralized water for cooling the electronics, and one containing house mixed chilled water. Considering the electronics cooling loop that runs through the Central Tracker first, it will be a leakless cooling system consisting of redundant vacuum pumps to pull de-mineralized water up into the system and into a level controlled reservoir to a vacuum pressure of from 400 mbar to 600 mbar (which corresponds to working liquid heights of from 6 m to 4 m, respectively). Thus, if any leaks occur, they will only admit $C0_2$ and not release water, as long as the vacuum pumps are functioning. Redundant hydraulic drive water pumps will be used to circulate water in the electronics cooling loop. The total inventory of recirculating de-mineralized water in the IPC tracker will be about 20 l. The vacuum pumps at the top of the loop, which pull a vacuum over the water reservoir, and the water reservoir at the bottom of the loop are not shown in Figure 4.2.7-1 . [Same Figure as above.] Considering the house-water loop to the right in Figure 4.2.7-1 , [Same Fig. as above.] it will direct house water through a 50 kW-plus refrigeration unit. The house water loop flow will pass through a heat exchanger coupled to the electronics cooling loop, which will serve to remove the IPC heat load.

Most of the IPC electronics cooling system will be located in the mechanical room planned for the GEM utilities shaft. Total water flow to the IPC tracker will be on the order of 138 l/min, but the flow in the individual IPC cooling passages will be laminar with a temperature rise of about 5 °C.

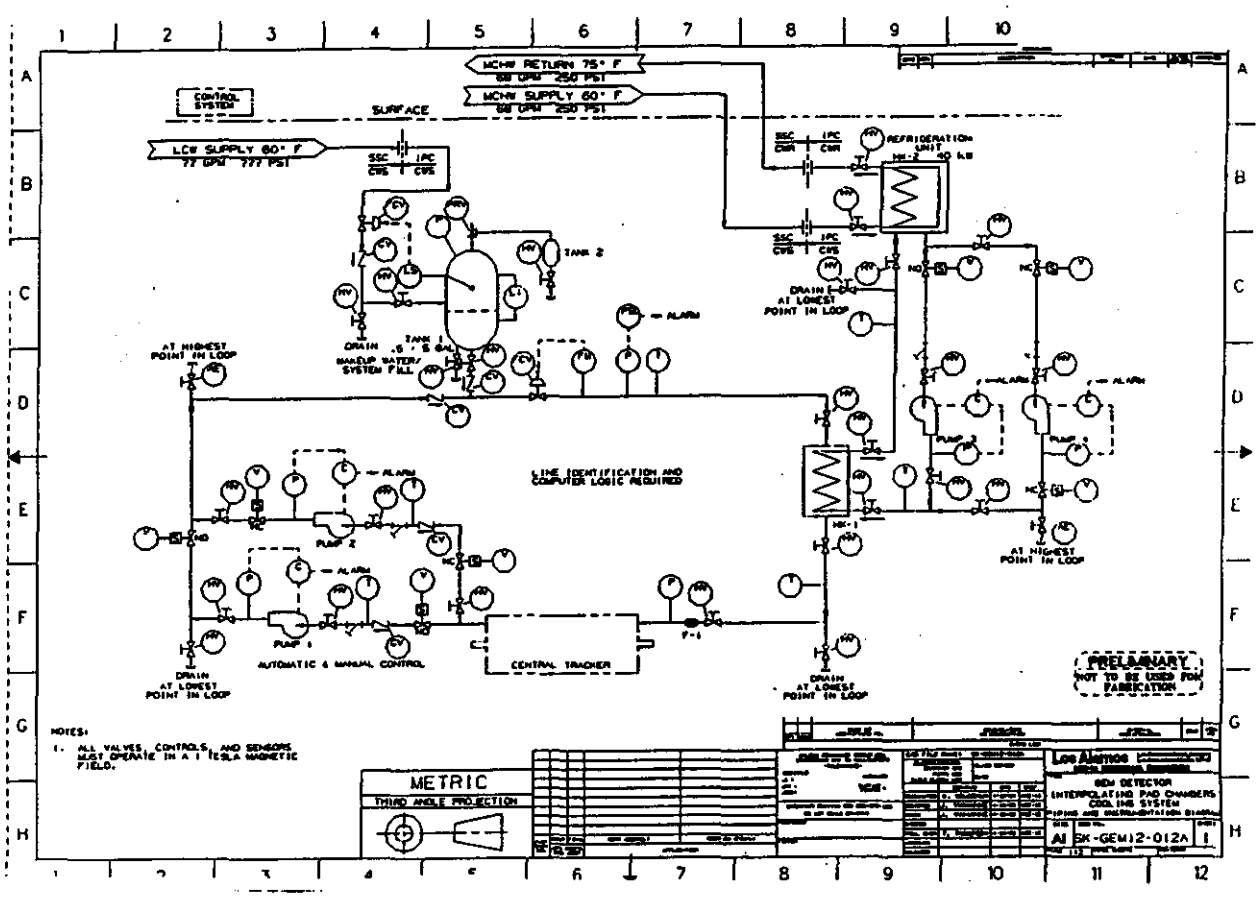

Figure 4.2.7-1

Leakless Water Cooling System Concept

In a conventional pumped cooling loop open to atmospheric pressure, p_a, at the highest point h = 0, the pressure in the cooling liquid at any point a distance h below the highest point is equal to p_a plus the pressure (ρgh) caused by the weight of a column of fluid of height, h (see top Figure 4.2.7-2). Since the pressure inside the system at any point is higher than p_a, the fluid will leak outward, given the opportunity. However, in a "leakless" water cooling system connected to a vacuum pump via a partially filled reservoir at the top, and a reservoir open to atmospheric pressure at the bottom, the pressure p at any point a distance h above the level of water in the bottom reservoir is equal to p_a minus the pressure caused by the weight of a colum of fluid of height h (see bottom Figure 4.2.7-2). Or,

$$p = p_a - \rho gh$$

Since the pressure inside the system at any point is lower than p_a, a surrounding gas will leak inward given the opportunity.

PRINCIPLE OF THE LEAKLESS SYSTEM

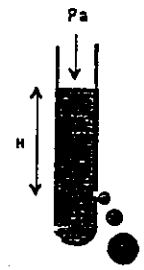

In classical systems, the pressure in the cooling liquid is equal to the atmospheric pressure PLUS the weight of the column of the liquid (H).
That is why the liquid gets out of the system in the case of the leak.

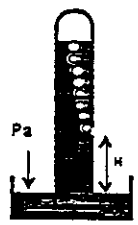

In the LEAKLESS system the pressure in the cooling liquid is equal to the atmospheric pressure MINUS the weight of the column of the liquid (H). Therefore, the air enters the system in the case of a leak and prevents the liquid to get out of the system.

Figure 4.2.7-2

For an assumed vacuum pressure of 400 mbar, it can be shown that for water the corresponding usable pressure differential is 600 mbar (8.8 psi) in terms of pressure, or 6 m in terms of h (pressure head). Thus, each 100 mbar of pressure differential available from the vacuum pump corresponds to about 1 m of working pressure head. Since the IPC tracker has an outer diameter of about 1.8 m, a leakless system may be feasible. However, further calculations are necessary to estimate the pressure losses because of flow with friction and other (minor) losses in the IPC cooling distribution system.

To start a leakless water system, the cooling water reservoir at the bottom of the system is filled with sufficient water to fill the entire cooling circuit. This bottom reservoir is vented to atmospheric pressure. The vacuum pump attached to the upper reservoir is then started to suck water up into the distribution lines. When the water level in the upper reservoir reaches a control level, the vacuum pump is turned off and the circulation pump is turned on. The vacuum pump is cycled on to maintain the control water level in the upper reservoir.

Supporting Calculations

Table 4.2.7-1 presents a summary of preliminary calculations to confirm the feasibility of the IPC electronics cooling system.

Table 4.2.7-1: IPC Electronics Cooling System Summary Calculations

- o Use a "leakless" system.
- o Use single pass flow geometry of 44.0 mm by 2 mm by 2 m aluminum channels with
- o After traversing the first IPC cooling channel, the water is routed to the second IPC of
- o Electronics heat load: Q = 300 W per IPC in barrel region and the same is assumed for
- o For an individual IPC:

  Power density = 0.17 W/cm^2
  G = 0.861 lpm
  v = .163 m/s
  Dh = .383 cm
  Re = 620 (< 1400 => laminar)
  xfd,h = 11.9 cm
  xfd,t = 83.3 cm
  Nu = 5.0 (assumed) => h = 779 W/m^2K
- o Apply Newton's law of cooling: Q = hA(Ts-Too) =hAΔT

  A = 1760 cm^2
  Calc: ΔT = (Ts-Too) = 2.19 °C

From the results of preliminary calculations summarized in Table 4.2.7-1, it can be concluded that the IPC electronics can be cooled with laminar flow of water in the cooling channels. The expected bulk water temperature rise from end to end in the cooling channel is 5 °C and the difference between the channel wall surface temperature and the bulk water temperature is about 2 °C.

IPC Electronics System Prototype

Preliminary plans to prototype a leakless IPC electronics cooling system are being developed. Such a prototype will be designed to simulate full size geometry for a leakless system demonstration. The flow loop will include all of the major cooling components including an IPC doublet flow passage with simulated electronics heating, a liquid-liquid heat exchanger to remove the input electronics heat, a circulating pump, a lower reservoir vented to atmospheric pressure, an upper reservoir with water level control connected to a vacuum pump, as well as instrumentation for loop pressures, temperatures, water flow rate, and IPC electronics power input. In particular, the temperature differences across the IPC heaters and across the heat exchanger will be monitored. The data acquisition system will consist of an Apple Quadra 950 running LabView by National Instruments interfaced via GPIB to a Hewlett-Packard HP3852A data acquisition and control unit.

Such a prototype IPC electronics cooling system will allow confirmation of full-scale performance in terms of flow distribution, pressure drops , and heat transfer. In addition, it will allow evaluation of the effect of vertical position of the IPC doublet in the loop. Since the sub-atmospheric pressure varies in the circuit according to vertical location, and since with local heating the local conditions can be close to the boiling point of water for this pressure, it is important to rule out the possibility of vapor locking of the water flow passages. The prototype

will utilize and evaluate actual materials and connectors planned for use on the SSC. Ultimately, actual IPC electronics could be installed on an actual IPC panel and evaluated in the test facility.

Schedule and Status

Preliminary design and calculations indicate that a leakless water cooling system for the GEM IPC electronics cooling package is feasible. Additional calculations are needed to evaluate the distribution system pressure losses, forces, and vibration associated with the water flow. Additional design work is needed to evaluate details of the IPC cooling passages, to determine equipment locations in the mechanical room and in the hall, and to evaluate the effects of corrosion in the aluminum cooling channels. Additional modeling is needed to understand the material temperature distributions and heat flow from the multichip modules and other powered components. In order to stay within the 6 m total heat restriction for a leakless system, it is expected that hydraulic pumps will be required in the hall for circulation of water in the IPC cooling system. Such pumps would be driven by conventional pumps located remotely, and shielded from magnetic field effects. Prototype IPC water cooling system design will commence in Summer 1993.

Heat Transfer Analysis

This section summarizes the finite element heat transfer analysis completed on the water cooling channel used to cool the IPC electronics module. The purpose of this analysis has been to predict temperature conditions in the module with the application of a steady-state heat load from the heat-producing IPC electronics.

The purpose for a cooling channel in the IPC electronics module is to ensure that the maximum temperatures experienced by the electronics will be within operating specifications. There is also a possibility that high temperatures in the module could produce undesired thermal expansion of the supporting structure. This could result in a multitude of problems, including changes in alignment. Finite element analysis in this case can provide a good indicator of any possible weaknesses in the cooling design and aid in predicting maximum temperatures reached in the module.

The finite element analysis was initiated with geometry based on the IPC electronics module shown in Figure 4.2.7-3. Note that in that design the electronics module is mounted in cantilever-type fashion to the fast-gas module with beryllium pins. The mounting of the electronics module is the primary change in the design shown in Figure 4.2.7-4. Although the fast-gas module is now physically removed from the electronics module, the dimensions critical to the cooling study have remained the same. The original finite element model, therefore, remains accurate. The latest evolution of the electronics module shown in Figure 4.2.7-5, however, changes the size of the cooling channel and the location of a heat-generating device,

the read-out controller. These latest changes have not yet been incorporated into the finite element model.

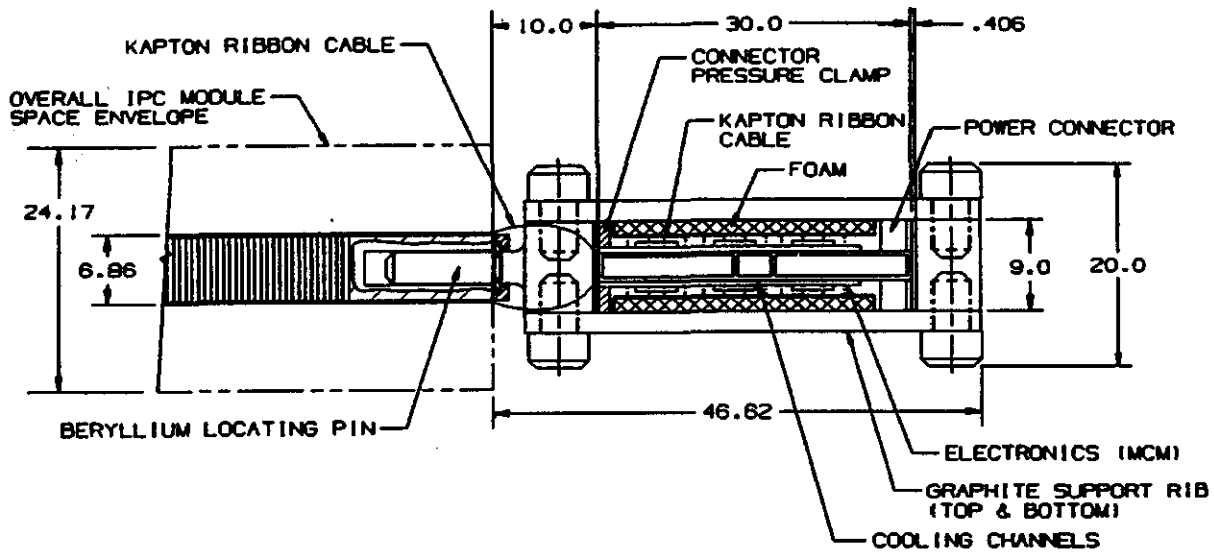

Figure 4.2.7-3: Initial concept of GEM IPC Tracker IPC electronics and fast-gas modules

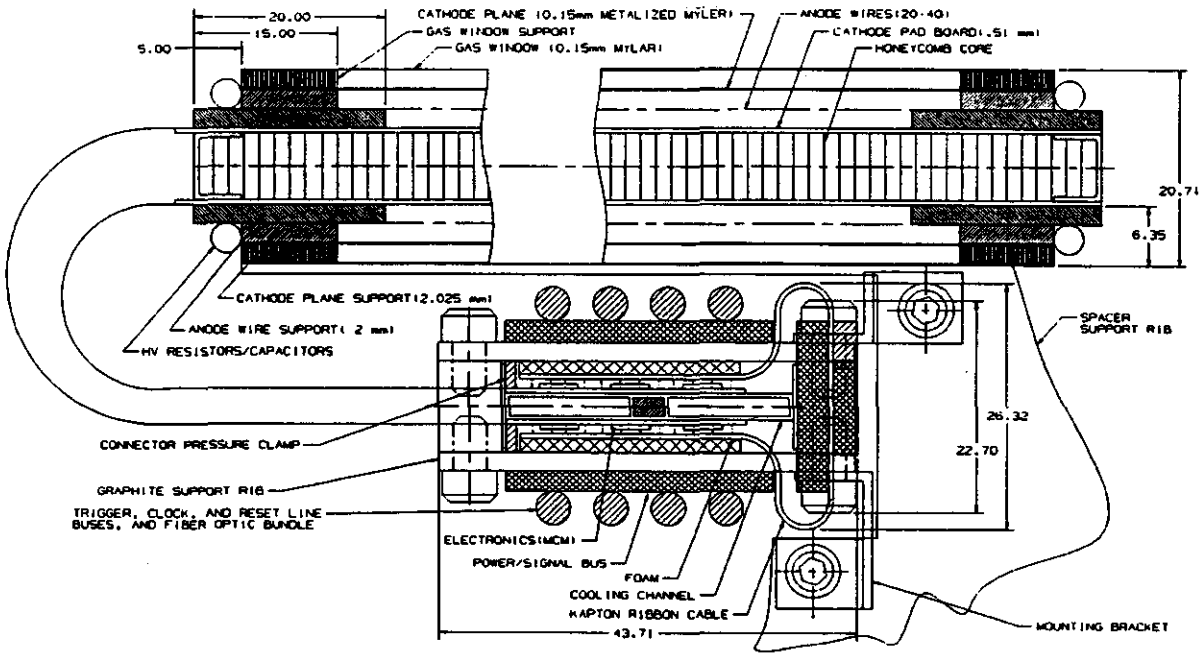

Figure 4.2.7-4: Second generation concept of GEM IPC Tracker IPC electronics and fast-gas modules

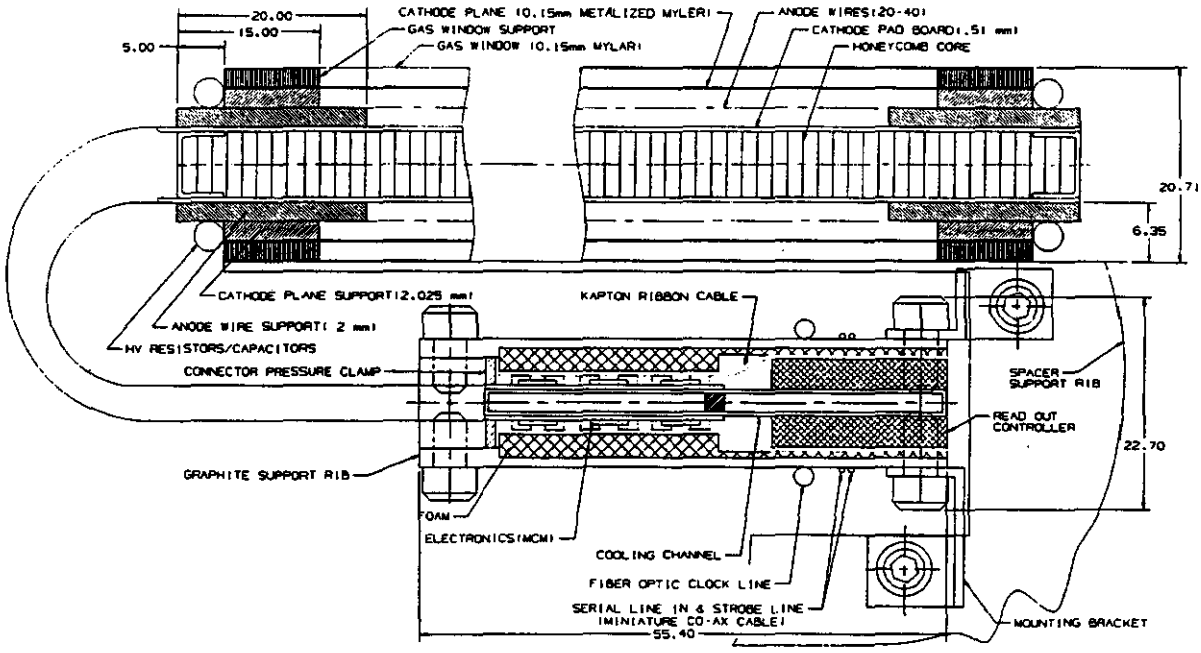

Figure 4.2.7-5: Latest concept of GEM IPC Tracker IPC electronics and fast-gas modules

The previous dimensions of the G/E cooling channel are shown in Figure 4.2.7-6.

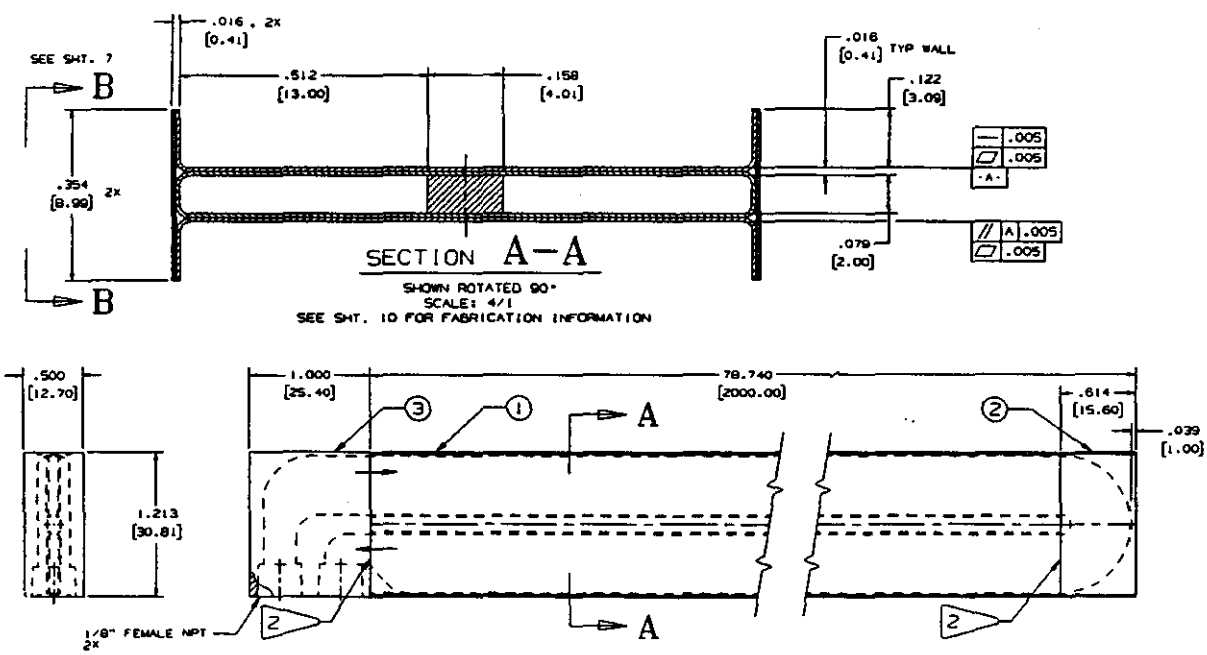

Figure 4.2.7-6: Graphite/epoxy cooling channel

Not all of the heat loads experienced in the IPC electronics module have been included in this analysis. The most significant of these is that from the read-out controller. This device is not included in the analysis due to earlier uncertainties with its mounting to the module and with its heat load. However, preliminary information regarding the device indicates that its low power density makes its inclusion in this particular analysis inconsequential to the final results.

The largest contribution to the heat load comes from the multi-chip modules (MCMs) and this analysis will therefore concentrate on them. The orientation of these modules are shown in Figure 4.2.7-7 and their heat loads are listed in Table 4.2.7-2.

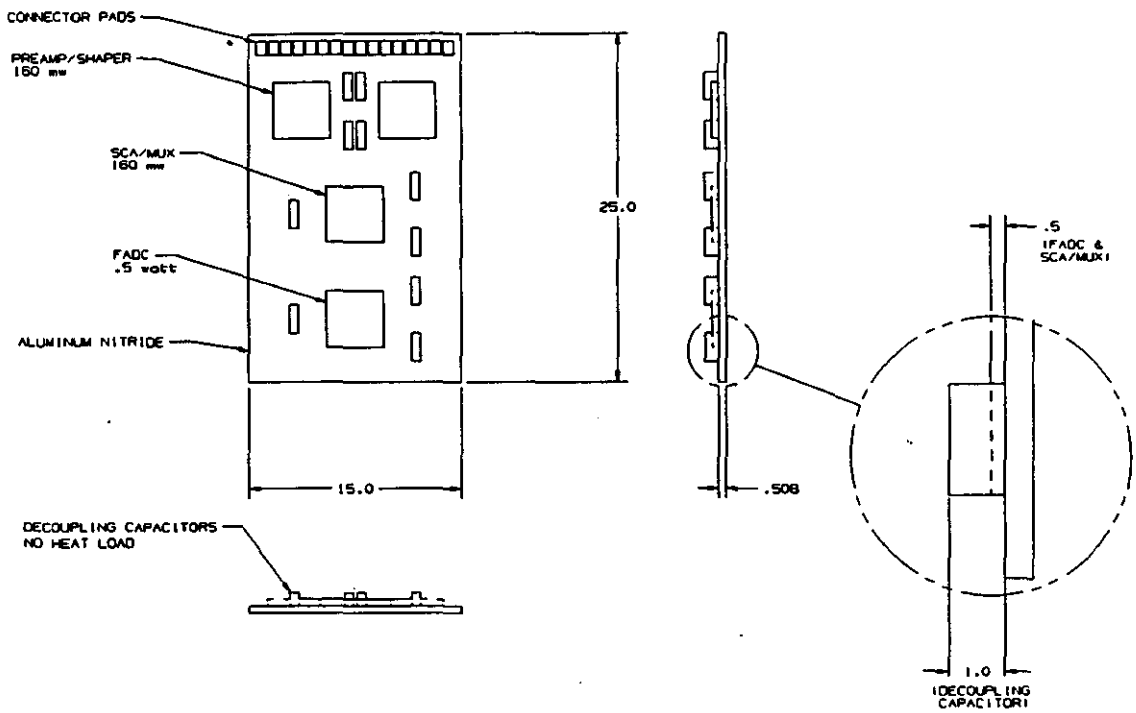

Figure 4.2.7-7: Placement of electronics on multi-chip module

Table 4.2.7-2 - Heat Load per IPC Multi-Chip Module

Name	# of Chips/MCM	Heat Load (W)	Heat Flux (W/m^2)
Preamp/Shaper	2	0.160 each	12,800 for both
SCA/MUX	1	0.160	6,400
FADC	1	0.5	20,000

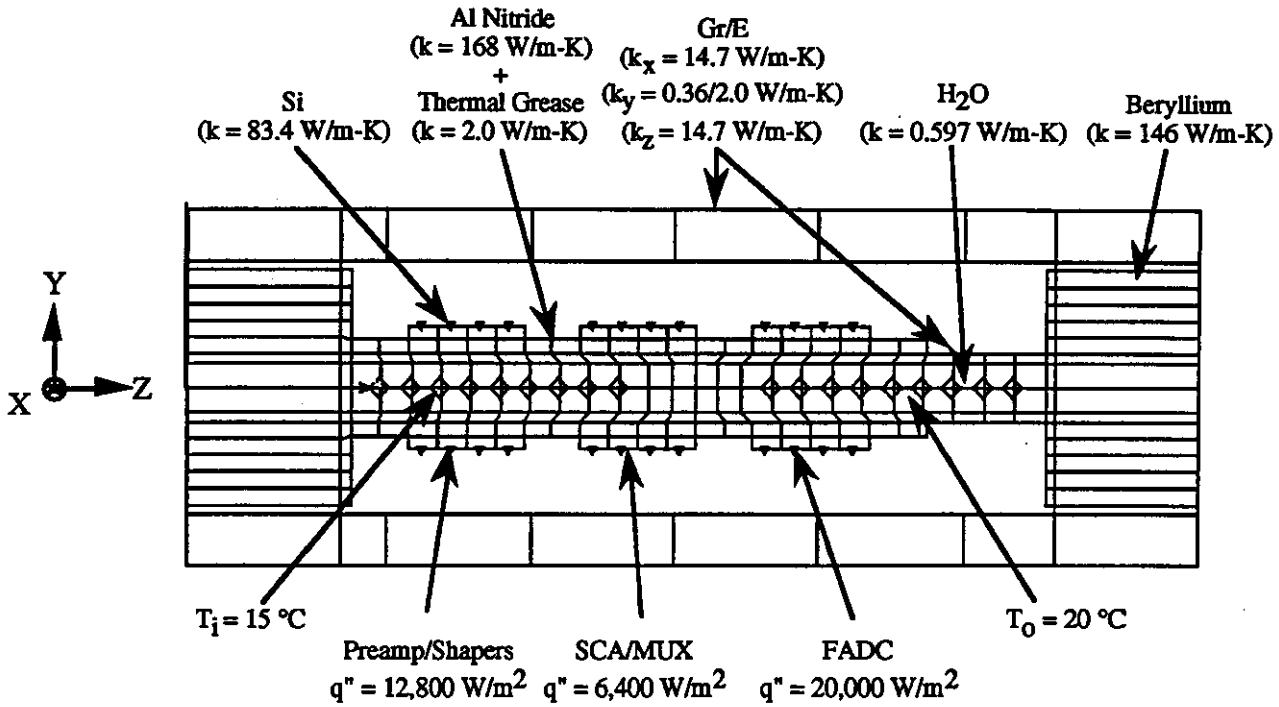

Figure 4.2.7-8: Finite element model showing material, loading, and boundary conditions

As shown in Figure 4.2.7-8, the inside of the cooling channel is modeled as solid conduction elements instead of a hollow channel. Although it is understood that there will be a combination of convective and conductive heat transfer to the coolant, this simplification allows for the prediction of a maximum temperature on the electronics. The heat transfer analysis necessary to most accurately describe the convection is complex and has not been performed yet. This analysis, however, definitely represents the upper boundary of the temperatures that could be seen in the IPC electronics module.

As can also be seen in Figure 4.2.7-8, the MCM chips are modeled using the conductive properties of silicon with a heat flux generated on the outer surface as shown. The diamond symbols in the center of the cooling channels indicate constant temperature nodes (a heat sink). Those nodes on the left are located near the cooling channel entrance to the IPC electronics module, those on the right near the channel exit. The temperature difference between the two sets of nodes (T_o - T_i) simulates the heat rise of the water coolant in its flow through the module.

Convective heat transfer from the IPC electronics module surfaces to the surrounding CO_2 atmosphere has been determined to be negligible under the current cooling conditions.

Figures 4.2.7-9 and 4.2.7-10 show the results of a steady-state thermal analysis on the IPC cooling channel at and between the support locations.

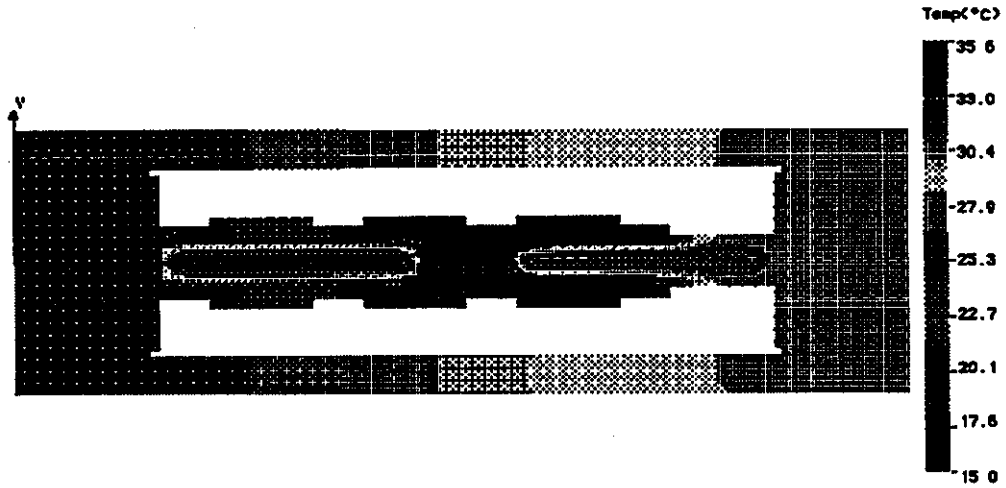

Figure 4.2.7-9: Predicted temperature distribution at the support locations

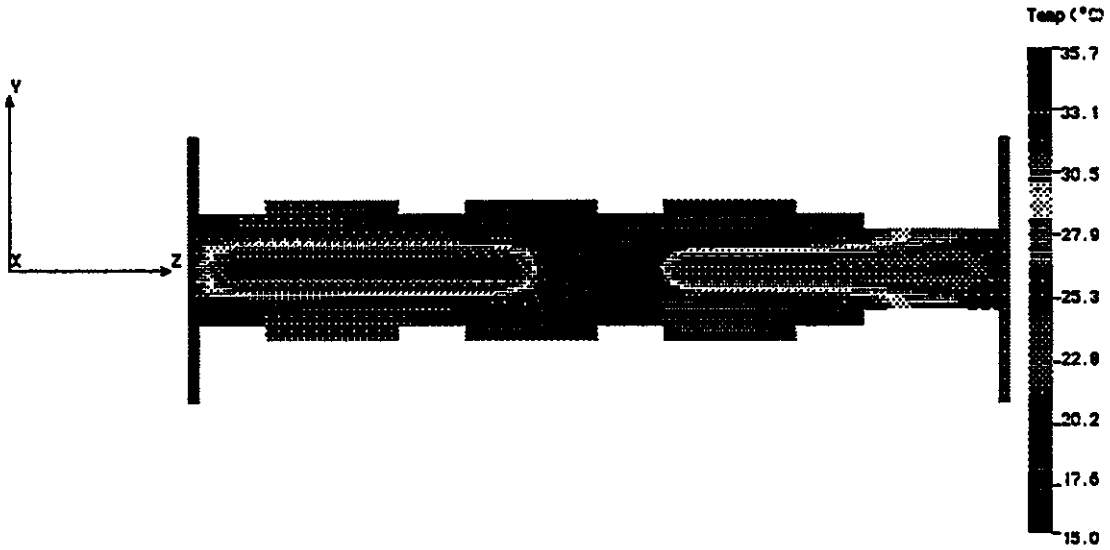

Figure 4.2.7-10: Predicted temperature distribution between the support locations

A comparison of Figures 4.2.7-9 and 4.2.7-10 show that there is little difference between the two models. The maximum temperature of 35.7°C is experienced by the FADC chip.

The analysis performed so far bounds the predicted temperature gradient through the IPC electronics module. A more accurate prediction must be made based on more intensive investigation of the precise heat transfer conditions and, ideally, experimentation. An important electronics package not examined in this analysis has been the read-out controller, a factor that could be significant depending on its proper heat load. It is also important to note that the configuration of the electronics module has changed. The new size of the cooling channel, as

well as the new placement of the read-out controller, will change the results of this analysis. The amount of change is uncertain and further analysis should be performed with a new model.

Results from the analysis performed on IPC electronics module finite elements models predict a maximum temperature of 35.7°C. This upper boundary might be reduced with more precise analysis, but could also increase as new information is obtained on the heat output from various IPC electronics and on the new geometry of the module.

REFERENCES

1. Miller, W.O., Thompson, T.C., Gamble, M.T., "Superconducting Super Collider Silicon Tracking Subsystem Research and Development," LA-12029, Los Alamos National Laboratory, Los Alamos, NM, 1990.

2. Thompson, T.C., Miller, W.O., "Development of Ultrathin, Dimensionally Stable Composites for the Superconducting Super Collider (SSC) Elementary Particle Detectors," Advanced Composites '93, International Conference on Advanced Composites, Wollongong, Australia.

3. Miller, W.O., Gamble, M.T., Thompson, T.C., "Silicon-Based Elementary Particle Tracking System: Materials Science and Mechanical Engineering Design," LA-93-1162 Los Alamos National Laboratory, Los Alamos, NM, 1993.

4. (J. A. Kadyk, Nuclear Instruments and Methods in Physics Research, A300, 1991, pp. 436-479).

4.3 IPC Front End Electronics

The readout electronics for the IPC system must satisfy four basic requirements. The first and most important is that the signal to noise ratio be maintained below 1% throughout the readout chain. It is likely that the position resolution of the IPCs will be determined by the noise inherent in the readout process. The second requirement is that the IPCs be read out time be consistent with a 100 kHz rate to level two. A third consideration which plays a key role in the design of the front end electronics is the requirement that it be rad-hard. Finally, the power requirements of the electronics must be compatable with the use of a low mass cooling system.

The approach followed in the IPC readout, shown schematically in Figure 4.3-1, is somewhat unusual, in that neither a peak sensing circuit nor gated integrator is used to obtain the induced charge values. Instead, after the induced signals are amplified and shaped, with a peaking time of 25 ns, the shaped signals are sampled at the 16 ns spill rate. These samples are stored in analog form in a switched capacitor array until the receipt of a level 1 trigger, at which

time the samples of interest are digitized, zero suppressed, and transmitted of the detector through an LED fiber optic link. For each pad with valid data, 3 to 4 samples are transmitted on each event. These correspond to a presample, which allows the baseline to be subtracted from subsequent samples, and the samples which span the shaped pulse. Because the time development of the signals on the pads with induced charge from the same avalanche is identical (in the absence of channel to channel variations in the readout electronics), each of the samples from a set of adjacent pads can be used to obtain a position measurement.

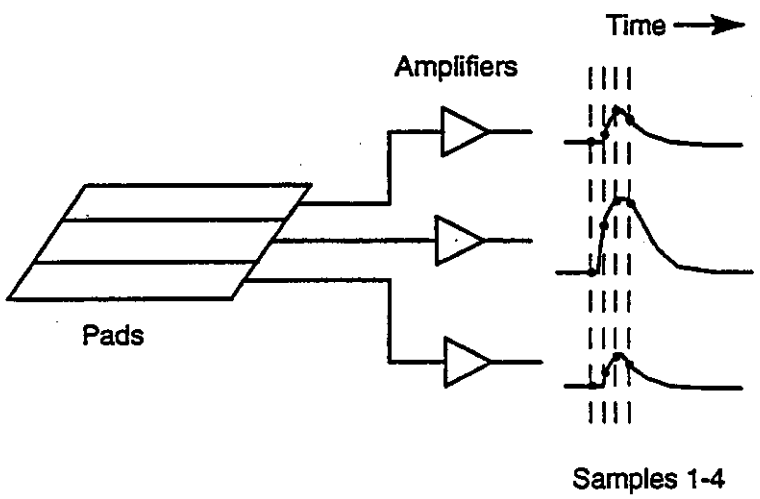

Figure 4.3-1: IPC Readout Approach

Radiation Tolerance

Recent Studies of the radiation environment in the GEM central cavity indicate that the charged particle radiation dose is approximately 0.44 $(10\ cm/r)^2$ MRad/SSC Yr. To allow several years of operation at $10^{34}\ cm^2\ s^{-1}$, IPC electronics at a radius of 40 cm must remain functional to a dose of 2 Mrad. The front end electronics being considered for the GEM outer tracker consists exclusively of CMOS ICs at the present time, although a bipolar preamplifier/shaping amplifier is currently under study. Neutrons are generally not as serious a problem in rad-hard CMOS as ionizing radiation, since CMOS is a majority carrier based process, and therefore not sensitive to bulk damage. Neutron fluences below 10^{15}neutrons cm^{-2}, corresponding to an exposure of 500 SSC years, can be handled without serious degradation in

performance in the CMOS processes under consideration by us. Ionizing radiation in CMOS effects the gate oxide and the field oxide regions. The primary effects are a shift in the threshold voltage of the transistor and channel mobility degradation, due to a buildup of holes at the Si-SO_2 interface. The consequence of the threshold shift is that N-channel devices become easier to turn on, and P-channel devices become harder to turn on. In analog circuitry, threshold shifts result in a change in the biasing of the circuit. In the rad-hardened CMOS processes under investigation by our group, threshold shifts of 0.2 V are typical for a 1 Mrad dose. At the present time, two rad-hard CMOS processes are being studied for possible use in the outer tracker electronics. The UTMC 1.2 micron UTE-R process has been studied by several groups, both in and outside of GEM, for use at the SSC. It is found to be an extremely radiation tolerant process which would be easily capable of handling the radiation doses experienced in the outer tracker. However, it is not, at this time, suitable for use in analog circuitry, due to the absence of a high quality capacitor. We have been working with UTMC to determine whether their process can be augmented to include this capability. A solution which fits within the framework of their existing process has been found, but must be developed and characterized. UTMC has expressed a willingness to pursue this development with our cooperation. For the short term, however, a more attractive process for development of the outer tracker electronics is the Harris AVLSIRA process, which is also radiation tolerant to the required level, and has all the capability needed for the outer tracker electronics, including high quality capacitors. As part of our R/D program, we are vigorously pursuing the development and testing of prototypes in this process, with essentially full scale prototypes of the critical front end components expected to be fabricated starting mid 1993.

IPC Readout Electronics Architecture

The full IPC readout architecture is shown in Figure 4.3-2. The readout electronics consists of five functional blocks. The first is the preamp/shaper, which in the current design would be packaged 8 channels per die. The second is an 16x128 analog memory, which stores the samples during the level 1 trigger latency period, and buffers samples during the readout to level 2. The third element in the readout chain is a 16 to 1 analog multiplexor, which will be included on the same die as the analog memory. The memory/MUX unit is followed by a 15 Mhz FADC, which digitizes the samples to 8 bits, with an effective 9-10 bits of dynamic range obtained through the use of a center tapped reference ladder. The final element in the readout chain is the controller, which services 128 pad channels. It consists of address drivers for the analog memory, a state machine to control the readout sequence, a zero suppression circuit, and a buffered frame builder which appends a beam crossing tag to the zero-suppressed data. These frames are output to the DAQ through a 50Mhz LED/fiber optic link.

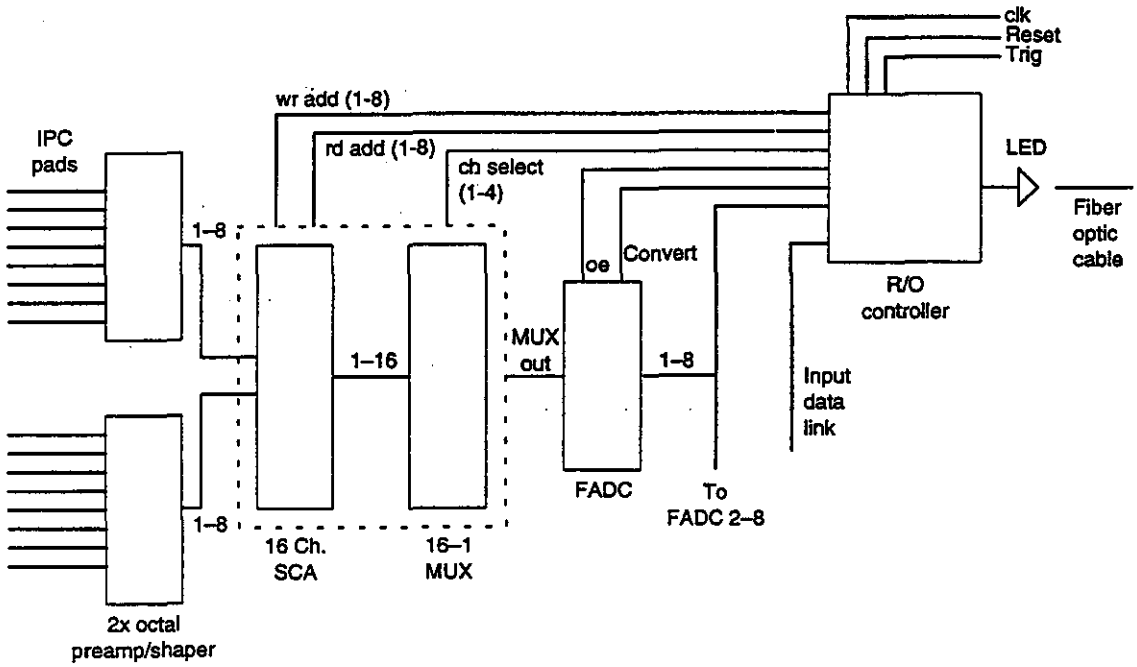

Figure 4.3-2: IPC Readout Architecture

IPC Preamp/Shaper

The IPC preamp and shaping amplifier circuits are based on a design developed by the instrumentation group at BNL. In implimenting this design, the front end preamp/shaper IC is packaged as a separate chip in order to minimize the noise coupling of the digital signals into the analog readout. Two technologies are being considered for the amplifier. Analog CMOS is available from several vendors and offers the advantages of cheap, fast multiproject service for rapid prototyping from several vendors, the availability of BSIM model parameters (the most advanced MOS model for analog design), and the fact that technology is well-integrated into commercial and public-domain CAD packages. In addition, a bipolar transistor is always available for use in the design. Bipolar processes remain a candidate for this device. Many

foundries have recently announced advanced processes optimized for high frequency analog work. The advantages of bipolar are that the devices generally have higher key performance ratios: gm/C, gm/I, gm/area, and bipolar devices are inherently more tolerant to gamma radiation damage.

The baseline preamp design uses an n-channel input device in a folded cascode configuration. The width of the input device must be selected to optimize the signal to noise ratio. First prototypes of this device have an input device of 10,000 micron gate width biased at 5 mA (nominal). At the short peaking times required in this application, the 1/f noise of the MOS transistor does not contribute significantly to the overall noise.

The CR-(RC)^n shaper response can be obtained with a variety of circuit configurations. We have chosen a low-pass stage that has a second-order transfer function. The natural frequency of the filter in this design can be changed by adjusting the bias current at points in the circuit. On the other hand, the Q factor (damping factor) is determined only by ratios of components, ie transistor W/L. Power dissipation is reduced by having two poles per op-amp. A passive differentiator and two stages of this type form a shaper whose peaking time can be controlled (for all channels on a chip) by a single bias without distorting the shape of the resulting pulses. In production, this could be a simple way to trim out the shapers' manufacturing variations.

Table 4.3-1: IPC Preamp/Shaper Characteristics

Peaking Time	25 ns
Input Capacitance	10-40 pf
RMS noise	~ 1000 e's
Power Dissipation	20 mW/ch
Linearity	<1 LSB
Gain	10 V/pC
Dynamic Range	1,000
Full Scale Charge	150 fC
Filter Shape	Unipolar Semi-Gaussian

Figure 4.3-3 shows the noise performance of the MOSIS prototype preamplifier circuit, in which the measured noise is plotted as a function of input capacitance and shaping time.

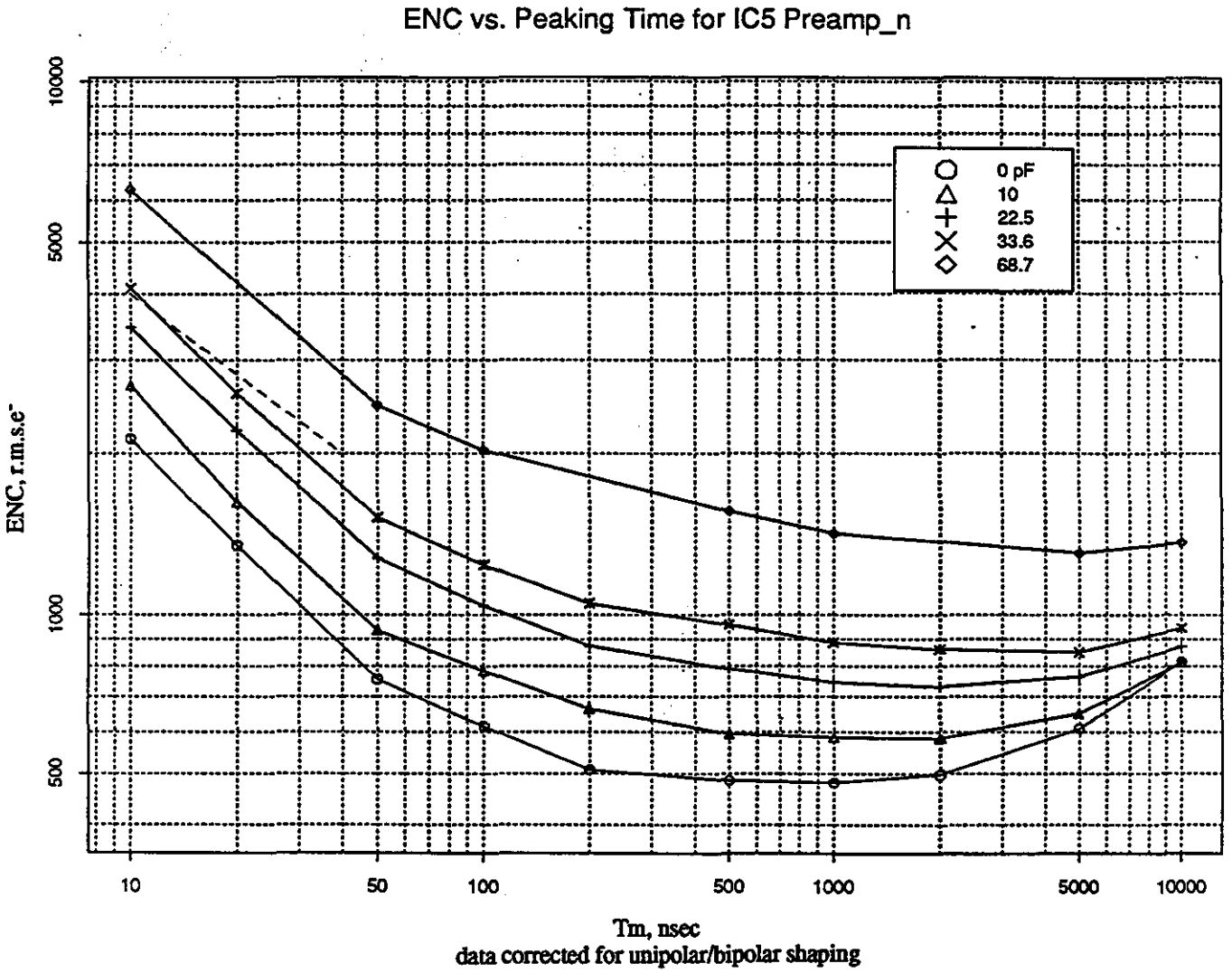

Figure 4.3-3: Prototype Preamp Noise Performance

Full scale front end amplifier prototypes have been fabricated using both MOSIS and the rad-hard Harris process. The layout of the rad-hard prototype is shown in Figure 4.3-4. The fabrication run for this chip is now in progress, and it is expected that devices will be under test by mid 1993.

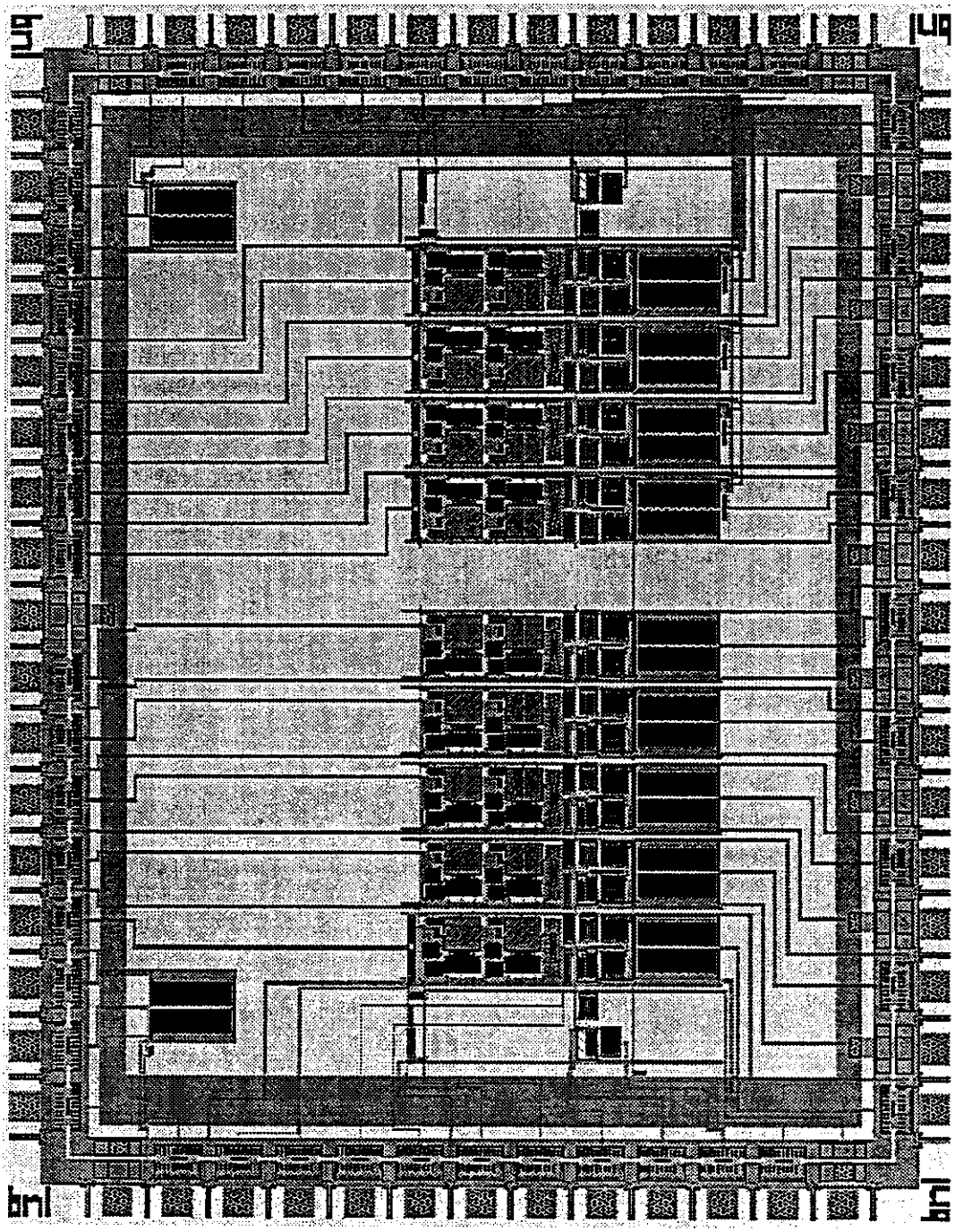

Figue 4.3-4: Rad-Hard Amp Layout

IPC Switched Capacitor Array

The IPC switched capacitor array is a 16 channel, approximately 128 deep array, and will be fabricated in the rad-hard Harris AVLSI process. The analog memeory has the ability to conduct simultaneous read and write operations, and can be clocked at 60 Mhz. The required length of the memory is set by the level 1 trigger latency, which has been established as roughly 2 microseconds for GEM, plus additional cells required to buffer level 1 triggers during readout. This rather short latency period is made possible by the proximity of the counting house to the detector in the baseline GEM design. Some of the critical design parameters are listed in Table 4.3-2.

Table 4.3-2: IPC Analog Pipeline Characteristics

# channels/chip	16
Pipeline length	~128
Channel Pitch	200 microns
Cell Length	30 microns
Dynamic Range	8 bits
Access Time	500 ns

The R&D plan for IPC electronics development in FY 93 calls for the fabrication of a prototype of this chip by mid 1993 in a rad-hard process. As mentioned above, the preamp/shaper will be fabricated on the same wafer as the SCA in this initial rad-hard fab run to help reduce the development costs of these chips. The IPC SCA chip is now under development at ORNL. The basic architecture for the first memory prototype has been finalized. The initial prototype design will include 8 channels with 128 cells per channel, and is now under fabrication. Two capacitor cell topologies are under consideration; voltage write-voltage read (VWVR), and voltage write-charge read (VWCR). These are shown in Figures 4.3-5 and 4.3-6. The readout presently planned is based on a VWCR topology. However, it is possible that, upon further study, a VWVR topology will be used. In the VWVR topology, the output offset voltage (or pedestal) could be easier to control using the residual charge generated by the switched feedback of the readout amplifier. The VWCR scheme gives an output offset not easily compensated by p- and n- device matching. A second reason for considering the VWVR topology is that amplifier compensation providing rapid and stable settling is easier for the VWVR topology than for VWCR. This results from the fact that the VWCR amplifier has a noise gain of approximately 2.5 for readout and 1.0 for reset, implying that fast, stable settling

times must be maintained over a 2.5:1 change in loop transmission. The VWVR topology, on the other hand, requires a noise gain of approximately 1.5 during sampling and 1.0 during reset. The loop transmission changes only 50% for VWVR instead of 150% for VWCR. Both readout topologies have been implemented in the rad-hard prototype, and tests will be conducted to evaluate the relative performance of the two approaches.

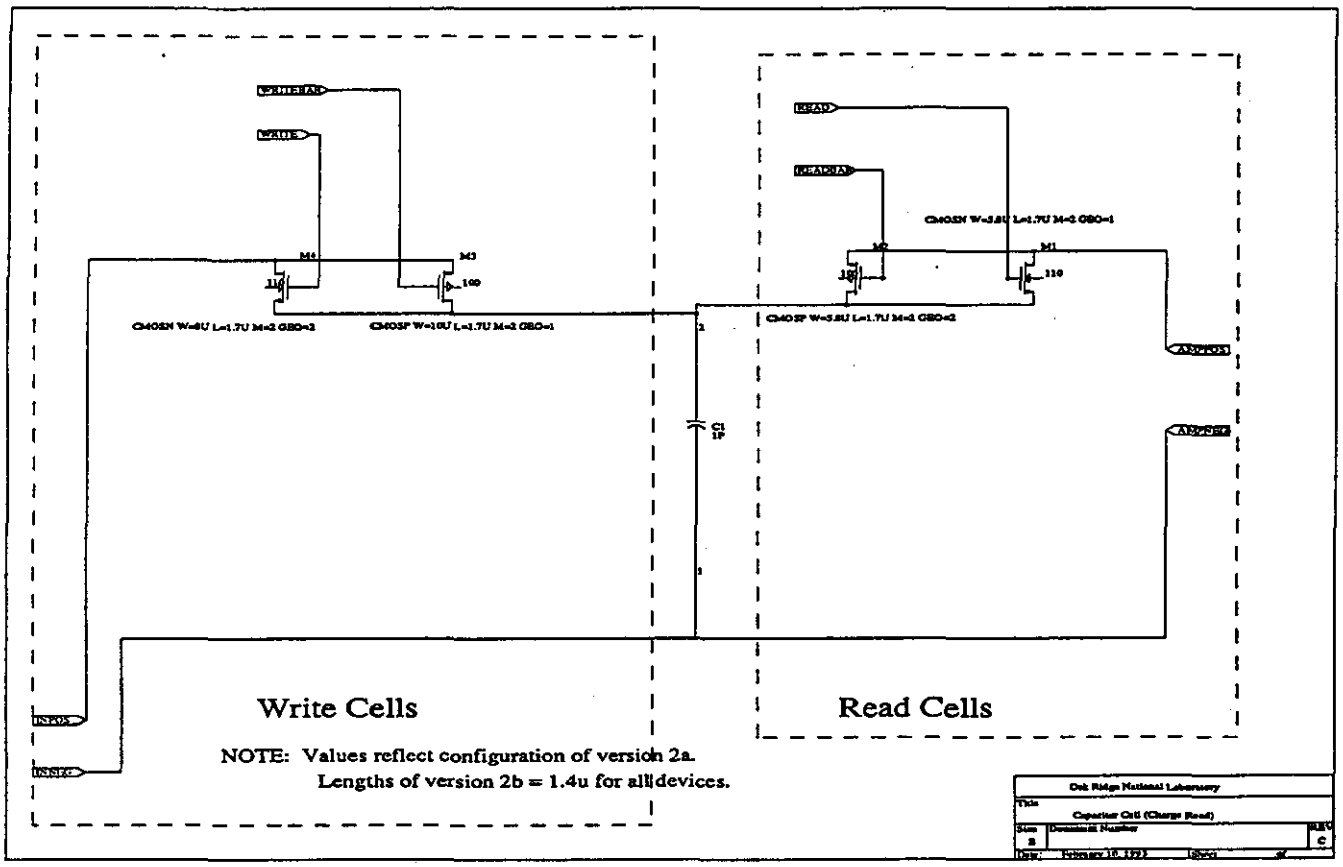

Figure 4.3-5: Voltage Write-Charge Read Cell

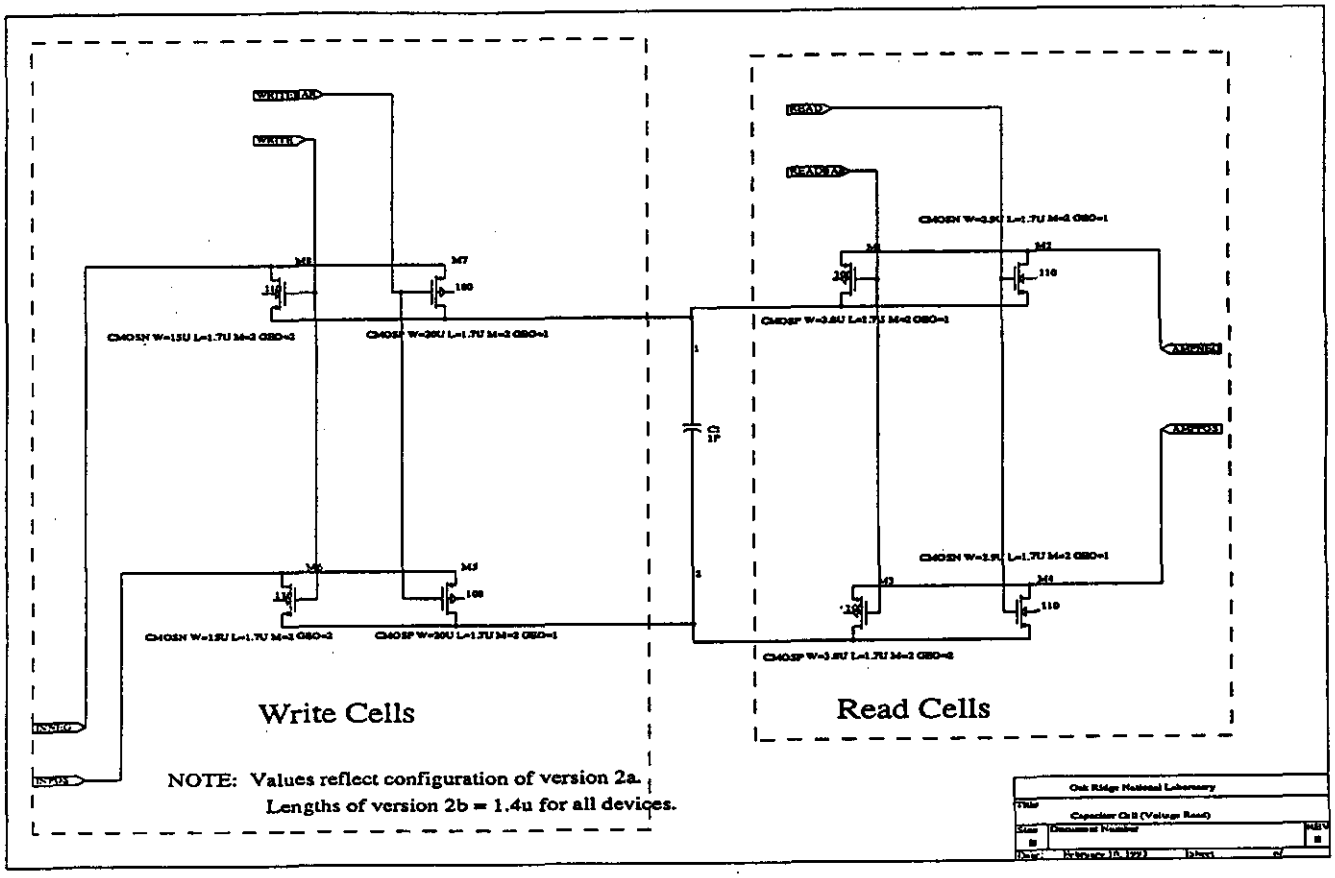

Figure 4.3-6: Voltage Write-Voltage Read Cell

Several amplifier topologies have been simulated using Hewlett Packard CMOS34 Semi-Empirical (Level 3) and BSIM (Level 13) models and Harris Semicondictor AVLSI-RA nominal pre and post-radiation models. We have settled on three candidate topologies, two of which will be used on the first prototype chip. Half of the channels will utilize one of the topologies, half the other. The address control for the initial design will use two 6-bit counters, one for even addresses, one for odd. This will allow at least 16 ns of settling time for the logic of either counter and will also allow maximum arrayability of the blocks under development. This circuit is shown in Figure 4.3-7. The settling time of this amplifier is critical in determining the readout time for the system. A BSIM simulation of this circuit indicates that the settling time to 11 bits is less than 500 ns. Post rad simulations in the Harris process show no significant increase in settling time. A typical post-rad BSIM result for this amplifier is shown in Figure 4.3-8.

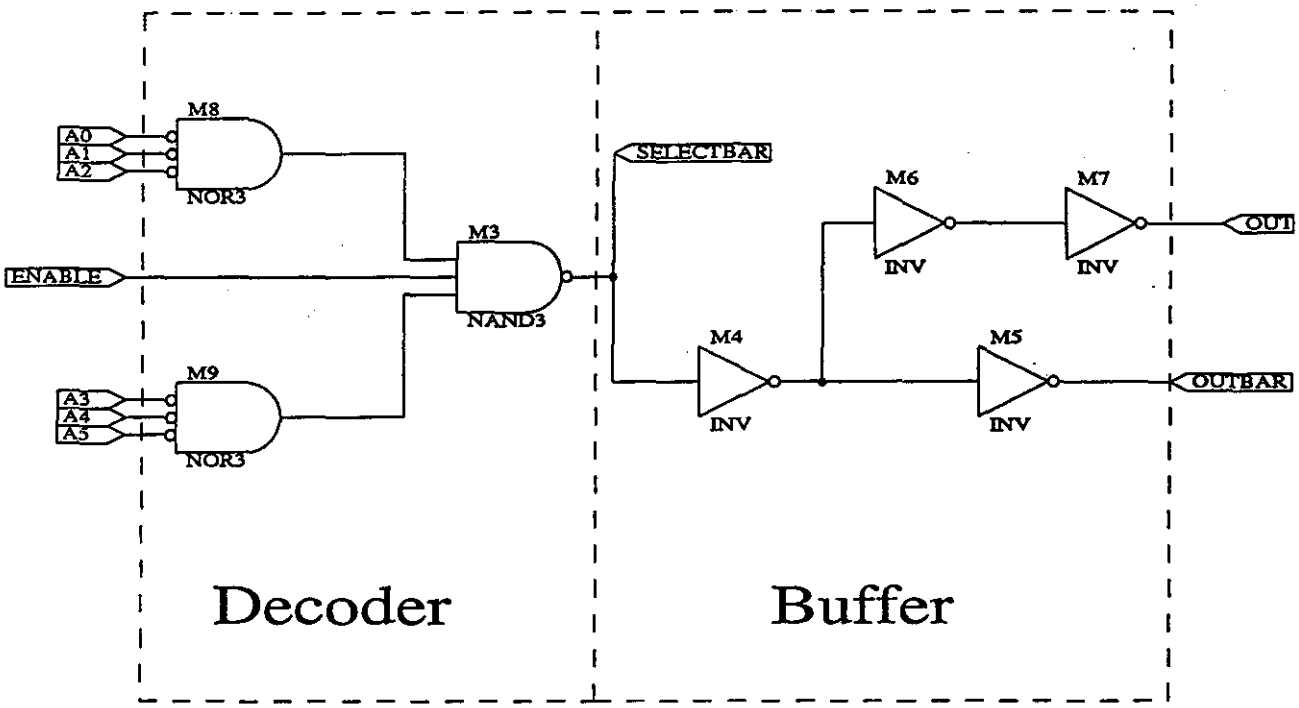

Figure 4.3-7: SCA Address Decoder Block

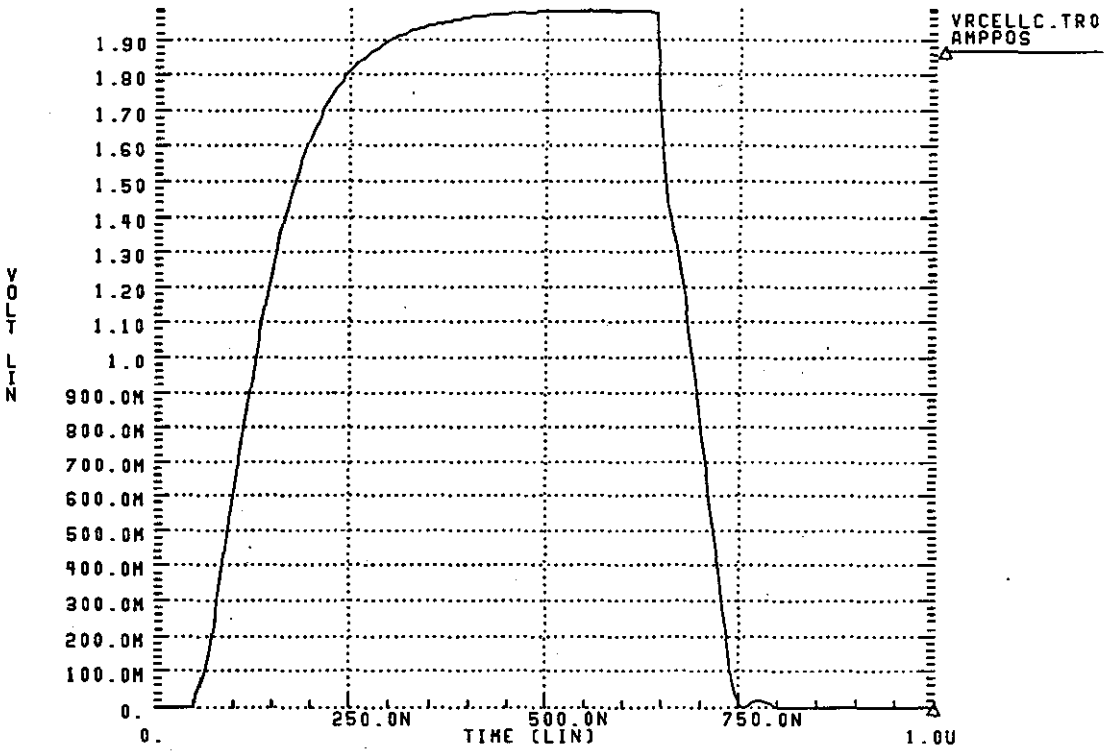

Figure 4.3-8: BSIM Model Port-Rad SCA Performance

IPC Flash ADC

Rad-hard Flash ADC designs exist which would, in principle, be suitable for GEM outer tracker use. An 8 bit 25 Mhz FADC has been designed at Harris in a the AVLSI process. Extensive studies conducted by our group has been shown this device to be rad-hard to 6 Mrad Co^{60}. In these studies, all critical parameters of the FADC performance, including the number of effective bits, the integral and differential non-linearities, the generation of speckle code, were measured as a function of dose. In Figure 4.3-9 we show a representative sample of the test results after a 2 Mrad exposure. Shown is the differential non-linearity in bits, measured at DC and with a triange shaped input waveform, the integral non-linearity as a percent of full scale, the RMS width of a single bin, the maximum error, and the sampling time jitter, all measured as a function of sampling rate. Our tests indicate a definite degradation in the performance of the device for sampling rates greater than 20 MSPS. This has been found to be due to a layout error which Harris has identified and has offered to fix. This device is equipped with a center tap which would allow an extension of the dynamic range by 1-2 bits. Alternatively, a similar extension of the dynamic range can be obtained by feeding a fraction of the input to the top of the FADC reference ladder.

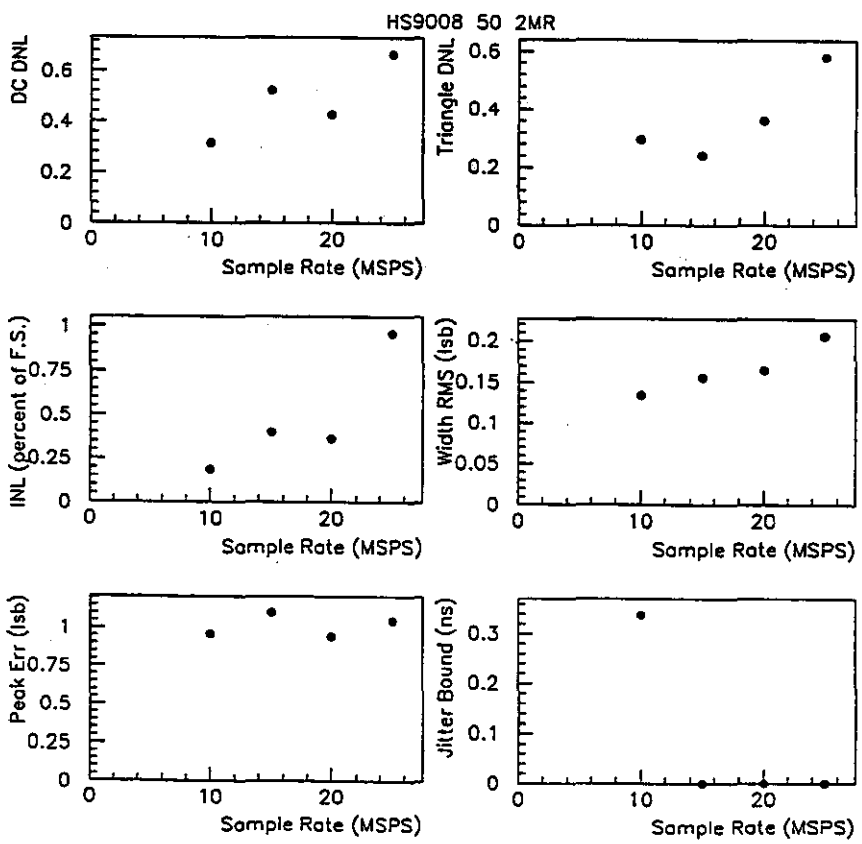

Figure 4.3-9: FADC Performance at 2 Mrad

IPC Readout Controller

A block diagram of the readout controller is shown in Figure 4.3-10. It consists of a state machine to drive the readout sequence, address drivers for the analog pipelines, a register holding the threshold value used in the zero suppression function, an 8 bit comparator, and an output buffer and frame packeter. The readout controllers on an IPC chamber are serviced by a single low bandwidth input link which allows the threshold values to be set, and to trigger test and calibration functions. The readout controller is responsible for driving the switched capacitor array write address lines, which are common to all arrays serviced by a single readout controller. Upon receipt of a level one trigger, the controller stores the write address on the level 1 pending stack. Asynchronously, the controller initiates a readout sequence, described in the section on readout timing below. The controller determines the read address appropriate to the time of the level one trigger and the current write address, asserts this address, and latches the capacitor voltage onto the readout amplifier for all channels, allowing that voltage to settle. The controller then scans through the pipeline chips and the channels within each pipeline chip, allowing the output multiplexer to settle on each channel selected. A FADC convert is initiated after the multiplexer settling period, and the digitized value is loaded into a readout pipeline in the controller chip. The zero suppression logic uses a comparator, which scans the digitized pad signal samples as they are generated. If a sample exceeds a preset value, then that sample, along with the corresponding sample from the previous and two subsequent pads are kept, as shown in Figure 4.3-11. This ensures that all samples required to reconstruct a position are available in the output stream. This operation is performed on the sample nearest the pulse peak, which is digitized first in the readout sequence. The location of the pads which were not zero suppressed on this sample are stored, and the remainder of the 4 samples for these pads are transmitted regardless of sample amplitude. The non-suppressed digital values and addresses are appended to a header containing the bunch and controller ID, and pushed out the LED output link. All the functions of the controller described above could be provided by a single gate array chip. Rad-hard gate arrays of the required complexity and speed are commercially available from LSI Logic. Initial prototypes of this chip, implimented in a field programmable gate array chip set, have been fabricated and are now under test.

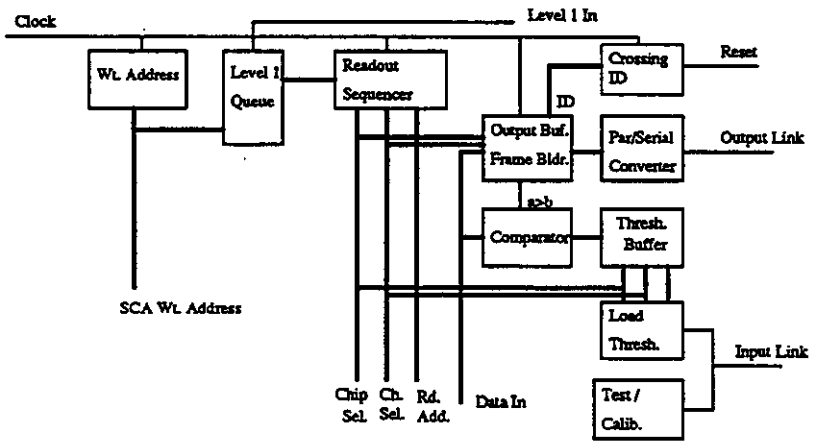

Figure 4.3-10: Readout Controller

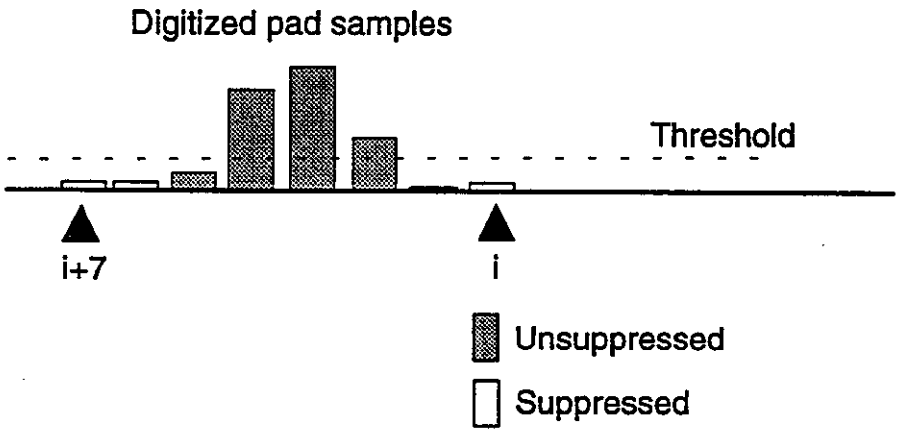

Figure 4.3-11: Zero Suppression

IPC Readout Link

In the baseline digital readout design, each readout link services 128 pad channels. With no zero suppression, and assuming three time slices are read out for each hit, the number of bits being transmitted per channel per event is n=128x(8 bits)x(3 samples)=3Kbits. If we assume a 10 ms readout time, the worst cast bit rate required by the link is 0.3 Gbit/s. Handling this bandwidth requires rather expensive technology, and it would be highly desirable to avoid these rates by zero suppressing on the detector. The basic scheme for doing this in the digital architecture has been described above. Zero suppression requires a very low bandwidth link running into the detector, through which the thresholds are adjusted. The thresholds are stored in a buffer located on the supervisor module, and are used during the readout sequence by a comparator located on the supervisor chip. In a zero suppressed system, the bit rate is given by $r=128x(f_{zero})x(N_s x8 \text{ bits}+8\text{bitsadd})/(10\text{ms})$. For $f_{zero}=0.1$ and $N_s=3$ we find that a 40 Mbit/s link is required. This is within the capabilities of a simple LED based system, as described under the Silicon Strip Optical Data Link in this document.

One of the requirements of the IPC readout electronics is the ability to maintain a100kHz rate to level 2. The readout time, assuming the readout of the pipeline is performed at the 60 Mhz accelerator clock rate, that three time slices will be read out for each pad, is calculated below. In the event of a 1st level trigger, the readout supervisor initiates a readout sequence by asserting the chip, time slice, and channel address on the address bus connecting the supervisor with the 8 pipeline chips it services. The access and settling time of the SCA is the time critical operation in the readout , and therefore, we wish to pipeline this process to the extent possible. This dictates a readout sequence in which the pipeline chip # is clocked at the highest rate, followed by the channel number, with the time slice address within the pipeline clocked at the slowest rate. Below, we detail the readout cycle, including timing estimates for each step. The access time of the switched capacitor array is based on BSIM models of the readout amplifier of the array, which predicts a settling time to 11 bits of 500 ns.

	Delta t
Assert Time Slice Address (1 of 3)	0
Wait for SCA to Settle	500 ns
Assert Channel # (1-16)	0
Wait for MUX Settle(2-16)	20 ns
Convert FADC	40 ns
Assert Chip # (1-8)	0
Load Data/Add	17 ns
Increment Chip #	0
Increment Channel #	0
Increment Time Slice #	0

Pipeline/MUX/FADC Timing Sequence

A full simulation of the IPC readout electronics has been performed, using GARFIELD to generated current waveforms for random trajectories through the chamber. Landau fluctuations and electron diffusion are included in the simulation These waveforms are then convolved with the transfer function of the preamplifier and shaping amplifier to obtain shaped anode signals. The cathode pad signals are generated by first selecting a random position across a pad. This position is used to determine the correct relationship between the signal on this pad and those on its nearest neighbors. The anode signal is then divided among the three pads according to these relationships, with an additional attenuation factor of 2 on each pad signal due to charge sharing with the other cathode plane. These cathode signals are then sampled at 16 ns intervals. The samples are subjected to smearing due to amplifier noise, clock skew, and shaping time differences between the three pads. Clock skew is simulated by adding a random component to the times at which the samples are acquired. This results in an error in the positions determined from the sample sets which is greatest for samples acquired on the leading or trailing edge of the pulse. Shaping time variations are modeled by varying the amplifier transfer function for each of the three pads on every event, so that each has the same nominal shaping time, but actual shaping times which differ over a set range. Amplifier noise is simulated by adding a random component of noise to each sample. After these operations are performed on the samples, the digitization is simulated, using a set number of effective bits, and the resulting digital values are used to determine the position. This reconstructed position is then compared with the true position to evaluate the effects of the various smearing processes. Some results from this simulation are presented here. In Figure 4.3-12, the relationship between position resolution and noise is presented. The vertical scale is in microns. In Figure 4.3-13, the dependence of the resolution of the position derived from the sample closest to the signal peak on time jiter is shown. In Figure 4.3-14, the dependence of the position resolution, again derived using the peak sample, on channel to channel shaping time variations is shown.

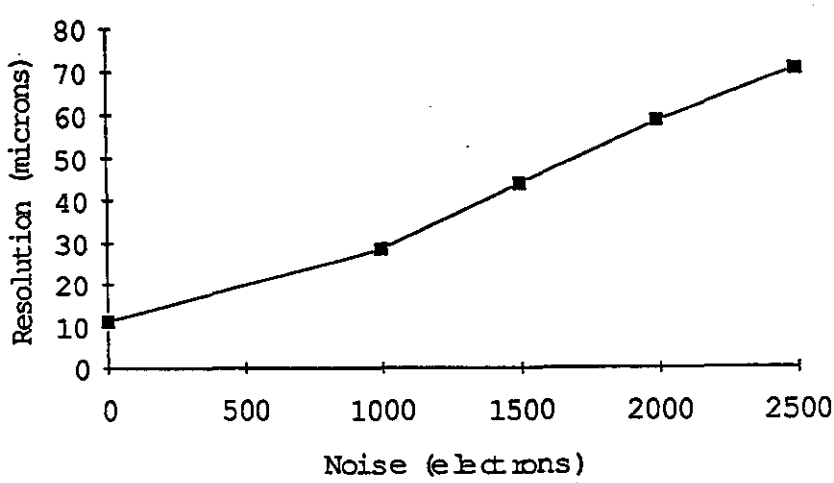

Figure 4.3-12: Resolution vs Noise

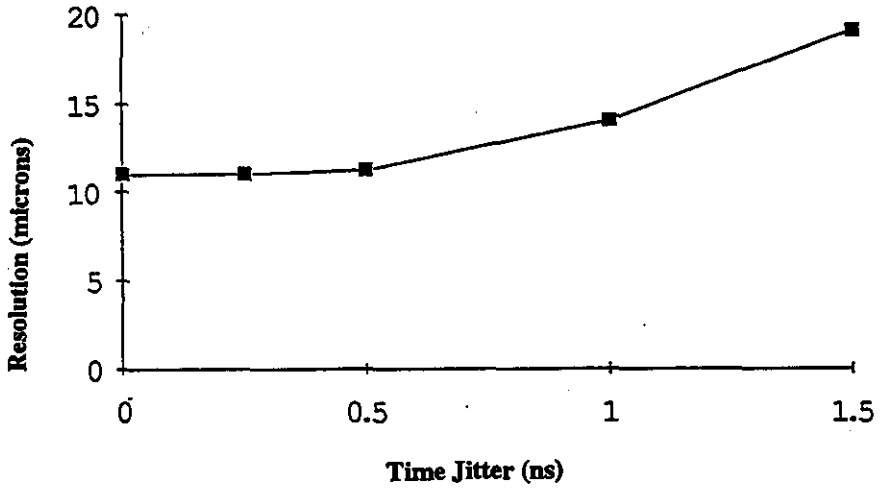

Figure 4.3-13: Resolution vs Clock Skew

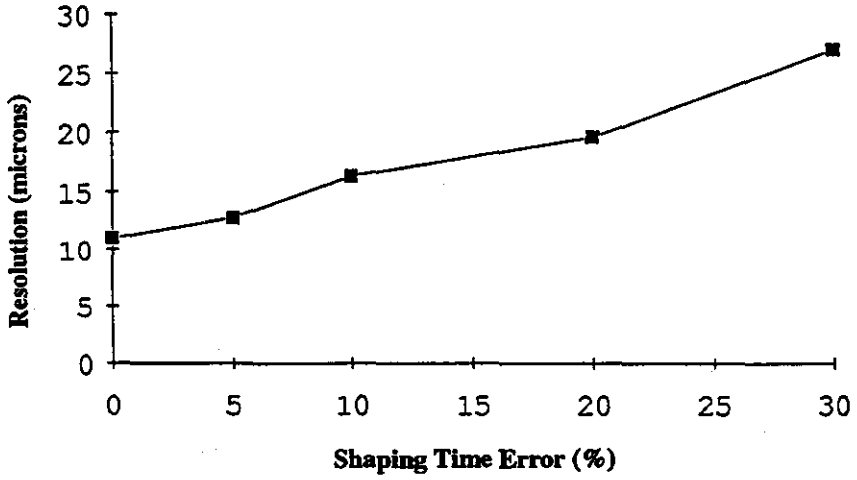

Figure 4.3-14: Resolution vs Shaping Time Error

5. INTEGRATION INTO GEM

5.1. Installation and Alignment

The installation of the Central Tracker into the Barrel Calorimeter will be a critical operation requiring careful planning and control. During the calibration and beam testing, the Central Tracker will have been surveyed to high precision. This alignment must be preserved as much as possible. The Central Tracker is not a robust structure. The requirement of low radiation length has resulted in the design of a delicate device that should be installed in GEM as late as possible.

An installation procedure will first be developed, then rehearsed with a mock structure. This structure will be the same physical size and weight, will contain the same mounting and installation hardware and will have optical targets simulating the center line and external targets. The entire installation sequence will be stepped through followed by optically aligning the center line to the Reference Beam Line.

Since the location of the Reference Beam Line with respect to the actual beam line is uncertain to several millimeters, the Central Tracker will not require precise placement. Placement within 250 - 500 μm of the Reference Beam Line will be adequate. The external targets on the mock structure will then be measured and referenced to similar targets on the end of the Barrel Calorimeter.

During the installation and removal of the mock structure, instrumentation willmeasure the vibration levels that the Central Tracker would experience. This monitoring would begin during handling at the assembly facility and continue throughout the Air Ride transport, off loading onto the elevator or crane, down hole lowering, transferring to the hall crane, and installation into the Calorimeter. Rough operations that could potentially disturb the Tracker precision will be identified and corrected prior to final installation. The effectiveness of the shock and vibration isolation platform will also be evaluated.

During the actual installation, the IPC Barrel Modules and Silicon Tracker willbe mounted in the support structure and installed as one unit. After the assembly is transferred to its mounts, the ends will be optically mapped with the same procedure usedon the mock structure. The external alignment fiducials will be mapped relative to the Reference Beam Line and relative to the Barrel Calorimeter. Anynecessary adjustments will be made at this point. The IPC End Caps will then be installed. They will also contain external alignment fiducials and will be optically mapped.This series of optical alignment measurements will define the locations of the Silicon Tracker, IPC Barrel and End Caps relative to the Reference Beam Line, aswell as their position relative to the Barrel Calorimeter.

Some final alignment checks are required after the services and beam pipe have been connected to verify that no external strain has repositioned the tracker. Additional optical monitoring will also take place as the Silicon Tracker is cooled down, the Calorimeter vacuum isapplied and theIPC cooling and gas systems become operational. An internal alignment monitoring system will continually monitor the relative positions of each major subassembly. This information will serve as input to the ultimate determination of the alignment of theCentral Tracker using particle tracks, which is discussed in Section 2.4.

5.2. Services and Connections

Services to the Central Tracker include: Power cabling, fiber optic readout, fast and slow control cabling, high voltage lines, coolant lines, gas lines, and safety systems lines. These service lines are supplied to both the Silicon and IPC Trackers and must be packaged internally in the Central Tracker assembly and routed out through the interface between the Barrel and End Cap Calorimeter cryostats. Adequate clearances need to be designed for cable routing inside the Central Tracker, through the Calorimeter and for locations where cable connectors and piping hook ups are placed. The Central Tracker will be installed with only shortservice leads on each end and then connected to lines which will have been installed on the ends of the Barrel Calorimeter. Table 5-1 is a summary of the Silicon and IPC tracker cabling.

Table 5-1: Services Summary

Tracking System	Service	Size (cm)	Quantity	Area (cm^2)
Silicon Tracker	Power	1 x .43	194	280
	Fiber Optic Readout	500 μm Ø	5052	
	Fiber Optic Timing	500 μm Ø	1000	61
	Internal Alignment.	1 mm Ø	220	9
	Liquid Butane	.250" Ø	16	
	Gas Butane	.5" Ø	16	
	Nitrogen Enclosure	2 x 8	4	62
	Nitrogen Supply	.750" Ø	2	
	Nitrogen Return	.750" Ø	2	
	Butane Vent	.750" Ø	2	
	Butane Purge	.750" Ø	2	32
IPC Tracker	Power	.5 x 3	160	800
	Fiber Optic Readout	500 μm Ø	4800	
	Fiber Optic Timing	500 μm Ø	960	50
	Anode HV	.3 Ø	160	30
	Water Supply	2 Ø	8	
	Water Return	2 Ø	8	128
	Gas Supply	2 Ø	2	
	Gas Return	2 Ø	2	
	Sensors	2 x 2.5	(Many)	34
Total Routing Area				1486

The first systems to be connected will be the gas and cooling systems. The Butane coolant supply and return lines will be hooked up, leak checked, and then sealed in the Nitrogen gas enclosures. The Nitrogen supply lines and other safetylines will be attached to complete the Silicon cooling system. At the same time the IPC cooling and gas system lines will be connected and leak checked. Safety system tests will be performed and verified as acceptable before any external electrical systems are hooked up. Butane flow tests may be done at this time, but no Butane will be in the Tracker while external hook ups are being performed.

Following the gas and cooling systems testing, the electrical power systems will be connected and tested for continuity. Slow controls, Fiber Optic cables andother sensors readouts will then complete the service connections. When all safety check have been completed, the Central Tracker electronics can be powered and verified.

5.3. Access

Access to all parts of the GEM Detector is discussed in detail in Section 10, Detector Operations, Access and Maintenance. The Central Tracker is the innermost element of this large and highly integrated experiment and is therefore the least accessible.Even when the entire detector is open and access to the tracker is optimal, thetight integration of the electronics and mechanical structure inside the assembly makes repairs in situ very difficult. Any major repairs to the Central Tracker will require its removal to the surface facility and can therefore only be considered during a lengthy shutdown. It is expected that the Silicon Tracker will require replacement when the integrated fluence of hadrons exceeds 10^{14} charged particles/cm^2 on the first layer of Silicon.

5.4. Surface Facilities

The Central Tracker will require a dedicated facility on site to complete the initial detector assembly and to conduct maintenance operations throughout its expected ten year life time. The facility will contain two 10 x 10m^2 Class 10,000 Clean Rooms for parallel assembly operations of the Silicon Tracker and Interpolating Pad Chamber System. A highbay, 20 x 20m^2, with a 5 ton crane covering the entire floor area will be used to combine thetwo subsystems and to perform systems tests and calibration. Within the highbaywill be an X-ray Calibration Lab lined with personnel shielding blocks, an Electronics power supply area with appropriate safety features, and a utility area which will house the Silicon and IPC cooling and gas systems. A storage room of about 150 m^2 is needed to house components at various stages of assembly. The entire assembly facility will require thermal and humidity control. The total space needed is approximately 750 m^2 and the facility should be available in 1997. A more extensive description ofthe facility can be found in Section 9 of the present report, Facilities, Assembly and Installation.

5.5. Safety and Environmental Impact

The Central Tracker presents a concentration of various safety concerns in its compact volume. In addition to the Butane used to cool the electronics of the Silicon Tracker, there is high and low voltage, heat producing electronics, Beryllium in the beam pipe, and the proximity of the vacuum; all within centimeters of the enormous power stored in the two proton beams of the SSC.

The Central Tracker engineering team has provided full details of all tracker systems to the GEM Safety Coordinator to assist in the development of a complete Conceptual Safety Analysis Review (CSAR) for the entire GEM Detector. The results of this review, including the Central Tracker, are detailed in Section 16, Environmental, Safety and Health Considerations.

6. RADIATION ENVIRONMENT

The lifetime of the Central Tracker depends on controlling the radiation environment in the central cavity. The radiation environment comes from three sources; charged particles from the interaction point (mostly hadrons), neutron albedo entering the central cavity from the calorimeters, and low energy debris (gammas, photons, and protons) from the material in of the central tracker.

6.1. Radiation Dose Due to Charged Particles

The major constraint that determines the inner radius of the Central Tracker is the flux of charged particles from the primary P-P interactions. One also has to take secondary interactions and γ conversions in the detector as well as soft particles trapped in the magnetic field (loopers) into account.

The flux of charged particles at a radius R from the beam line (R=r$\sin\theta$ where r is the distance from the interaction point) can be written as

$$\text{Charged Particle Flux} = \frac{KL\sigma}{2\pi R^2}\frac{dn}{d\eta} \quad \text{particles / cm}^2$$

where L is the integrated luminosity, σ is the total pp crossection, $\frac{dn}{d\eta}$ is the number of primary charged particles per unit of rapidity per interaction and K is the factor by which the flux is increased due to secondary interactions, γ conversions, loopers, etc. in the material of the tracker.

From Monte Carlo simulations of the GEM Central Tracker, K is estimated to be around 1.5. For one year of SSC running (10^7 seconds) at $L = 10^{33}\text{cm}^2/\text{sec}$ and a total pp crossection of $\sigma = 10^{-25}\text{cm}^2$, and the expected value of $\frac{dn}{d\eta} \sim 6.5$ charged particles per event, we calculate at R=10 cm from the beam line a flux of charged particles of

$$\text{Charged Particle Flux} = 1.5 \times 10^{13} \text{particles / cm}^2 \text{ / year.}$$

To convert this to a radiation dose i.e. the energy deposited per unit mass by ionization energy loss of the particles, we use the definition of the Gray

$$1 \text{ Gray} = 1 \text{ joule/kg}$$

$$= 6.24 \times 10^9 \text{MeV/gram}$$

A more usual unit is the rad,

$$1 \text{ Gray} = 100 \text{ rads}$$

For long term doses at the SSC, the Megarad is appropriate

$$1 \text{ Mrad} = = 6.24 \times 10^{13} \text{Mev/gram}$$

We can then write the radiation dose corresponding to a flux of charged particles as

$$\text{Radiation Dose (Mrads)} = \frac{\text{charged particles / cm}^2}{6.24 \times 10^{13}} \times \frac{dE}{dx}$$

where $\frac{dE}{dx}$ is the energy loss of charged particles in a given material in units of

$$\text{Mev / gram / cm}^2$$

In Silicon, the energy deposited by a minimum ionizing particle is

$$\frac{dE}{dx} = 1.66 \text{ Mev / gram / cm}^2$$

thus the radiation dose in silicon can be written as

$$\text{Radiation Dose (Mrads)} = \frac{\text{no. of min. ion. particles / cm}^2}{3.8 \times 10^{13}}$$

The charged particle flux calculated above (1.5×10^{13} particles / cm^2 / year) for one year of SSC of $L = 10^{33}$ at a radius of R=10 cm from the beams then corresponds to a radiation dose (see Figure 6.1-1) of

Radiation Dose =0.4 Mrads/year at R=10 cm

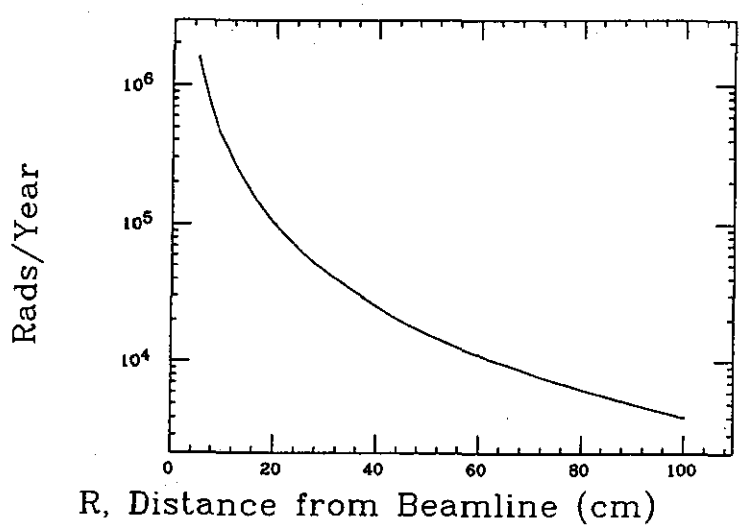

Figure 6.1-1 Yearly radiation dose from charged particles in the Central Tracker as a function of R_1 the distance from the beamline, for a luminosity of $L = 10^{33} \text{cm}^{-2}\text{sec}^{-1}$

At a tolerable lifetime dose of 4 Mrads for silicon this corresponds to a 10 year lifetime for the inner layer of silicon detectors at a radius of 10 cm and a luminosity of 10^{33} / cm^2 / sec.

In the vicinity of the IPC outer detector the radiation dose is much smaller.

Radiation Dose=25 Krads/year at R=40 cm

We are designing the IPC electronics to tolerate a lifetime dose of 2.5 Mrads, which corresponds to a lifetime of 10 years at a luminosity of 10^{34} / cm^2 / sec.

6.2. Neutral Particle Backgrounds

The Central Tracker volume will have a significant background from albedo neutrons generated in the surrounding environment. These will produce photons from (n,γ) reactions, as well as charged particles ranging from recoiling hydrogen nuclei to a variety of light products from nuclear reactions. This background will have three serious effects on the operation of the central tracker. First, charged products of neutron and associated photon interactions will produce radiation damage in any component in the Central Tracker, not only in the active elements of the Silicon and IPC detectors , but also in the electronics and passive support materials. Such damage may compromise the effective performance and lifetime of these devices. The actual dose expected may be accessed through simulated generation and tracking of individual reaction products, or through folding appropriate Kerma factors with the expected neutron energy spectrum. Secondly, the products of neutral particle interactions may produce unwanted signals in the detectors that could interfer with the pattern recognition capabilities for determining acceptable tracks. Lastly, the neutron fluences have the potential to activate any component, especially those in close proximity to the interaction region. Since the Central Tracker is the closest set of detectors to the interaction point, access to this region could be seriously affected by unwanted activation. The goal of the simulations to date have been to address these three concerns.

6.2.1. Neutral Particle Fluences and Dose Rates

Previous work has shown that the central volume is effectively isolated from areas outside the calorimeter, hence changes made in the FCAL, muon chamber shielding, and placement and shielding of the focussing quadrupoles have no effect on the central tracker fluences. The behavior of the neutron fluences is most influenced by the placement and composition of the electromagnetic calorimeter sections, a matter dictated by physics considerations. To shield the central volume from low energy neutrons created in the calorimeter, a borated polyethylene shield lines the outer boundary of the central tracker walls. This shield acts to reduce the neutron energy to levels where it is then lost via the (n,γ) capture reaction on B^{10}. In the present configuration an order of magnitude reduction in the neutron

fluence in the central volume is achieved. One consequence of using the boron in the polyethylene shield is to suppress the 2.2 Mev photon from the (n,p) capture reaction but introduce the 0.48 Mev photon from the (n,) capture reaction on B^{10}. The neutral particle fluences for the Central Tracker volume is listed in table 6.2-1. The results include all low energy neutrons from the calorimeter and shield as well as the high energy neutrons from the primary collider event. The low energy neutrons from the calorimeter are essentially uniformly distributed in the Central Tracker volume while the high energy neutrons have a flat distribution in eta.

Table 6.2-1

Energy Range	Yearly fluence (r =10 cm)	Yearly Fluence (r = 44 cm)
> 100 keV	7×10^{12}	2×10^{12}
all energies	8×10^{12}	4×10^{12}

Signals in the active regions of the detectors come from primary interactions of the neutral particles and from debri produced by all particles, neutral and charged, in materials surrounding the detectors and from shielding materials. In our physics simulations we have allowed charged particle interactions to occur, as well as electronic noise, to contribute to the signal rate for typical physics events but have not included the effect of neutral particles. This is primarily because the GEANT simulation does not treat low energy neutron interactions in a clearly physical manner. We expect the LAHET code system to do a much more physical job. Our concerns included the debri coming off of the borated polyethylene shield into the IPC chambers, conversions of photons in the silicon and IPC active regions, and neutron interactions in the active regions of the silicon and IPC detectors. This program of study is still in progress but some results are still available. The rates for two processes studied are shown in table 6.2-2. In the first row are tabulated the yearly photon fluence in the first silicon layer and the first IPC layer. In the second row are tabulated the (np,d,t,alpha) reactions in the silicon and IPC active regions. Both processes produce unwanted signals in the detectors but at low rates (< 1000 Hz). We don't expect these processes to effect the occupancy of the silicon or IPC detectors.

Table 6.2-2

Process	First Silicon Layer (r =10 cm)	First IPC Layer (r = 44cm)
Yearly Photon fluence	3.5×10^{12}	3.2×10^{12}
(np,d,t,alpha) reactions/SSCYear-cm^3	0.02×10^{12}	0.005×10^{12}

6.2.3 Activation of Central Tracker Components

The question of activation of central tracker components will be addressed through the use of the CINDER90 activation code. This code accepts as input the yield of spallation products from primary nuclear interactions from the LAHET code, along with the fluence of neutrons calculated by MCNP. The decay of the reaction products is tracked in the CINDER code, which produces the nuclear inventory, activity in curies, decay heating in watts and also the decay photon spectra. This may be done at user chosen time intervals. The photons may further be tracked with Monte Carlo methods to various places around the detector, and the equivalent dose in rads calculated. Preliminary calculations have indicated that the dose rates in the Central Region around the beam pipe are between 10 - 100 mrads/hr in the forward region. More detailed calculations are underway. The implication is that while the forward region is radioactive, access for minor repairs is clearly possible.

6.3. Lifetime Expectancy of the Central Tracker

The radiation levels discussed in the preceeding sections are summarized in Table 6.3-1.

Table 6.3-1

Radiation Hardness of Central Tracker

1. Charged particles, including secondary interactions, γ conversions, Delta rays, loopers, etc.

	Yearly Radiation Dose		Lifetime Dose Tolerance
	$L = 10^{33}$	$L = 10^{34}$	
Silicon	0.4 Mrad/yr	4 Mrad/yr	2.7 Mrads
Pads	0.025 Mrad/yr	0.25 Mrad/yr	2 1/2 Mrads

2. Neutron Flux with Polyethelene Shield

	Yearly Neutron Flux		Lifetime Dose Tolerance
	$L = 10^{33}$	$L = 10^{34}$	
Silicon	7×10^{12}	7×10^{13}	$10^{14}/cm^2$
Pads	2×10^{12}	2×10^{13}	$5 \times 10^{14} / cm^2$ $5 \times 10^{14}/cm^2$

7.1 Silicon R&D

7.1.1 Microstrip Detector R&D

The research and development plan for the GEM microstrip detectors has been designed to bring the performance of the detectors to the level demanded by the GEM tracker by the end of 1994. Early prototype production and testing is underway. The silicon detector R&D includes detailed simulation studies of the microstrip response to ensure full characterization and understanding of the detector operation.

The key issues being addressed for the microstrip detectors are:

- basic detector response
- multi-strip response (intra- and inter- charge coupling)
- strip length dependence
- minimization of microstrip capacitance
- reduction of microstrip resistance
- effect of 0.8 Tesla magnetic field on detector response
- effect of radiation on detector performance
- detector/electronics coupling

Many of these effects are being and will be studied with very fast amplifiers with nanosecond resolution mounted on a few strips. Studies of the time-structure of induced currents correlated with simulation studies will lead to a full understanding of detector performance and optimization.

The R&D effort on these topics has begun with the assembly of a number of tools and resources to address them.

(1.) Detector fabrication is focussed on a few sources. These have been Hamamatsu, Moscow State University, and ITRI in Taiwan. Others are under discussion. Existing studies of laser induced pulses show that the time needed to collect the charge from a track or laser pulse is primarily dependent on the resistivity of the strips. Figure 7.1.1-1 illustrates this trend, as the lower set of curves show a significant slowing of charge collection for strip resistances of 50 Ω/cm. We have detectors fabricated with different strip widths and thickness to see to what extent the resistance of the strips can be decreased. Increasing the strip width will tend to also increase the strip capacitance which is undesirable. We hope to find the optimum strip width for detectors to be used in GEM.

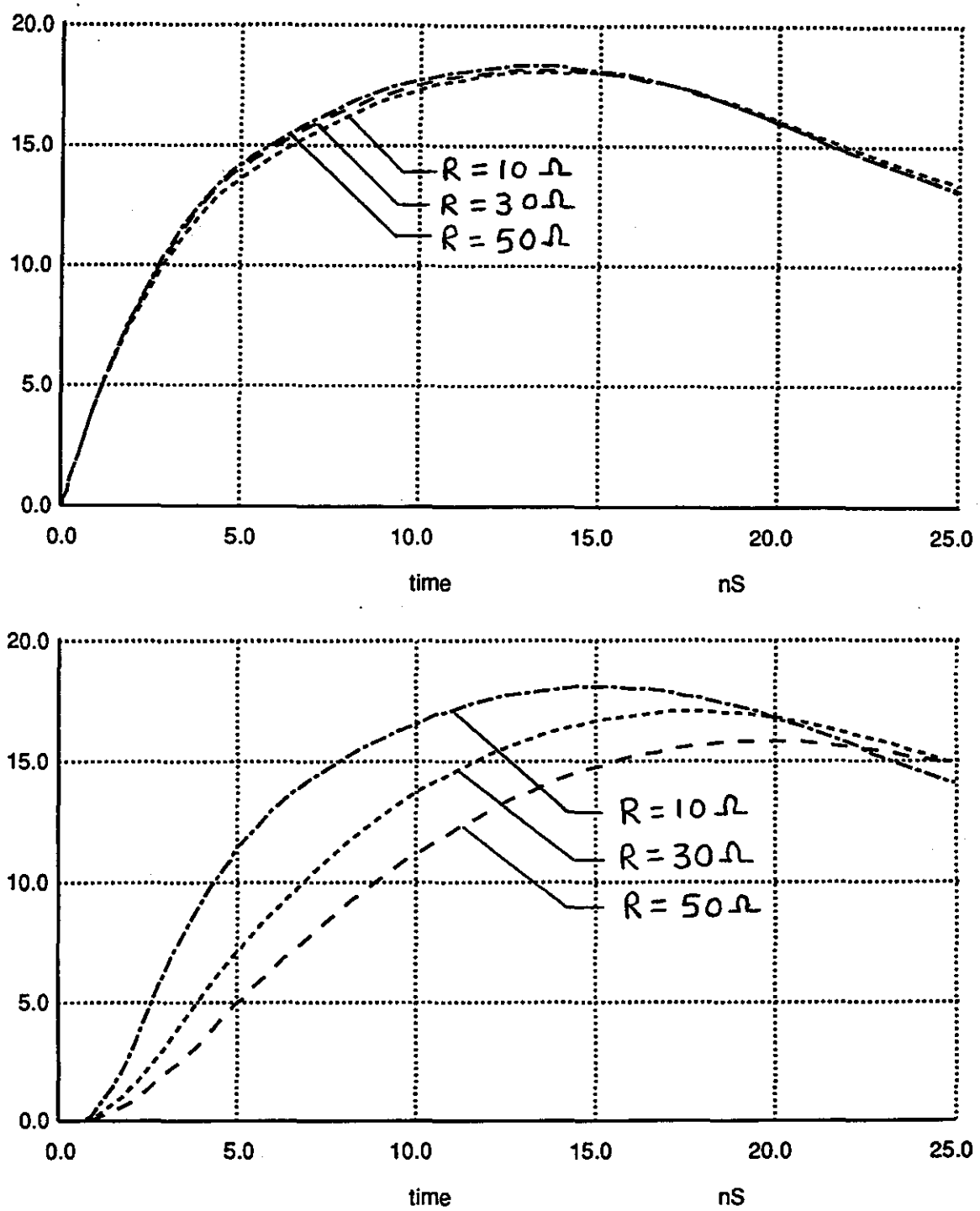

Figure 7.1.1-1: Calculated GEM preamplifier output waveforms as a function of strip resistance. The upper curves show the waveforms for 10 Ω/cm, 30 Ω/cm, and 50 Ω/cm where the charge is deposited at the end of the strip nearest the preamplifier. These curves show little dependence on strip resistance, as is expected. The lower curves show the waveforms for these strip resistances where the charge is deposited at the far end of the microstrip, 18 centimeters from the preamplifier. Here the effect of strip resistance is clear.

(2.) The Santa Cruz code PULSE for the simulation of the signals from silicon strip detectors was obtained from the Santa Cruz group. This code includes the effects of Landau fluctuations and the drift of electrons and holes in the electric and magnetic fields inside the detectors. It has been modifed at Oregon for single-sided detectors and for the deposition of charge from alpha particles.

To date, the code has been used to study the following issues:

- the difference in time-walk between different timing algorithms: one algorithm based on the time of threshold crossing for the early charge collection and one based on using the peaking time of the charge collection. While the peaking time gives a very good time for uniform charge depositon, this study found that the Landau fluctuations and the detailed pulse formation in adjacent strips for shared charged rendered the threshold algorithm more robust. Figure 7.1.1-2 illustrates this.

- the effect of detector tilt on microstrip response and charge sharing: the finite width of the detectors alone cause incident high momentum particles to pass through the detectors at angles of up to nearly ten degrees. In addition, there are mechanical motivations to tilt the detectors slightly, increasing the crossing angle for stiff tracks. Such crossing angles result in a sharing of charge between neighboring strips, and a weakening of the separation between signal and noise. These effects have been studied and have demanded a minimization of the tilt angle.

- the response of silicon detectors to alpha particles: alpha particles penetrate the detectors about 25 microns before coming to rest. This energy deposition so close to the surface creates quite different response compared to a minimum ionizing particle passing through the detector. Quantitative understanding has been possible with the PULSE code.

- Lorentz drift studies of the electrons and holes in the detectors and studies of the relative importance of each to signal formation: due to the 0.8 Tesla magnetic field within the GEM tracking volume the charges experience an E x B drift. For the single sided detectors of GEM, the holes contribute about 80% of the response and therefore the approximately 1.5° Lorentz angle of the holes dominates the larger angle for electrons.

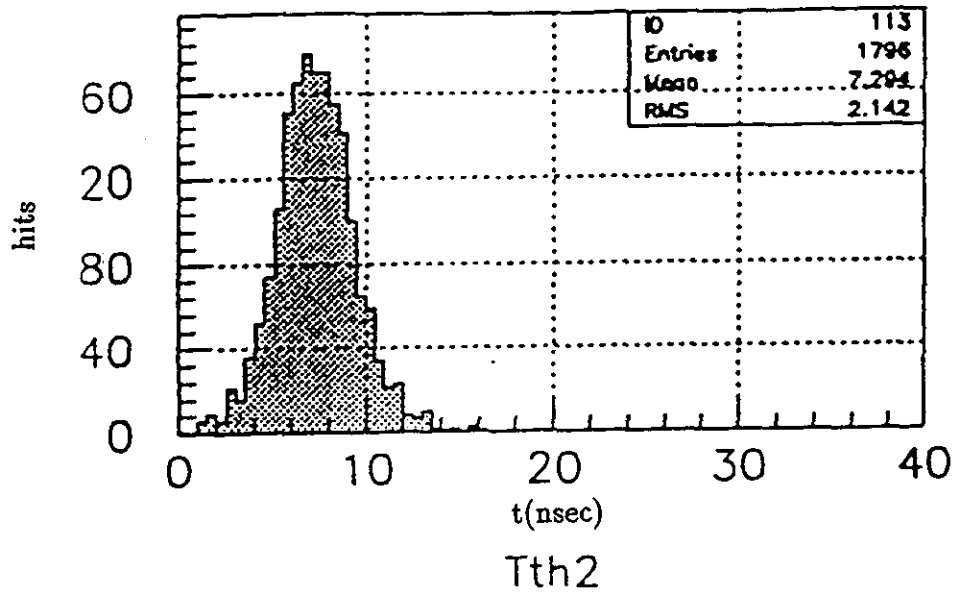

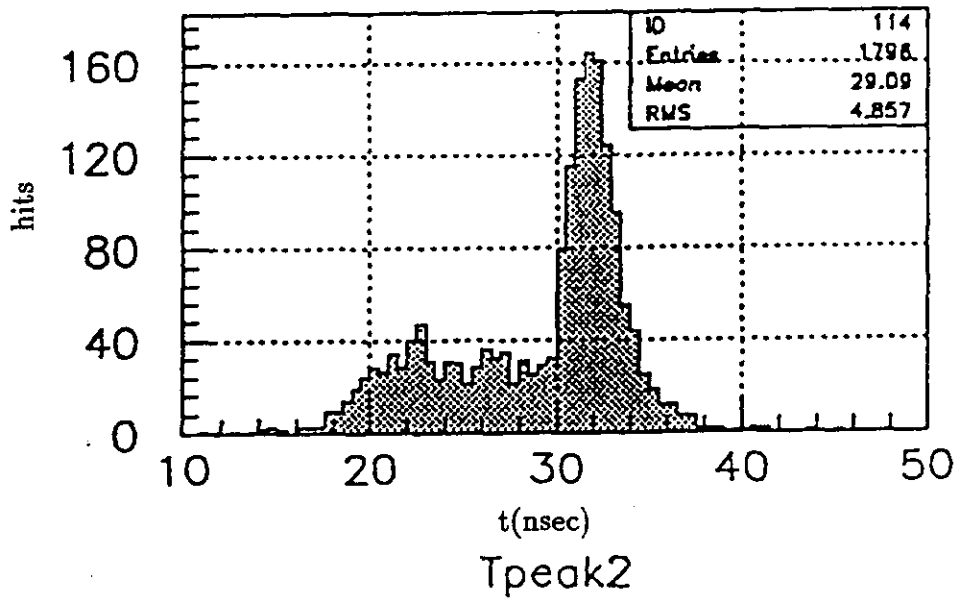

Figure 7.1.1-2 Timing of hits in microstrip detectors for two different time algorithms. The microstrip responses have been convoluted with a simulation of the preamplifier response having a 20 nanosecond shaping time. The upper figure results from using the time of threshold crossing with the threshold set to 1/4 mip. The lower figure results from using the peaking time of the convoluted pulse. 1000 particle crossings were simulated with 1796 hits (average 1.8 strips per crossing).

(3.) An infrared (1.06 micron) laser system has been established to study the attenuation and dispersion of signals on silicon strips. By using laser light to excite transitions from the valenceband to the conductance band of the silicon detectors it is possible to simulate the passage of charged particles. The infrared diode laser produces pulses of 1 ns FWHM. The advantage of using the laser over charged particles is that the tracks produced by the laser do not have the Landau fluctuations associated with charge particles, making it possible to measure the response averaged over many pulses. Figure 7.1.1-3 displays the typical response of a microstrip detector to the infrared laser pulse after amplification of the signal with a fast, current sensitive Hewlett-Packard amplifier.To study dispersion we can pulse the detectors at different distances from the end of the strip detectors and determine how the observed signal evolves withstrip length. Figure 7.1.1-4 presents a first preliminary measurement of the signal versus the distance the laser probe is located from the end of the strip for a few strips adjacent to the principal strip. Such studies have only just begun.

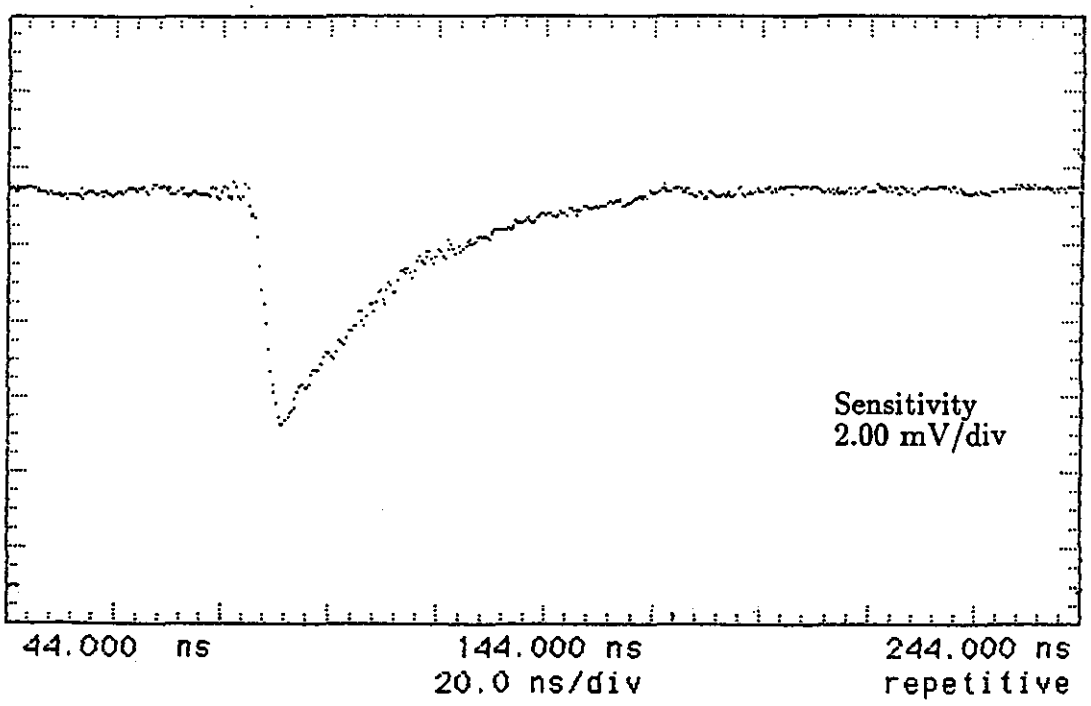

Figure 7.1.1-3: Measured average response over an 18 centimeter microstrip to the 1.06 μm laser pulse. The laser pulse has been located at the far end of the 18 centimeter strip from the fast current sensitive Hewlett-Packard preamplifier.

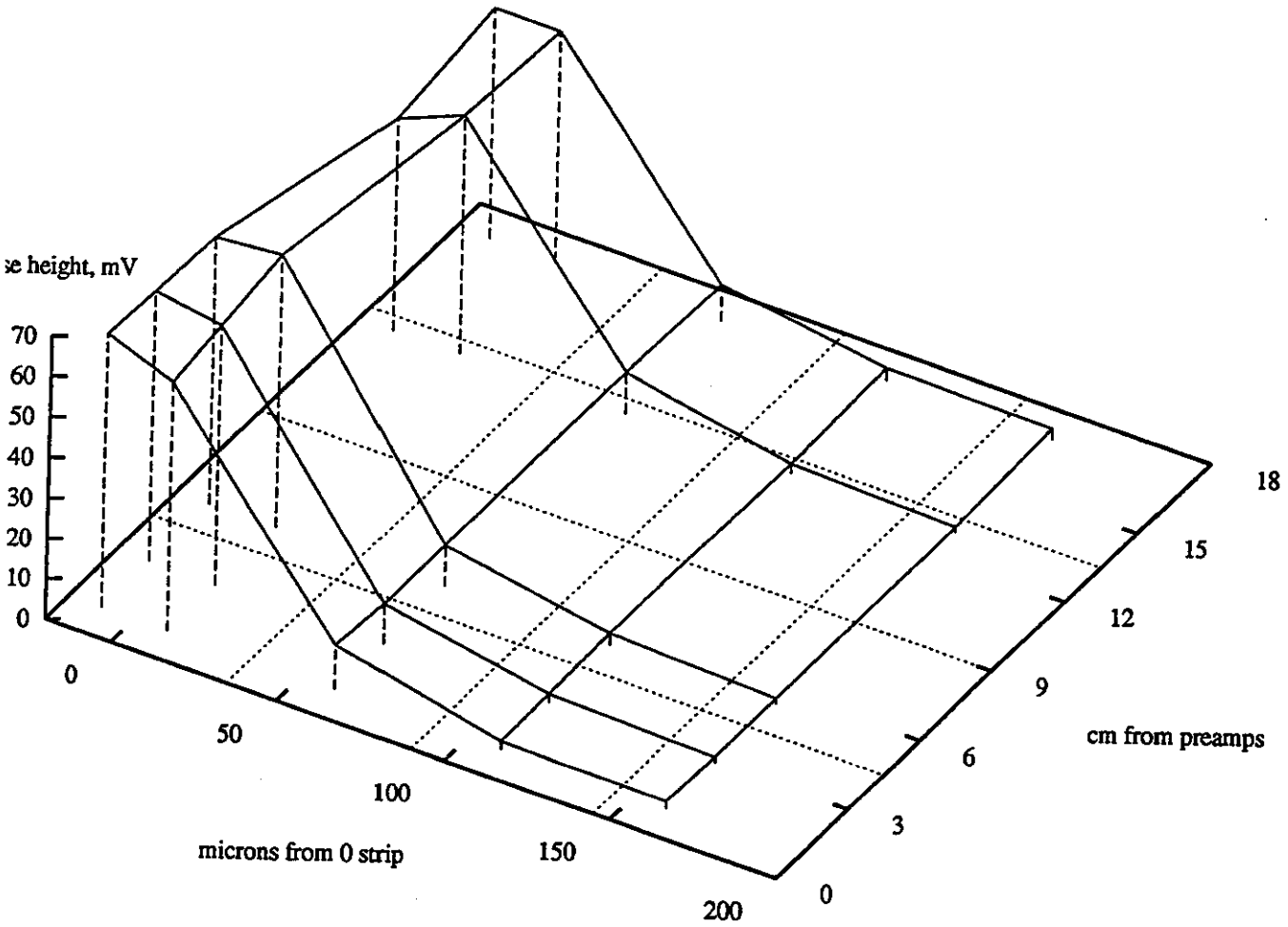

Figure 7.1.1-4: Response of charge sensitive preamplifiers to 1.06 μm laser pulse versus distance along the 18 centimeter strip for several adjacent strips.

An important element of the microstrip detector R&D, as described above, is the characterization of strip resistances and capacitances. The first such results are presented in Table 7.1.1-1. These measurements of strip resistance are based on single-sided detectors manufactured by Hamamatsu for GEM with several different strip widths on a single wafer. The strips on the detector are divided equally into groups with widths of 8 μm, 28μm, and 38 μm. The resistance of several of each of these types of strips were measured. Also a few strips with widths of 6 μm were placed on the detector, but only one ran the full length of the detector, so only one full measurement was possible. These results are consistent with a strip height of 1 μm for the wider strips assuming a conductivity of pure aluminum. It also suggests that 30 Ω/cm is possible for strips of about 10 μm width and 20 Ω/cm for strips of about 14 μm width.

Table 7.1.1-1. Measured strip resistance as a function of strip width.

width(μm)	R (Ω/cm)	ρ(Ω/cm x μm-width)
38	7.4	280
28	10.1	284
18	15.8	284
8	40.1	321
6	70.	420

Strip capacitance is also very important, perhaps more so, and coupled directly to the effort to reduce strip resistance. In microstrip detectors with 50 μm pitch the strip capacitance is typically 1-2 pF/cm, depending on strip width. The capacitance is primarily due to the coupling to neighboring strips. If a bipolar amplifier is used, the noise, in terms of electrons detected by the amplifier is given by:

$$Q_n^2 = 2e\frac{I_C\tau}{\beta} + 2\frac{(kT)^2}{eI_C\tau}C^2$$

where τ is the shaping time of the amplifier, I_C is the collector current and C is the sum of detector and input capacitance. If the second term dominates then the noise is proportional to the input capacitance. If the collector current is increased to give the minimum noise (at the cost of increased power consumption), then the noise only depends on the square root of the capacitance. In either case it is desirable to minimize the capacitance. A recent study found an increase in capacitance after irradiation at the levels expected at the SSC of about 50%. We plan to study the behavior of our prototypes before and after irradiation. We will also study what changes in fabrication techniques can be made in order to minimize the capacitance increase with radiation. Measurements of capacitance are being compared to model calculations of capacitance to understand the role of each element of the microstrip design.

7.2 IPC R&D Program

7.2.1. Chamber Development

The first stage of IPC development for the GEM Central Tracker involves addressing a number of performance issues which arise from the unique characteristics of the tracking environment at the SSC. These issues are discussed in section 4.1, and include the high beam crossing rate, high track density, and high radiation levels. This initial stage of the IPC development program, in which small IPC prototypes are used to test proof of principle, is essentially complete. Some of the key results of these studies, including the measured position resolution of an IPC prototype using fast gas and electronics, are presented in section 4.1 of this document. Further tests on these prototypes using a cosmic ray test stand will be conducted through 1993, with the primary goal of determining the position resolution of the IPCs for minimum ionizing particles in a 8 kG magnetic field. The next stage of the IPC R&D program involves the fabrication of a full scale prototype chamber, incorporating the results of the initial prototype studies, including optimal cathode layout, wire spacing, and other chamber parameters into the mechanical design. This detector will be instrumented with the same hybrid front end electronics used for the initial prototype studies. A beam test of this prototype will occur in early to mid 1993, as described in section 7.3. The key issues which will be addressed in these tests are the resolution and uniformity of a full sized prototype. Multi-track resolution will be measured, as well as single track resolution in the presence of a high rate background. During this time period the readout electronics development will progress to the point where a prototype readout system can be fabricated. The final stage of the IPC R&D program involves the integration of this front end electronics with a full scale IPC chamber. The culmination of the IPC R&D program will consist of a series of beam tests using this chamber, to take place in 1994 or 1995.

7.2.2 Generic IPC Chamber R&D

The SSC's high energy and intensity present unique requirements for the GEM detectors. The geometries of the detectors, the detector components (including fill gases) and the electronics must undergo demanding tests in prototype form before we can proceed to a final design. Over the past 17 months we have been investigating the properties of candidate drift gases and conducting tests on a prototype IPC to verify their performance in the SSC environment. This section describes some of the results of these studies.

<u>Drift Velocity and Lorentz Angle Measurements</u>

A operational requirement of the IPCs is that they have an electron collection time of order 20 nsec. At the same time, the Lorentz angle of the gas at 0.8 kG must be kept under 12 degrees, as the chambers must be canted at this angle with respect to the magnetic field to

minimize the position resolution degradation due spreading of the induced signal along the cathode. A gas mixture suitable for Central Tracker use in the IPCs must, therefore, be relatively fast, with a small Lorentz angle. These two requirements are contradictory, at least to first order, as the Lorentz angle of a gas mixture scales with the mean time between collisions of the electrons with atoms in the gas. However, mixtures of freon-14 (CF_4) and carbon dioxide (CO_2) exhibit both of these characteristics. The IU group has built a test chamber to measure these properties and have tested different ratios of these gases to find the proper optimization for the GEM IPCs. Figure 7.2.2-1 is a sketch of the chamber built to conduct these gas studies. An electromagnet was provided by the Indiana University Cyclotron Facility (IUCF) to generate a uniform magnetic field of 0.8 Tesla. A nitrogen laser (337 nm) was focused with two cylindrical fused silica lenses to provide a region of localized ionization within the drift region of the chamber. A MWPC with cathode strip readout was located adjacent to the drift region, and separated from it by a grounded mesh. The straight cathode strips were 4 mm in width on a 5 mm pitch, and were separated from the anode wires by a distance of 8 mm. The position was determined by a centroid finding method similar to that used in the prototype IPCs, and described below. The laser was used to generate ionization at three known positions, and the differences in times and measured centroid positions were then used to determine the Lorentz angle and drift velocity. The results are summarized below. Figure 7.2.2-2 shows the dependence of Lorentz angle on mixture at a fixed value for the electric field. Figure 7.2.2-3 shows the dependence of drift velocity on relative concentrations at a fixed value of the electric field. Figure 7.2.2-4 shows the drift velocity as a function of field for a 50-50 mixture, and Figure 7.2.2-5 shows the behavior of the Lorentz angle on field for a 50-50 mixture. Based on these measurements and the requirements on the IPCs, a nominal mixture of 62% CF_4, 38% CO_2 has been chosen for tests of the prototype IPC's. Further work is required to select an a gas mixture optimized for IPC use in the SSC environment. This work is part of the ongoing IPC R&D program.

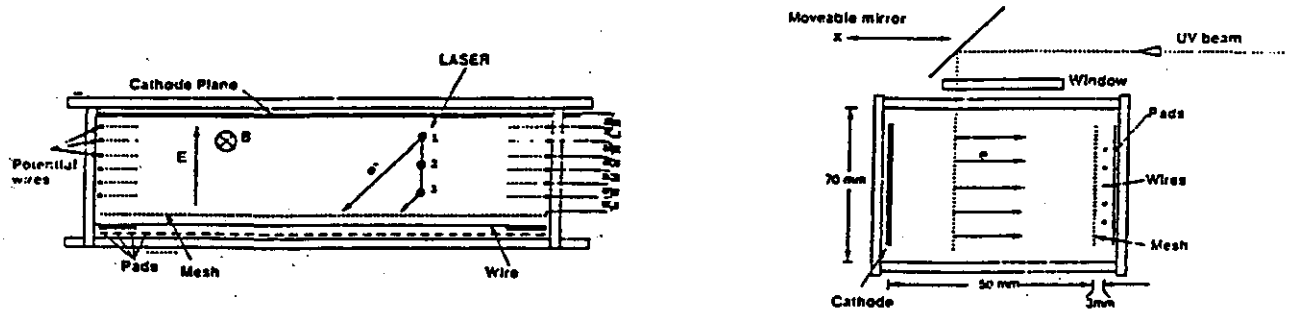

Figure 7.2.2-1: Gas Study Chamber

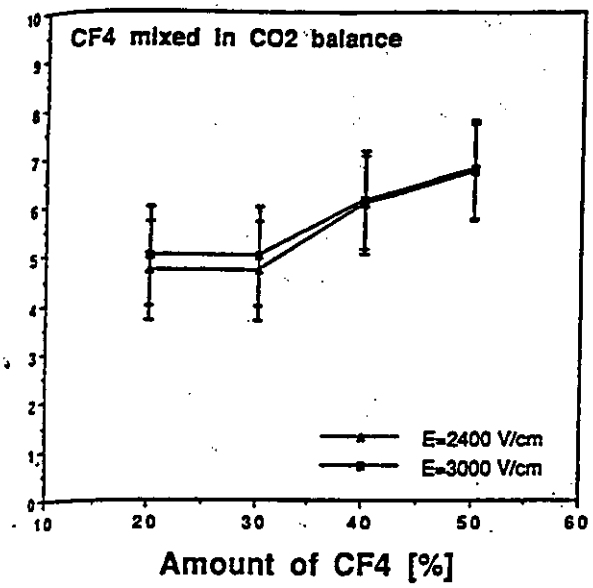

Figure 7.2.2-2: Lorentz Angle vs Freon Concentration

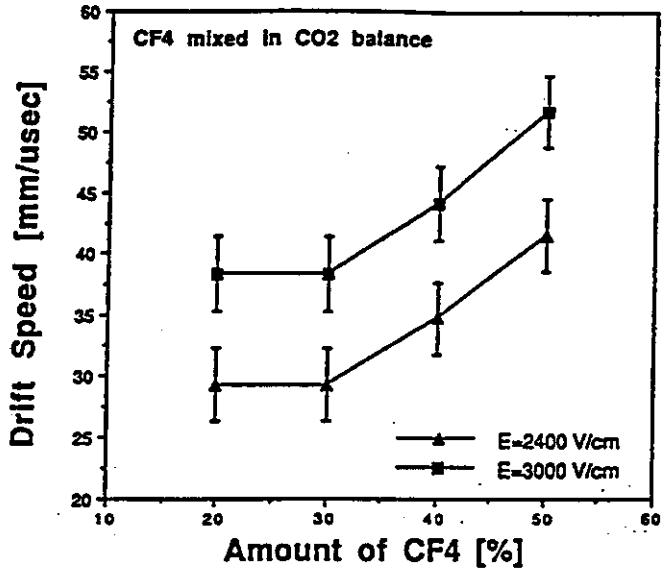

Figure 7.2.2-3: Drift Velocity vs Freon Concentration

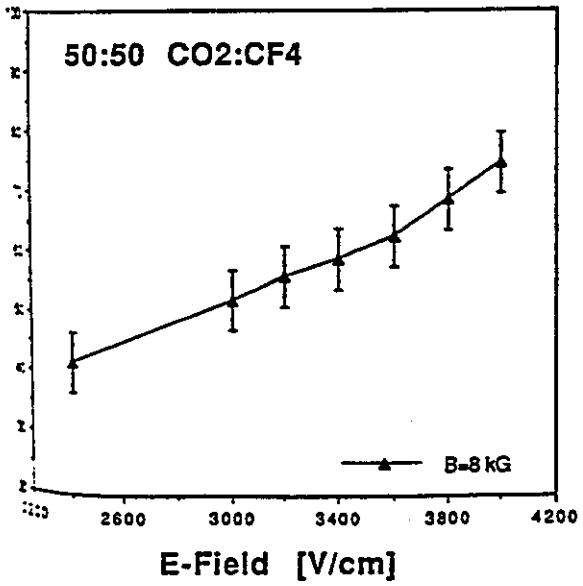

Figure 7.2.2-4: Drift Velocity vs Electric Field

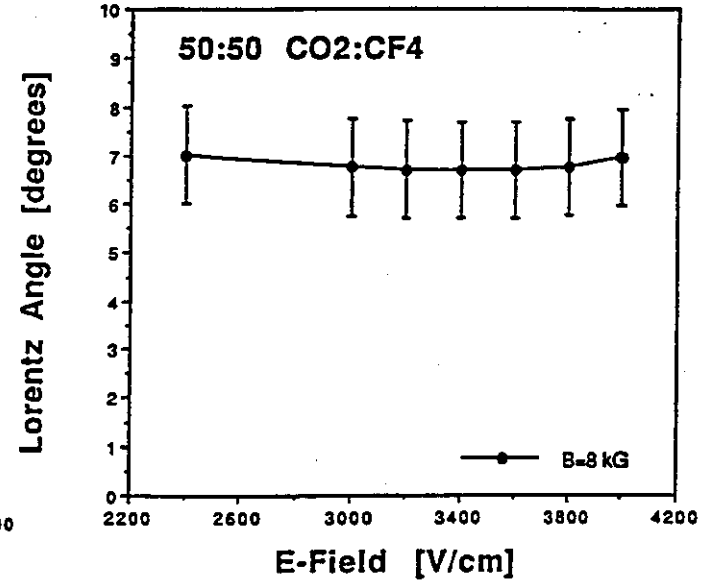

Figure 7.2.2-5: Lorentz Angle vs Electric Field

Central Tracker IPC Prototype Studies

Prototype IPC s have been designed and built at Indiana University to study the performance of these chambers for the GEM outer tracker. The initial set of tests were conducted using an X-ray source as the primary ionization source. Figure 7.2.2-6 shows a 3-dimensional assembly drawing of this chamber design. The anode wire size and spacing, the anode-cathode separation, and the cathode pitch and pad length are all taken from the GEM baseline design for the outer tracker.

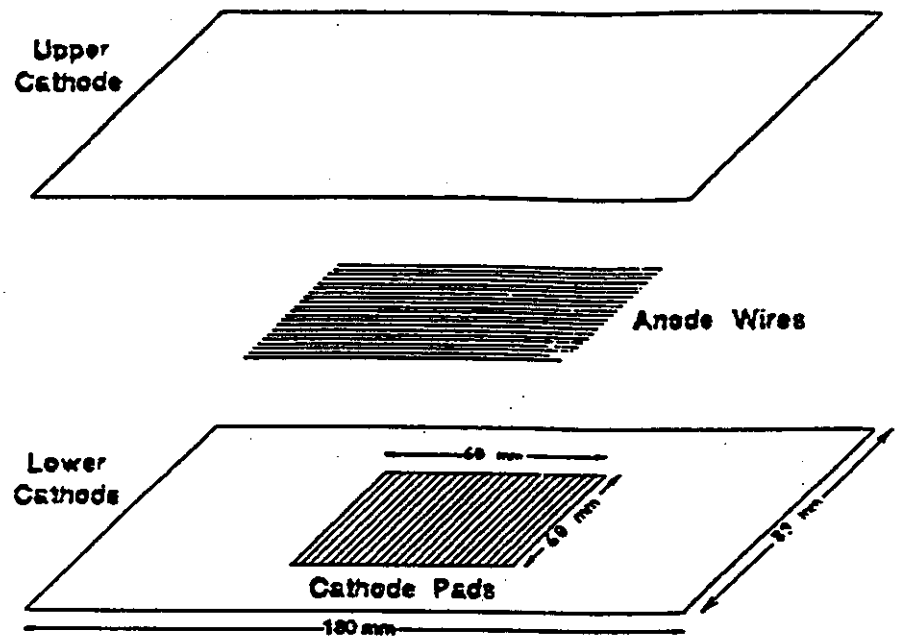

Figure 7.2.2-6: IPC Prototype

The preamplifiers and shaping amplifiers used n these studies were designed by our collaborators at the Brookhaven National Laboratory and have the fast response times required in this application. The total gain of the front end amplifiers is 10 mv/fC, and the shaper has a peaking time of 30 ns.

Most of our tests to date has been done using X-rays from a Philips-Norelco 3 kW x-ray generator. Both Copper (8 keV K-line) and Tungsten (8.4 and 9.7 keV L-lines) x-ray tubes have been used in our tests. Improved position resolution measurements is observed using the low energy (2 keV) Bremstrahlung photons from the Tungsten tube. Note that 2 keV is the expected energy loss of a minimum ionizing singly charged particle passing through the prototype IPC

when it is filled with the baseline gas mixture. A 2 cm thick brass collimator with a 25 mm wide slit was used to localize the x-ray beam and facilitate the measurements of the position resolution of the chamber.

Figure 7.2.2-7 shows the measured gain vs high voltage for our prototype IPC and a gas mixture of 62% CF_4, 38% CO_2. We have assumed an ionization yield of one electron-ion pair created for 34.3 eV of energy deposited in the gas.

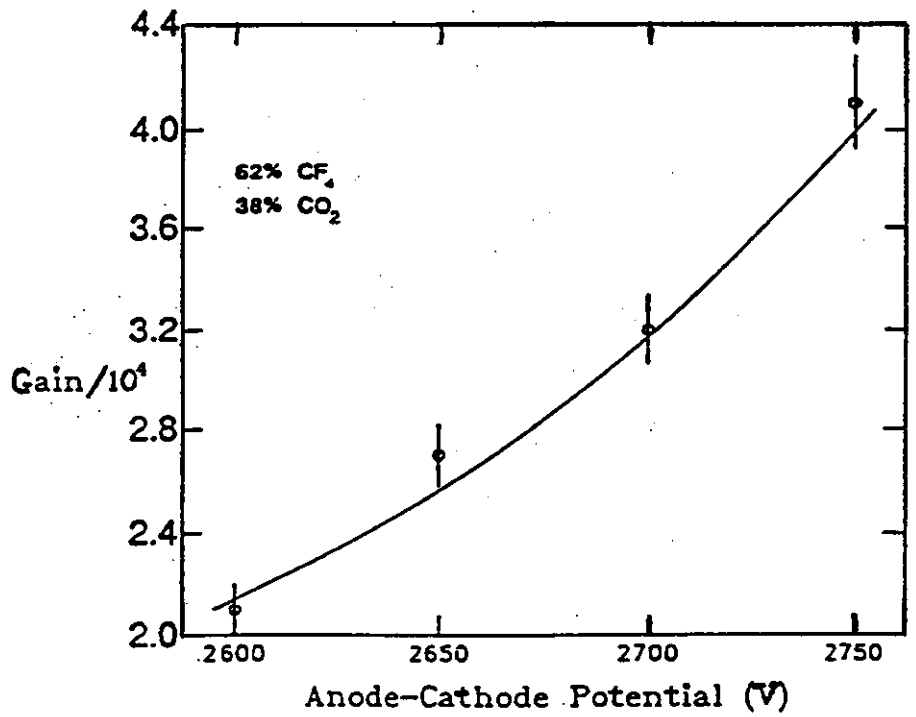

Figure 7.2.2-7: Gain vs High Voltage in IPC Prototype

The energy resolution measured on the anode and the position resolution vs gain is shown in Figure 7.2.2-8 for the prototype IPC. The minimum in the position resolution curve determines the optimum operating voltage for this gas mixture. There is a relationship between energy resolution and position resolution, as the dominant contribution to energy resolution degradation, electron recombination, also affects the position resolution. Therefore, we show the measured FWHM energy resolution as a benchmark against which to compare other gas mixtures and detector designs with known energy resolution.

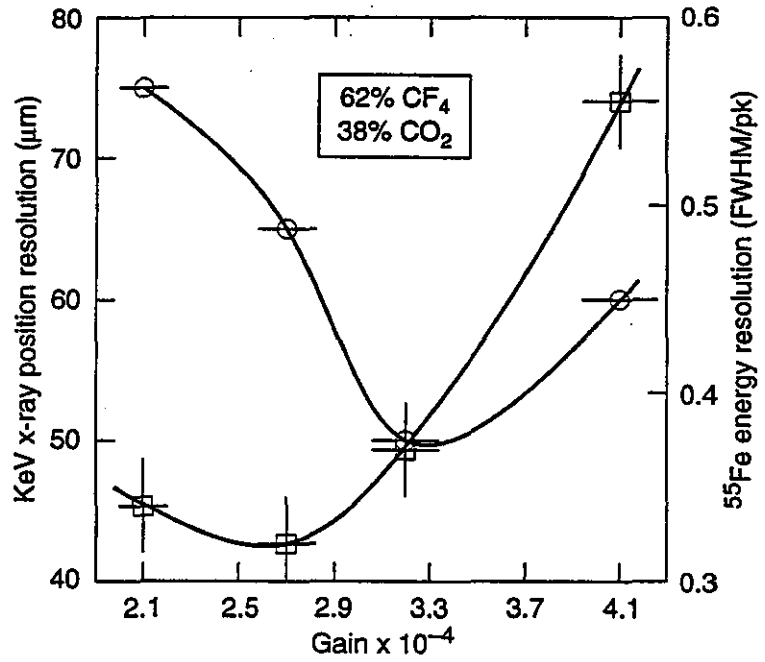

Figure 7.2.2-8: Resolution vs Gain

Due to the high beam crossing rate at the SSC, the chambers must be capable of clearing the ions generated in the chamber between events to avoid the buildup of space charge around the anode wires. We have estimated that a peak flux of 10^4 events per second per square mm of wire will occur in the innermost IPC layers during SSC operation at ultra-high luminosity (10^{34} $cm^{-2}s^{-1}$). We have measured the chamber response to Tungsten L X-rays as a function of X-ray intensity to determine the effects of space charge on chamber gain. The X-rays were transmitted through a 1 mm diameter, 6 cm long stainless steel collimator, ensuring that a uniform ionization region is produced. The chamber gain was determined to be independent of X-ray intensity to fluxes several times higher than that expected at the SSC during ulta-high luminosity operation. Further space charge studies are planned in the test beam phase of this program.

The studies conducted at IU on IPC prototypes leave a number of questions concerning their use as the GEM outer tracker still unresolved. These issues are being addressed in the FY 93 IPC R&D program. They include:

- The position resolution of IPCs for minimum ionizing particles.
- The effect of the GEM magnetic field on tracking resolution.
- Chamber aging and space charge studies.
- Tracking resolution in a high rate environment.

The IU group is now in the process of acquiring data on a cosmic ray test stand constructed for IPC prototype testing. This test stand includes a 0.8 kG magnet, obtained on loan from the IU cyclotron. The focus of the work conducted on this test stand will be addressing the issue of minimum ionizing particle resolution, and magnetic field effects. Magnetic fields oriented such that there is a component of the drift velocity vector across the cathode pads (perpendicular to the wire direction) lead to a degradation in the position resolution due to spreading of the ionization along that direction. Studies conducted at BNL indicate that tilting the chamber along the magnetic field axis at the Lorentz angle, so that the drift vector is aligned with the particle track, minimizes this effect. The position resolution in this configuration must be tested.

Preliminary Muon Test Stand Results

A muon telescope comprised of a stack of four IPC prototypes is currently taking data at the Indiana University Cyclotron Facility (IUCF). Each IPC prototype is built with the baseline GEM IPC geometry of 2 mm anode pitch and 2 mm anode-cathode spacing with pads which are 2.5 mm wide and 60 mm in length. Due to a limited supply of amplifiers, three of these prototypes are operating with an effective area of only 22.5 mm X 60 mm. The fourth chamber has its 30 anode wires ganged in groups of 5 to give a crude transverse position measurement. This fourth chamber has no cathode readout.

To date, data has been taken for cosmic ray muons in the absence of a magnetic field. In Figure 7.2.2-9, the predicted position in chamber 3 (based on the positions of the event in chambers 1 & 2) is compared with the actual position as measured by chamber 3. For these plots, we define the quantity d as the difference between the position of the event as seen by chamber 3 and the predicted position in chamber 3 based on the extrapolation of the positions in chambers 1 and 2. Figure 7.2.2-10 shows a scatter plot of d vs a, where a (measured in degrees) is the component in the measurement direction of the angle between the muon trajectory and the chamber normal. The dependence of the position resolution on a can be seen in this figure. The observed offset of the minimum in the position error from a=0 is not completely understood at this time, and is under investigation. A histogram of d values for the range $-6 < a < 12$ degrees is shown in Figure 7.2.2-11. A statistical factor of 1.63^{-1} should be applied to the standard deviation of this distribution to obtain the implied resolution of the third chamber. Although this analysis is still underway, this preliminary result shows resolutions consistent with 50 microns for normally incident, minimum ionizing particles.

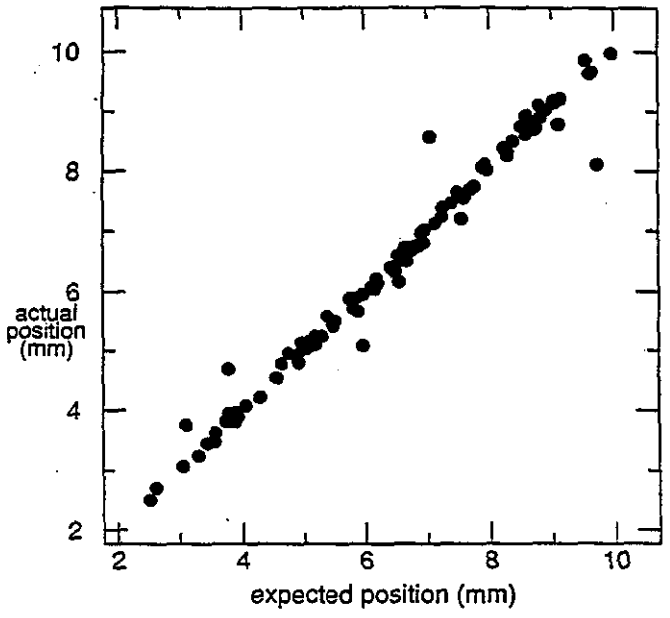

Figure 7.2.2-9

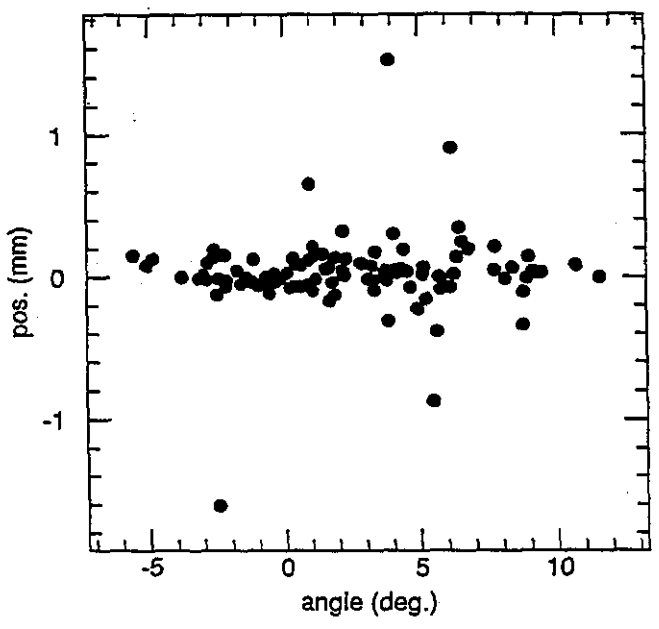

Figure 7.2.2-10

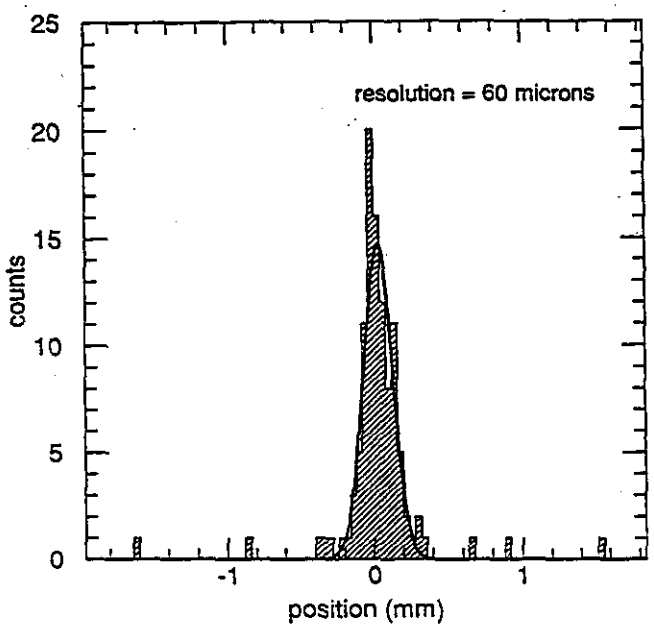

Figure 7.2.2-11

7.2.3. IPC Mechanical R&D

Engineering of the IPC chambers will be conducted at Yale during FY 93. The goal of this program is the construction of a full scale mechanical prototype of a barrel IPC during early FY 93. In addition, Yale will carry out a design study of the mechanical support for the IPC system. Included in this program is the evaluation of low mass, low temperature coefficient materials suitable for use in the chamber and support structure.

7.2.4. The Full Scale IPC Prototype Project

Introduction

The performance of the Interpolating Pad Chamber relative to the physics' needs of the central tracker was demonstrated by a small scale prototype built at Indiana University. Several parameters of the IPC prototype were measured, such as the spatial resolution, drift velocity of the gas system and the rise time of the cathode pad signal.

In order to insure that the above performance is achievable by an actual IPC, a full scale IPC prototype effort is undertaken at Yale University along with the active participation of the collaborating institutions. In addition, other goals were sought, such as testing and refining the details of the actual mechanical construction and their impact on the chamber's performance. Therefore, it is necessary to construct this prototype using up to date "final" mechanical designs and materials.

Overview of the IPC Full Scale Prototype Project

The mechanical designs of the IPC which were dictated by space and stability requirements, were adjusted to account for the electrostatic specification of the system. (See Chapter Four.) The construction of the prototype followed in detail the actual mechanical design, and in return provided a constant feedback which helped finalize that design.

The full scale prototype project is divided into four parallel efforts namely *prototype one through four*. Each manifested a step toward the construction of the actual IPC system. (See Table 7.2.4-1.)

Prototype one consists of a small, (20 cm x 30 cm), IPC system which equals the width of the final full scale system but it is about six times shorter. The construction of this prototype was a natural start, since the actual full scale IPC system is uniform along its length and most of the mechanical and electrostatic property of the chamber is related to the construction details along its width. Materials available in stock and similar (or identical) to the actual materials were used in order t o expedite the construction cycle. For instance, the printed circuit board (cathode pad board), the anode rails and cathode rail support were all made from G10 or/and FR4. On the

other hand Nomex honeycomb is used for the hard back and an aluminized Mylar is used for the cathode window. By constructing this prototype we expect to learn about the subtle details which directly affect the chamber performance, such as the connection of the anode wires to its rail support, the effects of various schemes in constructing the cathode window and the distribution of the high voltage power.

Table 7.2.4-1: Yale University full scale prototype projects

	Prototype 1	**Prototype 2**	**Prototype 3**	**Prototype 4**
Materials	G10 (FR4)	ASTRO	G10 (FR4)	ASTRO
Dimension	30 x 20 cm	30 x 20 cm	200 x 20 cm	200 x 20 cm
Pad Length	10 cm	10 cm	10 cm	10 - 20 cm
Electronics	BNL / Indiana/Yale	BNL / Indiana/Yale	Indiana/Yale	Indiana/Yale
Cathode Window	Mylar + Al, Cu Kapton + Cu, Au	Mylar + Al, Cu Kapton + Cu, Au	Mylar + Al, Cu Kapton + Cu, Au	Mylar + Al, Cu Kapton + Cu, Au
Honeycomb	1/4" Nomex	1/4" Nomex	1/4" Nomex	1/4" Nomex
Laminating Location	Yale	Industry/Yale	Yale	Industry/Yale
Date Needed /Expected	April 93	May/June 93	May 93	Summer 93
Status	Under test and evaluation	Ready for laminating Copper skin	Under construction	On hold, pending result from prototype two.

Prototype two is basically identical to the previous prototype in the mechanical and electrical aspects. The only difference here is that G10 (or FR4) is replaced by ASTRO QUARTZ the actual material proposed for the construction of the IPC modules. Obviously the purpose of building this prototype is to evaluate the impact (if any) of introducing ASTRO QUARTZ on the mechanical construction and on the chamber performance in general.

Prototype three is a real full scale prototype, (20 cm x 200 cm). Similar to the philosophy of prototype one, it is constructed from readily available materials such as G10 (FR4) etc. Obviously, the goal of building this prototype is to test and learn about the mechanical details needed to maintain the performance of *prototype one*. This particular prototype will be used in the approved AGS test beam run this year (see test beam section).

Prototype four is identical to prototype three but it is made from ASTRO QUARTZ which naturally makes it the ultimate goal for this prototype effort. Again one would like to compare and study the difference, (if any) between the construction of this prototype and *prototype three* which uses standard materials (G10 or FR4).

Progress and Future Plans

Naturally the start was with the construction of *prototype one*. Most of the construction details were worked out during this stage of the prototype project. A vacuum pack system was developed to laminate the G10 boards on the honeycomb core to produce the hard back of the IPC system, and a complete small scale chamber winding system was constructed. Several chambers were wound successfully. Furthermore, an anode rail design was worked out which called for segmented high voltage distribution to the anode wires and a detailed design of the gas plenum which allows the gas to flow on either sides of a cathode window is finalized. A recent completed IPC *prototype one* showed a promising success with its initial high voltage test. For instance, the leak current was measured to be less than 20 nA at 3000 v applied to the anode wires. Other tests are underway or planned to determine the rest of the performance parameters, such as measurements of the chamber gain and its uniformity throughout the active area of the chamber. These tests are underway at Yale University. Measurement of the spatial resolution using a collimated X-ray source will take place at the instrumentation group facility at BNL. On the other hand, a version of this prototype will be sent to the Los Alamos group to test a prototype for the IPC recycling gas system. Another version will be sent to SSC laboratory where it will be used in debugging and setting up the data acquisition system designed for the AGS test beam run this year.

In the case of *prototype two*, samples of the ASTRO QUARTZ are made into boards by the Los Alamos group, each about 0.05 cm x 20 cm x 30 cm . These boards will be sent out to a commercial vendor to be laminated by copper, then placing the pad pattern on them will be done via a standard printed circuit boards technique.

Prototype three is under construction. Basically, all the steps of building the first prototype is scaled up. For instance, an initial laminating test of a 200 cm long hard back using several printed circuit boards on a Nomex honeycomb proved to be a success. In this test several small boards of G10 (20 cm x 30 cm) are bonded next to each other and laminated on a honeycomb core to produce the 200 cm hardback. One should note, that the decision to use the segmented board is done to take advantage of the relatively fast manufacturing time and the low cost of these boards. However, in *Prototype four* the IPC hard back will be built from a continuous skin (not several segments) laminated on Nomex honeycomb core. In addition, the winding system is upgraded to handle two meters long chambers. Furthermore, a recent test of the proposed winding scheme yielded very positive results. No doubt that by now one can feel the benefits gained from building the previous IPC prototypes. This prototype will be subjected to the same testing and evaluation steps used to evaluate its predecessor. However, the spatial resolution and its uniformity along the entire length of the chamber will be studied extensively during the upcoming AGS test beam run, (see the next paragraph). Finally, *Prototype four* is on hold pending the results from *prototypes two and three.*

7.2.5. Interpolating Pad Chamber Electronics R&D

The FY 93 R&D program of IPC electronics development is presently divided into four areas. These are the front end amplifier design, development of a rad-hard analog memory, evaluation of a rad-hard FADC, and the design of the overall readout architecture. Details of the progress to date are presented in the Electronics section of the GEM TDR and are summarized below, along with the program of future development work.

A prototype preamplifier and shaping amplifier for use in the IPCs has been developed by the instrumentation group at BNL. This design is presently being fabricated in the Harris rad-hard AVLSI-RA CMOS process. Initial rad-hard prototypes will be available for testing in mid 1993. At this point, BNL will carry out a series of tests to evaluate the performance and radiation tolerance of this device.

The development of the rad-hard analog memory is being carried out by a group at Oak Ridge National Laboratory . A prototype 8 channel by 128 deep device has been developed by ORNL in the AVLSI-RA process, and is being fabricated in conjunction with the BNL amplifier. Testing of these prototypes will be conducted by ORNL in mid 1993. The development of the amplifier and analog memory will then proceed through a series of three fabrication cycles, during which the designs will be refined. A final pre-production fabrication run will occur in late 1994, prior to the start of full production.

A FADC developed by Harris in the the AVLSI-RA process is being tested by a group at the University of Michigan, using a FADC test facility being made available to them by Ames Research Laboratory. A full performance evaluation is being conducted at various ionizing and neutral radiation levels. Initial results indicate that this device maintains its specified performance to a dose of at least 2 Mrads, and therefore appears suitable for use in the outer tracker.

A readout controller prototype for the IPCs is being developed at Indiana University. The design and layout of the initial prototype controllers, which utilize Xilinx FPGAs, is now complete. The use of FPGAs will allow modifications to the readout to be made in a straightforward way during the initial development stage. This readout controller prototype will be combined with the rad-hard amplifier, analog memory, and FADC prototypes in a prototype readout system to be fabricated during 1993. The readout system prototype will be used in conjunction with full scale chamber prototypes in a series of beam tests, as described earlier. In 1994, the readout controller design will be implimented in a LSI Logic rad-hard gate array, and combined with the final versions of all front end readout devices in a pre-production readout card, which will be available for testing in early 1995. The milestones identified for the development of the IPC electronics are summarized in the GEM Central Tracker Subsystem Schedules at the end of this chapter.

7.3. Test Beam Plans

7.3.1. Silicon Detectors

Because silicon detector performance cannot be readily factorized from electronics performance, a beam test cannot be expected to yield meaningful results on the key questions of resolution and rate capability until realistic prototypes of detectors and electronics are available. We expect this to be possible beginning mid-1993. Wherever possible, silicon beam tests will be made in conjunction with IPC tests. The silicon group also will provide a telescope of standard silicon detectors and SVXD electronics for the IPC tests, starting in 1993.

We expect to begin receiving prototype silicon detectors from Hamamatsu, Taiwan, and Moscow during the first half of 1993. In addition, some of the Bipolar ASIC prototype electronics should become available during this time. These could possibly be used in the Brookhaven test beam in Summer 1993. However, we anticipate that a full beam test of detectors and electronics will not occur until 1994. At this time we will measure resolution, and signal response and noise, as a function of rate for various detector and electronics configurations. We assume that refinements of design will warrant additional test beam running in 1995.

<u>The AGS Test Beam Run</u>

A complete test beam run using *Prototype three* will be carried out in the summer of 1993 at the AGS newly commissioned test beam line, B2. The goals of this run are

- To study the intrinsic spatial resolution of the pad system and its uniformity over the active region of a full scale IPC module.
- To study single track resolution using several planes of full scale IPC.
- To study the overall performance of the IPC system under more realistic experimental condition.

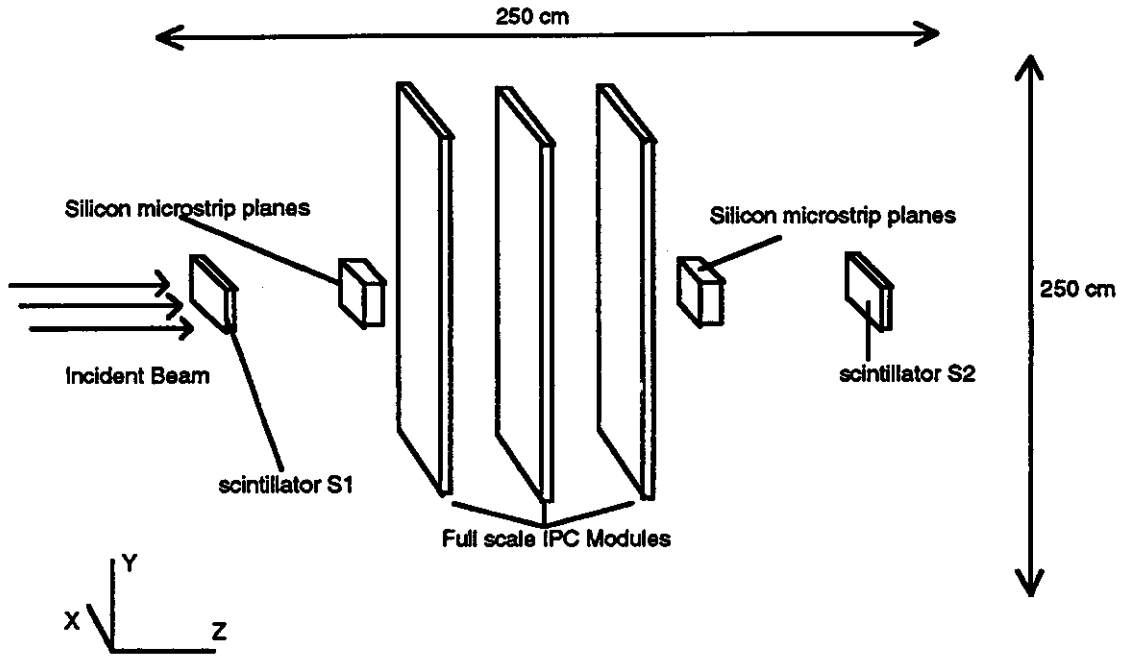

Figure 7.3.1-1: Experimental setup for the full scale IPC test beam run.

The AGS Test Beam B2 and the Experimental Setup

The AGS beam test line B2 is a secondary beam line. Particles are produced when a 24 Gev/c primary beam strikes a production target which is usually 7.5 cm x 0.6 cm x 0.6 cm Beryllium rod. The produced particles are extracted at a 6.0 degree angle and transported to the experimental area via the secondary beam line B2. The maximum fields of the bending dipoles in the beam line set the upper limit on the beam momentum to be 9 Gev/c. The lower momentum bond is 1 Gev/c and is set by the regulating quality of the magnets power supplies. An AGS calculation using RAY TRACE showed that beam size changes as a function of the position relative to the last quadrupole. For instance, the beam size at 250" from the last quadrupole is about 0.27" wide (along the X direction) and 0.05" high (along the Y direction), however, it has a maximum full widths of 1.4" along the horizontal direction and 0.2" along the vertical direction. Due to the nature of the secondary beam line, both hadronics and leptonics components are present in the beam. However, two Cerenkov detectors placed in the beam line will provide an electron ID tag. Particle flux will be limited by the radiation safety requirements of the experimental area which limit this flux to about 6 million particles per spill. The fraction of electrons in this beam is about 1-2% at about 1 Gev/c and drops off to about 0.1-0.2% at 5 Gev/c.

The experimental setup for the full scale IPC test beam run is fairly simple and straight forward. Three full scale IPC modules (*prototype three*) will be set vertically in the beam line separated roughly by about 20 cm, similar to the actual separation in the GEM central tracker system. (See Figure 7.3.1-1.) The vertical placement is chosen to allow a maximum beam spread across the pad system in an IPC. In addition silicon microstrip planes will be placed in front and behind the IPC modules to provide a beam defining telescope system. Scintillator counters S1 and S2 will provide a beam trigger signal for the overall trigger logic.

The basic idea of the test beam setup is to define the beam via the silicon telescope which is capable of about 10 micron resolution. Thus, the telescope provides a direct mean of measuring the intrinsic resolution of an IPC, which is expected to be on the order of 50 microns. No calculation or correction, just a straight forward measurement. However due to the relatively low energy of the beam line, the position of the silicon telescope relative to position of the IPC planes along the beam axis should be considered carefully in order to minimize the multiple scattering effects on the measured resolution. Therefore, several schemes of the experimental setup are under investigation via Montecarlo simulation by University of Albany and University of Michigan groups.

The silicon telescope will be provided and commissioned by groups from University of Albany and Los Alamos National Laboratory. On the other hand, the data acquisition system trigger electronics and the on line analysis system are designed and commissioned by the SSC Laboratory group. The IPC readout electronics will be provided by Indiana University and the Brookhaven group. In addition, a prototype for a recycling gas system for the IPC will be tested and evaluated by the Los Alamos group.

During the recent AGS test beam users meeting held on March 26, 1993 a final schedule of the test beam was worked out. According to this schedule the IPC test run will take place during weeks six, seven and eight of the AGS run. However, the central tracker team will share the space available and the beam time with several other users of the test beam at that time. Nevertheless, it was possible to find a common setup scheme for all users of the test beam during the above period, which allows (almost) simultaneous run time for most users. Figure 7.3.1-2 shows the overall experimental setup arrangement. This arrangement is a direct consequence of the nature of the various tests carried out by the different groups and it is obvious and self explanatory.

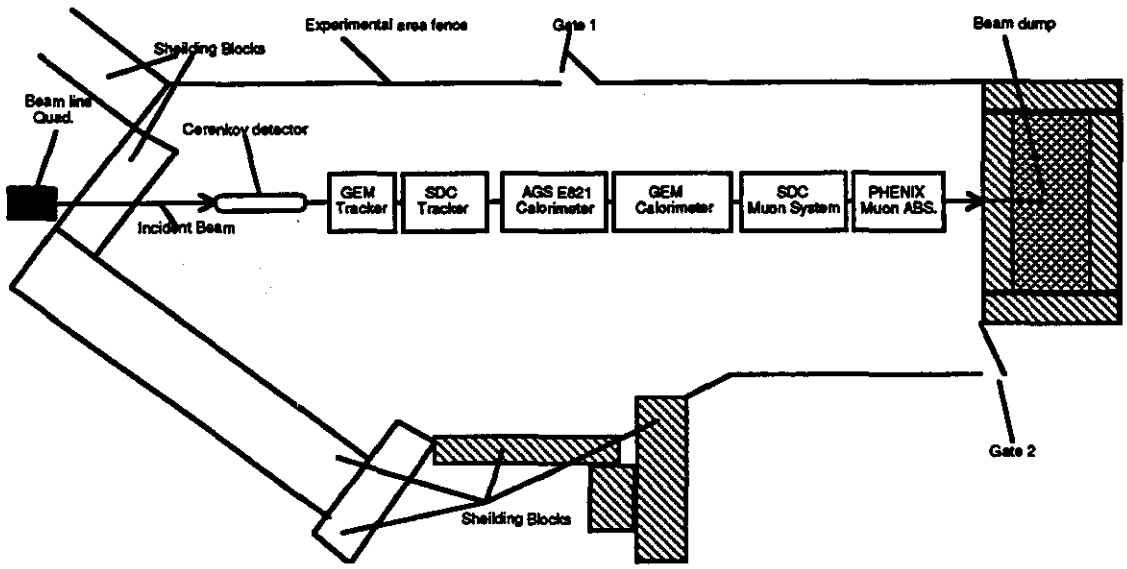

Figure 7.3.1-2: The over all experimental setup at the AGS beam line B2, during the IPC test beam run.

Table 7.3-1: GEM Central Tracker Silicon Test Beam Needs 1993 - 1995

Time	Device/Test	Beam Parameters	Required Beam Time
late 1993	Possible tests of new detectors in conjunction with bench tests	Low rate secondary beam.	2 weeks
1994	Full resolution and rate tests of prototype detectors and front-end electronics	Charged pions of at least 5 GeV/c to high rate (10^8 Hz over few cm^2); few GeV/c electrons. Use nearby Si triplets for resolution; Si telescope for external reference.	2 months
1995	Follow-up of above tests, including tests of engineering prototype units	same as above	2 months

Table 7.3-2: GEM Central Tracker Interpolating Pad Chamber Test Beam Needs 1992 - 1995

Time	Device/Test	Beam Location or Parameters	Required Beam Time
mid 1992	Operating parameters of a small chamber	low rate secondary beam, a few hundred MeV e's, μ's, π's	1 month
early 1993	Resolution of full sized prototype of barrel pad chamber, scan over the full length of the device	e's, μ's, π's of a few GeV, protons ≥ 5 GeV, rate: a few particles/sec.well collimated beamwith position measurement	3 months
early 1994	Rate capabilities of full sized prototype, both barrel and end caps	high rate secondary beam $\sim 10^9$ particles/sec. which can be spread over $\sim 30 cm^2$ in the chamber	3 months
1995	Systems Tests: gas, cooling, mechanics, etc. of final design, with final electronics	same as 1994	3 months

8. ORGANIZATION & MANAGEMENT

8.1. The Central Tracker Group

The GEM Central Tracker group consists at this time of 13 Institutions and over 110 scientists. They are as follows:

Academia Sinica, Taiwan, R.O.C.

Brookhaven National Laboratory

Indiana University

Los Alamos National Laboratory

Moscow State University

Nanjing University

Oak Ridge National Laboratory

Rutgers University

Superconducting Super Colliding Laboratory

University of Albany

University of Michigan

University of Oregon

Yale University

The management of the Central Tracker Project and the technical design is performed by the Central Tracker Steering Committee, which consists of the following scientists:

Central Tracker Steering Committee C. Baltay, J. E. Brau, D. Lee, S.C. Lee, K. Morgan, J. Musser, T. Thompson

The chairman of the Steering Committee is C. Baltay. The chief engineer for the Central Tracker project is T. Thompson. Budgeting support is provided by H. Pretty. The GEM Central Tracker Organization Chart is shown in Figure 8.1-1.

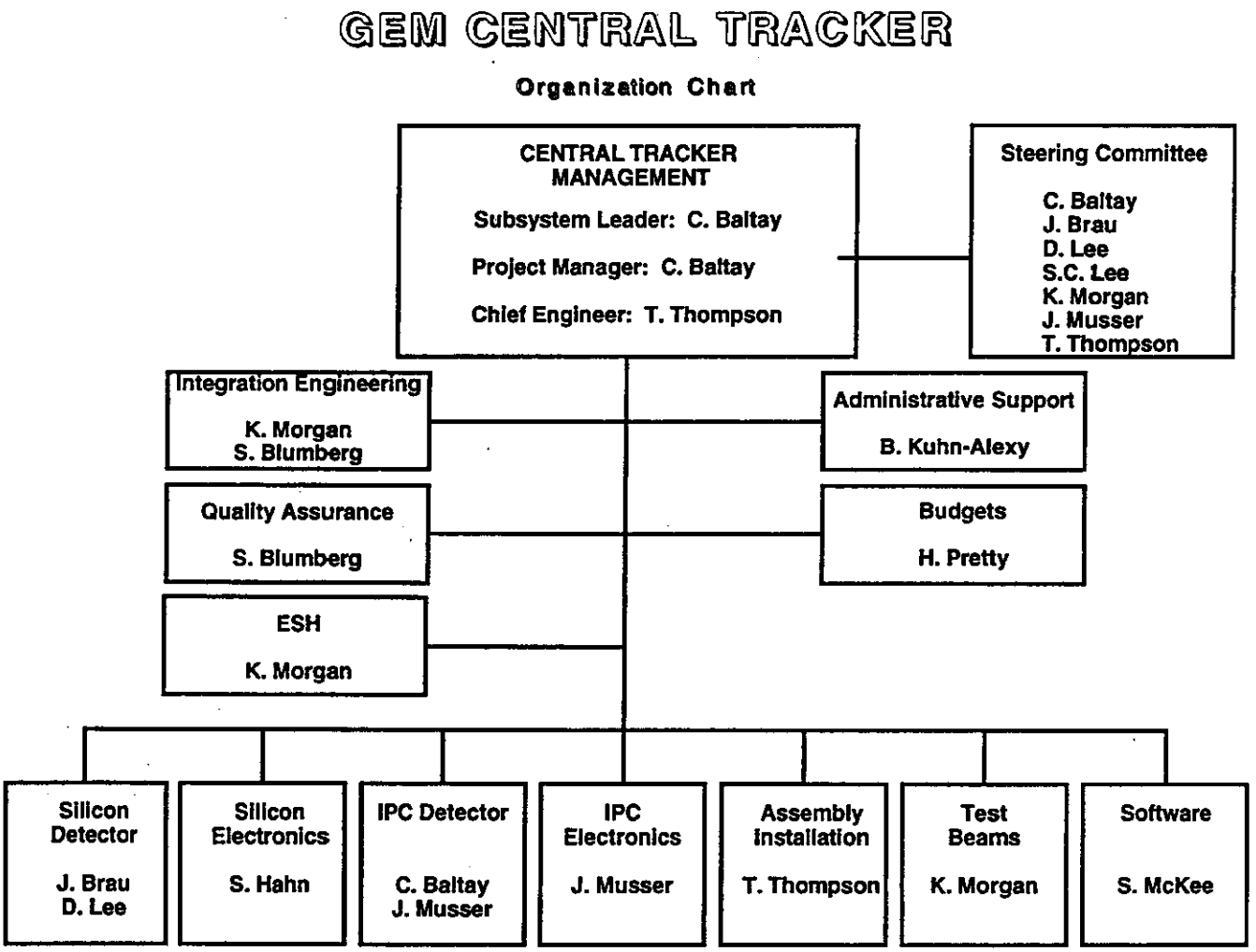
GEM CENTRAL TRACKER
Organization Chart
CENTRAL TRACKER MANAGEMENT
Subsystem Leader: C. Baltay
Project Manager: C. Baltay
Chief Engineer: T. Thompson
Steering Committee
C. Baltay
J. Brau
D. Lee
S.C. Lee
K. Morgan
J. Musser
T. Thompson
Integration Engineering
K. Morgan
S. Blumberg
Administrative Support
B. Kuhn-Alexy
Quality Assurance
S. Blumberg
Budgets
H. Pretty
ESH
K. Morgan
Silicon Detector
J. Brau
D. Lee
Silicon Electronics
S. Hahn
IPC Detector
C. Baltay
J. Musser
IPC Electronics
J. Musser
Assembly Installation
T. Thompson
Test Beams
K. Morgan
Software
S. McKee

Figure 8.1-1

8.2. Personal and Institutional Responsibilities

At the present time the effort on the Central Tracker consists mostly of R & D, detailed engineering design, and computer simlations of the performance of the detector. The personal and institutional responsibilities for this effort have been defined and is shown in Table 8-1. below. Engineering responsibilities are as shown in Table 8.2-2 and 8.2-3.

Table 8.2-1: Personal & Institutional Responsibilities

Area of Effort	Person Responsible	Institution Involved
Silicon Detector	D. Lee, J. Brau	Los Alamos Nat. Lab. U. of Oregon
-Mechanical	T. Thompson	Taiwan Moscow State
-Electronics	S. Hahn	
Pad Chambers	J. Musser, C. Baltay	Brookhaven Nat. Lab. Los Alamos Nat. Lab.
-Mechanical	W. Emmet	Yale U. Indiana U.
-Electronics	J. Musser, P. O'Connor	U. of Michigan Rutgers U. Taiwan
Integration into GEM	K. Morgan T. Thompson	All
Simulations	S. McKee	All
Beam Tests	K. Morgan	All
Budgets	H. Pretty	All

Table 8.2-2

GEM Central Tracker Engineering Responsibilities

Mechanical--Group A

Overall Coordination: T. Thompson

TASK	ENGINEERING STAFF
1) Silicon Tracker	T. Thompson
a) Support & cooling rings, ladders, etc.	T. Thompson, R. Barber
b) Support frame	T. Thompson
c) Cooling & gas flow	R. Barber M. Young
d) Alignment & monitoring	B. Smith
e) Cabling	R. Barber, B. Cooke
2) IPC Tracker	W. Emmet
a) Chamber modules	W. Emmet, D. Pilon
b) Support structure	D. Pilon, R. Hinckley
c) Cooling and gas flow	R. Martin
d) Alignment & monitoring	B. Smith
e) Cabling	W. Emmet

Table 8.2-3

GEM Central Tracker Engineering Responsibilites

Electronics--Group B

Overall Coordination: (Jim Musser)

TASK	ENGINEERING STAFF
1) Silicon Detector	S. Hahn
a) Detectors	R.T. Kollipara
b) Front end amplifiers	S. Hahn
c) Digital pipeline (CMOS1)	B. Cooke
d) Readout controller (CMOS2)	B. Cooke, R.T. Kollipara
e) Multichip module (MCM)	B. Cooke
f) Fiber optics/Power Dist.	B. Cooke
2) IPC Electronics	(Jim Musser)
a) Front end amplifiers	P. O'Connor
b) Switched capacitor array	C. Britton
c) ADC, Multiplexer	J. Mann
d) Readout controller	C. Bender
e) Fiber optics/Power Dist.	C. Bender

9. SCHEDULES

The first version of the GEM Central Tracker schedule is shown in Figure 9-1. We envision a three-year conceptual design and R & D period, 1992, 1993 and 1994. The bulk of the detailed engineering design will also take place during these three years, although some engineering design will stretch out through 1997. Building and testing of various prototypes will also take place from 1992 to 1994.

The construction of the various components of the tracker is anticipated to take place at the various collaborating institutions away from the SSC site over a four-year period from 1994 to 1997. The various components will be shipped to the SSC Lab and the assembly of the central tracker will occur in the surface building designed for this purpose at the experimental site between mid 1997 and mid 1998. Calibration, alignment and various test activities will also take place during this year.

We expect that the complete central tracker, including the pad chambers and the silicon detector, will be installed in GEM in mid 1998. This will be followed by a year of finishing up the cabling, cooling, and gas connections and the final commissioning of the detector. The schedule calls for the detector to be ready for data-taking by mid 1999. This schedule will be refined and updated as appropriate as the central tracker, the GEM detector and the SSC collider progress.

The schedules for the mechanical and electronics efforts on the Silicon Detector and the mechanical and electonics efforts on the IPC Detector are shown in Figures 9-2, 9-3, 9-4 and 9-5.

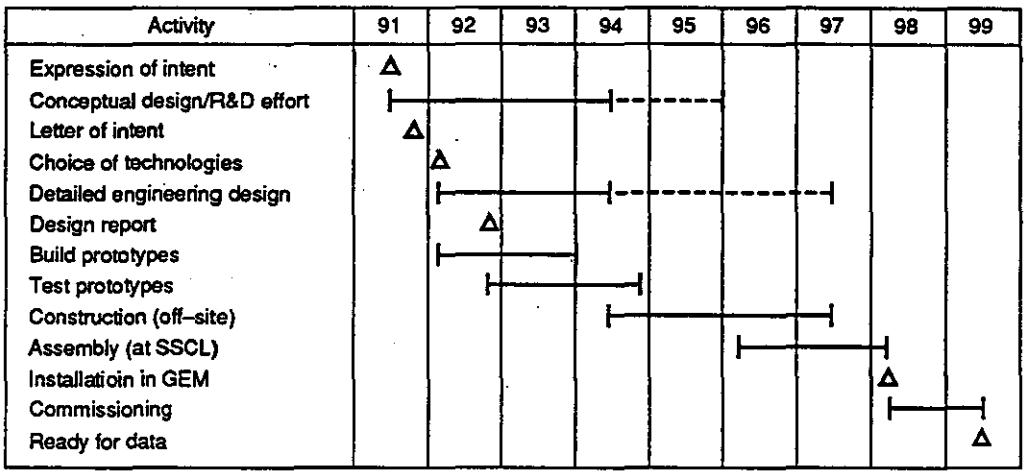

Figure 9-1 Central Tracker Summary Schedule

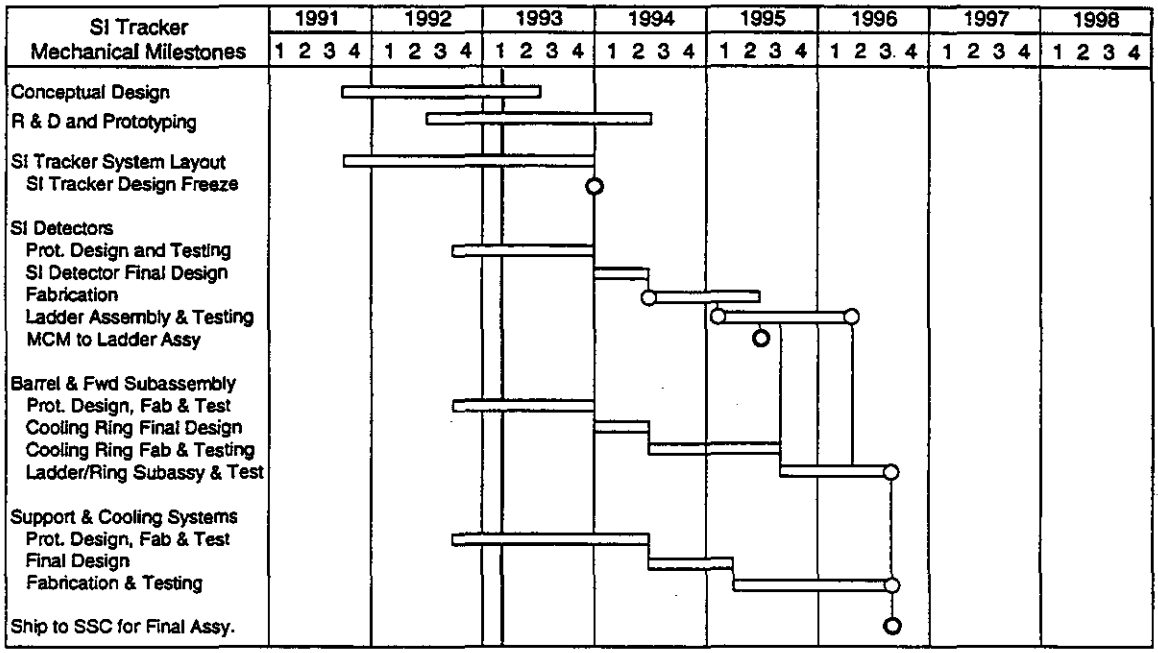

Figure 9-2 Silicon Tracker Mechanical Schedule

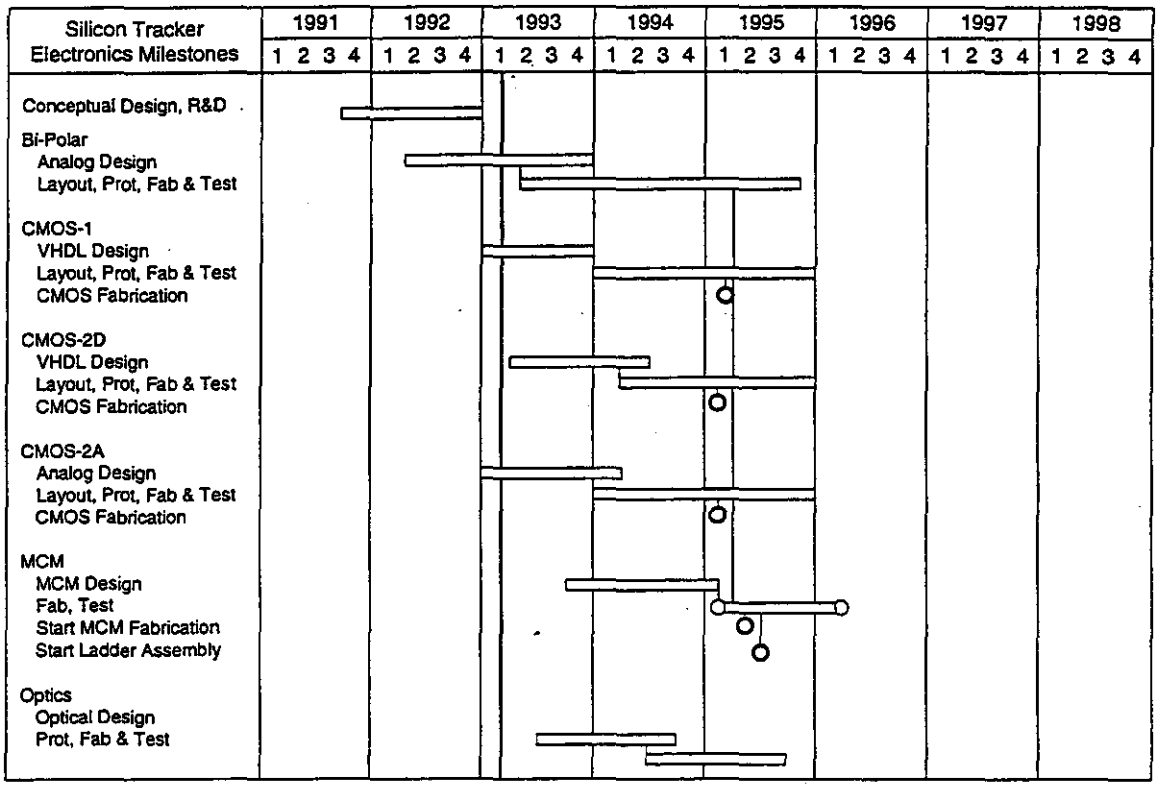

Figure 9-3 Silicon Tracker Electronics Schedule

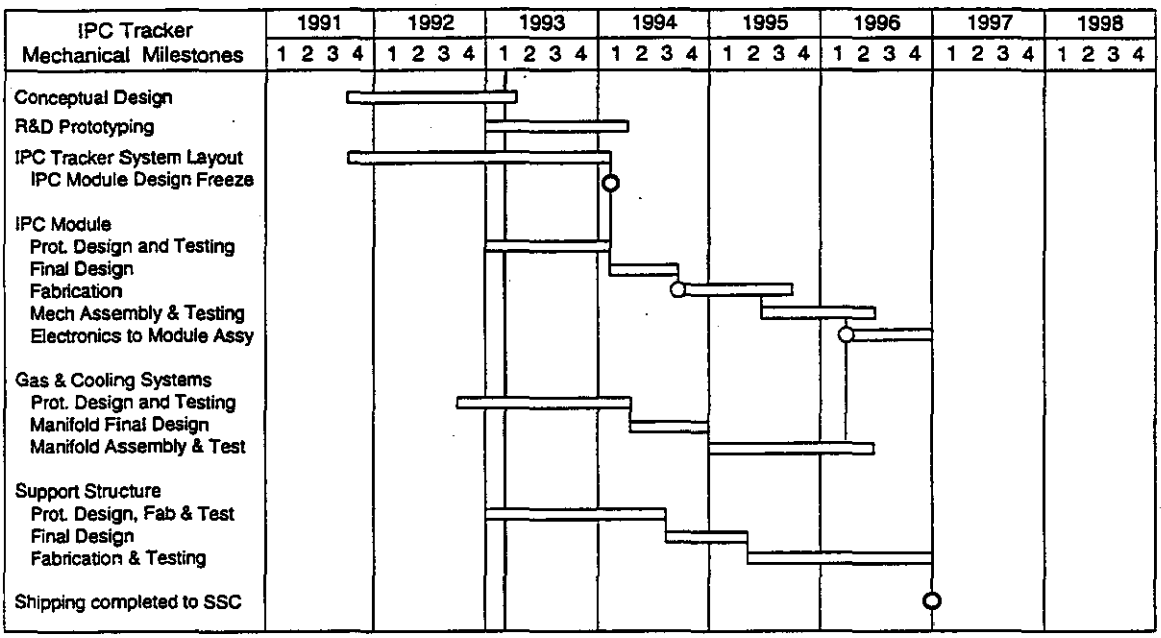

Figure 9-4 IPC Tracker Mechanical Schedule

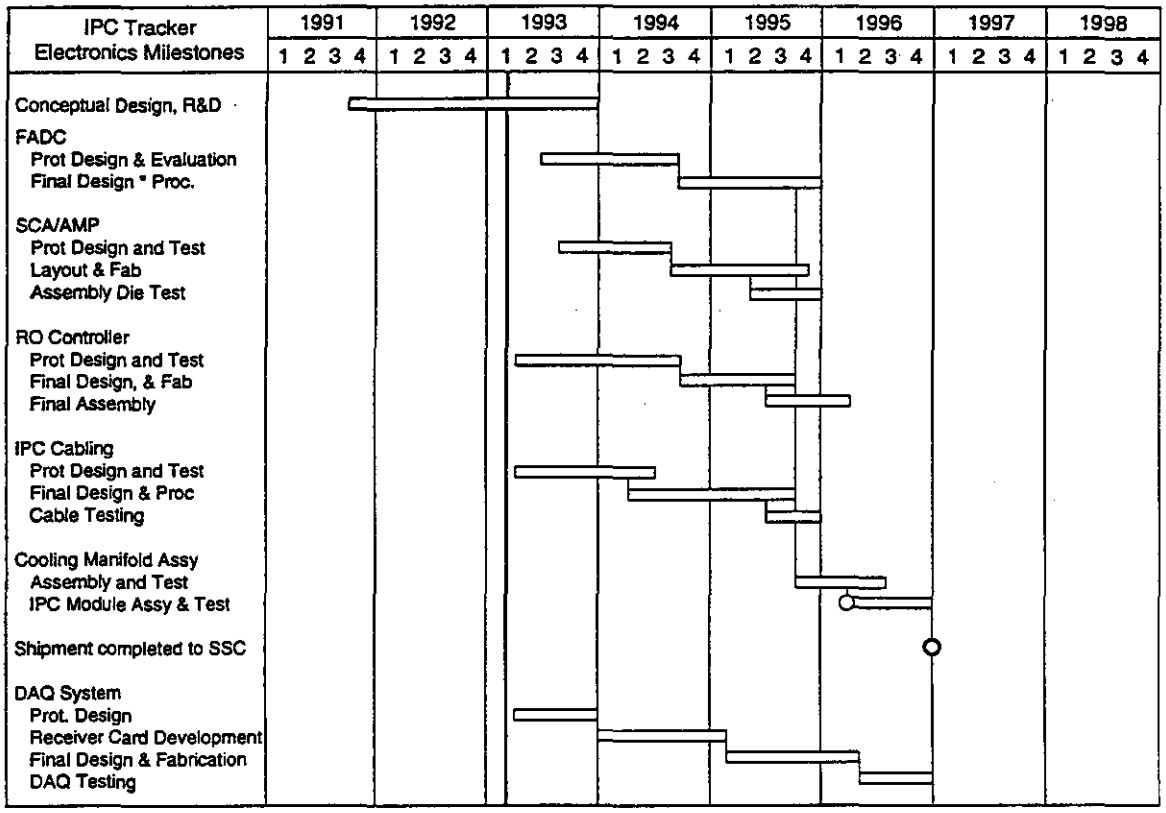

Figure 9-5 IPC Tracker Electronics Schedule